Cenozoic evolution of the Pamir Salient; timing, mechanisms and paleo-environmental impacts: Constraints from the Aertashi section, western Tarim Basin.

Tamsin Blayney

Thesis submitted for the award of PhD

June 2017

"Twenty years from now you will be more disappointed by the things you didn't do than the things you did. So throw off the bowlines, sail away from the safe harbour, catch the trade winds in your sails. Explore .... dream.... discover". Mark Twain

Table of Contents

Acknowledgements:

Although I am responsible for this thesis, it represents collaboration between myself and a team of people who have helped shape ideas and formulate conclusions, assisted in analysis and data collection and provided emotional support.

This thesis would not have been possible without the help and support of a number of people to whom I owe a great debt. In light of this I would like to make the following acknowledgements:

First and foremost, I would like to thank my funding body NERC and Metropole Rennes for the financial support provided for this project.

I would like to say a very special thank you to my supervisor Dr. Yani Najman. Yani has been my 'rock' throughout this process, from inspiring me to take this project on in the first place, to her constant encouragement and support. Not only is she an amazing supervisor, she has supported me above and beyond just this role. Thank you for keeping me going after the birth of my son and holding me up through the tiredness of new parenthood and for reinstalling in me the belief that I can do it when the road felt so long.

A special thank you also goes to my supervisor Dr. Guillaume Dupont-Nivet, who has worked tirelessly to support me in the field and beyond. I would also like to thank you especially for your support during my stay in France. I have really enjoyed our passionate debates and conversations and couldn't have done this without you.

My fieldwork in China was one of the most amazing and challenging experiences of my life, camping in the foothills of the Pamir was incredible and tough. I would like to say a special thank you to my 'p'mag angels' Dr Laura Fielding and Annabel Bernard. They were the most incredible, hard-working team! I could not have done this without them. We laughed, we cried, we made it. I would also like to thank my colleague, Chris Kneale, for taking the time out of his own fieldwork to assist me with sample collection.

A special thank you also to my colleague, Dr. Guangsheng Zhuang (GZ), it is thanks to him that I have a PhD at all. When my samples were lost travelling back and forth from Kashgar to Beijing it is GZ who worked tirelessly to make sure they were all retrieved, accounted for and couriered to the UK. He was incredible.

I would also like to say a special thank you to Professor Ed Sobel for his advice and input into this project. It has been a privilege to have benefited from the input of a true 'Pamir pioneer'. Thank you for keeping us in line and balanced, you are an encyclopaedia of knowledge which has been fantastic to tap into.

I would also like to thank my co-authors Dr Jean-Noël-Proust, Dr Ian Millar, Professor Andrew Carter, Dr Martin Rittner, Dr Eduardo Garzanti, Dr Sergio Andò, Dr Pierrick Roperch, Niels Meyer, Dr Peter Wynn and Dr Simon Kemp for their support, advice and input into this project.

For their technical support I would like to thank Dr Nathan Halcovich, Dave Hughes, Professor Will Blake, Dr Alex Taylor and Dr John Crosse.

To my family, a special thank you, I know that my mum Julie would do anything to help me to achieve this dream. Thank you for your financial, emotional and physical support in looking after me and Alfie throughout this process. From the time you drove 50 miles to submit my first assignment to the Open University you have always supported me proudly and been my biggest fan. I wouldn't be who I am today without you and I am so lucky that you are my mum.

To my sister and best friend Samantha, you have been my backup and my friend and I am so grateful for everything you have done for me throughout my PhD and beyond, you are my inspiration and my role model.

To my Nan Alice, I know how proud you were of me. You supported me financially and emotionally. I am so sorry you didn't live to see me make it to the end, but I am glad that in your final days I was able to tell you that I made it and see you proudly saying "Dr Blayney". I know you are watching over me and Alfie now with a smile knowing I did it.

To my husband Tom, thank you for all your support. I couldn't have done this without you. You kept me going through the hard times and I am very lucky to have you.

Thank you also to Shirley and Barry for their support in taking care of Alfie so that I could work.

I would also like to say a special thank you to all the amazing friends and colleagues that I have made along the way.

To Natalie and Marianna, it has been a privilege to share this journey with you, thank you for being there for me, for those many cups of tea and conversations, and for your never ending support. Thank you also to all my colleagues who I now get to call my friends, Ann, Ceri, Laura, you have kept me going through the dark days and celebrated the achievements with me. Thank you for making me laugh and keeping me sane.

Finally a tribute to my dear friend Gwladys, we shared our PhD journey together, she was always there for me, be it a shoulder to cry on or just a friend to laugh with. We talked geology and shared countless coffees and chocolate cake. I will think of her and miss her always and will try to live by her amazing example.

Statement of work

This thesis is my own work and has not been submitted for the award of a higher degree elsewhere. This thesis contains sections of work that have been published and/ or have had additional contributions from external sources for the purposes of publication. A summary of all work that is not my own is as follows:

Chapter 3: The sedimentology of the Aertashi section.

- Detailed sedimentology and composition of sedimentary logs and clast counts was conducted by myself with advice from Dr Jean-Noèl-Proust of Géosciences Rennes, UMR-CNRS 6118, Université de Rennes 1, Rennes, France.

Chapter 4: Pamir tectonic evolution recorded in the western Tarim Basin: a combined magnetostratigraphic and sedimentological analysis of the Aertashi sedimentary section (China).

- Magnetostratigraphy sampling, sample processing, demagnetisation and initial magnetic directional analysis was conducted by myself. Data processing was conducted by Dr Guillaume Dupont-Nivet of Géosciences Rennes, UMR-CNRS 6118, Université de Rennes 1, Rennes, France, and Department of Earth and Environmental Sciences, Potsdam University, Germany, and Key Laboratory of Orogenic Belts and Crustal Evolution, Ministry of Education, Beijing, China. Correlation of results to the geomagnetic polarity timescale of Gradstein et al. (2012) was conducted by myself and Guillaume Dupont-Nivet collaboratively.
- Anisotropy of magnetic susceptibility sampling and analysis was conducted by myself, data processing and interpretation was conducted by Dr. Pierrick Roperch of Géosciences Rennes, UMR-CNRS 6118, Université de Rennes 1, Rennes, France
- Interpretation of results and discussion for the paper was conducted by myself in consultation with Dr Guillaume Dupont-Nivet, Dr Yani Najman and Prof. Ed Sobel.

Chapter 5: Indentation of the Pamir with respect to the northern margin of Tibet: constraints from the Tarim Basin sedimentary record.

- Zircon Fission Track sample preparation and interpretation of results was conducted by myself, analysis and data reduction was provided by Professor A Carter and Dr Martin Rittner at the department of Earth and Planetary Sciences, Birkbeck College, Mallet Street, London, WC1E, 7HX, UK and the London Geochronology Centre, Department of Earth Sciences, University College London, Gower Street, London, WC1E 6BT, UK
- Zircon U-Pb sample preparation, analysis and interpretation of results was conducted by myself, technical support and data reduction was conducted by Dr Martin Rittner of University College London, Gower Street, London, WC1E 6BT, UK.
- Heavy mineral preparation and interpretation of results was conducted by myself, analysis was conducted by Dr Sergio Andò and Dr Giovanni Vezzoli of Laboratorio di Petrografia del Sedimentario, Dipartimento di Scienze Geologiche e Geotecnologie, Università di Milano-Bicocca, Piazza della Scienza 4, 20126 Milano, Italy
- Petrography results were interpreted by myself with analysis and data interpretation by Dr Eduardo Garzanti, Laboratorio di Petrografia del Sedimentario, Dipartimento di Scienze Geologiche e Geotecnologie, Università di Milano-Bicocca, Piazza della Scienza 4, 20126 Milano, Italy.
- Sm-Nd analysis, sample preparation, analysis and data interpretation was conducted by myself with technical support from Dr Ian Millar of the NERC Isotope Geosciences Laboratory, BGS Keyworth, Nottingham NG12 5GG, UK.
- Interpretation of results and discussion for the paper was conducted by myself, in consultation with Dr Yani Najman, Dr Guillaume Dupont-Nivet and Professor Ed Sobel.

Chapter 6 - The Climate Evolution of the Western Tarim Basin during Pamir indentation

- Stable isotopes sample preparation, analysis and interpretation of results was conducted by myself with technical support and data reduction from Dave Hughes of Lancaster University.
- X-Ray Fluorescence sample preparation, data analysis, data reduction and interpretation of results was conducted by myself with technical support from Dr Alex Taylor of the University of Plymouth.
- X-Ray Diffraction sample preparation, analysis and interpretation of results was conducted by myself with technical assistance from Dr Nathan Halcovich of Lancaster University, data processing was conducted by Dr Simon Kemp of the British Geological Survey, Keyworth, Nottingham NG12 5GG, UK.
- Overall interpretation of results and discussion for the paper was conducted by myself in consultation with Dr Yani Najman.

Abstract

The formation of the Himalayas and surrounding mountain ranges is one of the most significant tectonic events of the Cenozoic, with far reaching impacts on both regional and global climate. The Pamir represents the indented westward continuation of the northern margin of the Tibetan Plateau making them a key study area to examine internal deformation and intracontinental subduction processes. Yet the tectonics of the Pamir Salient is poorly understood. Much debate is ongoing, regarding the extent of indentation and mechanisms driving uplift of the Pamir. This project seeks to provide constraints on the timing of Pamir evolution and examine the impact of Pamir formation on the regional climate using a variety of techniques to date and interpret observed variations in terms of provenance, tectonism and climate, the results of which are presented here.

At ~41 Ma the Tarim Sea retreated from the Aertashi region. Continental deposition ensued, dominated by the western Kunlun to the south.

By 24-22 Ma, basinward expansion of the NW margin of Tibet coincides with the initiation of Pamir indentation. Activation of strike slip faulting, growth strata and exhumation along the Kashgar-Yecheng Transfer System is evidenced in the Aertashi region which may be linked to a pull-apart basin.

By ~18.5 Ma, the onset of northward thrusting of the Kunlun hinterland and southward migrating foreland of the Tian Shan positions the Aertashi region in the depocenter of the Tarim Basin.

By ~15 Ma, the Pamir Salient had propagated sufficiently far north, that the north Pamir, and by 11 Ma the Central Pamir were proximal to Aertashi.

The Eocene – mid Miocene climate in the Tarim Basin was highly seasonal with evidence of increased aridity. Aridification was interrupted by a short period of increased humidity at ~17.6-15 Ma which can be linked to the mid-Miocene climate optimum, or a facies change. Limited comparative studies make climatic conclusions tentative.

Introduction

Figure 1 Overview of the foothills of the Pamir mountain range

The India – Asia collision is one of the most geologically significant events of the Cenozoic era. Today this collision zone is home to some of the highest mountain ranges in the world, including the Himalayas and Tibetan Plateau.

The Himalayan range is formed by an amalgamation of terranes that progressively collided into Asia during the Mesozoic and early Cenozoic as a result of the closure of the Tethys Ocean, culminating in the final collision of India with Asia at ca. ~ 59-55 Ma (e.g. Najman et al., 2010, Hu et al., 2016 and references therein)

At the western syntaxes of the Himalayan ranges lies the Pamir and Western Kunlun Mountains, which form an orocline intruding into the western Tarim Basin (Figure 2).

Today the Pamir forms a prominent indenter separating the western Tarim Basin from the Tajik Basin and is a type example of intracontinental subduction. It has been indicated (Burtman and Molnar, 1993), that the Pamir has undergone ~300 km of Cenozoic shortening and has absorbed ~600-900 km of convergence since the India – Asia collision (Schmidt et al., 2011). Today the Pamir thrust currently absorbs more than one third of the total convergence between India and Asia making it host to one of the highest strain rates in the region (Schurr et al., 2014b).

Although there is a breadth of knowledge from the Himalayas and Tibetan Plateau, studies from the western syntaxis and the north-western margin of Tibet are limited.

Access to the western margins of the Pamir is limited due to politically sensitive borders such as Afghanistan and Pakistan. Along the eastern margins of the Pamir and western Tarim Basin, understanding of the internal deformation within central Asia is hampered by poor age control and the limited number of studies in this region. As a result, our understanding of the timing of uplift and evolution of the Pamir and Western Kunlun is limited.

The Pamir range itself has a complex deformation history linked to a double subduction zone which lies beneath this area of thickened crust, and has a number of models and mechanisms proposed for its formation and unusual curvature (e.g. Küfner et al., 2016, Sobel et al., 2013).

The subduction model suggests Pamir formation occurred through back arc processes as a result of slab break off of the northward dipping Indian plate at ca. 25 Ma (Sobel et al., 2013). This resulted in the activation of southward propagating subduction and roll back of the Alai plate beneath the Tian Shan. The crustal delamination model (Bird, 1979, Küfner et al., 2016) suggests that under thrusting of the Indian plate beneath the Pamir resulted in delamination and roll back of the Alai plate creating a detachment anomaly beneath the crust.

Both models have different predictions regarding the timing and evolution within the Pamir (models are described in detail in Chapter 1.4.2). Therefore further understanding of the timing of events within Pamir and Western Kunlun would allow the distinction between these two models.

The indentation of the Pamir range also had a major impact on the climate in central Asia. Prior to India – Asia collision the Tarim Basin was occupied by a vast internal sea known locally as the Tarim Sea, part of the Para-Tethys. By ~37 Ma (Bosboom et al., 2011) this internal sea had retreated from the Tarim Basin removing a critical moisture source from central Asia. Subsequent indentation and uplift of the Pamir range effectively cut off the Tarim Basin from the rest of western Asia. Coincident uplift of the Himalayan ranges and the formation of the Tibetan Plateau created orographic barriers to central Asia, resulting in a reorganisation of Asia air circulation, restricting the flow of moisture into continental Asia (Zhang et al., 2007c). This resulted in the intensification of the Asian monsoons and drove aridification of the

Asian interior, transforming the Tarim Basin into one of the largest sand shifting deserts in the world, the Taklimakan.

Dust from this desert contributes substantially to the global aerosol system, playing a significant role in modulating global climate (Uno et al., 2009). However the timing of desertification along with constraining the onset and evolution of aridification in the Asian interior is contentious. Ages proposed for the onset of desertification range from ~26.7 Ma (Zheng et al., 2015a) to ~3.4 Ma (Sun et al., 2011).

Coincident with regional climate change in central Asia was a period of global climate change making it difficult to deconvolve the two effects.

The Paleogene marks a key shift in global climate: the opening of tectonic seaways surrounding Antarctica resulted in the thermal isolation of the Antarctic continent, leading to the formation and expansion of extensive ice sheets and a reorganisation of ocean currents (e.g. Livermore et al., 2005, Barker et al., 2007, Barker, 2001, Lagabrielle et al., 2009, Scher and Martin, 2006, Kennett, 1977, Exon et al., 2004). In addition, during the mid-Eocene, large amounts of carbon were removed from the ocean/atmosphere system through increased siliceous plankton productivity and marine carbon burial (Pearson and Palmer, 2000), effectively reducing the greenhouse effect. These effects combined drove a long term change in the climate from greenhouse to icehouse conditions.

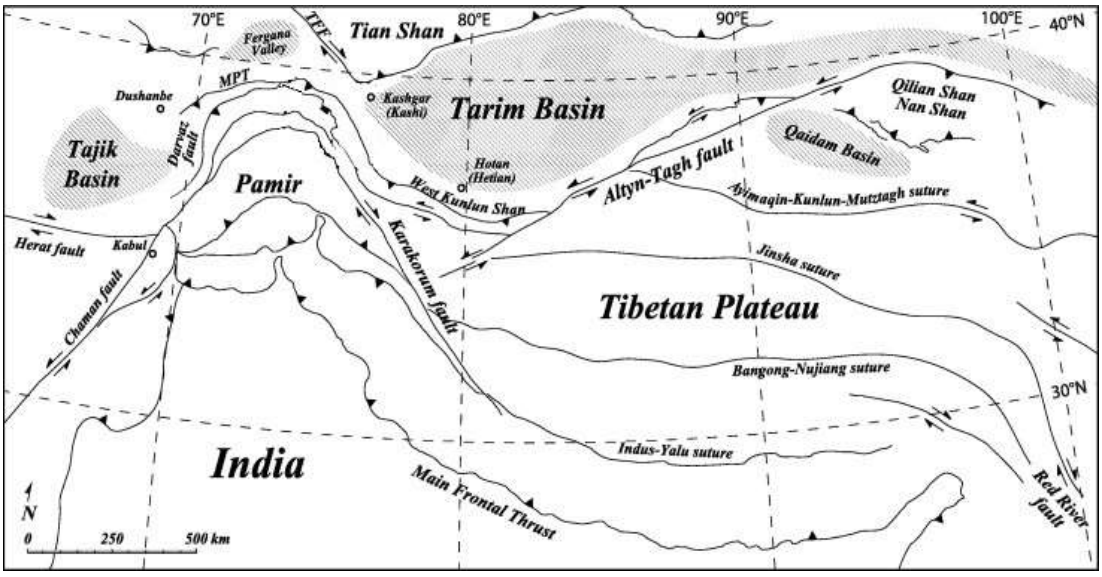

Figure 2 Overview of the India – Asia collision zone adapted from Bershaw et al. (2012) with fault kinematics for major faults and suture zones indicated.

By understanding the coincident timing and mechanisms driving the tectonic evolution of the Pamir range alongside changes in localised climate, we can start to unravel the complex history of post-collisional, central Asian evolution both tectonically and climatically, furthering our understanding of these complex processes.

Project Aims and Objectives

This project seeks to achieve a greater understanding of the evolution of the Pamir mountain range, which occurred sometime in the Oligo – Miocene, and examine the effects of Pamir indentation and uplift on both regional and global climate. The project focusses on constraining the timing of Pamir indentation using a sedimentary record that spans the Eocene through to mid Miocene and therefore records the transition of the Western Tarim Basin from internal sea to isolated desert. This record is examined in terms of provenance, tectonism and climate using a comprehensive multidisciplinary approach which will provide a reliable and accurate correlation of the major environmental and paleogeographical changes in geological time.

The specific objectives of this project are to:

1. Construct a palaeoenvironmental depositional model governing the sedimentation along the western margin of the Tarim Basin. This will provide the basis for examining the evolution of the depositional environment in response to tectonic and climatic events in the region.
2. Provide detailed age control for the timing of deposition in the subject area in order to examine the relationship between the depositional model and Pamir evolution.
3. Examine the sediments in terms of provenance in order to constrain the first instance of Pamir derived material in the subject area.
4. Examine the sediments in terms of climate to constrain the relationship between Pamir evolution, sedimentation and regional climate change.

Thesis Outline

Chapter 1 – Geological Background

This chapter provides a detailed summary of the previous work carried out in order to understand the paleoenvironmental, tectonic and global significance of central Asia during the Eocene to Miocene.

Chapter 2 – Methods

This chapter summarises in detail the methods and techniques used in this study.

Chapter 3 – The sedimentology of the Aertashi section.

This chapter presents a detailed summary of the sedimentology for the Aertashi section with a full grain scale log identifying the locations of all samples used in this study, alongside more detailed sedimentological logs for each 'type' formation with detailed analysis and interpretation.

Chapter 4 – Indentation of the Pamir with respect to the northern margin of Tibet: constraints from the Tarim Basin sedimentary record.

Here presented are the results of the detailed provenance study for the Aertashi section which examines the links between source terrane evolution of the Western Kunlun and Pamir ranges and deposition in the western Tarim Basin. A model is developed providing constraints on the timing and evolution of Pamir indentation.

Chapter 5 – Pamir tectonic evolution recorded in the western Tarim Basin: a combined magnetostratigraphic and sedimentological analysis of the Aertashi sedimentary section (China)

This chapter seeks to provide a detailed and revised magnetostratigraphic timeline for the Aertashi section, and includes anisotropy of magnetic susceptibility and detailed sedimentology. A time-stepped tectonic model is developed for the western Tarim Basin and Pamir from the Eocene through to mid Miocene.

Chapter 6 – The Climate Evolution of the Western Tarim Basin during Pamir indentation.

The transformation of the Asian climate are discussed using a series of climate proxies including clay mineralogy, stable isotopes and geochemical data in association with our provenance and tectonics studies to examine the relationship between tectonics

and climate. This is put into context of changes in global climate throughout the Cenozoic.

Chapter 7 – The relationship between tectonics and climate – Discussion

Here, all of the data from the Aertashi section is collated and discussed and the evolution of the Pamir mountain range is examined in terms of climatic changes in central Asia throughout the Cenozoic.

1. Geological Background

1.2 The Himalayas and Tibetan Plateau

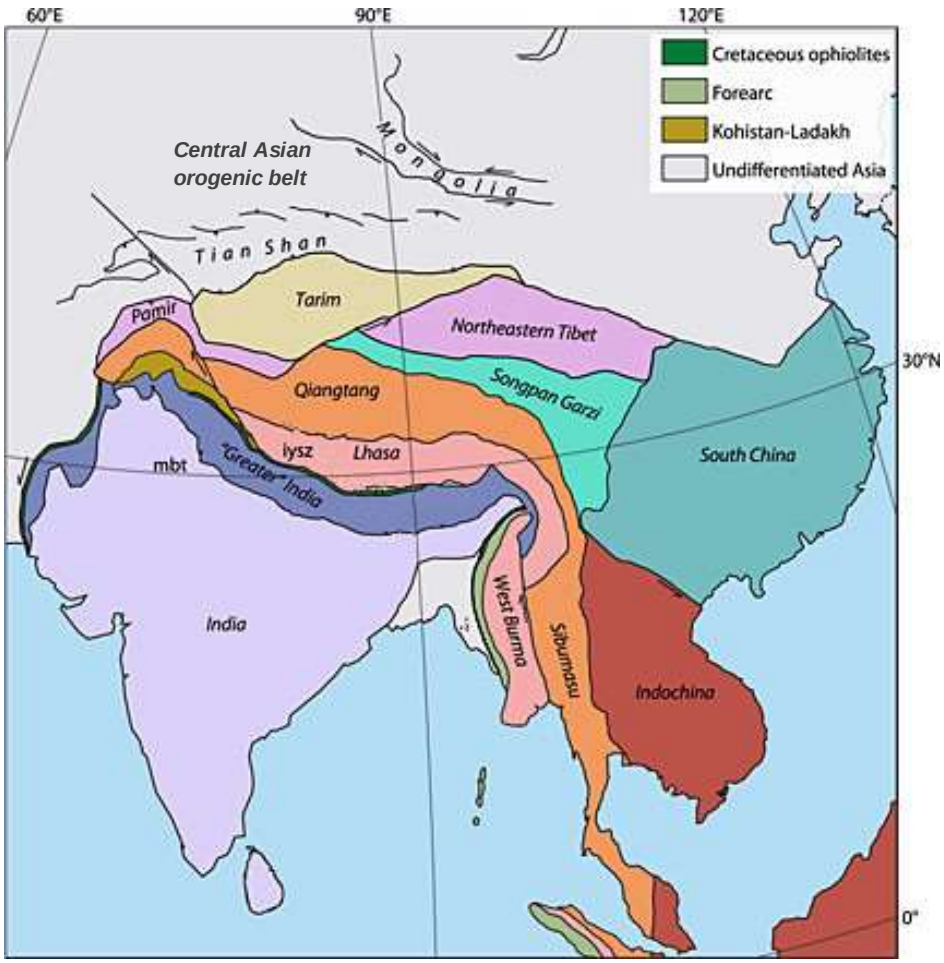

Figure 1.1 Simplified tectonic map of the India-Asia collision zone (originally modified from Van Hinsbergen et al. (2012)) (Huang et al., 2015). IYSZ: Indus-Yarlung Suture Zone; MBT: Main boundary thrust.

The Himalayan mountain belt is one of the most impressive active collision zones ever recorded, and the high Tibetan Plateau itself is home some of the highest mountains in the world. The Himalayas therefore provide a key study area to examine how the crust deforms during continent – continent collision.

The Himalaya formed as a result of a complex series of tectonic events beginning in the neo Proterozoic with the formation and break-up of the Rodinia continent and the subsequent Palaeozoic - Mesozoic amalgamation of a series of tectonic blocks (Roger et al., 2010), island arcs and remanent ocean basins (Figure 1.1). This progressively resulted in the closure of the Tethys Ocean, culminating in the final collision of India – Asia in the Cenozoic (Allegre et al., 1984, Searle, 1986, 1987, Windley, 1988, Windley et al., 2007, Metcalfe, 2013).

The timing of the final collision of India – Asia has been the subject of much debate. The general consensus is that final collision occurred during the Eocene at ~59-55 Ma (e.g. Hu et al., 2016, Najman et al., 2010 and references therein). However a range of ages have been proposed from 65 Ma (Jaeger et al., 1989) to 35 Ma (Aitchison et al., 2007).

One of the issues with constraining the timing of India – Asia collision stems from the definition of 'collision'. Initial models assume collision since ~59 Ma between the 'Greater India' representing a northwardly larger Indian continent before subsequent subduction, and 'Greater Asia' representing a southwardly larger Asia before subsequent N-S contraction (e.g. Argand, 1924, Allegre et al., 1984, Molnar and Tapponnier, 1975). However, this 'larger India' model requires ~1000 km of Asian shortening and ~2000 km of Indian continental subduction depending on paleomagnetic estimates (see Dupont-Nivet et al., 2010).

This has led to a range of alternative models with multiple collisions proposed. In the first set of models initiated by Ali and Aitchison (2006), Greater India collides first with a forearc at low latitudes around 60-50 Ma. Subsequently, the associated back-arc basin is subducted beneath Greater Asia until the harder continental collision of the Greater India - forearc stack with Greater Asia. This is estimated to have occurred by 45 to 35 Ma depending on the respective size of Greater India and Greater Asia. Another model proposed by Van Hinsbergen et al. (2012) assumes an initial 52 Ma collision between Greater Asia and a continental sliver that had previously drifted off Greater India. Following the subduction of this basin, a second hard collision between continental India and Greater Asia is estimated around 23 Ma.

The sequential amalgamation of terranes followed by the final collision of India – Asia has resulted in a complicated sequence of crustal thickening and extrusion, forming a deformation zone which extends from the central Asian orogenic belt in the north to Indo-China in the south (Figure 1.1).

The formation of the high Tibetan Plateau is complex. The plateau itself is composed of a series of accretionary blocks which began to form in the neo Proterozoic following the formation and break up of Rodinia (Roger et al., 2010 and references therein) followed by subsequent accretion during the Paleozoic and Mesozoic

culminating in the closure of the Tethyan ocean and the collision of India with Asia in the Cenozoic.

From the Tarim Basin in the north to India in the south these 'blocks' comprise the Kunlun terrane (described in detail in 1.3.1), Songpan – Ganze – Hoh Xil terrane (separated by the Kunlun fault in the north and the Jinsha suture in the south), the Qiangtang terrane (bound by the Jinsha suture in the north and the Bangong – Nujiang suture in the south), the Lhasa terrane (bound by the Bangong-Nujiang suture in the north and the Yarlung-Zangbo suture in the south) and the Himalaya (bound by the Yarlung-Zangbo suture in the north and the Main Boundary thrust in the south) (Figure 1.2).

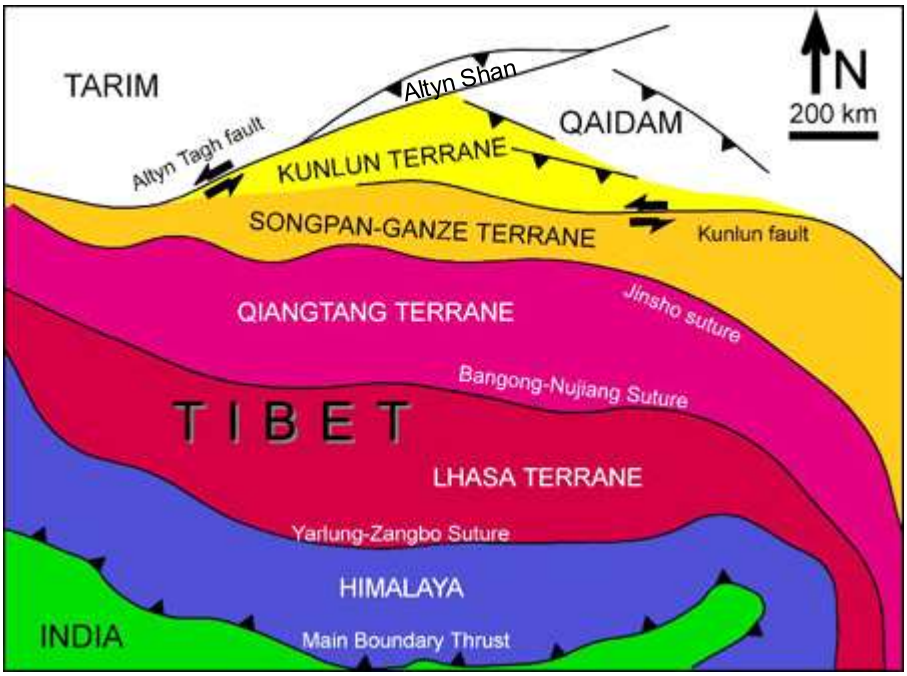

Figure 1.2 A simplified summary of the main tectonic blocks and sutures that comprise the Tibetan plateau and Himalaya (Ozacar, 2000).

However, deformation in central Asia was not continuous throughout this timeframe with a significant lack of major tectonic events within the Songpan Ganzi, Kunlun and Yidun blocks between c. 150 and 30 Ma (Roger et al., 2011).

Subsequent Tertiary tectonic activity resulting from the continued indentation of the Indian continent into Asia (Roger et al., 2010) has resulted in the reactivation of a number of the major Paleozoic and Mesozoic faults in this region.

As a result of this complex amalgamation of terranes, there is much debate on the timing and mechanisms which have led to the modern day elevation of the plateau. There are two main theories; the first considers the Tibetan Plateau to have uplifted in the Cenozoic as a result of the Indo-Asian collision. Models range from plateau uplift in the Oligocene and Miocene (Chung et al., 1998, Tapponnier et al., 1986, Copeland et al., 1987) to a 'late uplift' model, which suggests Plateau uplift in the late Pliocene and Pleistocene (Zheng et al., 2000, Hsu, 1976). The second assumes that uplift, at least in part occurred prior to the India – Asia collision with suggestions that the Plateau was already forming elevated topography since the Early Mesozoic (e.g. Murphy et al., 1997, Zhang et al., 2007a, Lease et al., 2012, Roger et al., 2010, Roger et al., 2011, Jolivet et al., 2015)

Theories proposed for 'how' the Tibetan Plateau uplifted are equally contentious.

In the 'under-thrusting' model, Argand (1924) suggests that the Tibetan Plateau is under-thrusted by the Indian lithosphere, with a variation on this model suggesting the entire delamination of the Tibetan mantle (Bird, 1979). This model predicts that the northward progression of surface uplift from the suture zone would progress at a similar rate to the northward motion of the Indian plate.

Gravitational collapse has been proposed by Dewey et al. (1988) in which lithospheric extension along orogenic belts contain structural inhomogeneities, and suffer extensional orogenic collapse resulting from isostatically compensated elevation. Collapse occurs where rapid thinning of the shortened thermal boundary conduction layer occurs beneath an orogen, resulting in rapid uplift.

In the fluid continental underplating model of Powell (1986), from 20 to 5 Ma the Indian lithosphere subducted into the mantle beneath Tibet, followed at 5 Ma by the uplift of the Indian continental lithosphere toward the base of the Tibetan crust. This model suggests that the uplift of the Tibetan Plateau was uniform and isochronous at ~2 Ma. This model also assumes a fluid mantle lithosphere and asthenosphere overlie the subducted (and subsequently uprising) continental crust.

In the Continental injection model of Zhao and Morgan (1987), the Tibetan Plateau rose as an integral unit through hydraulic processes, as a result of the injection of India into a low –viscosity 'fluid' lower Asian crust. This model predicts that significant topography did not appear until the middle Miocene.

In the distributed shortening model (see Harrison et al., 1992 and references therein), about 50% of Tibetan lithosphere shortening produced the thickened Tibetan crust, with predictions that the lithosphere thickened and uplifted progressively northward from the suture. Subsequent removal of thickened mantle lithosphere resulted in further uplift of the entire plateau (Clark et al., 2004).

More recently, Tapponnier et al. (2001) attributed the high elevations in Tibet to localised sheer between coherent lithospheric blocks. In this model, the crust thickened, decoupling from the mantle beneath. This resulted in sediment infilling of intermontane basins. Magmatic belts progressively 'young' towards the north, implying a sequence of subducting 'slabs' which was oblique, accompanied by extrusion along the left lateral strike-slip faults.

Each of these models make specific predictions about the timing of Tibetan uplift initiation, the evolution of crustal thickening, and the timing of full crustal thickness in the Tibetan Plateau which as yet remains unresolved.

The arcuate shape and internal deformation within the Tibetan Plateau has been linked to the development of the Himalayan thrust belt via a number of models (Figure 1.3). These include; Oroclinal bending of the Himalayan thrust belt resulting in arc – parallel extension within the Himalaya and Tibet and right slip faulting in the western Himalaya (Klootwijk et al., 1985, Ratschbacher et al., 1994, Li and Yin, 2008) (Figure 1.3A); thrusting and arcuate geometry of the Himalayan thrust belt, through radial spreading of the Himalaya arc (Seeber and Armbruster, 1984, Molnar and Lyon-Caen, 1988, Murphy and Copeland, 2005) (Figure 1.3B); oblique convergence between Indian and the Himalayan arc, which is divided into an arc-normal component (thrust faulting) and an arc-parallel component (extensional and strike-slip faulting) (Seeber and Armbruster, 1984, Seeber and Pêcher, 1998, McCaffrey and Nabelek, 1998) (Figure 1.3C); and in the continental extrusion model (Tapponnier and Molnar, 1976, Molnar and Tapponnier, 1975, Molnar et al., 1993) as much as 40 to 60% (Tapponnier et al., 1986) of the northward convergence of India into Eurasia has been taken up by lateral extrusion along strike-slip fault systems. Extrusion through the rotation of a series of blocks about a vertical pole has also been proposed (Dewey et al., 1988, England and Molnar, 1990) (Figure 1.3D).

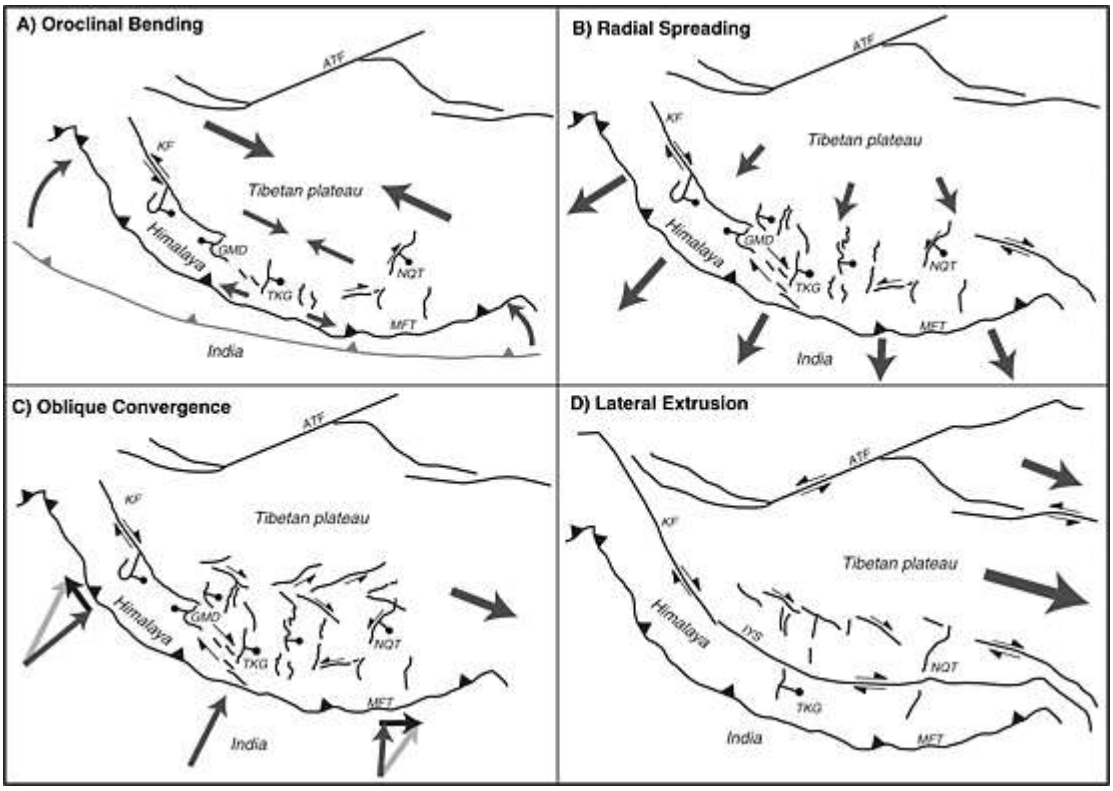

Figure 1.3 Models of Himalayan and south Tibetan kinematic development. (a) Oroclinal bending, (b) radial spreading, (c) oblique convergence, and (d) lateral extrusion. ATF - Altyn Tagh fault; KF - Karakoram fault; GMD - Gurla Mandhata detachment; IYS - Indus-Yalu Suture; MFT - Main Frontal Thrust; NQT - Nyainqentanglha Shan; TKG - Takkhola Graben by McCallister et al. (2014)

Irrespective of the model, the Cenozoic continental collision of India into Asia and the continued northwards motion of India into Asia are responsible for the reactivation of the Himalaya-Tibetan Plateau orogeny and propagation of deformation to the outer parts of the collision zone including the northern margin of Tibet, Tarim Basin, Tian Shan and Pamir Plateau.

Today, estimates of Cenozoic shortening strain (based on seismic reflection profiles) indicate that more than half of the total strain has been absorbed by the northern margin of the Tibetan Plateau, indicating that most of the present-day convergence between North China and Tibet is focused along this margin (Zuza et al., 2016).

The northern margin of Tibet is dominated by the Altyn Tagh fault system which is the longest active strike-slip fault of Asia (Tapponnier and Molnar, 1977, Peltzer and Tapponnier, 1988, Meyer et al., 1996, Sobel and Arnaud, 1999), separating the Tarim Basin in the north from the Qaidam Basin and Qiantang Terrane in the south (Figure 1.2). However, the timing of initiation of the left-slip ATF system is controversial with ages ranging from post-middle Jurassic (Sobel et al., 2001, Ritts and Biffi, 2000)

to ~ 15 Ma (Wang, 1997, Yue et al., 2005) with a range of ages in between including ~ 49 Ma (Yin et al., 2002), 40±10 Ma (Jolivet et al., 2001).

India – Asia collision also resulted in the reactivation of left lateral shear along the Altyn Tagh fault system at ~24 Ma (Chen et al., 2002). In addition, the Altyn Tagh fault system has been suggested to act as an oblique lithospheric plate boundary between the Tibetan Plateau and the Tarim Basin with the lithosphere of the Tarim Basin 'plunging' beneath the Tibetan Plateau (Wittlinger et al., 1998).

Uplift along the northern margin of Tibet has been suggested by Clark et al. (2010) to have occurred early in the Cenozoic with Eocene age thrust fault along the North Qilian thrust and Liupan Shan thrust system situated along the north eastern margins of the Tibetan Plateau. More extensive exhumation and deformation is reported along the northern margin of Tibet, the Tarim Basin and southern Tian Shan at ~25-20 Ma, constrained by apatite fission track data which records exhumation along the western Kunlun and southern Tian Shan (Sobel and Dumitru, 1997, Sobel et al., 2006, Jolivet et al., 2010), the eastern Kunlun (Yuan et al., 2006), the west Qilian Shan and Xining Basin (Xiao et al., 2012a) and the northern Qinling margin (Liu et al., 2013) at this time. This widespread deformation has been related to the initiation of indentation of the Pamir Salient (Bande et al., 2015) and widespread uplift of the Tibetan Plateau (Xiao et al., 2012b).

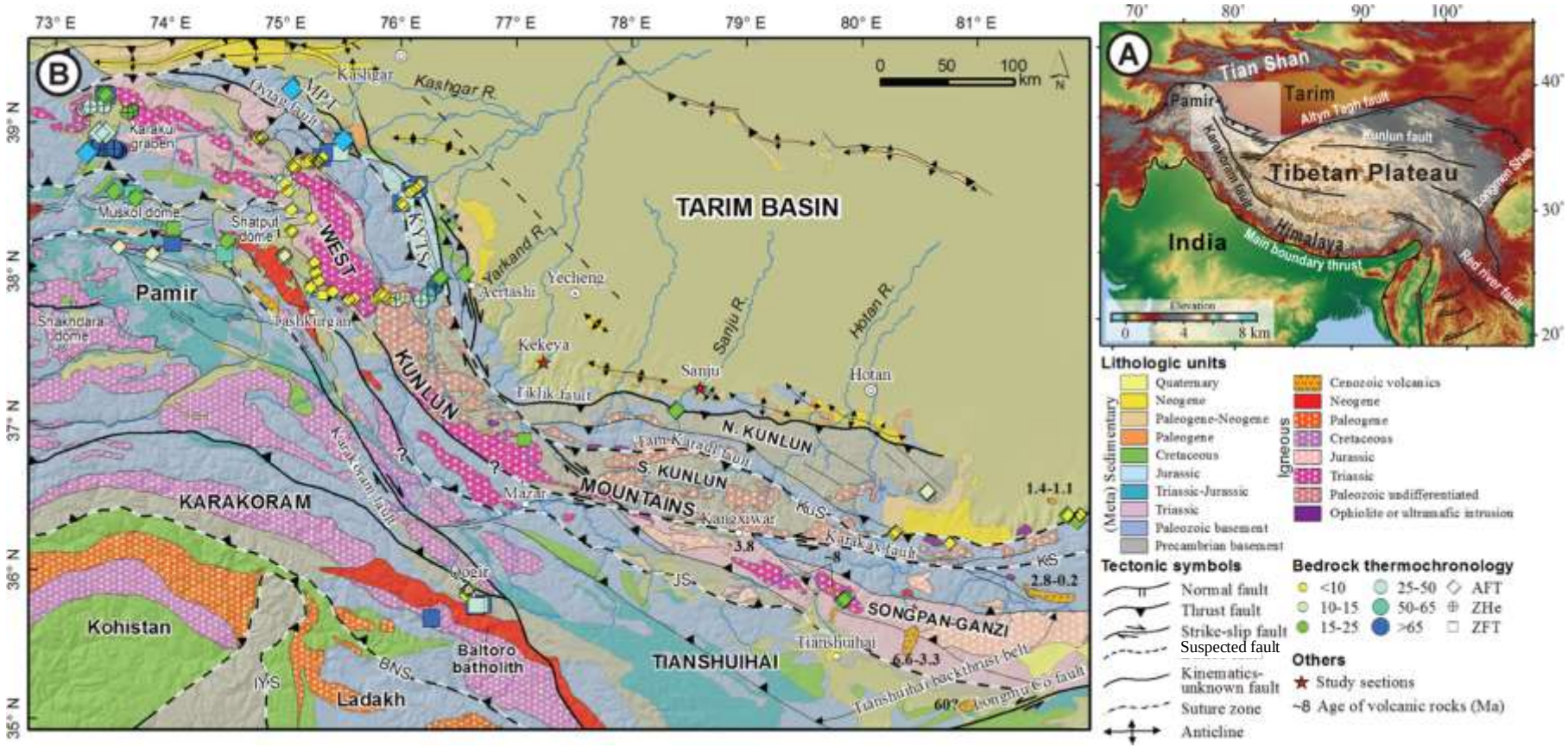

Figure 1.4 (A) Topography of the India–Asia collision zone. (B) Geological sketch map of north-western Tibet from Cao et al. (2015) BNS: Bangong–Nujiang suture; IYS: Indus–Yarlung suture; MPT:Main Pamir Thrust; JS: Jinsha suture; KS: Kunlun suture; KuS: Kudi suture; KYTS: Kashgar–Yecheng transfer system

1.3 Western Kunlun mountain range

The Western Kunlun mountain range (WKL) forms the northern margin of the western Tibetan Plateau, extending into the south-eastern Pamir (Figure 1.4). Very little work has been conducted on the western margin of the WKL to constrain the timing of crustal thickening and uplift of the range. However detrital and basement zircon fission-track ages (Cao et al., 2015, Jolivet et al., 2001) and the presence of well-developed Triassic to lower Jurassic magmatism (Matte et al., 1996) from the south western margin of the Tarim Basin, suggest that unroofing of the Kunlun terrane occurred in Triassic-early Jurassic times. This is related to the late-Triassic collision between the Qiantang and Kunlun blocks (Jolivet et al., 2001), indicating that an ancient WKL range is likely to have emerged above sea level by this time (Cao et al., 2015).

Subsequent periods of accelerated uplift of the WKL have been interpreted based on detrital zircon fission track ages (Cao et al., 2015). These show early Cretaceous exhumation related to thrusting along the Tam Karakul fault system (Figure 1.4), with a second phase of uplift related to activation of the Main Pamir – Tam Karakul thrust belt (Figure 1.4) during the middle – late Mesozoic to early Cenozoic.

These faults then became re-activated during the late Oligocene – early Miocene as a result of expansion of the Tibetan Plateau (Cao et al., 2015, Jiang et al., 2013, Jiang and Li, 2014, Sobel and Dumitru, 1997, Wang et al., 2003, Matte et al., 1996). The magnitude of Cenozoic upper crustal shortening within the WKL is estimated to range from 24- 54 km (Jiang et al., 2013) to 100 km (Cowgill, 2001).

1.3.1 Western Kunlun Terranes

The West Kunlun mountain range consists of a number of terranes accreted during the Paleozoic and Mesozoic including: the North Kunlun, South Kunlun, Songpan-Ganzi and Tianshuihai terranes (Yin and Harrison, 2000, Matte et al., 1996, Searle, 1996, Pan, 1990, Ding et al., 1996) (Figure 1.4).

The North Kunlun is bound by the Tiklik fault in the north and the Tam Karakul fault in the south and along with the South Kunlun consists predominantly of Precambrian-Palaeozoic metasedimentary rocks and Palaeozoic and Triassic plutons (Cowgill et al., 2003, Liu et al., 2015, Schwab et al., 2004, Xiao et al., 2003, Xiao et al., 2002, Youngun and Hsü, 1994) (Figure 1.4).

The Songpan-Ganzi terrane is bound by the Karakax fault in the north and the Jinsha suture in the south, and consists of a series of Triassic and Jurassic plutons, and a Triassic (meta)sedimentary flysch complex (consisting of a thick sequence of Triassic deep marine deposits). These have been intensely deformed by folding and thrusting during the Late Triassic and Early Jurassic (Yin and Harrison, 2000). This complex extends beyond the Songpan-Ganzi- Hoh Xil terrane itself towards the north into the Kunlun arc (Sengör and Natal'In, 1996) (Figure 1.4).

The Tianshuihai terrane, bound by the Karakoram fault to the south west, consists predominantly of Triassic-Cretaceous (meta) sedimentary rocks overlying a Palaeozoic basement (Cowgill et al., 2003, Liu et al., 2015, Matte et al., 1996, Robinson et al., 2012, Schwab et al., 2004) (Figure 1.4).

To the west of the Western Kunlun range lays the Pamir salient, and together with the westernmost extent of the WKL, this forms a prominent arc intruding into the Tarim and Tajik basins.

1.4 The Pamir

It is generally considered that the unique arcuate shape of the Pamir is the result of the northward propagation of deformation from the India-Asia collision through indentation (Cowgill, 2010, Tang et al., 2015, Sobel and Dumitru, 1997, Bande et al., 2015, Blayney et al., 2016). Prior to this indentation, the Pamir is thought to have formed a relatively straight east-west margin aligned with the Western Kunlun mountain range and the northern margin of Tibet with the Tarim and Tajik basins situated to the north of this margin (Burtman and Molnar, 1993, Robinson et al., 2012, Schwab et al., 2004, Robinson, 2009).

The Pamir are therefore considered the now indented, western continuation of these ranges, although little evidence for an originally straight margin exists. Following the collision of India with Asia, the southern edge of the Pamir is suggested to have migrated northward by at least 300 Km with respect to Eurasia (Burtman and Molnar, 1993).

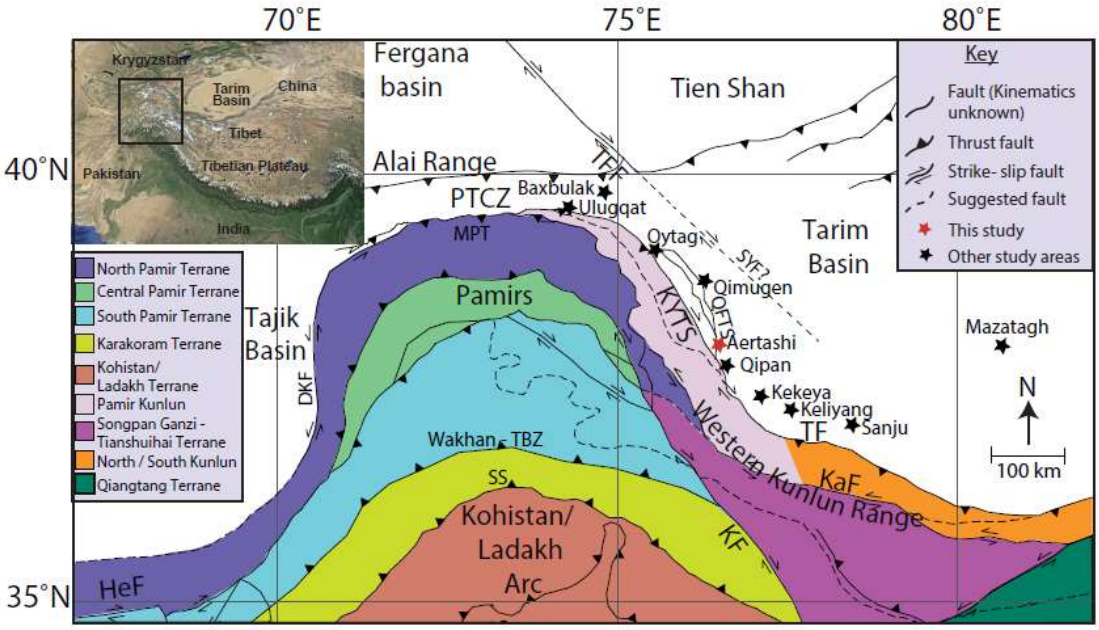

Figure 1.5 Adapted from Sippl et al. (2013) HeF = Herat fault, SS Shyok suture, DKF = Darvaz-Karakul fault System, MPT = Main Pamir Thrust, PTCZ = Pamir – Tian Shan Convergence Zone, TFF = Talas Ferghana fault, SYF = Sache-Yangdaman fault, KYTS = Kashgar-Yecheng Transfer System, KF = Karakorum fault, TF – Tiklik fault, KaF = Karakax fault, QFTS = Qimugen Fold Thrust System. Our study section Aertashi is highlighted with a red star with other study sections highlighted with a black star, insert shows the location of the Pamir range in its broader region.

This northward motion is accommodated along a series of Pamir bounding faults including the Main Pamir thrust (MPT) and the Pamir frontal thrust (PFT) to the north, the Darvaz-Karakul fault system on the western side and the dextral Kashgar – Yecheng transfer system (KYTS) to the east, with extension within the Pamir accommodated along the Karakoram fault system (KF) (Figure 1.5).

The main Pamir thrust and Pamir frontal thrusts form the surface expression of the active south-dipping Alai subduction zone (Burtman and Molnar, 1993, Fan et al., 1994, Hamburger et al., 1992, Negredo et al., 2007, Roecker et al., 1980) (Figure 1.5). Whilst the KYTS transfers shortening between the MPT and the north – vergent Tiklik fault which bounds the northern margin of the Western Kunlun mountain range (WKL) (Cao et al., 2013, Cao et al., 2015, Sobel et al., 2011) (Figure 1.5).

Along the western margin of the Pamir, the Darvaz fault forms the north western edge of the Indian plate (Trifonov, 1978) and separates the Pamir to the east from the Tertiary thrust belts in the Tajik Basin to the west (Cowgill, 2010). Data regarding the timing of activation and kinematics of this fault system are scarce. Evidence of displaced landforms of Holocene age are inferred to accommodate left slip at a rate of

~10–15 mm/a (Trifonov, 1978, Mohadjer et al., 2010) and provide some of the only reported evidence of slip along this fault.

The dextral KYTS has an estimated offset of ~280 km (Cowgill, 2010, Sobel and Dumitru, 1997), making it a key fault system in the northwards propagation of the Pamir salient. Activation along the KYTS is constrained using apatite fission track samples from the folded Jurassic deposits from Kusilaf near Aertashi. These yielded populations of single-grain apatite fission-track ages of 18.0 ± 0.8 Ma (Sobel and Dumitru, 1997). Thermal modelling of these data indicates that the samples cooled below ~120–100 ℃ between 21 and 19 Ma ago (Sobel and Dumitru, 1997).

In addition, anistropy of magnetic susceptibility (AMS) data from the Baxbulak section in the Pamir-Tian Shan convergence zone (PTCZ) by Tang et al. (2015), identified an increase in strain in basin sediments at 26 Ma. This, along with apatite fission track data from the southern Tian Shan dated at ~25 Ma (Sobel and Dumitru, 1997) and evidence of movement along the Talas – Fergana fault in the Tian Shan and the buried Sache-Yangdaman right-slip fault in the Tarim Basin, as well as late Cenozoic counter clockwise vertical axis rotations from the Fergana basin are all suggested (Bande et al., 2015) to be related to the initiation of Pamir indentation (Figure 1.5).

More recently, Wang and Wang (2016) used seismic data from the east-propagating Qimugen thrust system, which forms part of the larger KYTS, to show growth strata in what they term the "Upper Artux formation". More recent re-dating of this formation by Zheng et al. (2015a) indicates that the Qiumgen Thrust belt was active by ~15 Ma, which has been attributed to a transpressional setting resultant from the onset of Pamir indentation (Figure 1.5).

The Karakoram fault system extends from the Gurla Mandhata detachment or the Indus-Yarlung suture in the south (McCallister et al., 2014) to the Muji fault, in the north (Chevalier et al., 2011) and divides into a series of horsetail splays towards the northern extent. These 'splays' include the Aksu Murgab fault, Karasu fault, east Pamir fault, Rangkul fault and Kongur Shan Extensional System (KES) (Chevalier et al., 2015) which bound some of the Central Pamir gneiss domes (Schurr et al., 2014a, Strecker et al., 1995). However, the exact role of the Karakoram fault during Pamir indentation is poorly constrained due to uncertainties in its initiation age (Murphy et

al., 2002). Estimates for the timing of initiation range from 25-22 Ma (Lacassin et al., 2004, Valli et al., 2008, Sen et al., 2014), <18 Ma (Searle et al., 1998), 13.7 ± 0.3 to 15.7 ± 0.5 Ma (Phillips et al., 2004), <13 Ma (Murphy et al., 2002), ≥11 Ma (Matte et al., 1996) to <5 Ma (Searle, 1996).

Within the Pamir, Cenozoic shortening resulted in substantial crustal thickening between ~44 to 25 Ma with Paleogene tripling through imbrication and folding of the 7-10 km upper crustal strata suggested (Rutte et al., 2017b) to have resulted in a total thickening of up to 90 km.

N-S contraction within the Pamir salient is recorded by prograde metamorphism which commenced at ~35 Ma (Rutte et al., 2017a). This was subsequently followed by a phase of E-W trending synorogenic crustal extension associated with normal faulting at ~22 Ma (Stearns et al., 2013, 2015, Brunel et al., 1994, Arnaud et al., 1993). This extensional phase resulted in the exhumation of a series of gneiss domes within the Pamir including the giant Shakhdara dome in the South Pamir and the Central Pamir Muskol, Mustagh-Ata and Shatput gneiss domes which exhumed at around ~20 - 16 Ma (e.g. Stearns et al., 2015, Brunel et al., 1994).

At ~12 Ma shortening resumed within the Pamir marked by opposite – sense thrusting and folding focused along the dome margins (e.g. Stearns et al., 2015, Rutte et al., 2017b).

1.4.2 Pamir formation

Beneath the Pamir is a complex double subduction zone with a narrow sliver of Indian lithosphere beneath the Hindu Kush, and a broad, south-dipping 300-km long arcuate Alai slab roughly following the shape of the Pamir range forming the overriding Eurasian plate (e.g. Küfner et al., 2016, Sobel et al., 2013). There are two models proposed for the formation and uplift of the Pamir salient.

The continental subduction model (Figure 1.7) (Sobel et al., 2013) proposes that following slab break-off of the western end of the Indian slab at ~25 Ma (Mahéo et al., 2002, Replumaz et al., 2010, Amidon and Hynek, 2010, Wilke et al., 2012), a reversal of subduction vergence ensued, allowing the onset of a new south dipping intra continental subduction system, with the Pamir forming the overriding plate.

Continental subduction is driven by Indian indentation and trench suction, along with slab rollback of the narrow, south-dipping Alai slab, which is proposed to have led to the unique curvature of the Pamir salient and drove the northward motion of the Pamir into central Asia. This northward indentation was facilitated by a series of subduction- transform edge propagator (STEP) faults (Govers and Wortel, 2005)) such as the KYTS.

However, a number of alternative theories are proposed to explain the unique curved shape of the Pamir (Figure 1.6), including: 1) oroclinal bending or radial thrusting (Yin et al., 2001, Robinson et al., 2004, Strecker et al., 1995) which is associated with extensive vertical-axis rotations (Figure 1.6A); 2) transfer faulting induced by shear faults along the eastern and western margins (Burtman and Molnar, 1993, Searle, 1996) which is associated with limited rotation in the surrounding basins (Figure 1.6B), or 3) a hybrid model involving north-west radial thrusting with anticlockwise rotation at the western margin and transpressional right-slip transfer faulting at the eastern margin (Cowgill, 2010) (Figure 1.6C).

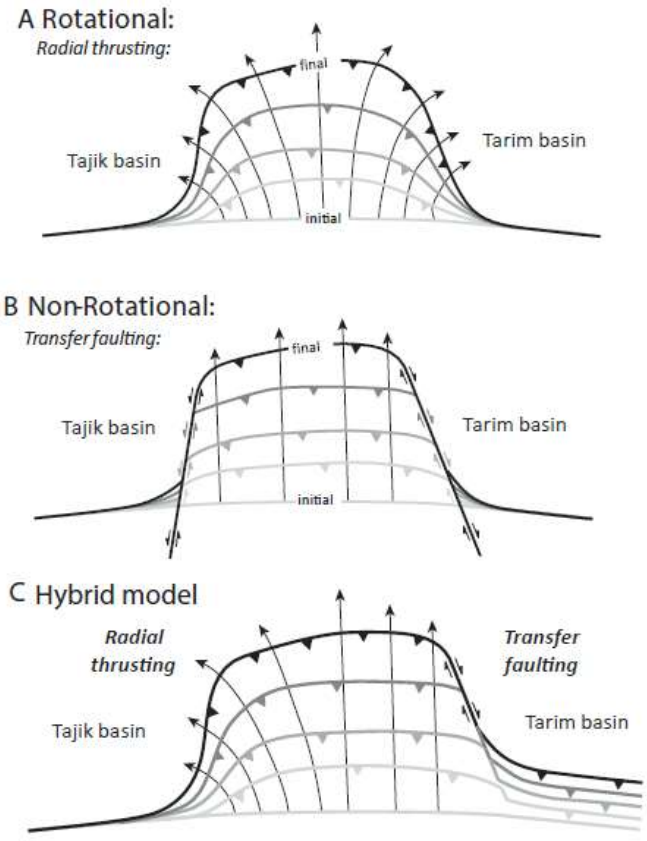

Figure 1.6 Models for the unique curvature of the Pamir adapted from (Cowgill, 2010), A) vertical-axis rotation of the eastern and western margins of the Pamir salient through radial

thrusting, B) deformation via conjugate strike-slip transfer fault systems and C a hybrid model with radial thrusting along the western margin of the syntaxis and transfer faulting along the eastern margin.

Estimates of North Pamir exhumation are limited, implying that the bulk of the shortening accommodated during Pamir indentation is facilitated by large scale underthrusting and subduction erosion during the middle Miocene. In the latest Miocene – present, an influx of syn-tectonic sediments resulted in increased coupling and promoted subduction accretion as the MPT and PFT propagated northwards creating an accretionary wedge (Figure 1.7).

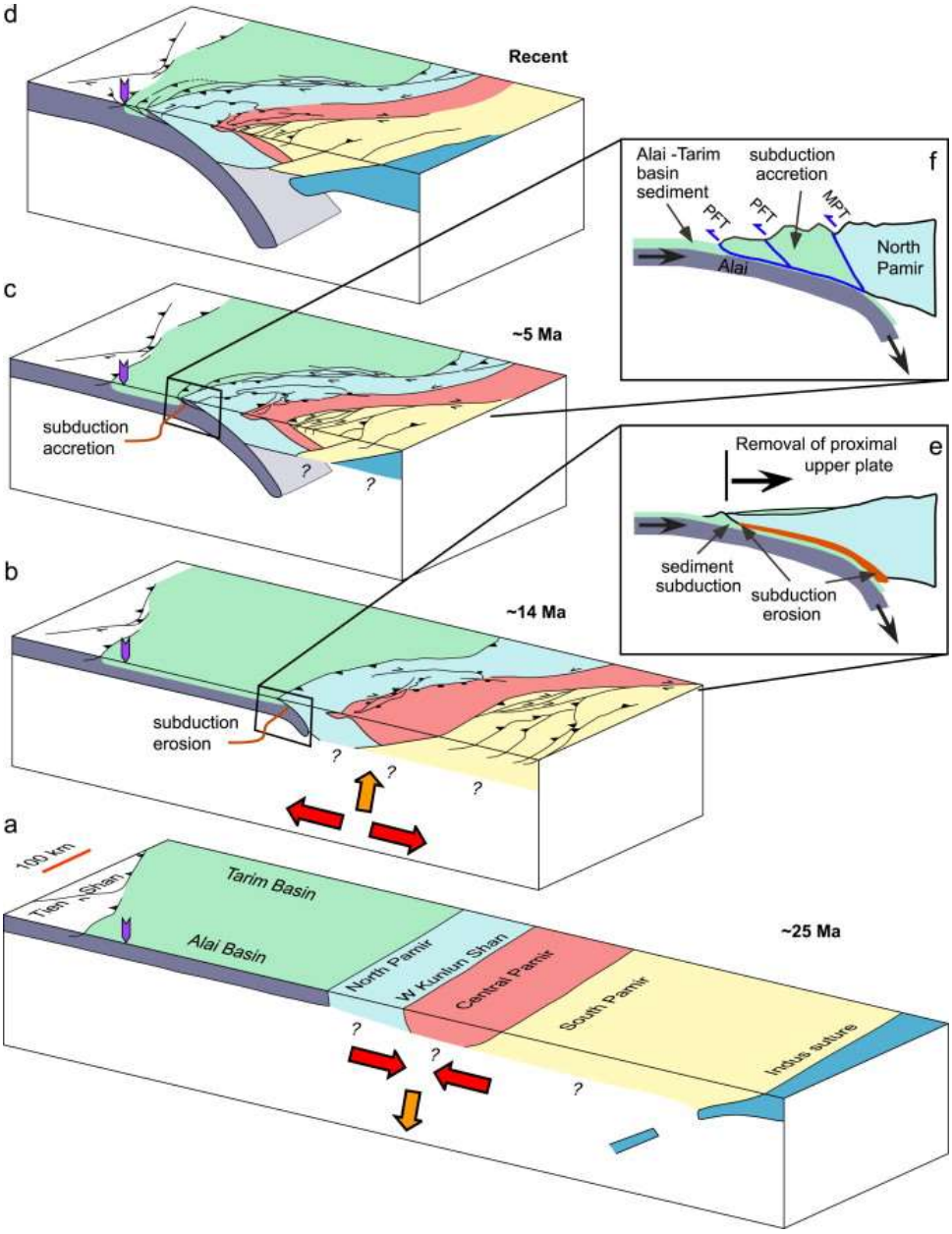

Figure 1.7 Four schematic cross-sections (a-d) illustrating slab-rollback model for the late Cenozoic evolution of the Pamir (Sobel et al., 2013).

The crustal delamination model (Figure 1.8) (Bird, 1979, Küfner et al., 2016, Ducea, 2011, Rutte et al., 2017b, 2017a) proposes that the buoyant north-western salient of cratonic India drove into cratonic Asia, forcing delamination and rollback of its lithosphere. India's thinned western continental margin then separates from India and subducts beneath Asia forming a prominent anomaly down to the mantle transition zone.

The Pamir salient is under-thrust by the Indian plate, resulting in uplift and exhumation of the Pamir, whilst the indented Cratonic Asian plate delaminates and rolls back. This model implies limited northward motion of the Pamir salient itself prior to 10 Ma. Crustal thickening is driven from the south by the motion of the Indian plate into Asia, facilitated by under thrusting of the Indian plate beneath the Pamir. Exhumation of the Pamir gneiss domes exhumed as a result of crustal extension driven gravitational collapse (Küfner et al., 2016, Rutte et al., 2017a, 2017b) that was initiated by Indian slab breakoff, followed by buckling due to ongoing convergence.

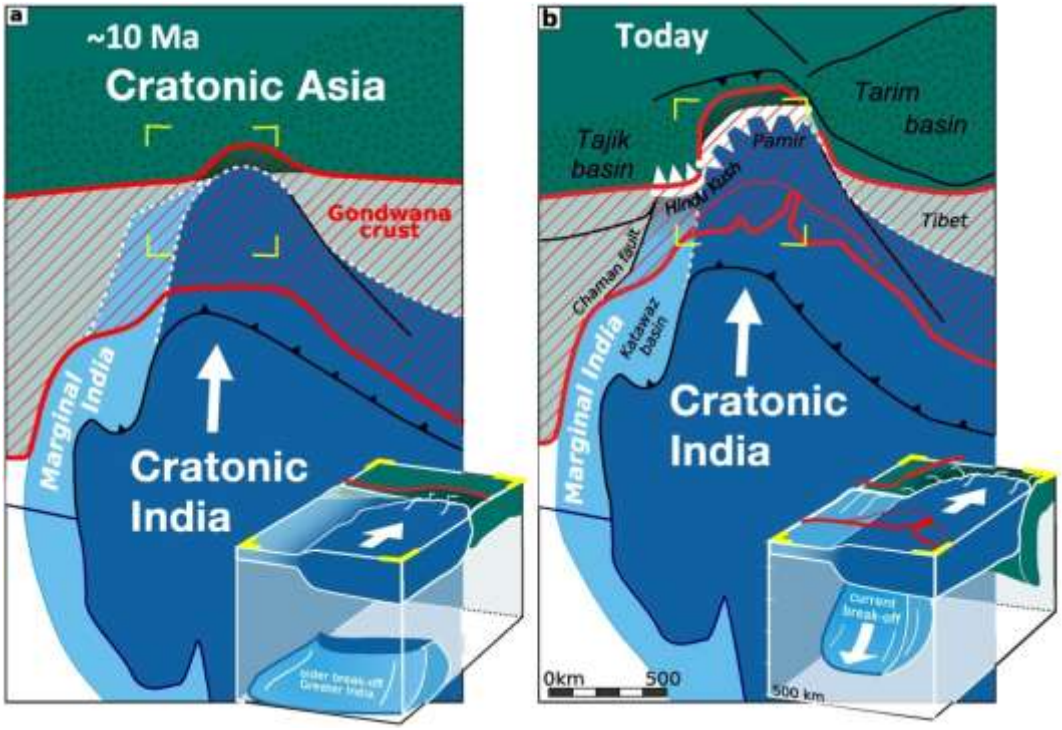

Figure 1.8 Overview figure of the delamination model for Pamir formation and evolution of Küfner et al. (2016)

Both models result in different predictions regarding the timing of indentation and uplift of the Pamir. The subduction model suggests that Pamir formation was dominated by the northward indentation of the Pamir salient, controlled by slab pull, whilst Pamir extension is controlled by a form of back arc extension. The

delamination model suggests that the Pamir formed by uplift resultant from the underthrusting of the Indian plate beneath the Pamir region, whilst extension within the Pamir is controlled by crustal collapse through lateral extrusion. A key difference between these models is the timing and causes of lithospheric roll back of the Alai plate beneath the mantle. The continental subduction model requires the subduction roll back coeval with the 22-12 Ma dome exhumation, and at the same time as the 300 km indentation and associated slip on the indentor bounding strike slip faults (the KYTS and Darwaz faults). The delamination model suggests limited Pamir indentation into Tarim before 10 Ma with most of the indentation (~300 km) post 10 Ma. Understanding the timing of Pamir indentation and evolution provides a critical tool in distinguishing between these two models.

1.4.1 Pamir Terranes

The Pamir region can be subdivided into three main terranes separated by major sutures; these terranes were formed by sequential collisions during the progressive closure of the Tethyan Ocean (Burtman and Molnar, 1993, Robinson et al., 2012, Schwab et al., 2004) (Figure 1.9).

The North Pamir, bound by the Main Pamir Thrust (MPT) in the north, and the Tanymas suture in the south, is composed of predominantly Palaeozoic and Triassic (meta) sedimentary and meta volcanic rocks intruded by Triassic-Jurassic granitoids (Schmidt et al., 2011, Schwab et al., 2004) (Figure 1.9).

The Central Pamir is bound by the Tanymas suture to the north and the Rushan-Pshart zone to the south. It consists of Palaeozoic and Triassic-Jurassic (meta)sedimentary rocks (Schwab et al., 2004) and gneiss domes of various protolith types and ages, including the Muztagh Ata dome. These domes were metamorphosed and exhumed during the Cenozoic (Robinson et al., 2007, Schmidt et al., 2011, Schwab et al., 2004, Stearns et al., 2015).

The South Pamir, bounded by the Rushan-Pshart suture zone to the north and the Bangong-Nujiang suture to the south, is composed of Palaeozoic, Triassic and Jurassic (meta)sedimentary rocks. These have been subsequently affected by Cretaceous and Cenozoic magmatism and metamorphism (Schwab et al., 2004). The South Pamir contains the giant Shakhdara dome of Cretaceous and older protolith, which has been metamorphosed and exhumed during domal formation in the Cenozoic (Stübner et al.,

2013b). In the eastern Pamir, horsetails splaying from the northern termination of the Karakoram strike-slip fault (KKF) delineate the boundary between the South and Central Pamir.

To the south of the Pamir lie the Karakoram and the Kohistan-Ladakh arc, separated by the Shyok suture (Figure 1.9). The former consists of deep crustal metamorphics, Cretaceous and Cenozoic intrusives as well as sedimentary rocks (e.g. Fraser et al., 2001), the latter consisting of predominantly Cretaceous age oceanic island arc (e.g. Tahirkheli and Jan, 1979).

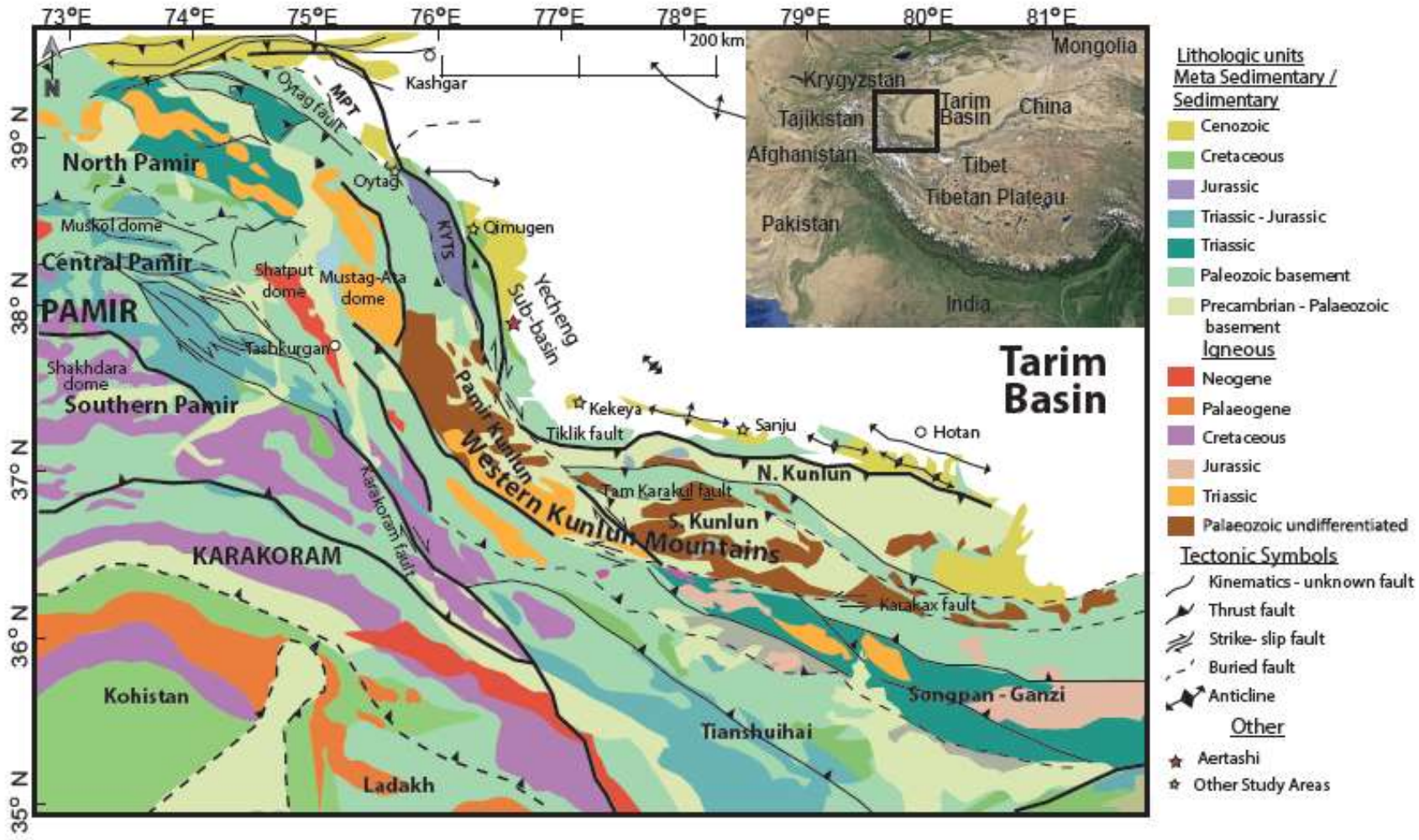

Figure 1.9 Summary of the Pamir and Western Kunlun terranes with key sedimentary sections and major faults and sutures indicated.

1.5 Tarim Basin

The Tarim Basin itself is a craton which today forms a large intracontinental basin. The basement is composed of Archean and Proterozoic oceanic crustal fragments comprising predominantly crystalline metamorphic gneisses (Tian et al., 1989). These are overlain by a series of Palaeozoic and Mesozoic platform carbonates and fine to medium clastics.

From the late Cretaceous ~95 Ma through to the mid Eocene ~37 Ma, a series of 5 shallow marine transgressions and regressions are recorded in the sedimentary record of the Tarim Basin, with the final regression at ~37 Ma only recorded in the far north western part of the Basin (Bosboom et al., 2011, Bosboom et al., 2014a, Tang, 1989, Lan and Wei, 1995, Burtman, 2000, Wang et al., 2014) (Figure 1.10).

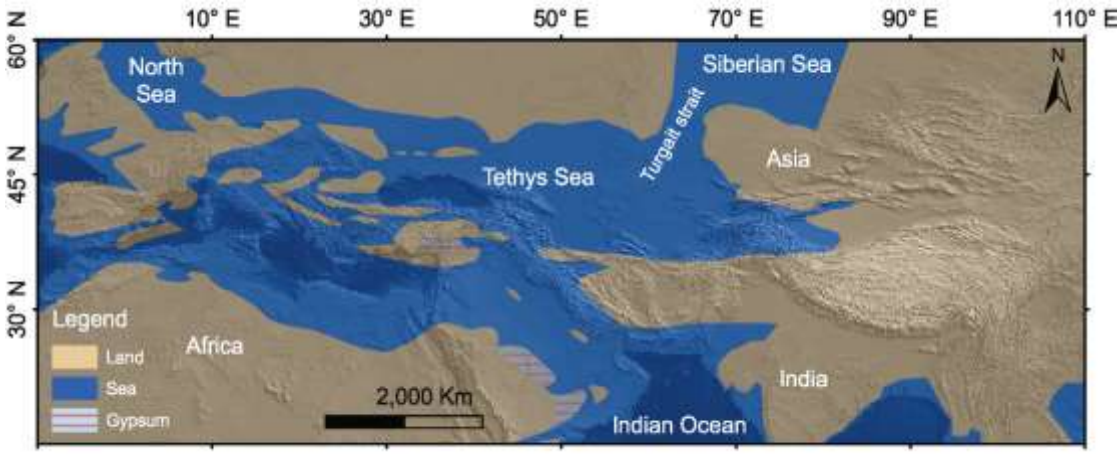

Figure 1.10 Map showing the known extent of the land–sea distribution of the Tethys Sea in the late Eocene overlain on the present day topography and geography of Asia, Africa and India by Wang et al. (2014).

The causes of final retreat of the Tarim Sea is debated, with over-thrusting by the surrounding mountain ranges and associated sedimentary basin infilling (Burtman and Molnar, 1993, Burtman, 2000, Coutand et al., 2002), a eustatic fall in global sea level associated with the growth of ice sheets in Antarctica (Dupont-Nivet et al., 2007, Haq et al., 1987, Sobel and Dumitru, 1997) or a combination of the two mechanisms (Bosboom et al., 2011, Bosboom et al., 2014c, Bosboom et al., 2014a) all being discussed.

Subsequently, the Tarim Basin has been over-thrust by the Tian Shan in the north, the Kunlun and the Tibetan Plateau to the south and the Pamir in the west, the latter acting

as a divide between the Tarim Basin and the Tajik Basin (e.g. Burtman and Molnar, 1993, Cowgill, 2010, Jia, 1997, Yin and Harrison, 2000).

Indentation of the Pamir in the Oligo-Miocene resulted in the clockwise rotation of the Tarim Basin (Bosboom et al., 2014b), modern GPS measurements indicate that this rotation continues at a rate of 11 ± 1 nrad/yr today (Shen et al., 2001). Previous rotational studies yield inconsistent results along the western Tarim Basin (Bosboom et al., 2014b), however 7.0 ± 0.25° of wholesale clockwise rotation of the Tarim block has been recorded around an axis at the eastern end of the basin (96°E; 43.5°N) by Avouac et al. (1993). Some of this rotation is accommodated by opposite clockwise rotation of the Tarim block coincident with counter clockwise rotation of Tibet (Avouac et al., 1993, Van Hinsbergen et al., 2012). However, the basin itself has remained relatively undeformed (Zheng et al., 2000). In the south-western region the basin is separated from the Western Kunlun (WKL) hinterland by the Tiklik Thrust and from the Pamir by the Kashgar-Yecheng Transfer system (KYTS) (Figure 1.8).

1.5.1 Sediments of the Western Tarim Basin

Cenozoic depositional units of the western Tarim Basin include the Palaeogene Kashi Group, composed of the Aertashi, Qimugen, Kalatar, Wulagen and Bashibulake formations and the Cenozoic Wuqia Group composed of the Keziluoyi, Anjuan and Pakabulake formations. These are overlain by the Artushi (Artux) and Xiyu formations, originally thought to be Pliocene in age (Mao and Norris, 1988, Tang, 1989, Jia, 2004). However, more recent age control has reassigned the Artushi and Xiyu formations to Miocene age in this region (e.g. Cao et al., 2015, Zheng et al., 2015a) (Figure 1.11).

The Kashi Group are mainly composed of a series of marine facies (Tang, 1989, Mao and Norris, 1988, Jia, 2004, Wei et al., 2013), formed in a epicontinental sea known locally as the Tarim Sea. Note that the extent of the marine incursions varies for each of these formations; in particular, the marine incursions of the marine Bashibulake Formation in northwest Tarim did not reach very far south, where time equivalent non-marine deposition is recorded.

Following final regression of the Tarim Sea was a series of terrestrial red clastic units of the Wuqia Group. These mainly consist of fluvial facies siltstones and mudstones in the lower portion (Zhou, 2000, Bosboom et al., 2011, Jia, 2004, Wei et al., 2013)

with the upper Wuqia Group and overlying Artushi and Xiyu formations dominated by fluvial and alluvial fan facies sandstones, gravels and conglomerates (Yin et al., 2002, Zheng et al., 2006, Zheng et al., 2010, Zheng et al., 2015a, Jia, 2004) (Figure 1.11).

Basinward thrusting by the WKL and Pamir mountain ranges (Cao et al., 2015, Jiang and Li, 2014, Jiang et al., 2013) has resulted in weak deformation of these sediments.

Summary of stratigraphic formations of the Western Tarim Basin.

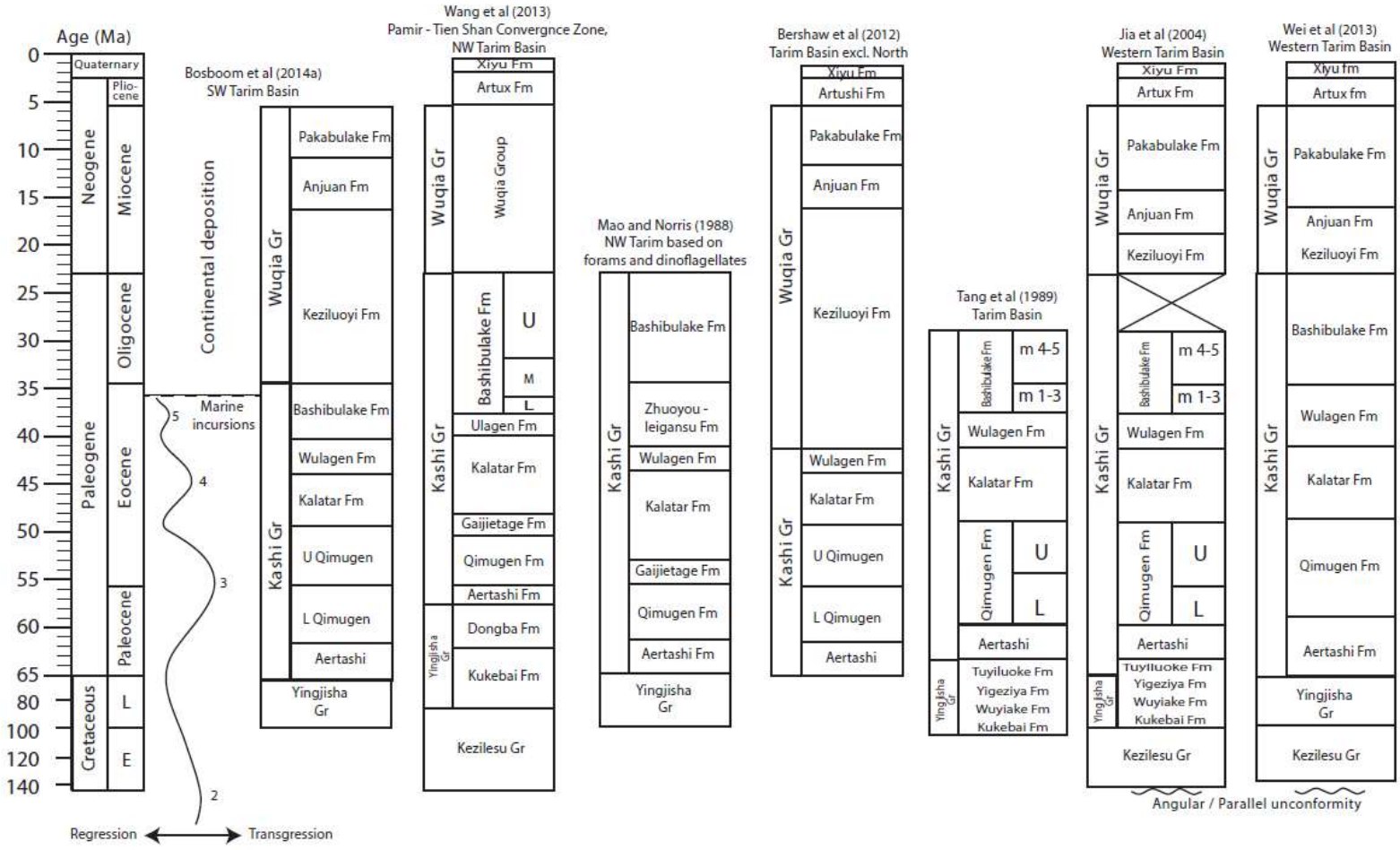

Figure 1.11 Summary of the sediments identified in the western Tarim Basin showing the comparison of the ages of the formations at different sections around the Tarim Basin by (Bosboom et al., 2014c, Wang et al., 2013, Mao and Norris, 1988, Bershaw et al., 2012, Tang, 1989, Jia, 2004, Wei et al., 2013).

1.6 The Tian Shan

The Tian Shan Mountain belt is situated along the northern margin of the Tarim Basin, and forms a key part of the Central Asian Orogenic Belt (CAOB), which extends from the Ural Mountains in Russia to the west Pacific Ocean. The CAOB was formed through a complex amalgamation of terranes throughout the Palaeozoic and Mesozoic (e.g. Biske and Seltmann, 2010, Windley et al., 2007, Gao et al., 2009, Lamb and Badarch, 1997) (Figure 1.4)

Cenozoic reactivation of the orogen is attributed to the far field effects of the India – Asia collision and resulted in the formation of the present-day topography of the range (e.g. Tapponnier et al., 1986, Avouac et al., 1993).

Cenozoic deformation along the Southwest Chinese Tian Shan (SWTS), is recorded by a series of uplift events commencing at ~25–20 Ma attributed to initial activation along the Talas Fergana fault (TFF) (e.g. Burtman et al., 1996, Heermance et al., 2007, Käßner et al., 2016, Jia et al., 2015), with shortening and uplift in the SWTS and its piedmonts at ~25-20 Ma (e.g. Hendrix et al., 1992, Sobel and Dumitru, 1997, Sobel et al., 2006) and 19 ± 3 Ma (Sobel et al., 2006, Heermance et al., 2007), and subsequent deformation progressing in a stepwise manner at ~16- 13 Ma (e.g. Heermance et al., 2007), ~11 Ma (Charreau et al., 2006), 11–7 Ma and ~4–2 Ma (Heermance et al., 2007, Li et al., 2011, Liu et al., 2017). Ages from 11 Ma onwards are attributed to the onset of 'collision' between the Pamir – Western Kunlun and the Southwestern Tian Shan (Liu et al., 2017).

Today, the Tian Shan and Pamir mountain ranges are separated by a narrow corridor known as the Alai corridor, which marks the last remaining connection between the Tarim and Tajik basins.

1.7 Global climate during the Cenozoic.

The Eocene marks a critical transition in the global climate from 'greenhouse' to 'icehouse' which had far ranging impacts on our planet, driving evolution and a key adaptation of photosynthetic plant life. What drove this climatic transition is key to our understanding of land / climate interactions.

The formation of the Himalayas is indicated to have played a vital role in the evolution of the Cenozoic climate. However, their formation coincides with a global reorganisation of plate tectonics making links between tectonics and climate complex.

In the southern hemisphere, the opening of tectonic seaways around Antarctica including the Drake Passage between Antarctica and South America and the Tasman Gateway between Antarctica and Australia, is suggested (e.g. Kennett, 1977, Exon et al., 2004), to have resulted in the development of the Antarctic Circumpolar Current (ACC) and the Polar Frontal Zone (PFZ). These passages progressively thermally isolated the Antarctic continent leading to the formation of extensive ice sheets in Antarctica during the late Eocene and a reorganisation of ocean currents globally (Figure 1.12).

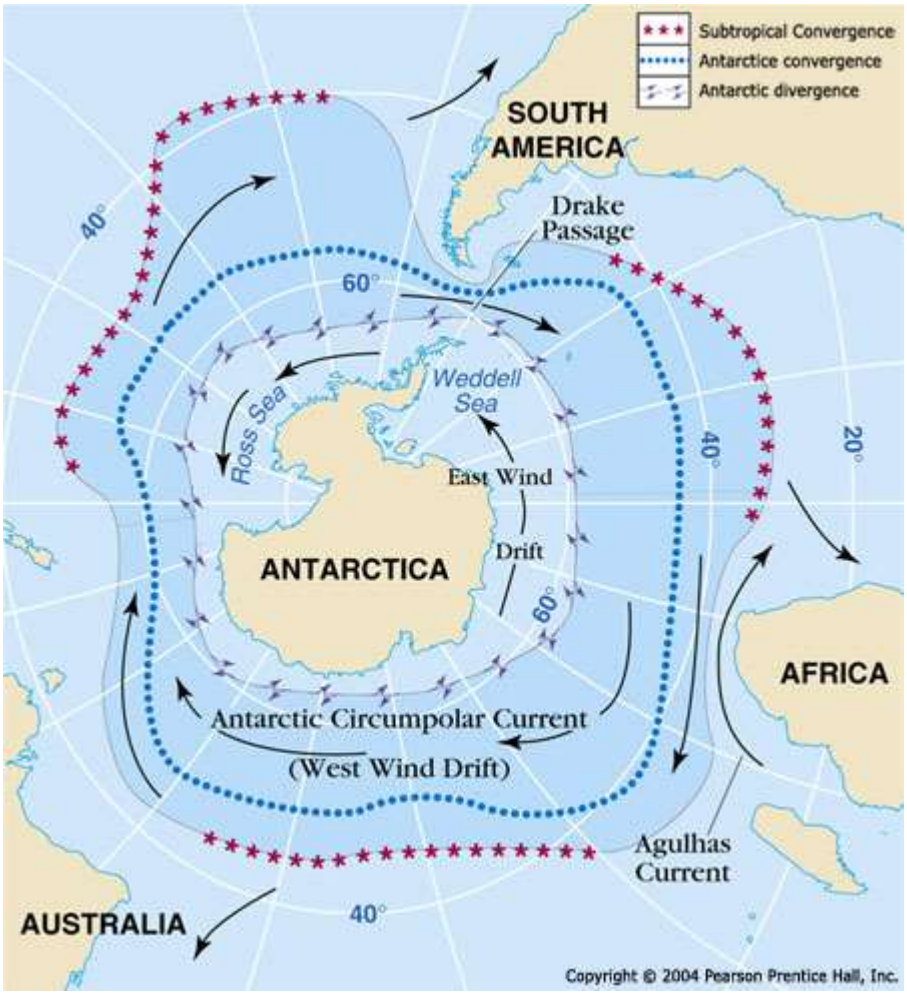

Figure 1.12 Antarctica following the opening of the Drake passage and activation of the circumpolar current which thermally isolates Antarctica. The subtropical and Antarctic convergence zones are indicated by pink stars and blue dots respectively. Figure copyright 2004, Pearson Prentice Hall, Inc.

A model of the Cenozoic climate has been compiled by Zachos et al. (2001) using a deep sea stable isotope record from bottom-dwelling deep-sea foraminifera. The oxygen isotope record provides an overview of the deep–sea temperatures and continental ice volume, whilst the deep sea carbon isotope data provides insights into the global carbon cycle perturbations. Together, they reflect global warming and cooling and ice-sheet waxing and waning.

The onset of the Eocene marked a peak in a long term global warming trend culminating the Early Eocene Climate Optimum (52-50 Ma), which was followed by a marked cooling trend resulting in a 7.0˚C reduction in deep sea temperature. This cooler period continued throughout the remainder of the Eocene and early Oligocene triggering the onset of ice sheet formation towards the end of the Eocene (Zachos et al., 2001). The boundary between the Eocene and Oligocene (around 34 Ma) marks a key shift from a 'relatively' ice-free climate to the formation and expansion of continental ice sheets in Antarctica (Zachos et al., 2001).

During the Oligocene, ice sheets remained a substantial feature of the global climate system (DeConto and Pollard, 2003, Zachos et al., 1994, Miller et al., 1987). At ~30 Ma, a prominent transition in global atmospheric carbon (pCO_2) concentration had occurred. This transition marks a critical point in bringing about an evolution in plant photosynthesis and the emergence of C_4 photosynthetic pathways (Tipple and Pagani, 2007); however, the exact timing and details of the C_4 pathways' earliest origins remain elusive.

By ~ 28-26 Ma a global warming trend began, known as the late Oligocene warming event (LOWE) which continued until the middle Miocene (~15 Ma). This trend resulted in an overall reduction in global ice volume and slightly higher bottom water temperatures (Zachos et al., 2001 and references therein). This warming phase was punctuated by a series of brief glacial (Miocene isotope (Mi)) events during the early Miocene including Mi.1 at ~24 Ma, Mi1.a at ~21.8 Ma and Mi1b at ~18.2 Ma (Wright and Miller, 1993).

Global warming peaked in the early to middle Miocene (17-15 Ma) in an event known as the Mid-Miocene Climatic Optimum (MMCO). This period was characterised by increased precipitation, with mid-latitude warming of ~6°C higher than modern day values (Savin et al., 1975, Shackleton and Kennett, 1975).

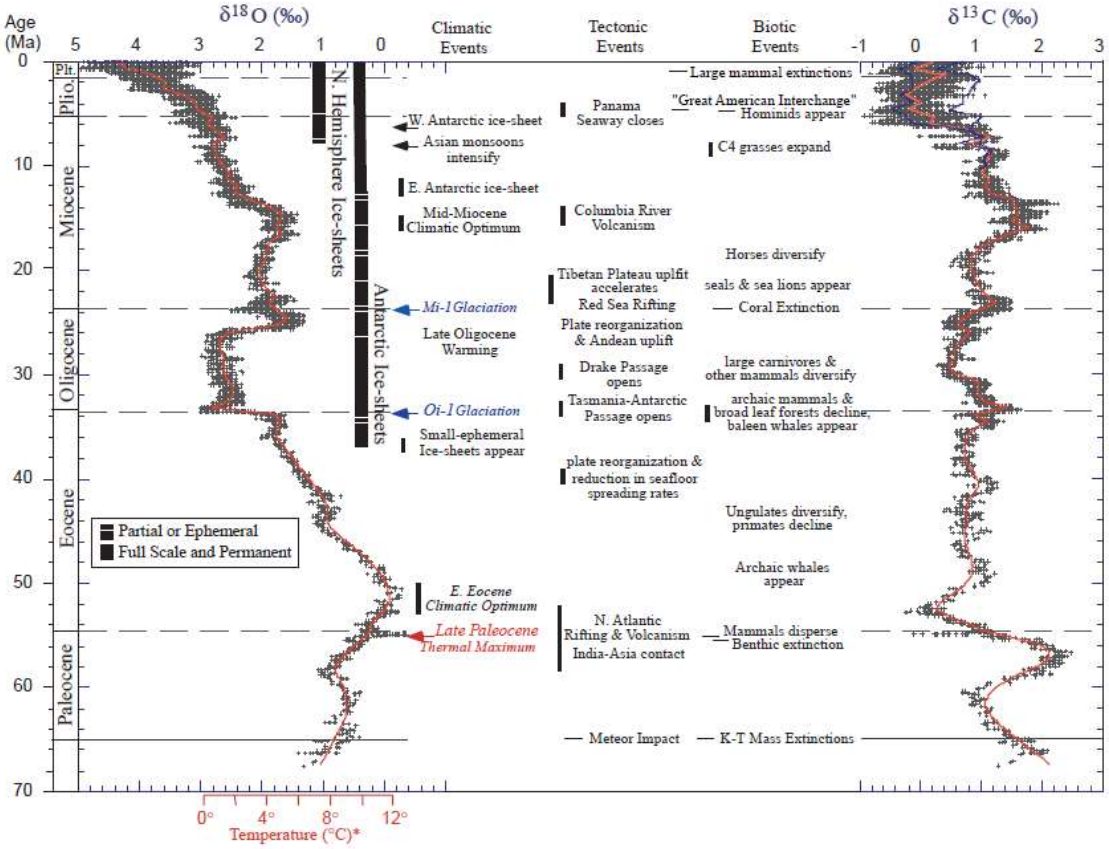

Figure 1.13 Global deep-sea oxygen and carbon isotope records from Zachos et al. (2001)

The MMCO ended at a global cooling event (Mi3/4), which has been related to an expansion of the East Antarctic Ice-Sheet (EAIS) (Flower and Kennett, 1994, Zachos et al., 2001, Miller and Mountain, 1996).

An extensive cool and dry period followed known as the 'Middle Miocene climate transition'. The drop in global temperature caused a reduction in the volume of water vapour held in the atmosphere and a global reduction in CO_2 levels (Zachos et al., 2001, Tipple and Pagani, 2007, Pagani et al., 2005). This created a positive feedback scenario through a reduction in the greenhouse effect and precipitation (Ruddiman and Kutzbach, 1989), leading to increased global cooling.

A rise in $\delta^{18}O$ throughout the late Miocene (~10Ma) until the early Pliocene (Figure 1.13) was recorded by additional cooling and ice sheet expansion in both Antarctica and the development of ice sheets in the Arctic (Zachos et al., 2001). A subtle

warming trend marks the early Pliocene between ~6-3.2 Ma which coincides with an increase in $\delta^{18}O$ coinciding with the onset of Northern Hemisphere glaciations (Zachos et al., 2001 and references therein), marking climatic conditions akin to those experienced globally today.

1.8 The Cenozoic Asian climate

From the Cretaceous to the early Eocene a shallow epicontinental sea occupied Eurasia, extending from the Mediterranean though to the Tarim Basin in central Asia, and across the location of the modern Pamir (prior to its indentation and uplift) (e.g. Bosboom et al., 2011, 2014a, 2014c, Mao and Norris, 1988). Throughout this time, the Tarim Sea advanced and retreated from the Tarim Basin in a series of 5 steps with the last major retreat at ~41 Ma, as recorded at Aertashi, followed by minor advance and retreat at ~37 Ma (Bosboom et al., 2011), only recorded at the north-western most edge of the Tarim Basin (Figure 1.11).

The final retreat of the Tarim Sea had a major effect on central Asian climate through the removal of a critical source of moisture (Ramstein et al., 1997, Zhang et al., 2007c). Coincident with the retreat of the Tarim Sea ~40 Ma (Bosboom et al., 2011, Bosboom et al., 2014c), was a marked increase in aridity in central Asia, which is evidenced by changes in lithofacies and pollen records from the Kezi, Aertashi and Keliyang sections (Bosboom et al., 2011, Bosboom et al., 2014c) (Figure 3.1).

Coincident uplift of the Tarim Basin surrounding ranges also created orographic barriers in central Asia, resulting in a reorganisation of the pressure system and atmospheric circulation. This resulted in the intensification of the Asian monsoonal systems (Zhang et al., 2007c) creating a positive feedback scenario, further driving the aridification trend in central Asia (Ramstein et al., 1997, Zhang et al., 2007b).

The effect of changes in atmospheric circulations for central Asia have been studied by Caves et al. (2015) who compiled a record of $\delta^{18}O_{carbonate\ (carb)}$ from 23 publications in central Asia from the Eocene through to today. Interestingly they found that $\delta^{18}O_{carb}$ changed little over the last 50 Ma with the average Eocene $\delta^{18}O_{carb}$ value of 21.22 ‰ similar to late Cenozoic (10–0 Ma) values 20.83 ‰ (Caves et al., 2015). This, they suggest, is evidence that the same atmospheric processes that control central Asian climate today have been operating since the early Eocene, implying that southern moisture sources have been blocked by a high, southern topographic barrier

throughout the Cenozoic, and a westerly moisture flux has governed the observed step-wise drying of central Asia since the early Eocene.

Within Asia, the monsoonal system plays a critical role in governing the climate. Today, during the warm summer months, high insolation over continental regions creates a strong land-sea pressure gradient resulting in abundant rainfall. Conversely, the cool winter continents create a reverse effect leading to a long, cold and dry season. Within central Asia a high seasonality akin to a monsoonal climate has been identified since at least the Eocene (Licht et al., 2014, Huber and Goldner, 2012, Caves et al., 2014, Zhang et al., 2012, Zhang et al., 2007b). However, unlike the modern monsoons this paleo-monsoon is characterised by a pronounced dry summer and high precipitation in the winter (Zhang et al., 2007b, Bougeois et al., Submitted).

The cause of this monsoonal climate has been attributed to enhanced greenhouse conditions at this time, which resulted in higher atmospheric water vapour loading (Licht et al., 2014). Although the Tarim Sea is unlikely to have had a significant moisture effect on the monsoonal climate (Bougeois et al., Submitted), a decline in monsoonal intensity is recorded at the final retreat of the Tarim Sea (Zhang et al., 2007b, Licht et al., 2014, Bosboom et al., 2014c, Bosboom et al., 2014d). A reduced ancient monsoonal seasonality subsequently continued throughout much of the later Eocene attributed to a remnant of the Para-Tethys Sea further to the west (Licht et al., 2014, Zhang et al., 2007b). By 34 Ma, an abrupt change in global climate and atmospheric CO_2 led to a reduction in air flow from the Westerlies. This resulted in a decreased pressure gradient from continent to ocean and a reduction in monsoonal intensity in central Asia (Licht et al., 2014)

Throughout the Cretaceous to Cenozoic, aridification in central Asia progressed in a series of aridity steps punctuated by wetter periods (Harzhauser et al., 2016), and with spatial as well as temporal variation.

A recent study of the Tarim Basin by Wang et al. (2014) identified a series of aridity shifts throughout the Cenozoic at ~34, ~23, ~16 and ~5 Ma based on lithology, grain size analysis, SEM and magnetic susceptibility. The timing of onset of desertification remains the subject of debate and is proposed to have occurred any time between ~26.7 Ma (Zheng et al., 2015a) and ~3.4 Ma (Sun et al., 2011).

Other studies from the Western Tarim Basin include oxygen isotope data of carbonates from the Oytag section (Figure 1.8) along the eastern margin of the Pamir range by Bershaw et al. (2012). This study shows a distinct shift in $\delta^{18}O$ to more negative values around Eocene to Oligocene time. This shift marks the transition from marine facies to terrestrial facies which they relate to the growth and uplift of the Pamir-Kunlun terrane in response to the collision of the Indian Plate with the Kohistan-Ladakh arc (Sun et al., 2016b). Other studies from the Sanju section (Figure 1.8) in the western Tarim Basin (Sun and Liu, 2006, Sun et al., 2009), following revision of age control by Cao et al. (2015), show a clearly defined increase in $\delta^{13}C_{org}$ at ~15 Ma, coinciding with a facies change from fluvial floodplain to braided river facies. Although the authors attribute this change to increased aridity in the region, due attention should be paid to the possible effect of the facies change and the potential influence this may have on stable isotope composition. A study published by Galy et al. (2008) has shown that total organic carbon can be directly influenced by petrogenetic carbon formed through graphitization. This study (Galy et al., 2008) found that at least 30% (40 ± 10%) of the organic carbon contained in Himalayan rocks is preserved and recycled during the erosion cycle and subsequently deposited in sedimentary fluvial deposits. In sediments where total organic carbon (TOC) values are very low, this inherited signature can have a significant effect on the organic carbon signal.

A comprehensive study of the northern margin of Tibet and the western Tarim Basin was conducted by Kent-Corson et al. (2009). More recent age control for the Aertashi section along the western Tarim Basin by Zheng et al. (2015a) allows for the reinterpretation of this data set (supplementary item 4). $\delta^{18}O$ carb in many of the sections show a decrease in average oxygen isotope values during the Paleogene, which the authors ascribed to a change in water source to a more integrated high altitude drainage as the Tibetan Plateau uplifted to the south. Uplift of the Tarim-bounding ranges or retreat of the Para-Tethys sea was also suggested by Bershaw et al. (2012) to explain a similar trend they documented in the region. By contrast, Kent-Corson et al. (2009) record an increase in both oxygen and carbon isotope values in many of the sections in the Neogene, which they ascribed to a regional increase in aridity and temperature.

1.8.1 C_4 photosynthesis evolution in China

The evolution of C_4 plant photosynthesis marks a key transition in the global climate. Prior to the Miocene, C_3 plants dominated and thrived in a CO_2 - rich, moist climate. The development of C_4 plants was driven by evolutionary selection for a photosynthetic system that was able to overcome a long-term change in climatic conditions, which included a reduction in the partial pressure of CO_2 (pCO_2) (Tipple and Pagani, 2007) and exposure to 'water stressed' conditions (e.g. Ehleringer, 2005). Therefore the evolution and onset of C_4 photosynthetic evolution in central Asia marks a key transition into CO_2 - reduced/ drier conditions.

Records of C_4 plant photosynthesis in the region come from numerous soil carbonate records from the Potwar Plateau of Pakistan (Quade et al., 1989, Quade and Cerling, 1995), and southern Nepal (Quade et al., 1995). An abrupt positive $\delta^{13}C$ shift occurred ~ 7.7 – 7 Ma (Quade et al., 1989, Quade and Cerling, 1995) which indicated a transition from C_3 dominant to C_4 dominant grasses. This ~7 Ma age also marks a global record of expansion of C_4 photosynthetic plants. However, a number of studies from East Africa and North America show that C_4 plants made up a sizable component of the plant community throughout much of the Miocene (Kingston et al., 1994, Fox and Koch, 2003, 2004) and by the Mid–Miocene C_4 plants were likely to represent an important component of plant biomass (Tipple and Pagani, 2007).

Sage (2003) documented five centres of origin relating to the regions and habitats in which C_4 photosynthesis evolved. These centres are located in the arid tropics, subtropics and warm temperate regions. One such centre is located in central Asia, which is characterised by vast interior basins and dry salinized soils. The ten origins in the Chenopodiaceae family are centred here (Kadereit et al., 2003). Expansion occurred in warm temperate deserts and zero-saline habitats with zero water (Ehleringer et al., 2006).

C_3 and C_4 plants exhibit very different isotopic signatures, which are related to their uptake of CO_2. Therefore a valuable tool to distinguish between these two families can be utilised by their $\delta^{13}C$ signatures, with C_3 plant types exhibiting highly negative $\delta^{13}C$ values of between −33 and −22‰ (O'Leary, 1988, Bender, 1971, Hatch et al., 1967), whilst C_4 plant types typically have less negative values between −20 to −10‰ (Hatch et al., 1967).

Isotopic evidence from the South China Sea indicates that $\delta^{13}C$ values remained relatively stable during the Oligocene with a mean $\delta^{13}C$ of -25.8 ‰. However, during the Miocene there were 5 less negative excursions at 20, 14.2, 11, 5.2 and 2-0.8 Ma (Jia et al., 2003a) with an overall positive trend from ca. 18-16 Ma through to ca. 1 Ma, which the authors ascribe to a gradual appearance of C_4 plants in East Asia since the early Miocene related to the evolution of the East Asian monsoons (Jia et al., 2003a).

1.9 The Aertashi section

The study area is located near the village of Aertashi which is situated to the west of Yarkand River along the margin of the Western Kunlun thrust belt, forming part of the larger Yecheng sub-basin, with its depo-centre near the town of Yecheng (Wei et al., 2013) (Figure 1.9).

The Yecheng sub-basin is interpreted by Wei et al. (2013) and Bande et al. (2015) as a trans-tensional 'pull apart' basin, formed in the Miocene as a result of the synchronous activity of the unconfirmed, buried Sache-Yangdaman fault in the Tarim Basin and the Pamir and Western Kunlun bounding KYTS dextral strike slip fault (Figure 1.4 and Chapter 5, Figure 5.1). The NW-SE-trending Shache-Yangdaman right-slip fault (SYF) has been identified using a single seismic line and has been extrapolated to continue into the subsurface of the western Tarim Basin by Wei et al. (2013). This structure is suggested (Bande et al., 2015, Wei et al., 2013) to have been active syn-depositionally with the Wuqia Group and Xiyu Formation. The SYF has been tentatively connected to the dextral Talas-Fergana fault (TFF) to the northwest, which experienced significant slip during the late Oligocene - Middle Miocene (Bande et al., 2015), however little evidence for this fault exists.

Wei et al. (2013) provide seismic data from the Pamir margin Qimugen Thrust belt (QFTS), located adjacent to Aertashi which shows growth faulting in what they term the 'Upper Artux' at ~15 Ma, which they note is equivalent to the Xiyu Formation of Zheng et al. (2000) (redated by Zheng et al. (2015a)).

1.9.1 Sedimentology

Within the Aertashi section, Paleogene - Neogene eastward dipping sedimentary rocks are well exposed along the Yarkand River and the roadside from Aertashi to Poskam

(38° 11’29.56”N, 77°16’18.11”E) and provide a continuous record of the transition from marine facies of the Kashi Group to a continental fluvial system in the Wuqia Group.

Previous work on sedimentology at this section identified the underlying Kashi Group as a series of marine successions including the Aertashi, Qimugen, Kalatar and Wulagen formations, which record the third and fourth marine regressions of the Tarim Sea (Bosboom et al., 2011). Overlying these rocks is the Wuqia Group, present at the Aertashi section as a series of terrestrial red sandstones, siltstones and mudstones interpreted to be fluvial, lake and delta facies (Yin et al., 2002, Bosboom et al., 2014c, Zheng et al., 2006, 2015a).

In the Aertashi region, the non-marine / continental Bashibulake Formation (time equivalent) (Bosboom et al., 2014a,c) has been subject to some confusion of the nomenclature of this unit. As a result, the first non-marine unit in the sedimentary section is either assigned to the Bashibulake Formation (Zheng et al., 2015a) or the Keziluoyi Formation (Bosboom et al., 2014a,c) owing to its non–marine nature.

The Wuqia Group is overlain by a sequence of conglomerates, sandstone and siltstones of the Artushi Formation, suggested to be formed in a distal alluvial fan and braided and meandering fluvial environment (Yin et al., 2002, Zheng et al., 2010, 2015a). An abrupt change in lithofacies is recorded in the overlying Xiyu Formation, which contains massive cobble conglomerates interpreted to be proximal alluvial fan deposits (Zheng et al., 2010, 2015a).

1.9.2 Existing age control in Aertashi

A low resolution magnetostratigraphic study in Aertashi was conducted by Yin et al. (2002). Sampling in this study is estimated to begin around 200 m above the upper Eocene – lowermost Oligocene Bashibulake Formation and continued through to the onset of large grey conglomerates at ~4050 m stratigraphic height assigned to the Xiyu Formation (Zheng et al., 2010, 2015a) (Figure 1.11). However, given the uncertain start point and a sampling resolution of 22.5 m, this study was insufficient to make an accurate correlation with the geomagnetic polarity timescale (GPTS). It thus yielded a number of possible correlations from 31-24 Ma or from 20-15 Ma for the section under study, with a high level of ambiguity.

Subsequently Bosboom et al. (2014a, c) co-ordinated a biostratigraphic and magnetostratigraphic analyses of the Aertashi section. They recognized the last marine deposits at Aertashi as belonging to the Wulagen Formation, with a late Eocene age constrained by bivalves, calcareous nanofossils and dinoflagellate cysts. The onset of continental deposition in Aertashi is dated to commence at the base of C18.r (ca. 41 Ma) and is magnetostratigraphically dated through to C9.n (ca.27 Ma). More recently this section has been dated by Zheng et al. (2015a) using their own magnetostratigraphy combined with the palynology by Bosboom et al. (2014c), with an upper constraint, provided by Ar-Ar age control from a volcanic ash layer located at ~6700 m stratigraphic height (See Chapter 4, Figure 4.2 for an illustration of these studies)

This ash layer is suggested to have formed during an eruption possibly related to the Tashkorgan Alkali complex and provides a depositional age of 11 Ma for this location. However, there is some dispute as to whether this dated layer is a volcanic ash deposit as suggested by Zheng et al. (2015a,b), or a reworked sedimentary deposit (Sun et al., 2015), which would alter the interpretation of this layer to have a depositional age of <11 Ma.

This study builds upon this earlier work in order to further constrain the tectonic and climate evolution of the Pamir range using this well situated and complete Cenozoic section.

2. Methods

In order to achieve the aims and objectives of this project as discussed in the introduction, the following tasks were performed:

2.1 Construction of a reliable stratigraphy for the Aertashi section

This work leads on from a detailed sedimentological and magnetostratigraphic log published by Bosboom et al. (2014a) for the lower part of the section. The Aertashi sediments were examined in detail by constructing a metre scale grain size log for the upper 2500 m of the section, starting at a tie point of GPS 37˚ 58.284”E 76˚34.785”N. After dividing the section into lithologically distinct units, a detailed ‘type’ log was produced for each unit. This then provided the basis for detailed depositional environment interpretation; which was carried out alongside magnetostratigraphic dating, to provide a depositional ‘timeline’ for the Aertashi section (Appendix 2).

2.2 Establishment of the age of the Aertashi section

2.2.1 Magnetostratigraphic analysis

The continental sediments of the Aertashi section contain a preservation sequence of over 2000 m of continental red beds. The section has undergone very little internal deformation and there are no folds or thrusts, today the beds are tilted ~50˚ making them easy to access. The continental sequence is devoid of fossil records and therefore biostratigraphy is not suitable for providing an age control. However, they are abundant in magnetic minerals which makes them ideal for magnetostratigraphic age control using the biostratigraphy of the marine section directly beneath the continental sediments as a ‘tie point’.

Paleomagnetic analysis seeks to measure the direction of Earth’s magnetic field at the time of the sample’s deposition. Primary Natural Remanent Magnetism (NRM) may be overprinted by magnetic components acquired later in geologic history. An overprint can be removed by using the thermal demagnetisation and/or alternating field demagnetisation techniques (Butler, 1992, Tauxe, 1998). By subjecting samples to increasing temperatures and measuring the residual magnetisation at each temperature step, the complete characteristic remanence can be attained.

The results of NRM analysis can then be visualised on vector end-point demagnetisation diagrams (Figure 2.1); from which the most stable component can be identified, the 'characteristic remanent magnetisation' (ChRM).

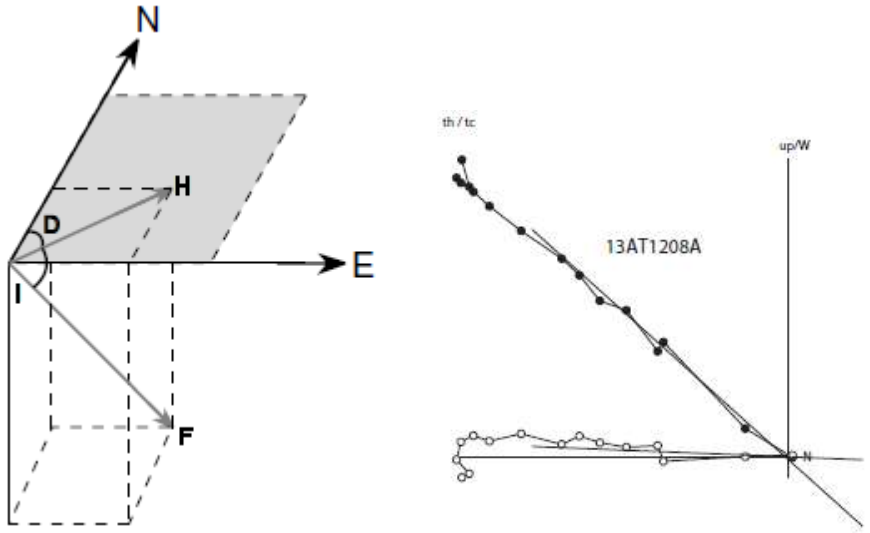

Figure 2.1 a) The magnetic field on any point on the Earth's surface is a vector (F) that possesses a horizontal component (H) which makes an angle (D) with the geographical meridian. The declination (D) is an angle from north measured eastward ranging from 0° to 360° (Langereis et al 2010). B) an example of a vector end point diagram for an Aertashi sample showing the remanent magnetisation for each temperature step.

Line fits are then determined using a minimum of 4 temperature steps. In the case of the Aertashi section, line fits were forced through the origin where directions were clustered in a distinct normal or reverse direction but did not decay to the origin. ChRM directions with a maximum angular deviation (MAD) over 30° were systematically rejected - resulting in an average MAD of 12.7°. Line fits were then categorised into quality 1, 2 or 3 depending on the reliability of the results defined as follows:

Quality 1 (Q1) – ChRM directions (declination and inclination) were precisely determined and the polarity (normal or reversed) unambiguously identified.

Quality 2 (Q2) – ChRM directions were less precise but the polarity was well established and could be unambiguously determined.

Quality 3 (Q3) - The polarity could not be determined from ChRM directions. These ChRM directions were then rejected from further analysis.

Of the remaining ChRM directions, the iterative cut-off criteria of Vandamme (1994) was used and applied separately on normal and reversed polarity directions; any outlying or transitional directions were then removed.

The VGP (Virtual Geomagnetic Pole) latitudes were calculated from the obtained ChRM directions. The remaining directions separate into two antipodal clusters from which the mean normal and reversed ChRM directions were calculated (Fisher, 1953).

The reliability of the ChRM for magnetostratigraphic analysis is assessed using a reversals test (Tauxe, 1998). This tests a common mean for two modes where one of these modes has been flipped to its antipode. If the confidence intervals for the normal and reverse antipodes overlap, the two means cannot be distinguished at the 95% confidence interval; if they do not, they pass the reversals test. Figure 2.2 is an example of a positive reversals test for the Aertashi section.

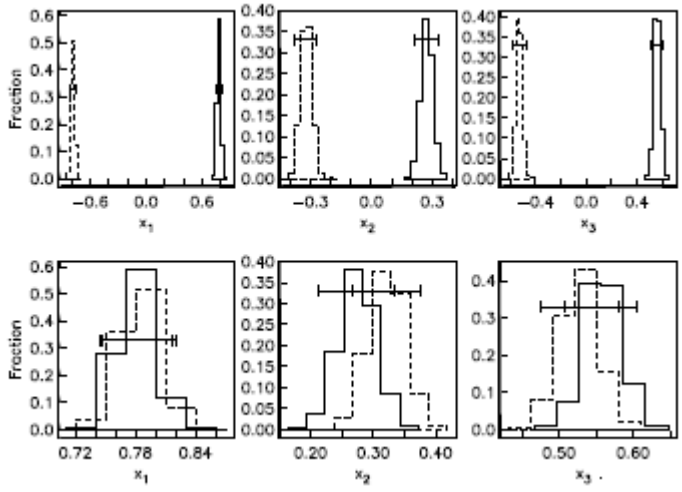

Figure 2.2 Magnetic reversals test (Tauxe, 1998) yielding a positive result, confirming the primary origin of the dataset.

In order to determine the age of a sedimentary section, the ChRM directions obtained for the sedimentary section need to be plotted stratigraphically and compared to an established geomagnetic polarity time scale (GPTS). The construction of the GPTS relies on the establishment of a continuous record of magnetic reversals of known age. One of the most reliable records is that obtained by the marine magnetic anomaly record. The magnetic remanence of the sea floor is acquired during the process of sea floor spreading at mid ocean ridges, where rising magma solidifies at the surface preserving the remanent magnetic field at the time of deposition. This, in conjunction

with biostratigraphic analysis, enables the geological time scale to be defined. Using a tie point of known age, such as biostratigraphy or radiometric dating of an extrusive igneous layer, a starting age for the correlation can be determined. This known age can then be used to compare the magnetic polarity reversals of the sedimentary section to a published and well established geomagnetic timescale.

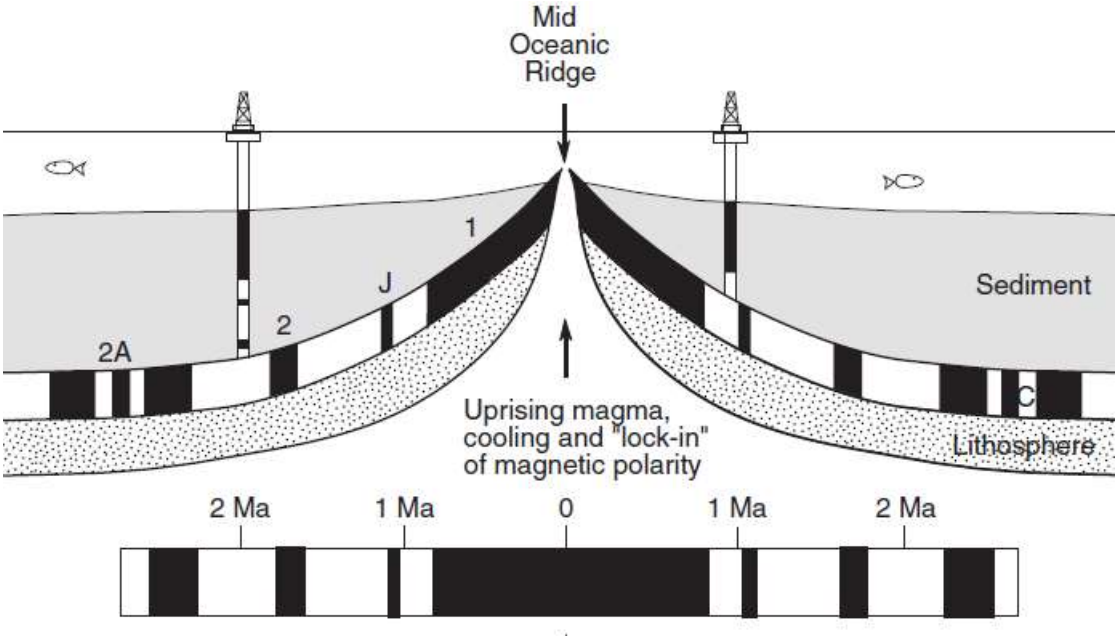

Figure 2.3 Formation of marine magnetic CHRMs during sea floor spreading with the black areas recording 'normal' magnetic directions and the white bars recording magnetic reversals (Langereis et al., 2010).

In this study the geomagnetic timescale developed by Gradstein et al. (2012) was used to interpret and date the Aertashi section. Gradstein et al. (2012) was chosen due to the high resolution of this study, particularly with relevance to the Miocene where a high interval of magnetic reversals is identified which is of particular interest in this study.

2.2.1.1 Sampling methods and analysis

Paleomagnetic sampling at the Aertashi section was performed using a battery operated electric drill with an air cooled diamond bit, yielding standard core samples of ~2.5 cm in diameter and ~2.5-10 cm in length. Samples were orientated using a Pomeroy orienting tool with a Brunton magnetic compass and a clinometer. The sampling strategy involved digging trenches to preferentially sample the finest grain size in order to prioritise the single–domain magnetic particles, which are more stable at longer timescales (Butler, 1992) and are the most likely to align with the magnetic

field during deposition. 662 samples were collected over a 2500 m section at a resolution of 0.4-5 m (average 3.7 m). Occasional sampling gaps were minimal (<40 m) and were reduced by digging deeper trenches in less well exposed parts. Following the fieldwork, samples were cut into cores of 2.2 cm in length.

Analysis was performed in the magnetically-shielded room at the archeo-palaeomagnetic laboratory at the University of Rennes 1. A first set of pilot samples were processed using both Alternating Field and Thermal demagnetizations in a shielded oven in order to determine the best processing strategy and identify potential magnetisation carriers. Thermal demagnetization yielded better results and therefore was subsequently applied to most samples using 10 - 18 temperature steps between room temperature and 690°C. The remanent magnetization was measured using a 2G cryogenic magnetometer. To monitor mineral transformation upon laboratory heating, bulk magnetic susceptibility was measured at room temperature for each sample between each temperature step using a Bartington MS2 magnetic susceptibility meter.

2.3 Determination of sediment provenance

The Pamir, Western Kunlun and northern margin of Tibet are characterised by a number of geologically distinct terranes (see Section 1.4.1). By analysing a range of modern sand and mud sediments derived from rivers draining each of these terranes, it is possible to characterise the distinct geological and isotopic signature of each terrane. By applying the same isotopic and petrographic analysis to the detrital sediments collected in Aertashi, it is possible to identify the terrane of origin for these detrital sediments. Therefore, by analysing a range of stratigraphically and chronologically placed samples from Aertashi, it is possible to identify the lowest stratigraphic interval which records detritus derived from the Pamir range, and thus the timing of the first instance of Pamir-derived material in Aertashi. This provides constraints on the northward motion and evolution of the Pamir range into the Tarim Basin. To achieve this task the following petrographic and isotopic analyses were conducted on both modern river sediments and sedimentary rock samples.

2.3.1 U-Pb dating of detrital zircon grains

U-Pb dating of detrital zircons provides the age of crystallisation for each individual zircon grown during cooling through igneous or metamorphic processes. A minerals closure temperature is the temperature at which a system has cooled to the point where

there is no longer any significant exchange of parent or daughter isotopes between the mineral and its external environment. This therefore determines a minerals radiometric age. Zircons have a high closure temperature for Pb diffusion greater than 900˚C (Cherniak and Watson, 2001), which makes them relatively resistant to 'resetting' of the original crystallisation age as a result of subsequent deformational and metamorphic events.

The Pamir and Western Kunlun ranges have a range of chronologically distinct terranes as described in Chapter 1.4.1, Figure 1.9 and Appendix 9. This makes detrital zircon U-Pb dating a particularly useful tool in determining sedimentary provenance for the Aertashi section.

U-Pb ages are determined by measuring the relative quantity of parent and daughter isotopes involved in the ^{238}U to ^{206}Pb and ^{235}U to ^{207}Pb decay systems. In the case of zircon, where it is assumed that the contribution of initial lead is negligible compared to the radiogenic component, the decay system can be calculated using the following equations (where * stands for radiogenic).

$$\left(\frac{^{206}Pb^*}{^{238}U}\right) = \left(e^{\lambda_{238}t} - 1\right)$$

$$\left(\frac{^{207}Pb^*}{^{235}U}\right) = \left(e^{\lambda_{235}t} - 1\right)$$

These decay equations can then be used to construct isochron diagrams which provide an age for the zircon.

However, this assumes that the dated mineral has remained in a 'closed' system, which is not always the case. In order to determine if a zircon has remained in a closed system since the time of formation, a parametric Concordia curve can be drawn based on the results of the above equations. On the Concordia plot, all samples that remained in a closed system since the time of formation are concordant, and therefore fall on the Concordia curve; those that do not are discordant and have either experienced some form of open-system behaviour, or contained initial Pb in the system (Figure 2.4).

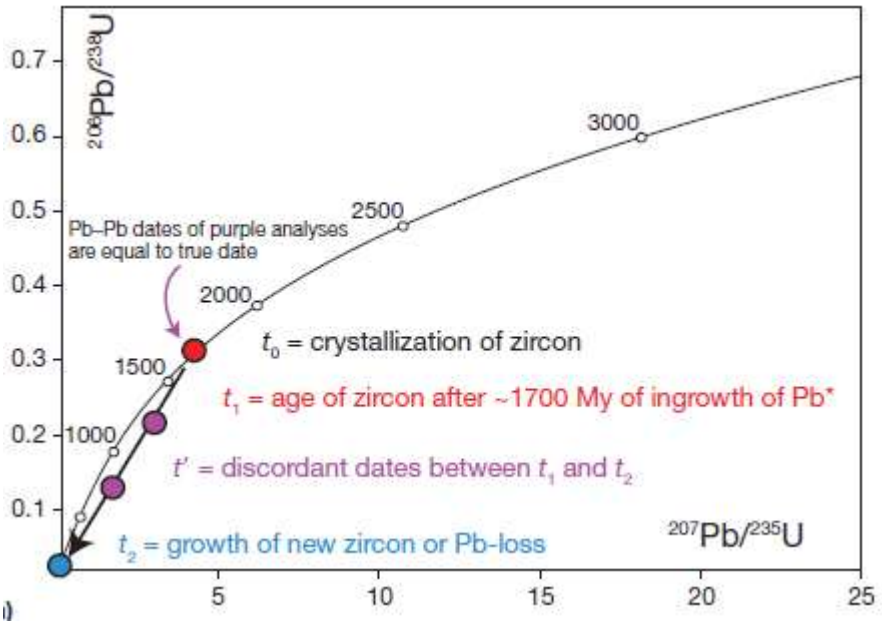

Figure 2.4 Example of a 1700 Ma zircon, after 1700 My in a closed system the zircon appears on the Concordia plot at t1, at t2 the zircon suffers Pb loss or growth of new zircon around the older core, t' represents zircons that are discordant following partial Pb loss or mineral overgrowth at t2 (Schoene, 2014).

Analysis for detrital zircon U-Pb was conducted at the London Geochronology Centre, University College London using a New Wave 193 nm excimer laser ablation system coupled to an Agilent 7700x quadrupole-based inductively coupled plasma mass spectrometer (ICP-MS). A typical laser operating condition for zircon uses an energy density of approximately 2.5 J.cm^{-2}, spot size of 20-25 µm, and a repetition rate of 10 Hz. Repeated measurements of external zircon standard PLESOVIC (TIMS reference age 337.13±0.37 Ma; (Sláma et al., 2008)) and NIST 612 silicate glass (Pearce et al., 1997) were used to correct for instrumental mass bias and depth-dependent inter-element fractionation of Pb, Th and U. Temora (Black et al., 2003) and 91500 (Wiedenbeck et al., 2004) zircon were used as secondary age standards. Data were filtered using standard discordance tests with a 15% cut off. The $^{206}Pb/^{238}U$ ratio was used to determine ages where < 1000 Ma and the $^{207}Pb/^{206}Pb$ ratio for older grains. Data were processed using GLITTER 4.4 data reduction software. Time-resolved signals that record evolving isotopic ratios with depth in each crystal enabled filtering to remove spurious signals owing to overgrowth boundaries, inclusions, or fractures.

2.3.2 Zircon fission track dating

Detrital zircon fission track analysis is a well-established technique in provenance studies and provides information about the thermal history of a sample or region (Naeser et al., 1989, Carter, 1999, Garver et al., 1999).

Zircon fission track analysis is an isotopic dating method that uses the U decay system. Fission tracks are preserved in minerals that contain small amounts of uranium, such as zircons. These tracks come from the spontaneous fission of ^{238}U present in the mineral, which decays at a known rate; fragments emitted during this process leave trails of damage in the crystal structure of the mineral, which are known as fission-tracks. The density and length of these tracks provide insights into the thermal history of the zircon (Garver et al., 1999) (Figure 2.5).

Subsequent to formation, fission-tracks begin to 'anneal' (and progressively disappear). The rate of annealing is dependent on the temperature that the mineral is exposed to; the higher the temperature, the faster the annealing. Zircons begin to lose their tracks when the temperature reaches or exceeds ~200-350°C (Tagami et al., 1998, 1996, Bernet, 2009), which is known as the zircon partial annealing zone (PAZ). As long as the zircon remains cooler than this temperature, the tracks will accumulate, and thus provide an age of crystallisation for the zircon.

However, if a zircon is exposed to temperatures exceeding the PAZ, then the age of the zircon becomes reset, resulting in a 'younger' age of crystallisation (Naeser et al., 1989, Garver and Kamp, 2002). In addition, if the zircon remains within the PAZ for a long time, the apparent age will be reduced although not completely reset (Naeser et al., 1989).

In the absence of zircon 'resetting', the number of tracks developed in the zircon provides the minimum age at which the zircon passed through the PAZ, and therefore remained sufficiently 'cool' to preserve this age, whereas the length of the tracks provide information about how quickly the zircon passed through this zone (Naeser et al., 1989).

Once exposed at the surface, the zircons host rock begins to be eroded due to natural weathering processes. Zircons typically remain unaltered due to their high durability and resilience, and form part of the sediment that becomes transported by rivers into adjacent basins, where they are deposited. The time for erosion and sediment transport

(lag time) has often been regarded as geologically instantaneous (Heller et al., 1992, Bernet et al., 2004); however in a continental setting, sediment recycling and storage are major factors influencing the lag time of the sediment (Yang et al., 2013)

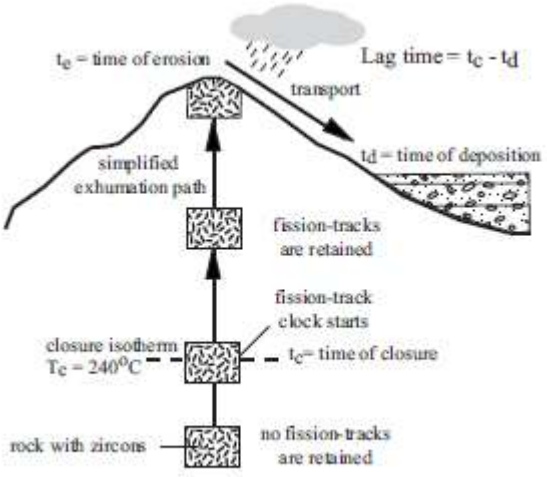

Figure 2.5 An example of the lag time of a sample based on the PAZ temperatures for zircons (Bernet and Garver, 2005)

In order to determine the cooling age, the number of fission tracks and the uranium (U) content of the zircon needs to be determined.

There are two methods used for determining the uranium content of a zircon. The first induces fission of U^{235} in a sample through neutron irradiation in a reactor, with an external detector such as mica fixed to the grain surface. During irradiation the induced fission tracks leave scars in the overlay detector which can be revealed by chemical etching; the ratio of spontaneous U^{238} to induced U^{235} tracks is proportional to its age.

The second method involves laser ablation using a laser ablation inductively coupled plasma mass spectrometer (LA-ICP-MS), where the zircon is hit with a laser and ablated before being analysed using mass spectrometry.

The number of tracks is a function of time and the U content of the sample:

$$F_s = \left(\frac{\lambda_f}{\lambda_\alpha}\right)^{238} U\left(e^{\lambda \alpha t} - 1\right)$$

where F_s is the number of tracks produced by spontaneous fission, λ_α is the α decay constant for ^{238}U, and λ_f is the spontaneous fission decay constant - the best estimate for which is $8.46 \pm 0.06 \times 10\text{-}17yr^{-1}$.

This equation can be solved directly for t, simply by determining the number of tracks and number of U atoms per volume of sample.

Determining fission track density involves polishing and etching a thin section, and then counting the number of tracks per unit area. A minimum track density of 10 tracks per cm^2 is required for the results to be statistically meaningful and a fission track must also intersect the surface to be counted (Galbraith, 2005).

As fission tracks anneal, they become shorter. Thus when a grain is subjected to elevated temperature, both the track density and the mean track length will decrease. As a result, determining if partial annealing of fission tracks has occurred can be overcome by also measuring the length of the tracks.

2.3.2.1 Sampling and analysis

A total of 6 samples were submitted for zircon fission track analysis; however, only 3 samples contained zircons of sufficient size and quality to produce useable results (see Appendix 1 and Figures 3.5 and 3.6 in Chapter 3 for sample locations).

Zircon fission track analysis for this project was conducted by A. Carter at the London Geochronology Centre, University College London. Zircons were mounted in PTFE ('Teflon') and polished for etching to reveal the natural spontaneous fission tracks. Several mounts were made for each sample and each etched for a different time to take into account variations in etch rate associated with radiation damage and age. Step etching used a binary eutectic of KOH:NaOH at 225°C for between 6 and 48 hrs. Etched grain mounts were packed with mica external detectors and corning glass (CN2) dosimeters, and irradiated in the FRM 11 thermal neutron facility at the University of Munich in Germany. Following irradiation the external detectors were etched using 48% HF at 20˚C for 25 minutes. Sample ages were determined using the zeta calibration method and IUGS recommended age standards (Hurford, 1990).

2.3.3 Sm-Nd decay system

Both Sm and Nd are rare earth elements, ^{147}Sm decays to ^{143}Nd by alpha decay with a half-life of 106 Ga ($l = 6.54 \times 10\text{-}12y^{-1}$).

Rare earth elements are refractory. It is assumed that the solar system was isotopically homogeneous when Earth formed. In a closed system we therefore know the Earth's Sm/Nd ratio at a given point in time. Therefore we can consider relative deviations of $^{143}Nd/^{144}Nd$ from the bulk-Earth value.

These deviations are small, and are written in parts per 10,000. This is the Ɛ (epsilon) notation which is defined using the following equation:

$$\text{ƐNd} = \left(\frac{\left(^{143}Nd/^{144}Nd\right) \text{ sample} - \left(^{143}Nd/^{144}Nd\right) \text{ CHUR}}{\left(\frac{^{143}Nd}{^{144}Nd}\right) CHUR} \right) * 10000$$

CHUR stands for 'chondritic uniform reservoir' (the value of the $^{143}Nd/^{144}Nd$ ratio in chondrites).

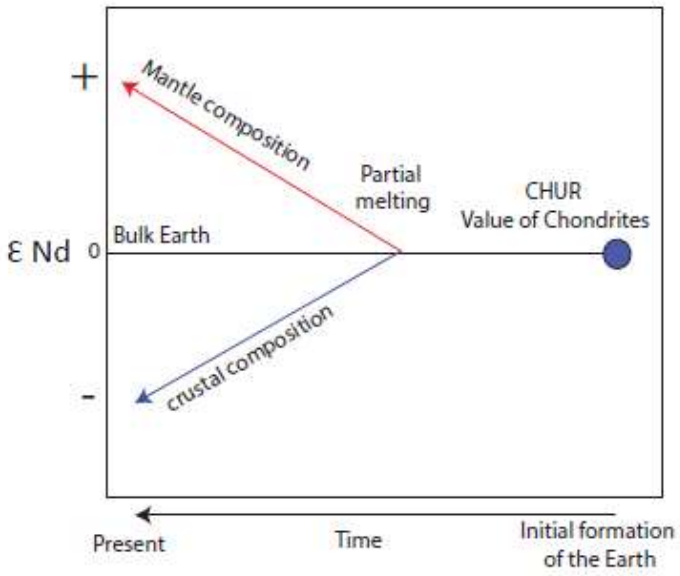

Figure 2.6 A generalised evolution curve for ENd

During fractional crystallisation of magma, Sm is less soluble than Nd and preferentially fractionates into the first forming crystals. This results in the removal of Sm from the originally homogeneous melt, resulting in enrichment of ^{144}Nd in the melt. The epsilon notation denotes the amount by which a sample's $^{143}Nd/^{144}Nd$ ratio differs from that of CHUR. The εNd value therefore reflects the evolution of the source rock. Crustal, more evolved sources have more negative εNd values whilst more mafic, less evolved sources have more positive εNd values (Figure 2.6).

Since both Sm and Nd are relatively immobile and insoluble, the εNd value is little affected by weathering, and low grade metamorphic processes. Therefore the εNd value in fine-grained sediments does not generally differ much from the source rock. However, this generally does not work for coarse-grained sediments because they contain accessory minerals whose Sm/Nd ratios can be quite different from that of the whole rock.

εNd makes a useful provenance tool when examining petrographically distinct source terranes such as those found in the Pamir and WKL ranges. The Pamir terranes are composed of crustal, more evolved rocks compared to the more mafic, less evolved WKL and Himalayan sources. When source rocks are compared with the Aertashi sediments, a model for the evolution of the provenance in Aertashi can be obtained.

A total of 24 samples of the finest mud fraction available were collected from the Aertashi section (see Appendix 1 and Figures 3.5 and 3.6 for sample locations).

2.3.3.1 Sample preparation and analysis

Samples were powdered using a ball mill at the University of Lancaster. 150-200 mg of < 63μm sample was weighed into Savillex Teflon beakers. Samples were then leached in warm dilute (10%) Romil uPA acetic acid in order to remove any carbonate material. After centrifuging, washing and drying, samples were reweighed and mixed ^{149}Sm-^{150}Nd, isotope tracers were added. Samples were dissolved using HF/HNO_3 before conversion to chloride form. The samples were then dissolved in ~2 ml of 1M HCl/0.1M HF in preparation for column chemistry and centrifuged.

Primary columns, consisting of 2 ml of Eichrom AG50x8 cation exchange resin in 10 ml Biorad Poly-Prep columns, were used to separate a bulk rare-earth element fraction.

Sm and Nd were separated using columns containing Eichrom LN-Spec resin. Sm and Nd fractions were loaded onto one side of an outgassed double Re filament assembly using dilute HCl.

Analysis for εNd was carried out on a Thermo Scientific Triton mass spectrometer at the Natural Environment Research Council (NERC) Isotope Geoscience Laboratories, Keyworth. Nd isotope data were normalised to ^{146}Nd/^{144}Nd = 0.7219. Fifteen analyses of the JND-i standard gave a value of 0.512106 ± 0.000005 (9.1 ppm, 1-sigma). All

other standard and sample data is quoted relative to a value of 0.512115 for this standard. Seven analyses of La Jolla gave 0.511864 ± 0.000006 (11.5 ppm, 1-sigma).

2.3.4 Petrography

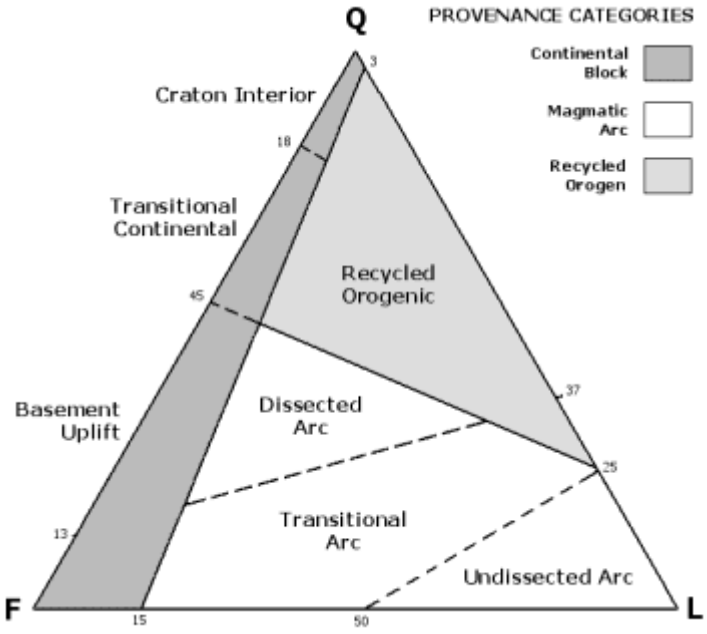

Figure 2.7 QFL diagram first classified by Dickinson (1985) - (Q) quartz, (F) feldspar and (L) lithics.

Petrography is a well-established provenance technique, focusing on the identification of minerals present in thin sections made from rock samples. Analysis is conducted using a polarising microscope which enables precise mineral identification.

The technique was first used by Dickinson (1985) to identify the proportions of different minerals and lithic clasts in sandstones. Results can then be classified into provenance by generating ternary plots which group the minerals into 3 end member compositions - quartz (Q), feldspar (F), and lithics (L) - frequently referred to as a QFL plot. By classifying the sandstone samples in this way, they can be grouped into 3 distinct provenance regions, recycled origin, magmatic arc, and continental block (Figure 2.7).

2.3.4.1 Sampling and analysis

A total of 16 samples were collected for petrography (see Appendix 1 and Figures 3.5 and 3.6 for a summary of sample locations). Petrographic analysis was carried out by Eduardo Garzanti at the University of Milano-Bicocca, Italy using the Gazzi-Dickinson method (Ingersoll et al., 1984). Results were plotted using the QFL method.

Full quantitative information was collected on coarse-grained rock fragments, and metamorphic types were classified according to protolith composition and metamorphic rank. Rock fragments for each sample were ranked using the Metamorphic Indices MI and MI*.

MI varies from 0 (in detritus shed by exclusively sedimentary and volcanic cover rocks) to 500 (in very-high-rank detritus shed by exclusively high-grade basement rocks), whereas MI* considers only metamorphic rock fragments, and thus varies from 100 (in very-low-rank detritus shed by exclusively very low-grade metamorphic rocks) to 500 (Garzanti and Vezzoli, 2003).

Very low- to low-rank metamorphic lithics (for which a protolith can be inferred) are then subdivided into metasedimentary (Lms) and metavolcanic (Lmv) categories; whilst medium- to high-rank metamorphic lithics are subdivided into felsic (metapelite, metapsammite and metafelsite; Lmf) and mafic (metabasite; Lmb) categories.

2.3.5 Heavy mineral analysis

Heavy minerals represent the detrital components of rock-forming minerals that have specific gravities greater than 2.8 $g.cm^{-3}$.

Heavy mineral analysis is a well-established sedimentary provenance tool because there are a large number of detrital minerals that are exceptionally source diagnostic in this category (Morton, 1991), including minerals such as zircon, rutile and apatite. Analysis is commonly used in conjunction with petrography to identify the mineral composition of a rock, which can be related to specific source lithology, and thus to specific provenance areas.

Results for heavy minerals are plotted in a biplot (Gabriel, 1971) (Figure 2.8), where the length of each ray is proportional to the variance of the corresponding element in the data set. If the angle between two rays is close to 0°, 90°, or 180°, then the corresponding elements are respectively directly correlated, uncorrelated, or inversely correlated.

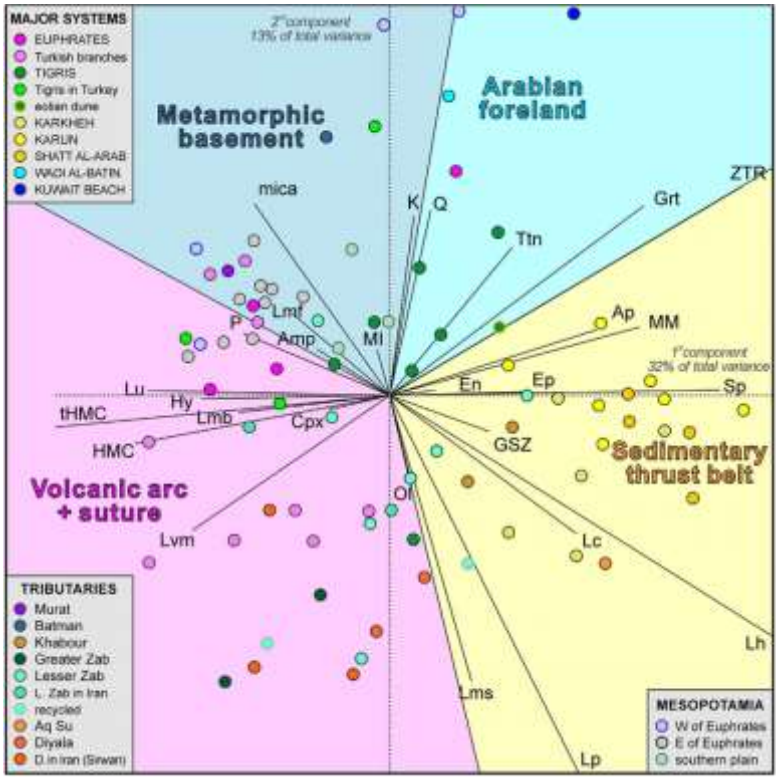

Figure 2.8 Provenance discrimination with the compositional biplot (Gabriel, 1971). All major petrographic and heavy mineral parameters are considered, and both multivariate observations (points) and variables (rays) are displayed. GSZ = grain size (in µm); KF = K-feldspar; L = lithic grains (Lp = shale/siltstone; Lms = low-rank metasedimentary; Lmf = high-rank felsic metamorphic; Lmb = high-rank metabasite); HMC = Heavy Mineral Concentration; MM = chloritoid + staurolite + andalusite + kyanite + sillimanite (Garzanti et al., 2016).

Chemical processes, weathering, composition of the source material, fractionation during transport, sedimentary recycling and particularly diagenesis tend to eliminate the unstable grains that carry the most useful provenance information. This, therefore, needs to be taken into account when determining sediment provenance (Morton, 1991).

Zircon (Z), tourmaline (T) and rutile (R) grains have a high mechanical and chemical stability and are more resistant to the effects of recycling or depletion in mineral species during diagenetic dissolution. Therefore, as siliclastic rock becomes more mature, the relative proportions of ZTR increase. Because of this the maturity of sediments can be examined by calculating the relative proportions of these heavy minerals relative to the total percentage of heavy minerals in the sample (ZTR index). The ZTR index can be calculated as the volume percentage of total (HMC) or transparent (tHMC) heavy minerals (Garzanti and Andò, 2007). High ZTR values are

characteristic of a mature sediment and, conversely, low ZTR values represent an immature sample (Hubert, 1962).

2.3.5.1 Sample preparation and analysis

A total of 15 samples collected from Aertashi were submitted for heavy mineral analysis (see Appendix 1 and Figures 3.5 and 3.6 for a summary of sample locations).

Heavy mineral analysis was carried out by Sergio Andò at the University of Milano-Bicocca, Italy. For each sample 200 points of 63-355 μm size fractions were counted. Heavy minerals were obtained by dry sieving and heavy liquid separation. Although bulk-sample analyses represent the only correct option to accurately estimate the percentages of detrital minerals, the presence of grains with great size differences in poorly-sorted sediments makes mounting and identification difficult. Therefore, the lower and upper size limits were set to a size range of 63-355 μm which should be large enough to include most of the detrital population, and thus obtain a faithful characterisation of the heavy mineral suite (Garzanti et al., 2009).

2.4 Determination of tectonic fabric

2.4.1 Anisotropy of magnetic susceptibility (AMS)

AMS is the study of the preferred orientation of magnetic minerals in a rock or sediment. It is principally used for the study of primary structures and rock fabric, but can also be used to determine weak deformation when lineation and foliation have not developed (Dubey, 2014).

A rock contains a range of minerals with a variety of magnetic properties. The amount each grain contributes to the total (bulk) susceptibility and its anisotropy depends on its magnetic properties.

The directional susceptibility of rocks is generally measured by low field bulk susceptibility; the anisotropy of a sample is determined by measuring the susceptibility of a sample in a minimum of six orientations. This produces a multidimensional image of the sample in terms of its susceptibility, allowing a strain ellipsoid to be determined

The shape of this strain ellipsoid can be described in terms of oblate, neutral or prolate. This allows for the quantification of the strain fabric for the rock sample (Dubey, 2014).

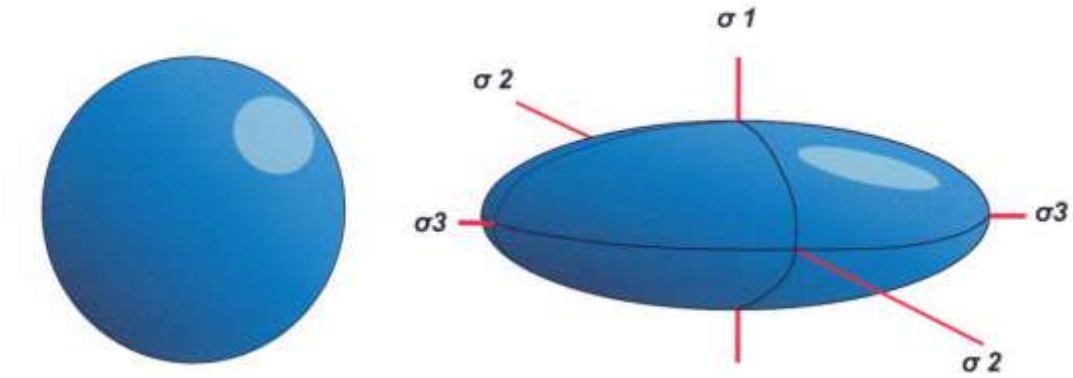

Figure 2.9 An example of a strain ellipsoid a) an example of a grain prior to deformation, b) a strain ellipsoid as a result of compression in a primary direction along the σ1 axis.

A Jelineck shape plot can be used to depict the magnitude and shape of susceptibility ellipsoids using the parameters Pj and T, where Pj is the degree of anisotropy and T is the shape parameter (Figure 2.9).

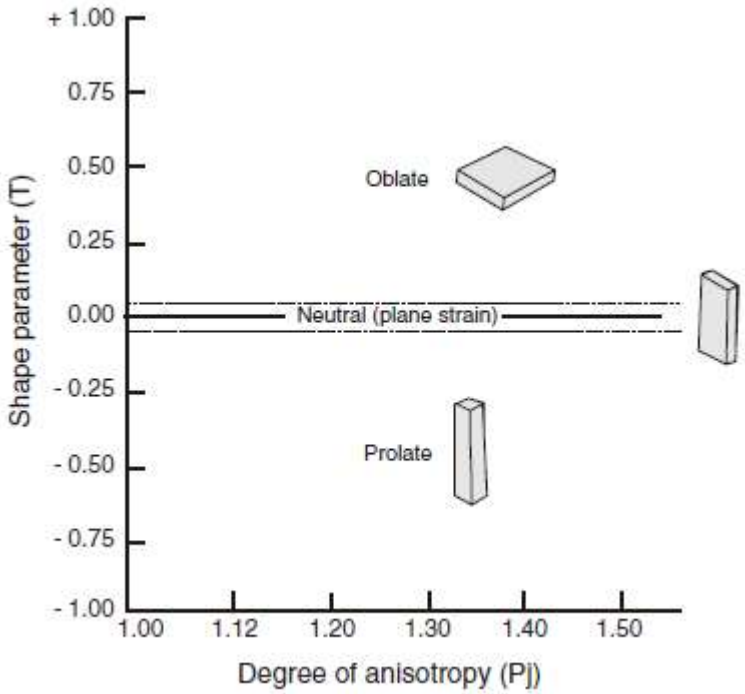

Figure 2.10 Jelinek plot showing the degree of anisotropy (Pj) and shape parameter (T) from Tarling and Hrouda (1993)

Depositional or compactional loading normally results in oblate ellipsoid, whereas a prolate ellipsoid represents a sheath type fold (Figure 2.10).

By applying AMS to the sediments at Aertashi, a picture of the strain fabric can be obtained during the time of deposition.

2.4.1.1 Sampling and analysis

Sampling for AMS was conducted by the author utilising the paleomagnetic cores collected for the magnetostratigraphic study (see Section 2.2.1), yielding a total of 345 samples of the finest fraction available. These samples were selected at regular intervals throughout the section (with the lowermost 82 samples provided by Bosboom et al. (2014c)).

Analysis for AMS was conducted at the archeo-palaeomagnetic laboratory at the University of Rennes 1, using a KLY3 – CS Kappabridge instrument. For each sample the principal susceptibility axes (Kmax, Kint and Kmin) were obtained and used to infer the fabric variations throughout the section. Interpretation of results was conducted by Dr. Pierrick Roperch of the archeo-palaeomagnetic laboratory, University of Rennes 1.

2.5 Determination of the regional climate

Because paleoclimate cannot be directly measured, climate proxies must be used. These proxies provide information related to the interaction between climate and geological processes such as weathering but also provide information on the response by plants and organic material to regional and localised climate changes. By understanding these proxies, we can develop a model of the environment during the Eocene through to mid Miocene for the Aertashi section. This can then be related to climate changes occurring both regionally and globally. Together with a greater understanding of the evolution of the Pamir range, the relationship between tectonics and climate can be studied. This has implications for understanding not only paleoclimate but also for our understanding of future climate changes.

2.5.1 X-Ray Diffraction (XRD)

Clay minerals form as a by-product of weathering processes. The type of weathering mechanism, morphological environment, and the composition of a source rock determines the resultant clay mineral formed.

In general, a very cold or hot-dry climate leads to the formation of clays dominated by illite, mica and chlorite, provided there is sufficient Si, Mg and Al which are generally

sourced from aluminosilicates in the host rock (Moore and Reynolds, 1997). Illite and chlorite are the products of high levels of physical weathering and are typical of Himalayan and mountain-derived sediments (Huyghe et al., 2011). Illite is also commonly formed through the diagenetic alteration of smectite (Moore and Reynolds, 1997, Chamley, 1989). During burial and early metamorphosis, at around 2700 m depth, smectite is replaced by smectite-illite mixed layers; this transformation implies a pressure of approximately 900 $kg.cm^{-2}$, and a paleo temperature of about 100˚C. Illite-rich layers become abundant below 3750 m at pressures of 920 $kg.cm^{-2}$ and temperatures around 140 ˚C (Chamley, 1989).

Illite or chlorite crystallinity is a measure of the diagenetic or metamorphic grade of the clay.

Crystallinity values of:

- >1˚ 2-theta (2θ) correspond to the shallow diagenetic zone;
- 0.42˚ to 1˚ 2θ the deep diagenetic zone;
- 0.30˚ to 0.42˚ 2θ correspond to the low anchizone;
- 0.25˚ to 0.30˚ 2θ correspond to the high anchizone;
- and <0.25˚ 2θ the epizone (Kemp et al., 2016 and references therein).

Temperate climates tend to lead to the formation of minerals which are often partially altered such as exfoliated illite and chlorite, irregular mixed layer clays, vermiculite and degraded smectite with changing proportions which reflect the local petrography, level of precipitation, drainage and temperature (Chamley, 1989).

A semi-arid environment favours the formation of well-crystallised Fe-smecite particularly in warm, mildly alkaline and poorly drained regions with a long dry season (Chamley, 1989).

A hot and wet climate leads to the formation of kaolinite and goethite (an iron oxyhydroxide), and of gibbsite under very intense leaching (Chamley, 1989). Kaolinite develops as a result of the intense hydraulic weathering of aluminosilicates such as feldspars (Chamley, 1989, Thiry, 2000, Bolle and Adatte, 2001, Robert and Kennett, 1994, White and Brantley, 1995).

Analysis to determine the clay mineralogy of a sample is conducted using X-ray diffraction. X-ray diffractometers consist of three basic elements: an X-ray tube, a

sample holder, and an X-ray detector. In XRD, an X-ray beam is directed at the sample while slowly rotating the incident angle of the beam. This beam then reflects through each crystalline layer of the clay mineral producing a series of diffracted beams. The diffraction 'pattern' of the intensity of X-rays at different angles is used to produce a diffraction spectrum. A typical diffraction spectrum consists of a plot of reflected intensities versus the detector angle (2θ).

The 2θ values for the peak depend on the wavelength of the anode material of the X-ray tube. It is therefore customary to reduce a peak position to the inter-planar spacing d (Moore and Reynolds, 1997). The value of the d-spacing is obtained by the application of 2θ from Bragg's law:

$$d = \frac{\lambda}{2 \sin \theta}$$

Clay mineral diffraction patterns are identified by identification of the position, intensity, shape and breadth of a series of peaks, which correspond to a particular clay group. At small diffraction angles the various peaks for each clay group are equidistant.

In order to distinguish individual clay minerals from the diffraction patterns a 3 stage process is required:

1) Sample is analysed in an air dried state to gain a full trace.
2) Sample is reanalysed after being exposed to an ethylene glycol vapour in order to expand smectite clay and distinguish between smectite and illite.
3) Sample is then heated to 500˚C for a minimum of 2 hours to distinguish kaolinite from chlorite; this is because above 60˚C kaolinite is lost leaving only chlorite.

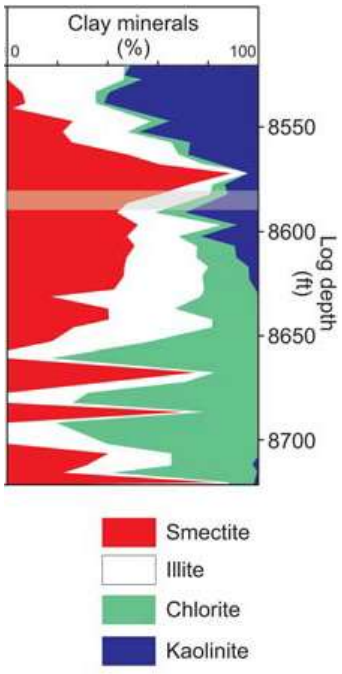

Figure 2.11 Sediment core clay mineralogy for the North sea Basin (Kemp et al., 2016)

The relative proportions of clay minerals in a sample are then corrected to produce semi-quantitative estimates, based on the assumption that they collectively add up to 100% (Biscaye, 1965) (Figure 2.11). However the results of this method are not a direct measure of the absolute abundance of a mineral. This is due to variations in

analysis conditions such as sample mount thickness which can vary between individual samples and within the smear mount of an individual sample, beam placement, the degree of clay mineral preferred orientation, and the variable 'diffractability' of different clay minerals (Biscaye, 1965).

Precision estimates for this method are around 5-10% of the 'true' value in compositional percentages >15% (Schultz, 1964). This method also does not take into account variations in crystal order and chemical compositions of different species of the same mineral (Kemp et al., 2016).

As absolute values of clay mineral assemblages are not obtainable, the relative variations in the abundance of different minerals can be applied in order to interpret clay mineralogy as a climate proxy (Chamley, 1989).

A series of climate proxies are used to do this including the relative proportions of kaolinite/ smectite (K/S) and kaolinite/ illite (K/I) (Robert and Kennett, 1994, Bolle and Adatte, 2001), illite chemistry index (Esquevin, 1969), and illite crystallinity (Chamley, 1989). Typically low K/(I-S) values indicate a seasonal, tropical climate, whereas higher values indicate an increase in kaolinite interpreted to indicate a transition to a hot, humid climate (Kemp et al., 2016).

2.5.1.1 Sampling and analysis

XRD analysis was conducted on 20 mudstone samples collected from the Aertashi section by the author (see Appendix 1 and Figures 3.5 and 3.6 for sample locations). Sample preparation was conducted following the methods of Moore and Reynolds (1997). Samples were gently broken down into smaller pieces using a standard agate pestle and mortar before disaggregation in an industrial Waring Blender and rinsed using deionised water into 250 ml glass beakers. Samples were then put onto a low temperature (50˚C) hotplate to remove the excess water without drying down the samples. Samples were then decalcified using 1M acetic acid and allowed to react overnight before being rinsed in deionised water.

Following decalcification, the samples were wet sieved on a 63 μm aperture sieve and the <63 μm fractions were transferred to 250 ml cylinders and re-suspended. After standing for a period determined from Stokes' Law, the <2 μm fraction was removed.

Slide mounts of <2 μm material were made using the 'smear' method as outlined in Moore and Reynolds (1997). Analysis was conducted at Lancaster University using a Rigaku Smart Lab 9kW XRD using a Dtex detector in OD mode. Parallel beam optics were used with incident slit and receiving slits configured to 1 mm. The slides were scanned from 2 to 35°2θ at 1°2θ.min^{-1} after air-drying, ethylene glycol-solvation (room temperature for 4 days) and heating at 550°C (2 h).

Clay mineral species were then identified from their characteristic XRD peak positions and intensities, and their reaction to the three diagnostic conditions (air dry, Ethylene glycated and heated) which are outlined in Moore and Reynolds (1997). The relative proportions of clay minerals in each assemblage were determined from their characteristic peak area measurements and the application of corrective multipliers to determine semi-quantitative estimates following the method of (Biscaye, 1965). The results of this method yielded precision estimates of around ±5-10% of the 'true' value in compositional percentages >15% (Schultz, 1964). XRD peak width measurements (full width at half maximum, FWHM, Δ°2θ) were made for illite (d001, ~10 Å) and chlorite (d002, ~7.1 Å) in order to assess their relative degree of crystallinity. Note that these measurements cannot be regarded as strict illite (Kübler Index, KI) and chlorite (Árkai Index, AI) crystallinities as the diffractometer had not been calibrated with the Crystallinity Index Standards (CIS, e.g. Warr and Rice (1994); Guggenheim et al. (2002)).

2.5.2 Organic $\delta^{13}C$ on clays and sandstones

Carbon occurs in nature as two stable isotopes, ^{12}C and a rarer ^{13}C form. During photosynthesis, fixation of the lighter ^{12}C is favoured over that of the heavier ^{13}C, resulting in organic matter that is enriched in ^{12}C and depleted in ^{13}C relative to the inorganic carbon in the atmosphere.

The carbon isotopic signature is expressed in terms of its $^{13}C/^{12}C$ ratio which is referred to as $\delta^{13}C$. Higher values of $\delta^{13}C$ correspond to a higher proportion of ^{13}C incorporated into the plant during photosynthesis. $\delta^{13}C$ for a sample is determined using the equation below, which standardises the $^{13}C/^{12}C$ ratio to that of a known standard - Vienna Pee Dee Belemnite (V-PDB), which has a $^{13}C/^{12}C$ ratio of 0.0112372 (Slater et al., 2001).. Therefore, most organic material has a lower $^{13}C/^{12}C$ ratio than V-PDB, and will typically have a negative $\delta^{13}C$ value.

$$\delta^{13}C = \left(\frac{\left(\frac{^{13}C}{^{12}C}\right)_{sample}}{\left(\frac{^{13}C}{^{12}C}\right)_{standard}} - 1 \right) * 1000\ ^{o}/_{oo}$$

An increase in primary productivity causes a corresponding rise in $\delta^{13}C$ value. There are two distinct groups of plants determined by their photosynthetic pathways, a C_3 group that follow the Calvin photosynthetic cycle and have $\delta^{13}C$ values of −33 to −22‰ (O'Leary, 1988, Bender, 1971, Hatch et al., 1967), and a C_4 group that follow the C_4 dicarboxylic acid pathway with $\delta^{13}C$ values of −20 to −10‰ (Hatch et al., 1967).

The $\delta^{13}C$ value of a plant is a function of the carbon isotopic composition of atmospheric CO_2 ($\delta^{13}C_{CO2}$) and the ratio of partial pressure of atmospheric CO_2 (pCO_2) inside the leaf (pi) relative to atmospheric pCO_2 (pa) (Farquhar et al., 1989, O'Leary, 1981).

The $\delta^{13}C$ of a C_3 plant can be expressed by the following equation (Tipple and Pagani, 2007, Farquhar et al., 1989):

$$\delta^{13}C_{C3plant} = \delta^{13}C_{CO2} - a - (b - a)\frac{pi}{pa}$$

where a is the carbon isotopic fractionation that occurs during diffusion of CO_2 into the leaf (4.4‰) and b is the carbon isotopic fractionation expressed by carboxylation by ribulose-1,5-bisphosphate carboxylase/oxygenase (RuBisCO) (27‰).

C_4 photosynthetic plants have a more efficient CO_2 fixing mechanism, consequently the $\delta^{13}C$ of C_4 plants can be expressed as:

$$\delta^{13}C_{C4}\ plant = \delta^{13}C_{CO2} - a - (b4 + b\varphi - a)\frac{pi}{pa}$$

where a and b are the same as in the C_3 equation, b4 is the fractionation associated with carboxylation of PEP-C (−5.7‰), and φ is the proportion of carbon fixed by PEP-C that leaks out of the bundle sheath cell (Tipple and Pagani, 2007, Farquhar et al., 1989).

The $\delta^{13}C$ value of a plant is strongly influenced by its environment. Variations in light, nutrients, temperature, and water availability are the primary factors (Farquhar et al., 1989, Tieszen, 1991, O'Leary, 1995). The significance of an environmental factor will often depend on the degree to which it limits photosynthesis. C_3 plants

exposed to high water stress conditions incorporate more ^{13}C as a result of lower stomatal conductance (O'Leary, 1981, 1988, Ehleringer and Monson, 1993). Similarly, variations in temperature can decrease stomatal conductance, resulting in a decrease in photosynthesis, respiration and growth. However, this impact is varied depending on the species of plant and its optimum photosynthesising conditions, for example some species open their stomata with higher temperature. However, if temperature continues to increase, stomata close to avoid water loss.

Today C_3 plants are typically woody and round leaf plants (including wheat, rye, and oats) are favoured in a temperate, cool and humid climates, whilst C_4 plants (such as Sudan grass, pearl millet, corn and sugarcane) favour intense light, warm and water-stressed environments typical of desert type conditions (Ehleringer, 1989). All C_4 plants have a significant advantage over C_3 plants under low atmospheric CO_2 conditions, and a drop in atmospheric CO_2 towards the end of the Miocene is suggested to have been a major driving factor in the evolution and expansion of C_4 plants (Ehleringer et al., 1997), see Section 1.8.1.

2.5.2.1 Sampling and analysis

A total of 78 samples were analysed for organic $\delta^{13}C$ at the University of Lancaster. Samples were crushed and milled using a planetary ball mill, and decalcified by acid digestion using 10% dilution of 1M HCl before being rinsed repeatedly using de-ionised water and centrifugation. The dried sample was then reground to ensure homogeneity before being weighed into 100-200 mg tin foils for analysis.

Analysis for $\delta^{13}C$ of bulk organic matter was conducted at the University of Lancaster using an Isoprime100 IRMS, with a Vario Micro elemental analyser, linked to a VisION continuous flow isotope ratio mass spectrometer. The carbonate content of each sample was removed by acid digestion using 10% dilution of 1M HCl and the resultant sample washed repeatedly using de-ionised water and centrifugation.

Each prepared sample was combusted within tin capsules at 960°C to yield CO_2 for determination of $\delta^{13}C_{org.}$ $\delta^{13}C$ values were corrected against V-PDB standard using internal reference materials calibrated to international standards. Within-run $\delta^{13}C$ replication (1σ) was <0.2 ‰ for standards and <0.25 ‰ for samples.

2.5.3 X-Ray Fluorescence (XRF)

XRF is based on the principle that individual atoms, when excited by an external energy source, emit X-ray photons of a characteristic energy or wavelength. By counting the number of photons emitted from a sample, the elements present may be identified and quantified.

There are two main types of XRF spectrometers: wavelength dispersive (WD) (Figure 2.12) and energy dispersive (ED). For this study we used a PANalytical Wavelength Dispersive X-Ray Fluorescence Spectrometer (WD-XRF) (Axios Max) at the University of Plymouth. WD XRF operates on the principle of Bragg diffraction in which 'crystals will reflect X-rays of specific wavelengths and incident angles when the wavelengths of the scattered X-rays interfere constructively'(Zahrt, 1983). Crystals are used to disperse the fluorescence spectrum into individual wavelengths of each element, providing high resolution and low background spectra for accurate determination of elemental concentrations.

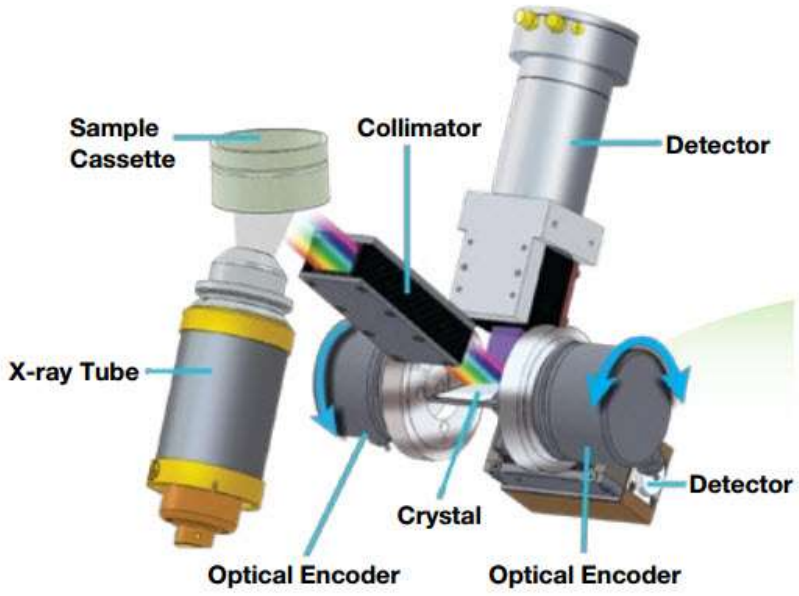

Figure 2.12 Diagram illustrating the principal of WD XRF (image provided by Thermo-Fisher Scientific)

For the identification of major elements, samples were prepared by grinding into a powder before being weighed and mixed using a lithium tetraborate flux. Samples were then transferred to a platinum crucible and heated to 1200^{o}C and poured into a platinum disk, producing a glass disk. This method eliminated the effects of particle size and heterogeneity.

Loss on ignition (LOI) was calculated independently as a quality control for the fusion method by taking an initial sample weight and heating to 1050˚C for 1 hour. LoI was calculated using the formula:

$$\text{LoI (\%)} = (Ws - WA)/(Ws - Wc) \times 100$$

where Ws = crucible + sample dried at 105°C (g), WA = crucible + ignited sample (g) and Wc = preconditoned crucible (g).

Results were produced in the form of an X-ray spectrum, in which peaks were indicative of the presence of unique elements. The heights of each the peak is proportional to the number of X-rays counted, which in turn is proportional to the mass of each element present in the sample. From this, a table of elemental concentrations in wt % was produced.

Data can be plotted in terms of chemical weathering indices, including the chemical index of alteration CIA (Nesbitt and Young, 1982), which is calculated by the equation:

$$\text{CIA} = \left(\frac{Al_2O_3}{(Al_2O_3 + CaO* + Na_2O + K_2O)}\right) \times 100$$

Where CaO* is the amount of CaO incorporated in the silicate fraction of the rock and the resultant value is a measure of the proportion of the Al_2O_3 versus the liable oxides in the sample (Nesbitt and Young, 1982).

Or alternatively using the chemical index of weathering CIW can be used (Harnois, 1988) which is calculated by the equation:

$$\text{CIW} = \left(\frac{Al_2O_3}{(Al_2O_3 + CaO + Na_2O)}\right) \times 100$$

where the value increases as the degree of weathering increases, and the difference between the CIW and the value of the silicate parent rock and soil or sediment reflects the amount of weathering experienced by the material studied (Harnois, 1988).

However, both of these indices involve the relative proportions of the silicate fraction of the rock. In the case of sediments - especially in modern rivers - ratios of clay proxies vs silica are dominantly controlled by the grain size. Lupker et al. (2012), (2013) suggest that grain size and sorting effects can be eliminated by normalising mobile to immobile ratios (X=Si) to a common Al/Si (which is a proxy for grain size).

This model assumes that the coarse-grained end member composition can be assigned to the low Al/Si mixing end-member, and that the weathering signature is mainly carried by the finer clay fraction. Chemical weathering preferentially removes more mobile elements such as K and would lower the relative K/Si ratio relative to Al/Si during increased chemical weathering (Lupker et al., 2013) Figure 2.13.

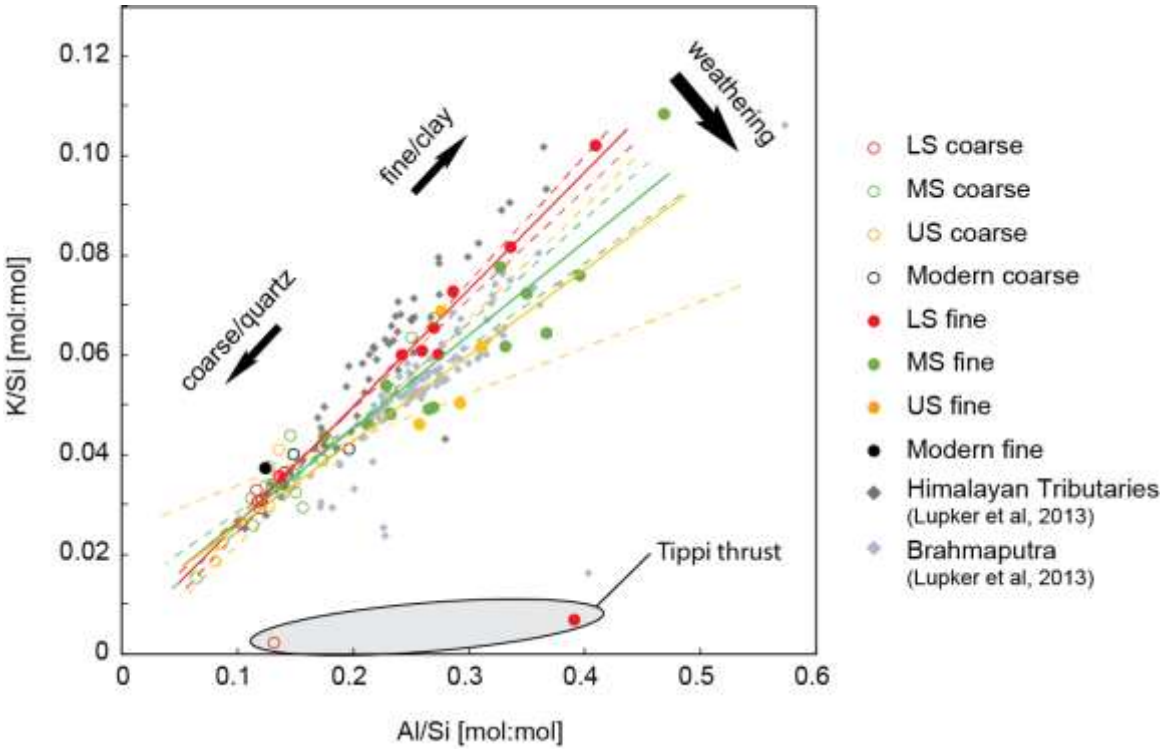

Figure 2.13 Evolution of K/Si vs. Al/Si of fine-grained (full circles) and coarse-grained (empty circles) Siwalik sediments of the Kameng section (Vögeli et al., 2017).

2.5.3.1 Sample collection and analysis

A total of 70 samples were submitted for XRF analysis from the Aertashi section using a combination of cores collected for the magnetostratigraphic study (as described in Section 2.2.1.1) and additional samples collected by hand of the finest fraction. Samples were chosen to provide an even distribution throughout the section.

Samples were milled at the University of Lancaster using a planetary ball mill into powders before being analysed at the University of Plymouth CORIF ISO9001 facility. Samples were prepared as fused disks using the PANalytical Eagon 2 fusion system with a lithium tetraborate flux. Fused disks were then analysed for major elements using a PANalytical Wavelength Dispersive X-Ray Fluorescence Spectrometer (WD-XRF) (Axios Max) instrument. LOI was obtained independently by heating to 1050˚C for 1 hour and calculated using the formula:

$$LoI\ (\%) = (Ws - WA)/(Ws - Wc) \times 100$$

where Ws = crucible + sample dried at 105°C (g), WA = crucible + ignited sample (g) and Wc = preconditioned crucible (g).

Samples were then plotted using the K/Si vs Al/Si method in order to obtain weathering trends as a factor of grain size.

2.5.4 Magnetic susceptibility

Magnetic susceptibility (MS) 'χ' is a measure of the contributions from various magnetic minerals in sediment. Magnetic susceptibility intensity varies depending on the components present. For example, ferrimagnetic minerals (e.g. magnetite and maghemite) yield the highest magnetic susceptibility, followed, in descending order of magnitude, by antiferromagnetic minerals (e.g. haematite and goethite), paramagnetic minerals (e.g. silicates, clays) and diamagnetic minerals which produce negative values (e.g., quartz, calcite) (Liu et al., 2012a).

Most climate studies that use MS as a rainfall or paleoclimate proxy are based on the development of pedogenic magnetic minerals as a result of post-depositional alteration due to weathering of the sediment and development of paleosols (Balsam et al., 2011, Maher and Thompson, 1995).

There are two models for interpreting climate in this way. The first model (Kukla et al., 1988) considers MS to be a factor of sedimentation rate and assumes the accumulation rate of nano-sized magnetic particles is constant through time. At times of high dust accumulation, magnetic grains are therefore diluted by other dust particles, resulting in a lower MS signal. During times of lower dust accumulation, less dilution by other types of dust results in a higher concentration of magnetic grains and therefore a higher MS signal.

The second, and generally preferred, model focusses on the post depositional pedogenic development of MS. This model assumes that pedogenic susceptibility is a rapidly formed soil property. In general, ultrafine grains of magnetite and maghemite are efficiently produced in a well-drained but alternately wetted and dried soil. As a result of this, soil will form higher concentrations of magnetite / maghemite in regions of higher rainfall (Maher and Thompson, 1995). As a basic rule, the more rainfall the

higher the MS signal; however, when rainfall is below 200 $mm.yr^{-1}$, the MS signal is too low for a positive correlation (Balsam et al., 2011, Heller et al., 1992).

A drier climate results in increased oxidation resulting in the production of more oxic forms of iron such as haematite and goethite. This in turn would produce a lower MS signal.

In other sedimentary deposits the formation of pedogenic magnetic minerals is a far less dominant process. MS is dependent on the concentration, grain size and mineralogy of magnetic minerals present (Sun et al., 2011). Variations in these values are dependent on the composition of the source material, fractionation of detrital magnetic minerals during transport and deposition and alteration of magnetic minerals after deposition (Garzanti and Resentini, 2016, Sun et al., 2011). Observations made by Sun et al. (2005) identified variations in the relative content of magnetite and haematite which were affected by tectonic processes. Sources that contain particles with both magnetite and haematite were transported to their sinks more rapidly during increased tectonic phases. During periods of tectonic quiescence, source materials underwent more prolonged in situ chemical weathering resulting in an increase in the oxidation of magnetite to haematite (Sun et al., 2005).

The facies of the sediment also plays a key role in affecting the MS; Sun et al. (2011) observed that MS was highest in paleosol deposits when compared with other sedimentary facies. They attributed this to the increased presence of magnetic minerals of pedogenic origin. Maher and Thompson (1995) also noted a higher MS signal as a result of an increase in the concentration of ultra-fine ferrimagnetic grains ($\leq$0.03μm) making loess/paleosol deposits particularly useful for interpreting paleoclimate, especially rainfall signals.

Sun et al. (2011) observed that the lowest MS signal was identified in aeolian sand due to its coarser grain size and weaker pedogenesis. Lacustrine sediments also produced a very low MS signal (less than $5x10^{-8}$ SI) whilst fluvial sand and clay have slightly higher values. However, it should be noted that variations in magnetic susceptibility are dependent on the magnetic mineral composition of the original source, which should be taken into account in any magnetic mineral study.

Interpreting MS in sedimentary deposits is therefore far more complicated than paleosols. A more detailed analysis of the magnetic mineral content is required. Maher

and Thompson (1995) noted that in samples containing ferrimagnetic minerals of 'non-varying' grain size the value of MS is a reliable indicator of the sample's magnetic content. MS of sediments when analysed in the context of provenance and grain-size factors can provide an indication of the paleoenvironmental conditions. For example, when all other factors (grain – size, facies and provenance) are equal, an increase in high susceptibility magnetic minerals can be attributed to a relative decrease in the production of oxic forms of magnetic minerals. This may be the result of either more rapid burial of the sediment/ increased accumulation rate, or alternatively to a change in the climate to less arid conditions (Gilder et al., 2001, Lu and Xiong, 2009) as previously described.

2.5.4.1 Sampling and analysis

Bulk MS (χ) was measured on 495 samples throughout the sampled section using cores collected for the magnetostratigraphy study (as described in Section 2.2.1.1) using a Bartington MS2 magnetic susceptibility meter at the archeo-palaeomagnetic laboratory at the University of Rennes 1.

3. The Sedimentology of the Aertashi section

Figure 3.1 An overview of the Aertashi village and Yarkand River with ripple bedding in the upper non-marine Bashibulake Formation visible in the foreground.

The study area is located near the village of Aertashi (Figure 3.1), which is situated to the west of Yarkand, along the margin of the West Kunlun Shan thrust belt (Figure 1.9). The Paleogene - Neogene eastward dipping sediments are well exposed along the Yarkand River and the roadside between the villages of Aertashi to Poskam (38° 11'29.56"N, 77°16'18.11"E) and provide a continuous record of the transition from marine facies in the Kashi Group to a continental fluvial system in the Wuqia Group (Figure 3.2 and 3.3)

3.1 Depositional environment of Aertashi

Throughout the Cretaceous to the Eocene, the Western Tarim Basin was dominated by a series of 5 marine transgression-regression sequences. This internal sea, referred to as the Tarim Sea in this region, was linked to the west with the Para-Tethys, a vast sea which extended throughout much of the European continent (Figure 1.10). The Palaeocene - Eocene marine sediments which outcrop in Aertashi are referred to as the Kashi Group (Tang, 1989, Lan and Wei, 1995) and comprise the Aertashi, Qimugen, Kalatar, Wulagen and Bashibulake formations (Figure 3.2). These formations were deposited during the 3rd, 4th and 5th marine transgressions (Figure 3.2). However, the 5th and final marine incursion into the basin did not extend as far south-east as Aertashi and therefore is not recorded in the sediments of this section. As a result of this, the 4th marine incursion marks the last marine deposition in Aertashi (Bosboom et al., 2011) and has been allocated to the Wulagen Formation by Bosboom et al. (2011).

The Kashi Group is characterised by a series of transgressive intervals which are dominated by subtidal facies, with shallow marine, carbonate platforms and tidal flat deposits (Mao and Norris, 1988, Tang, 1989). Each formation contains abundant fossil assemblages composed of bivalves, dinoflagellate cysts and ostracods (Mao and Norris, 1988, Tang, 1989, Bosboom et al., 2011). During regressive intervals, facies consist of supratidal and intertidal lagoonal and tidal flat facies dominated by massive gypsum beds and brownish-red gypsiferous mudstones (Mao and Norris, 1988, Tang, 1989).

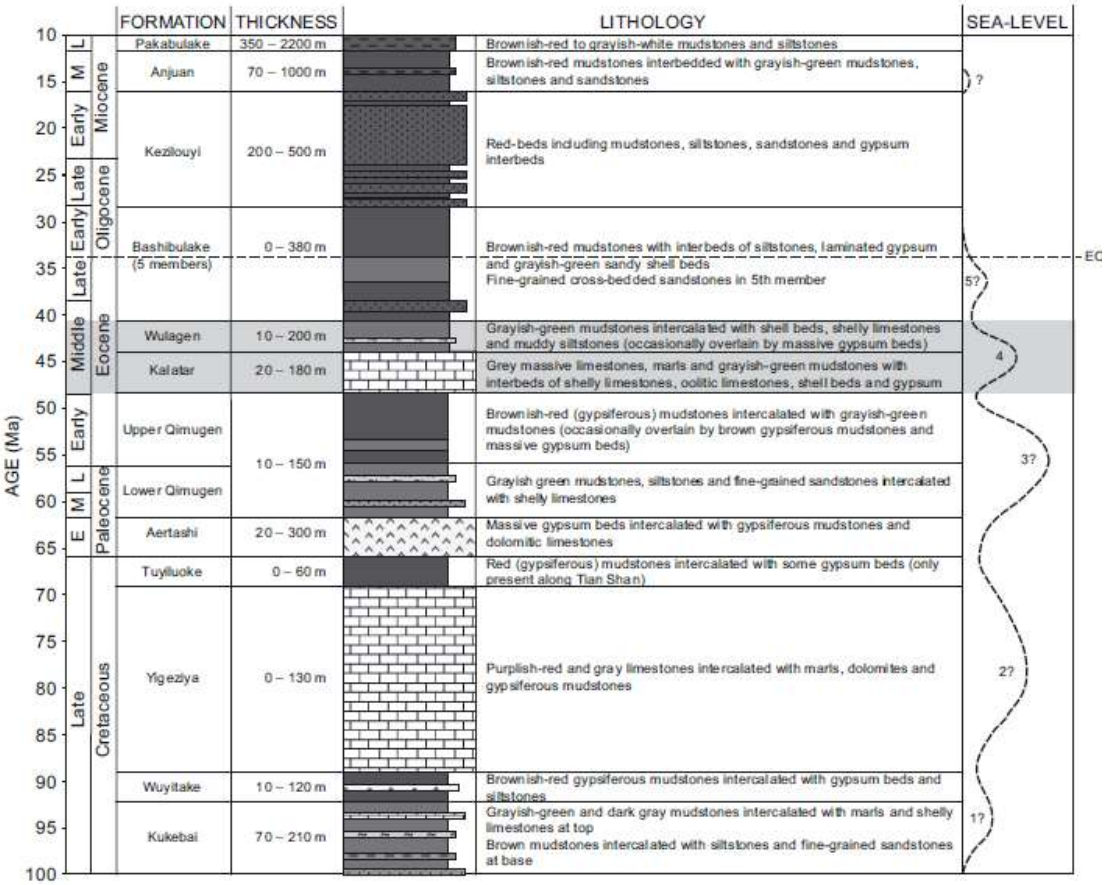

Figure 3.2 Simplified regional lithostratigraphic framework of the marine incursions in southwest Tarim Basin from the Cretaceous through to the late Eocene with formation names, estimated thicknesses and descriptions, based on a review of existing Chinese literature (Bosboom et al., 2014c).

Laying directly above the Wulagen Formation is the first non-marine formation, which has been allocated by Bosboom et al. (2011) to the lower Wuqia Group, Kezilouyi Formation. However, a number of authors have allocated the first continental depositional formation in Aertashi to the non-marine Bashibulake Formation (Zheng et al., 2006, Yin et al., 2002), which is time equivalent to the 5th marine incursion in the north-western part of the Tarim Basin. This has led to some discrepancy regarding the nomenclature of the Aertashi sediments. For the purposes of this study we refer to the first non-marine formation as the non-marine Bashibulake

Formation in keeping with the general consensus and refer to the sediments above this formation as units A-F.

The first onset of continental deposition, the ‘non-marine’ Bashibulake Formation, is described as red, fine-gained mudstone and fine sandstones, with abundant gypsum which are interpreted to be low-energy, meandering river, lacustrine, and playa deposits (Zheng et al., 2006, Zheng et al., 2015a). Overlying this formation is the Wuqia Group, which in Aertashi is composed of the Kezilouyi, Anjuan and Pakabulake formations (Figures 3.2 and 3.3.)

The Wuqia Group is characterised by thickly bedded sandstones and conglomerates interbedded with mudstones which grades upwards in grain size throughout the sequence (Yin et al., 2002, Zheng et al., 2015a). These sediments are interpreted to be fluvial and lacustrine facies prograding into alluvial fan facies.

Overlying the Wuqia Group is the Artushi Formation (Figure 3.3), which is dominated by red to grey sandstones and siltstones, interpreted to be a distal to mid alluvial fan and the Xiyu Formation (Figure 3.3), which consists of large grey cobble and bolder conglomerates and sandstones interbedded with occasional volcanics, interpreted to be a proximal alluvial fan (Zheng et al., 2015a, Wang et al., 2003).

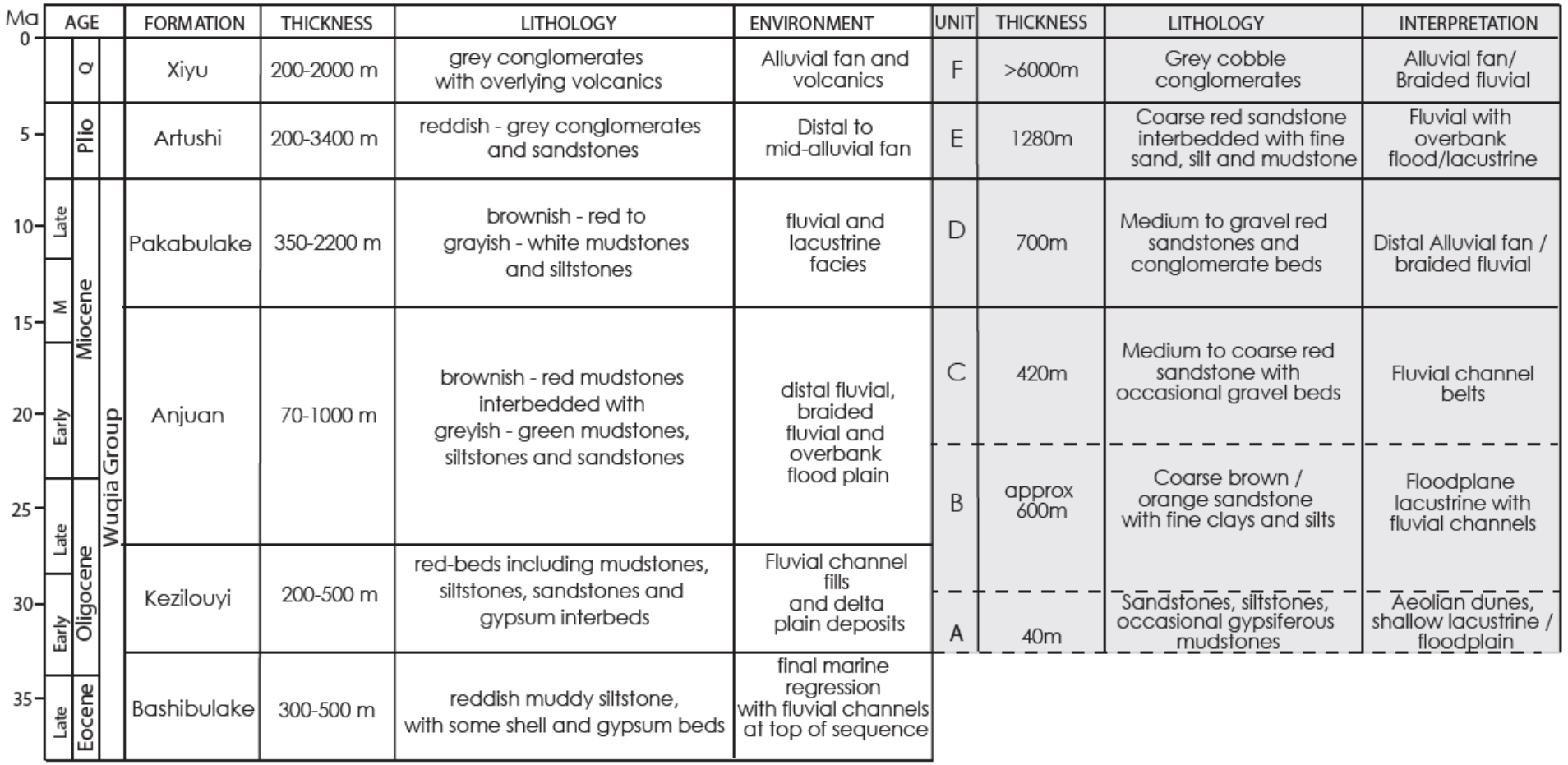

Figure 3.3 Summary table of the Aertashi section stratigraphy and adjacent areas adapted from Bosboom et al. (2014c), Jia (2004), Mao and Norris (1988), Wang et al. (2003), Zheng et al. (2000) and Wei et al. (2013). Grey shaded box shows the sediments observed in Aertashi during this study and their estimated formation associations.

3.2 Age control for the Aertashi section

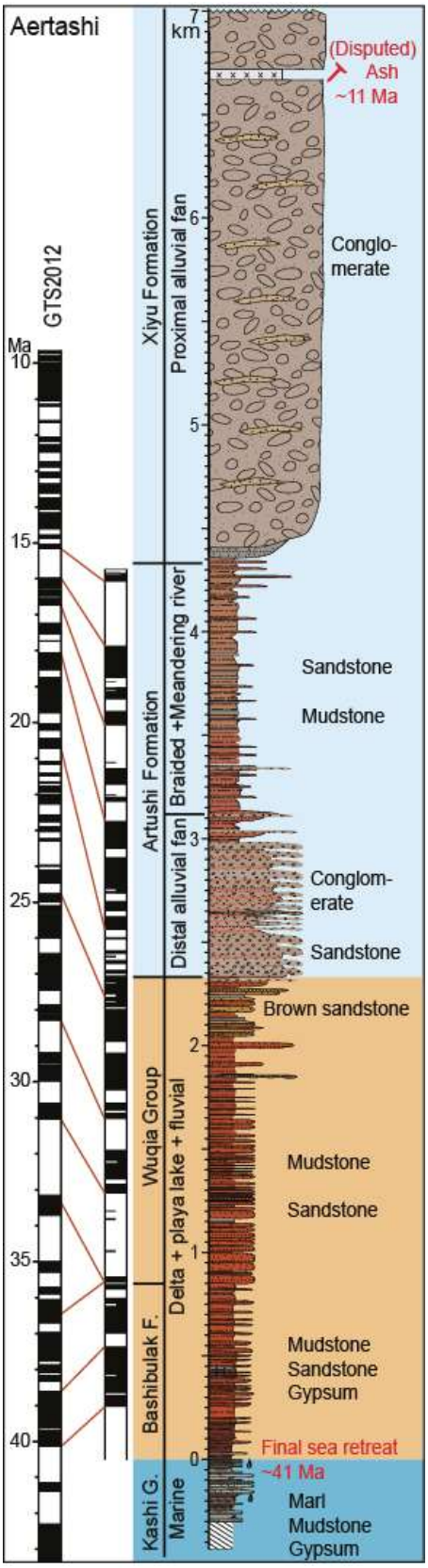

Figure 3.4 Full log of the Aertashi section with age control and depositional environments as described by Zheng et al. (2015a)

Bosboom et al. (2014a, b) conducted a detailed biostratigraphic and magnetostratigraphic analysis of the marine and lower continental deposits in the Aertashi section. They identified the last marine deposits at Aertashi as late Eocene in age, which has been constrained by bivalves, calcareous nanofossils and dinoflagelate cysts. Using the ages of these fossils as a basal age constraint, Bosboom et al. (2014c) completed a high resolution magnetostratigraphic study on the lower continental section, providing an age control for Aertashi from the final retreat of the Tarim Sea in Aertashi at ca. 41 Ma through to ca.27 Ma. More recently, the Aertashi section has been re-dated by Zheng et al. (2015a) (Figure 3.4) using magnetostratigraphy combined with the previous palynology by Bosboom et al. (2011) and a newly identified volcanic ash layer located at ~6700 m stratigraphic height (Figure 3.4). This ash layer, provides a depositional age of 11 Ma for these sediments leading to a revised age for the continental section in Aertashi from ~41 to 15 Ma which marks the onset of the large scale conglomerates of the Xiyu Formation (Figure 3.4), although there is some dispute as to whether the volcanic ash deposit is actually a reworked sedimentary deposit (Sun et al., 2015) which would alter the interpretation of this layer to have a depositional age of <11 Ma (see Section 5.4.1 for a full discussion).

3.3 Sampling and analysis of the Aertashi section

Sampling at Aertashi for this study was conducted in conjunction with magnetostratigraphy and sedimentology and builds upon the earlier work of Bosboom et al. (2011, 2014b) and Zheng et al. (2015a) as described above. As part of the magnetostratigraphic sampling strategy, a detailed grain scale log was composed, commencing at the last measured bed of Bosboom et al. (2014c) (GPS 37˚ 58.284”E 76˚34.785”N) (Figure 3.5). However, we observed and recorded details on the sedimentology of Aertashi below this point, starting at the lowermost continental deposits which lay directly above the last marine section (see Figure 3.7 for the contact between marine and continental deposits) (GPS ref: N 37° 58.839’, E 076° 33.333) at the 0 m stratigraphic level (Figure 3.5). We then recorded the sedimentology for the Aertashi section up to the onset of large scale grey conglomerates which mark the onset of the Xiyu Formation at ~4100 m stratigraphic height (See Figures 3.4, 3.5 and 3.6).

Detailed sedimentary logs were composed for each ‘type’ section as a representative of the characteristics for each formation; with the locations of these logs recorded on our grain scale log for the upper part of the section (Figure 3.6) and on the log produced by Bosboom et al. (2014c) for the lower part of the continental section (Figure 3.5). Included on these logs (Figures 3.5 and 3.6) are the locations of all samples selected for this study and the locations of all conglomerate clast counts conducted as part of this study (Appendix 18).

Conglomerate clast counts were conducted on units D and F of the Aertashi section, the method used for this study was to identify 100 clasts within a specified area 1 m^2, with the exclusion of clasts too small to identify. Each clast was categorised by type (sedimentary, igneous, metamorphic), size, angularity and colour in order to examine any changes in clast composition throughout the studied section.

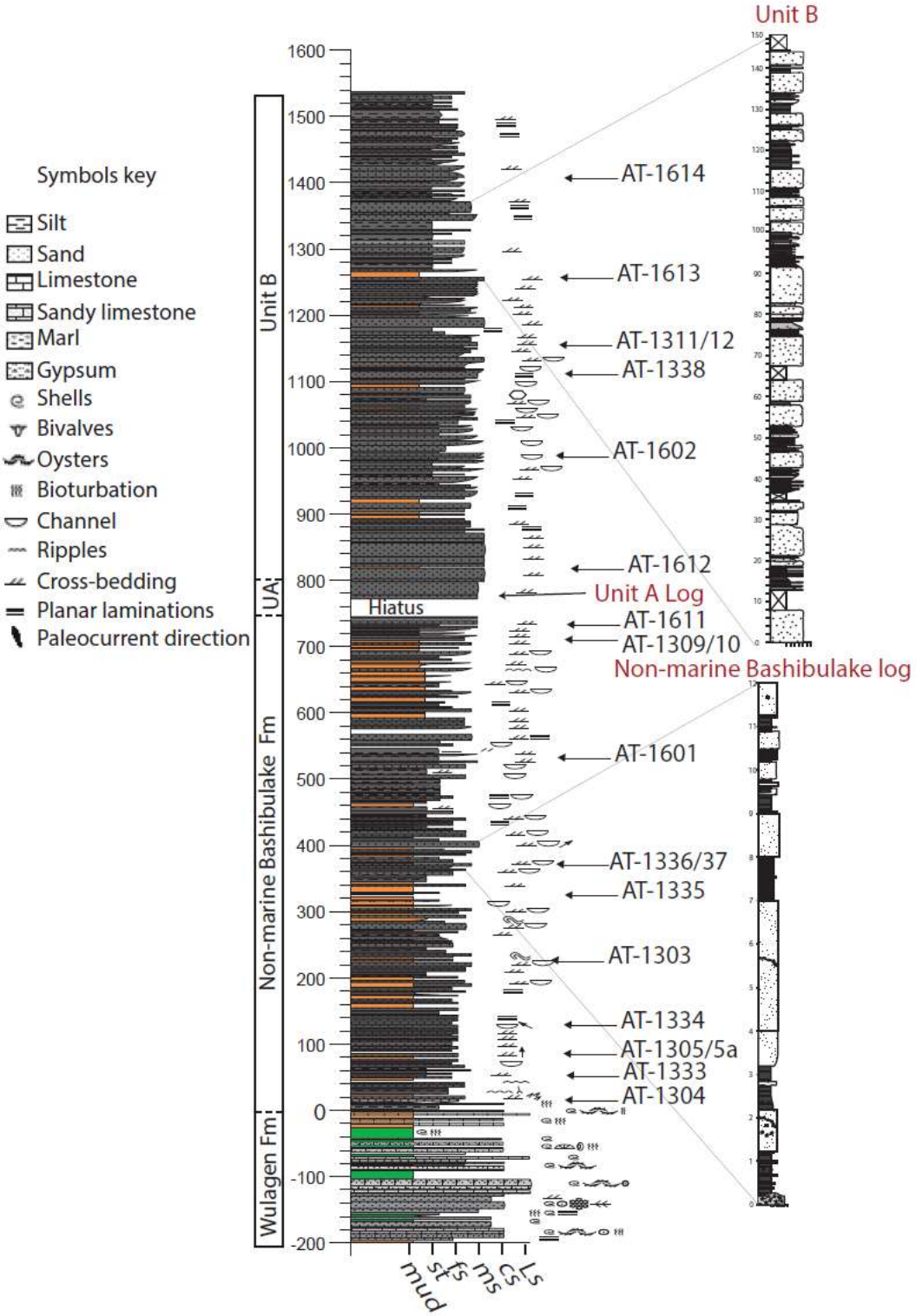

Figure 3.5 A summary of sampling locations for the Aertashi section based on the sedimentology and age control of Bosboom et al. (2014c). Logs indicated in red highlight the locations of more detailed sedimentology examination conducted in this study.

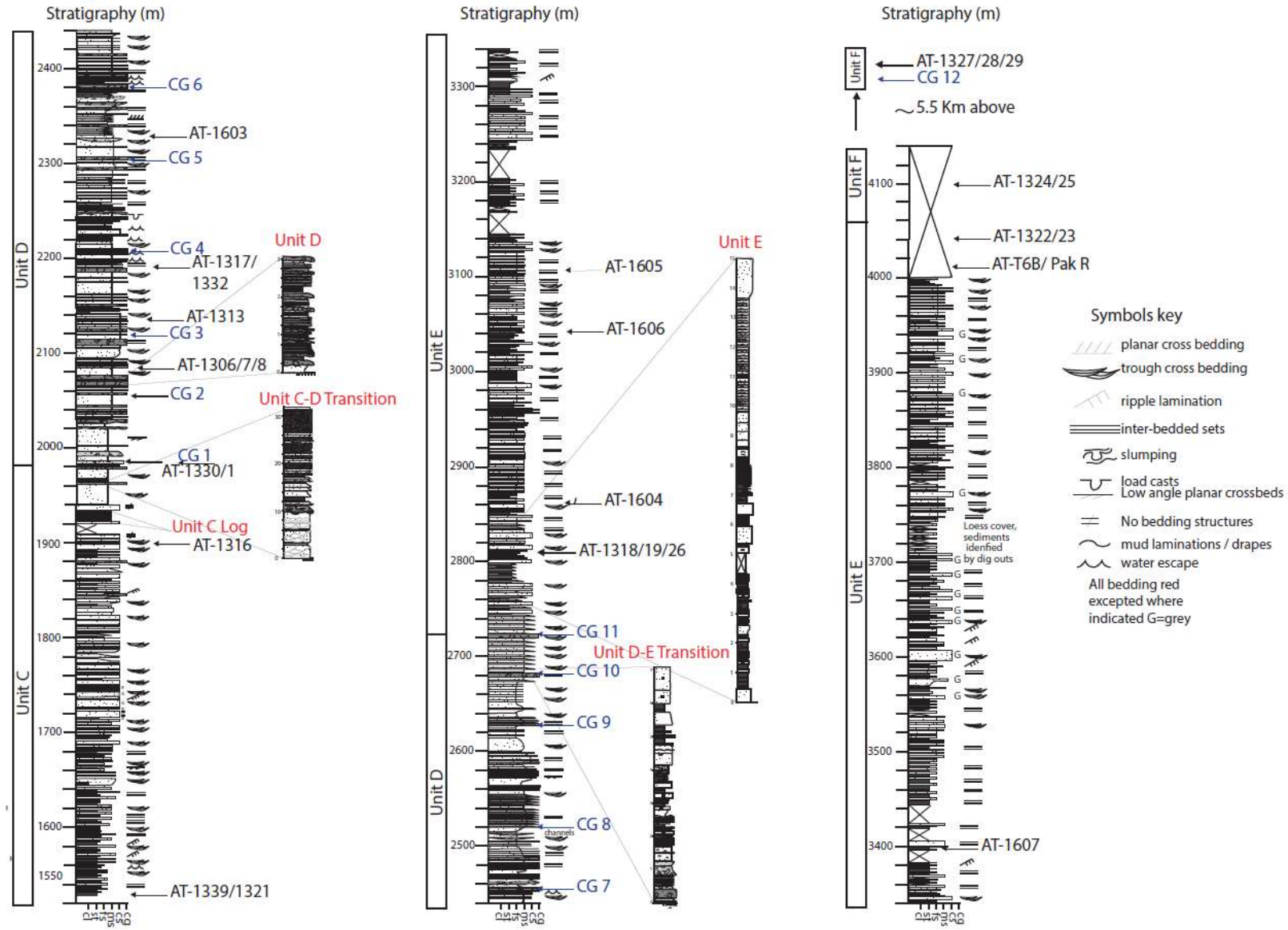

Figure 3.6 A grain scale log for the Aertashi section used in this study with full sampling locations indicated by sample numbers and detailed log location indicated in red. CG = conglomerate clast count locations used for clast identification.

3.4 Architectural elements of the Aertashi section

For this study we use the Miall (1985) approach for facies analysis and depositional environment interpretations. Full facies descriptions and associations are provided in Table 3.1 and 3.2 with references indicated on each of the main logs and figures in this chapter.

Table 3.1 Architectural elements in fluvial deposits modified from Miall (1985). Facies classification from Miall (1977)

Element	Symbol	Principal lithofacies assemblage	Geometry and relationships
Channels	CH	any combination	finger, lens or sheet; concave-up erosional base; sale and shape highly variable; internal concave-up 3rd order erosion surfaces common
Gravel bars and bedforms	GB	Gm, Gp, Gt	lens, blanket; usually tabular bodies; commonly interbedded with SB
Sandy bedform	SB	St, Sp, Sh, Sl, Sr, Se, Ss	lens, sheet, blanket, wedge, occurs as channel-fills, crevasse splays, minor bars
Sediment gravity flow	SG	Gm, Gms	sheet, typically interbedded with GB
Laminated sand sheet	LS	Sh, Sl, minor Sp, Sr	sheet, layered
Overbank fines/ flood plain	OF	Fm, Fl, Fsc	thin to thick layers; commonly interbedded with SB; may fill abandoned channels

Table 3.2 Lithofacies classification from Miall (1977)

Facies codes	Lithofacies	Sedimentary Structures	Interpretation
Gms	massive, matrix supported gravel	grading	debris flow deposits
Gm	massive or crudely bedded gravel	horizontal bedding, imbrication	longitudinal bars, lag deposits, sieve deposits
Gt	gravel, stratified	trough cross beds	minor channel fills
Gp	gravel, stratified	planer cross beds	longitudinal bars, deltaic growths from older bar remnants
St	sand, medium to very coarse, may be pebbly	solitary or grouped trough cross beds	fluvial dunes (lower flow regime)
Sp	sand, medium to very coarse, may be pebbly	solitary or grouped planar cross beds	linguoid, transverse bars, sand waves (lower flow regime)
Sr	sand very fine to coarse	ripple cross lamination	ripples (lower flow regime)
Sh	sand, very fine to very coarse may be pebbly	horizontal lamination parting or streaming lineation	planar bed flow (upper flow regime)
Sl	sand, very fine to very coarse may be pebbly	low angle (<10˚) cross beds	scour fills, washed-out dunes, anti-dunes
Se	erosional scours with intra-clasts	crude cross bedding	scour fills
Ss	sand, fine to very coarse, may be pebbly	broad, shallow scours	scour fills
Fl	sand, silt, mud deposits	fine lamination, very small ripples	overbank or waning flood

3.5 The Aertashi sediments

3.5.1 Non-marine Bashibulake Formation (0-720 m): Semi-arid fluvial floodplain.

The non-marine Bashibulake Formation outcrops near the mine at Aertashi (GPS ref: N 37° 58.839', E 076° 33.333) and lays directly above the final marine Wulagen Formation recorded in Aertashi. The marine to continental transition is clearly visible in Aertashi, due to the marked colour change from the grey green of the marine Wulagen Formation, to the red beds of the continental deposits directly above (Figure 3.7).

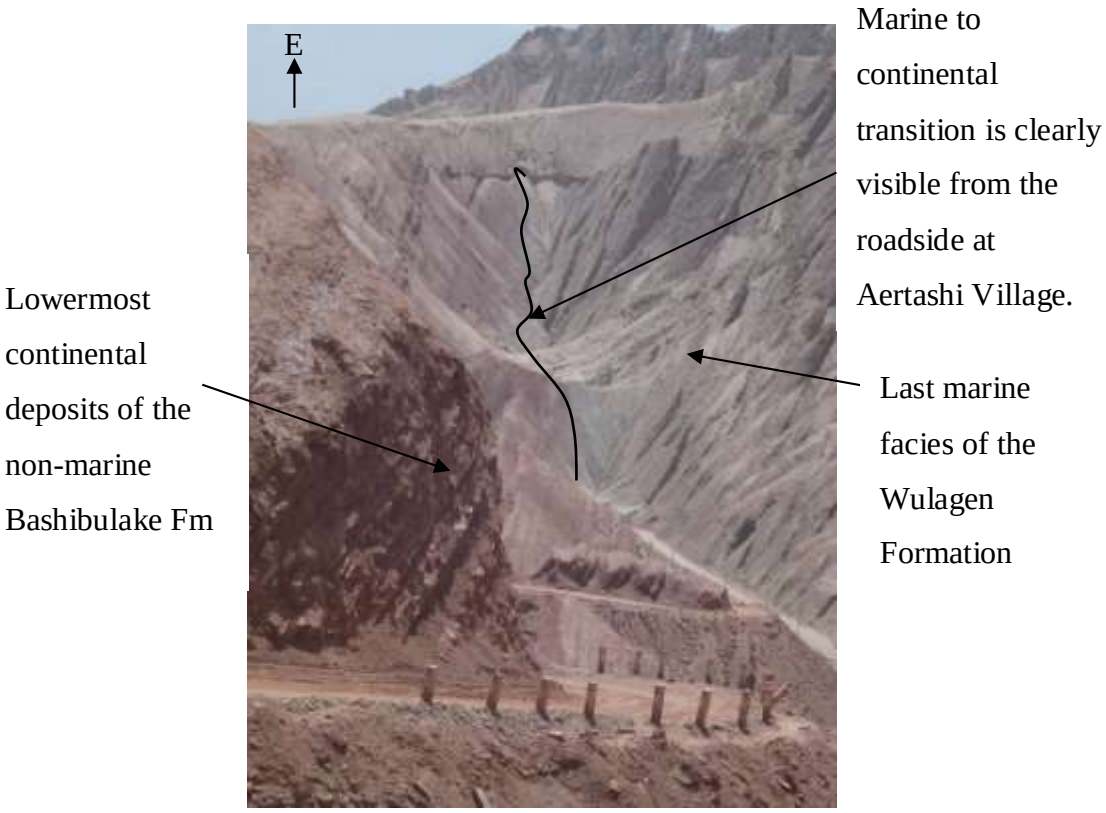

Figure 3.7 Overview of the marine to continental transition at Aertashi.

The non-marine Bashibulake Formation is approximately 720 m thick and begins at 0 m stratigraphic height as illustrated in Figure 3.5. In overview, the non-marine Bashibulake Formation is composed of large sets of interbedded sandstones and siltstones (Figure 3.8).

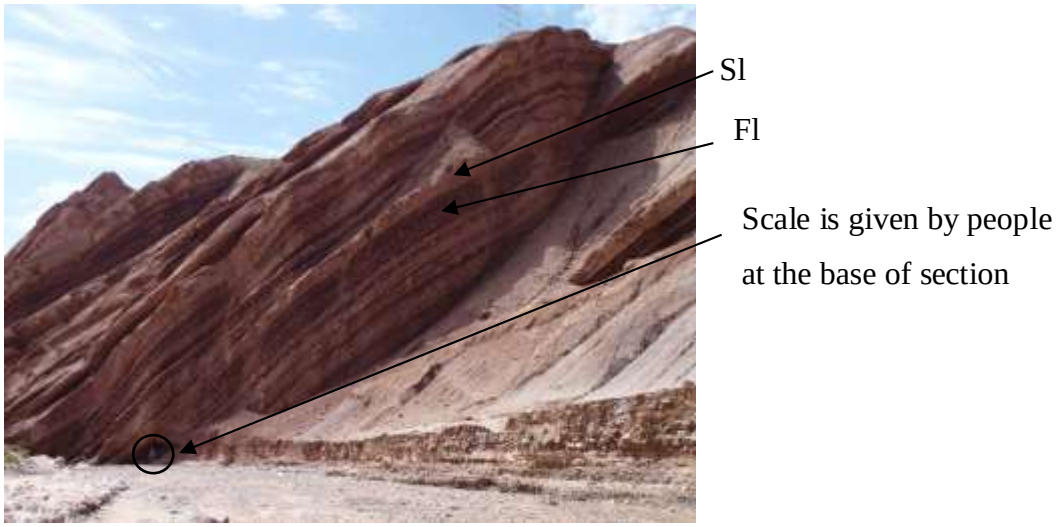

Figure 3.8 Overview of the non-marine Bashibulake Formation, looking south, GPS ref: N 37° 58.839', E 076° 33.333.

These sets are composed of fine to medium grained sandstone layers up to 4 m thick, with low angle crossbedding. Each cycle is interbedded with layers of finely laminated mudstones, siltstones and sandstones up to 1 m thick (Figure 3.9) with abundant gypsum in both clusters and veins present throughout the sandstone layer (Figures 3.9 and 3.10).

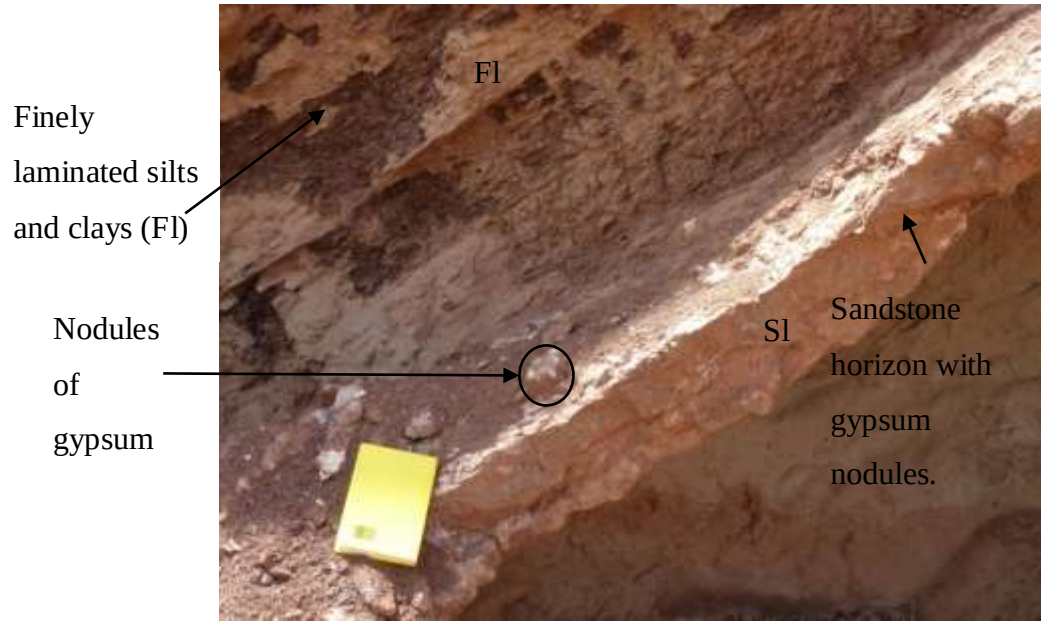

Figure 3.9 The non-marine Bashibulake Formation with a gypsiferous sandstone horizon interbedded with finely laminated siltstones and clays GPS ref: N 37° 58.839', E 076° 33.333.

Figure 3.10 Close up of a gypsum nodule within the non-marine Bashibulake Formation.

Within the siltstone sections are occasional bioturbations with clear evidence of burrowing activity (Figure 3.11)

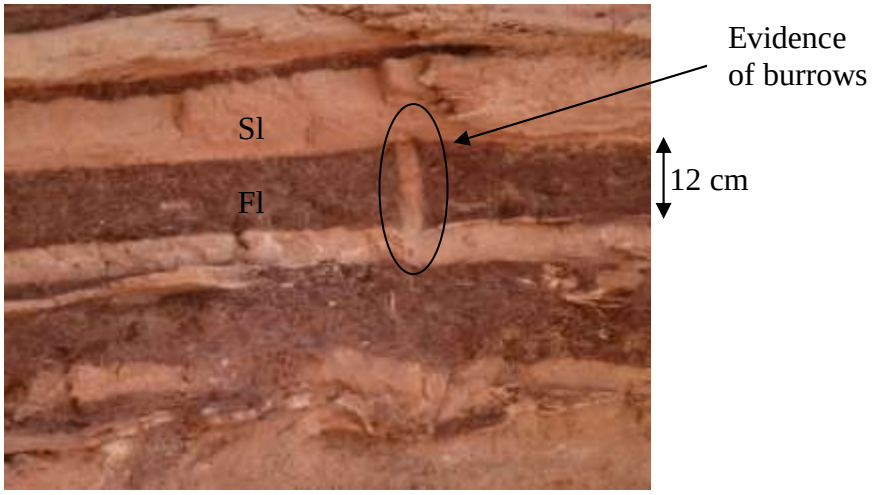

Figure 3.11 Close up of a burrow within the non-marine Bashibulake Fm, GPS ref: N 37° 58.839', E 076° 33.333

3.5.1.1 Description

A detailed log of the non-marine Bashibulake Formation is presented in Figure 3.12. This formation is composed of thick sequences (up to 4 m) of fine to medium sandstone with shallow low angle cross bedding (Sl) and occasional gypsum nodules and veins. Towards the top of the sequence, sandstones have convolute bedding structures. These sandstones are interbedded with thin clay and siltstone bands with planar parallel lamination (Fl) and abundant gypsum nodules. Occasional sets of thin fine sandstone beds with siltstone lenses (ranging from 3-10 cm thick) interrupt the

larger sequences. At the base of the sequence is a coarse gravel deposit with abundant gypsum, which is poorly sorted with no grading (Gm).

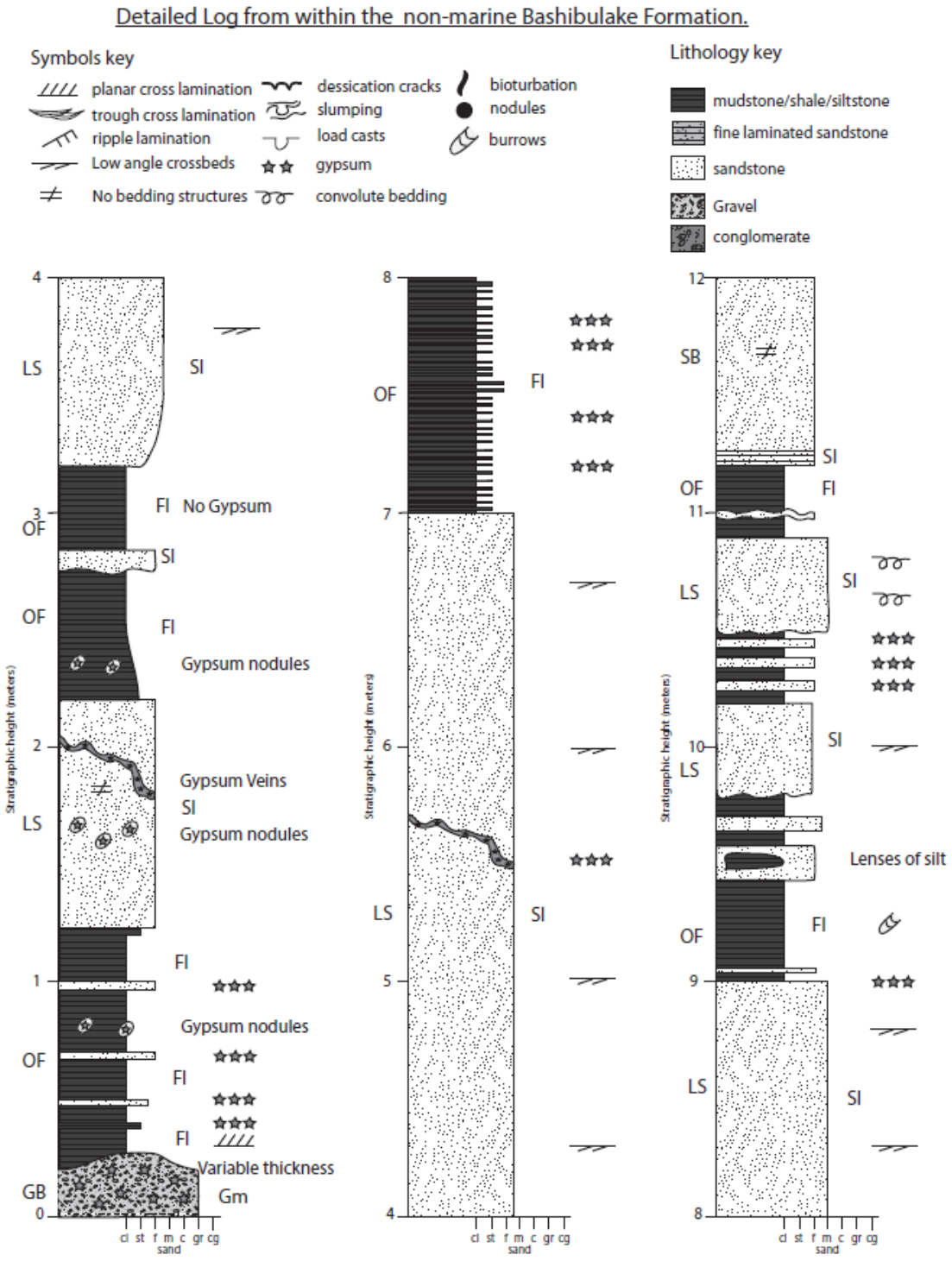

Figure 3.12 Detailed log of the non-marine Basibulake Formation GPS ref: N37°58.839' E076°33.333'

3.5.1.2 Interpretation/ Depositional Environment

This unit is dominated by finely laminated sand silt and mud deposits (Fl) typical of overbank/flood facies (OF), sandy bedforms (Sl and Se) with low angle cross bedding typical of scour fills, washed out dunes and anti-dunes (SB) with an isolated gravel deposit (Gm) at the base typical of a channel fill deposit.

The thick sequences of sand are likely to be caused by ephemeral channels (SB and LS) followed by periods of surface exposure and evaporation resulting in gypsum precipitation. Gypsum 'veins' are likely to be post depositional hydrothermal features. The convolute bedding is formed when tectonic activity occurs simultaneously with deposition/prior to solidification of the bedform. The fine channel overbank/sheet flood type deposits (OF) indicate a low energy environment with occasional periods of evaporation giving rise to the precipitation of gypsum. The basal gravel sequence is indicative of channel flow lag deposits (GB).

These deposits are typical of an ephemeral, high capacity fluvial flood plain with meandering channels and point bars in an arid or semi-arid climate. The convolute bedding suggests tectonic activity occurred simultaneously or shortly following deposition of this sequence.

3.5.2 Unit A (760-800 m): Aeolian dune, inter-dune and arid flood plain.

Following deposition of the non-marine Bashibulake Formation is a depositional hiatus of ~3 Ma which spans the Eocene – Oligocene boundary (ca. 36-33 Ma) as recorded by Bosboom et al. (2014c) (Figure 3.5), based on field observations of an erosive basal contact at 737 m level. According to Bosboom et al. (2014c), this hiatus is marked by gypsum nodules and coincides with a minimum in bulk magnetic susceptibility. We found access to the hiatus was limited, preventing detailed examination of these features.

The unit directly above the hiatus is labelled as unit A to avoid confusion with nomenclature as previously discussed in section 3.1.

3.5.2.1 Description

Our study of unit A begins at the 760 m stratigraphic level. Unit A is 45 m-thick (~755-800m) and made up of two parts.

The lower part is ~20 m-thick and composed of massive sandstones and siltstones, whilst the upper part is 25 m-thick and composed of 3 to 5 m-thick sequences of pinkish to reddish brown medium-grained locally coarse sandstones, siltstones and minor gypsiferous mudstone alternations (Figure 3.13).

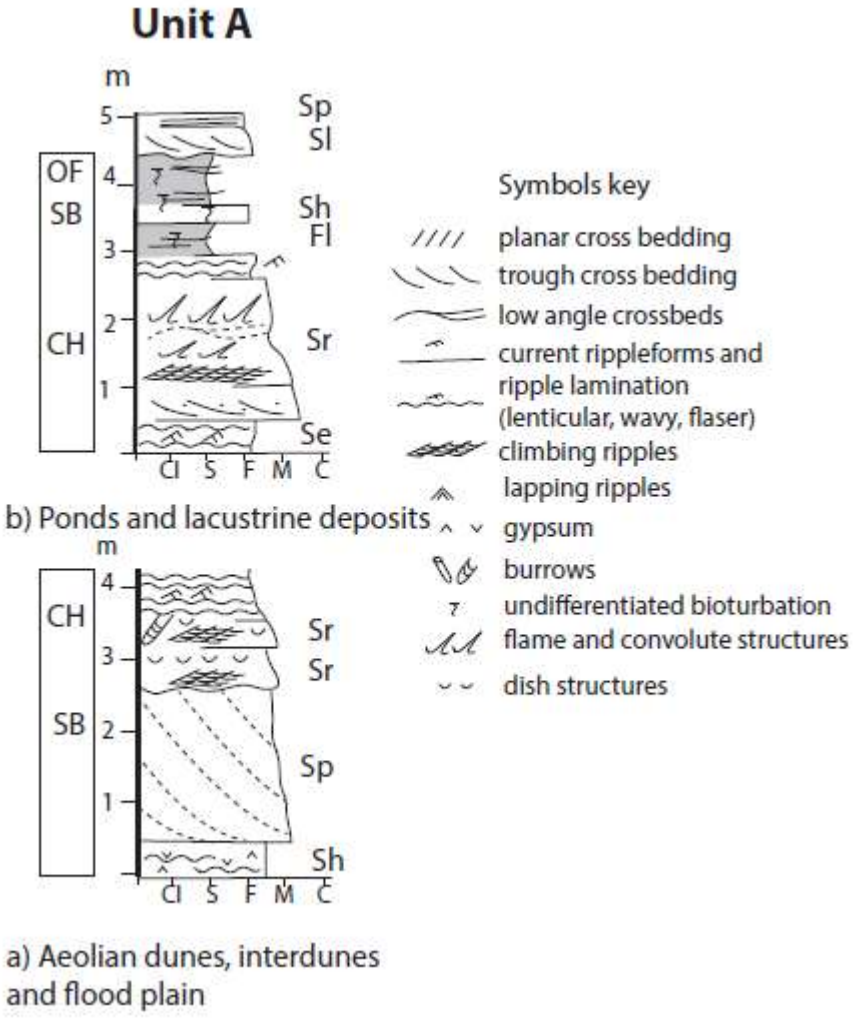

Figure 3.13 Sedimentary log of the lower and upper unit A sediments

The base of the lower unit comprises a 0.5 m thick fine grey sandstone (Sh) with abundant gypsum nodules. Above this layer; 2 m thick fining up sequences of medium to fine red sandstones with planar and ripple cross laminations are observed (Sp), which contain burrows and bioturbations. Sedimentary structures show alternations of trough cross bedding and cm-scale rippled (Sr) and low angle planar laminated beds (Sp). The upper part of the large cross beds have inverse grading which wedge out in mm scale wind-ripple laminas in the lower part of the cross bed.

The top part of unit A is composed of 2 m thick fining up sequences of medium to coarse sandstones which contain erosional scours (Se) at the base of the coarser units with ripple laminations (Sr), water escape features, convolute bedding and flame structures (Figure 3.13 and 3.14).

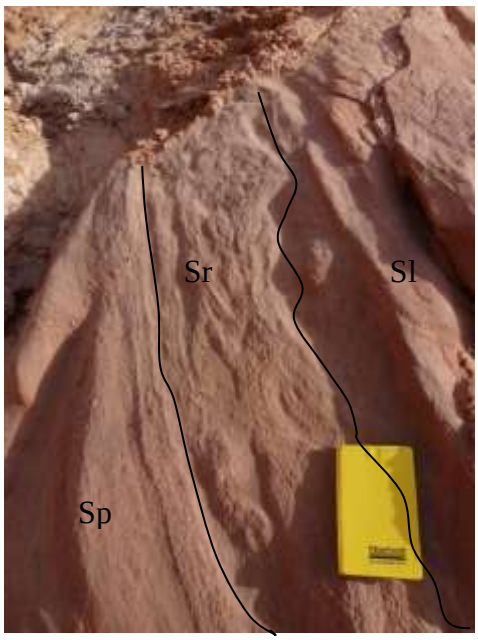

The top of the sequence fines-up into bioturbated fine sandstones and siltstones. These contain horizontal laminations (Fl, Sl) with occasional 0.3 m thick fine sandstone beds (Sh, Sp).

Overall the mud content increases up section.

Figure 3.14 Unit A upper part with water escape structures and convolute bedding

3.5.2.2 Interpretation/ Depositional Environment

Unit A base consists of facies associations dominated by sandy bedforms (SB) and channelised sandstones (CH). The large cross beds of the lower part of unit A are interpreted to be wind driven aeolian deposits with the inverse grading at the top of the sequences typical of avalanche deposits.

The top of the sequence is characterised by an increase in mud content with facies associations dominated by channelised sandstones (CH), sandy bedforms (SB) and overbank fines (OF). These facies are typical of flood plain type deposits with shallow ponds or inter-dune environments. The top of sand bodies have flame structures indicating a current dominated depositional environment such as a high energy crevasse splay.

In the upper part of unit A, the aeolian dune deposits disappear, giving rise to larger ponds or lakes in a muddy flood plain environment with occasional crevasse splays. The presence of abundant gypsum at the base of the unit indicates an arid to semi-arid environment, although gypsum is not observed further up the sequence. Unit A observations are consistent with the presence of aeolian dunes in a distal floodplain environment.

3.5.3 Unit B (800-1520 m): Flood-controlled lacustrine sandy delta plain.

Directly above unit A, are sequences of thick, red sandstone and siltstone deposits of unit B (GPS: N37° 58.001', E076° 34.234') (Figure 3.15), however due to limited access the contact between unit A and B was not observed.

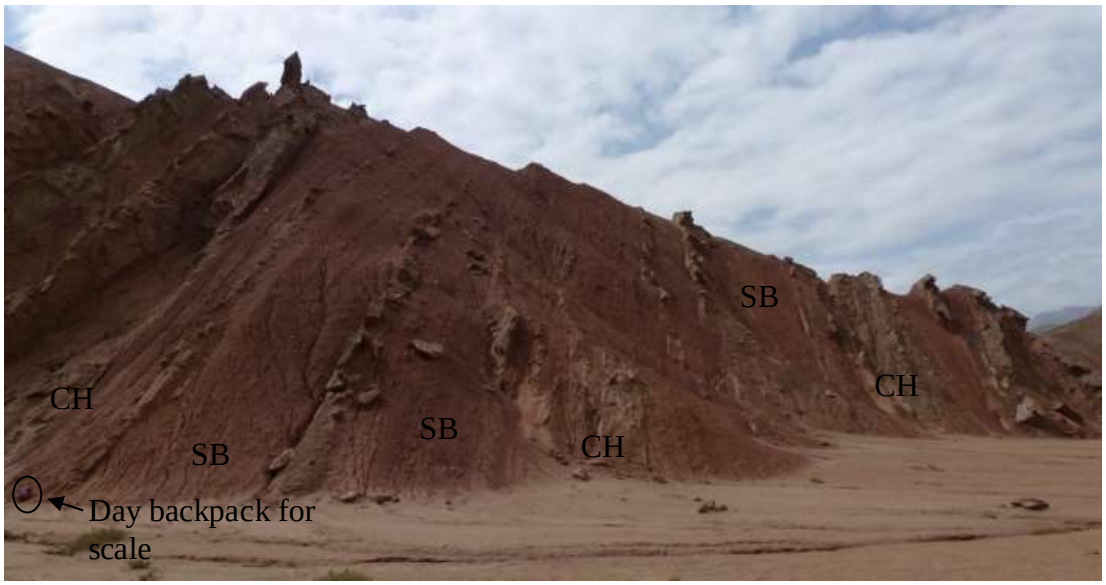

Figure 3.15 Overview of the large scale sandstone sets of unit B

3.5.3.1 Description

Unit B is ~720 m thick and is characterised by sets of 5-8 m thick fine red sandstone beds, which contain cycles of coarse grained brown/orange sandstone (Figure 3.15). Sequences are composed of planar laminated bases (Sp), grading up into ripple and climbing ripple cross bedding (Sr), interbedded with sporadic metre scale sets of fine to medium structureless sandstones (Se).

Within each set are smaller up to 2 m thick, medium to coarse sandstones which contain erosional scours (se) and low angle cross bedding (Sl). These sandstones are interbedded with fine clays and silts which contain planar and ripple laminations (Fl). These finer sequences contain abundant burrows and bioturbation (Figure 3.16).

The upper part of unit B contains up to 8 m thick sequences of fine to medium red sandstone beds which contain a range of planar (Sp), ripple, climbing ripple (Sr) and trough (St) cross bedding. Within the large scale sequences are smaller sets of fine - medium grained sandstone with small ripples (Sr) often grading up to planar cross bedding towards the top of the bed (Sp) (Figure 3.17), along with coarsening up sequences from siltstones to medium grained sandstones, with planar laminations (Fl).

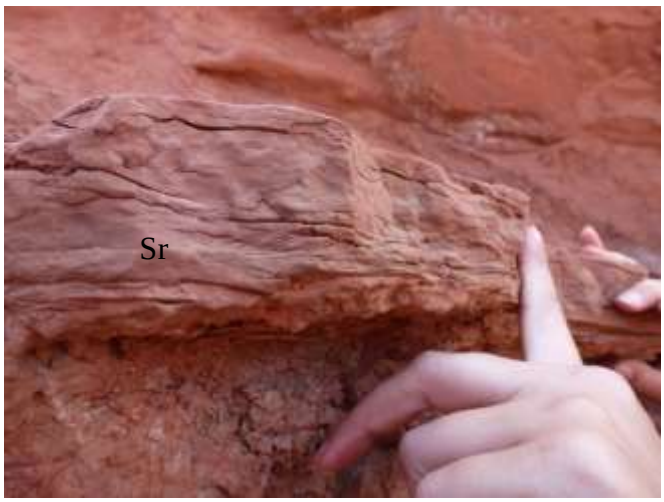

Figure 3.16 Low angle climbing ripples with trace burrows.

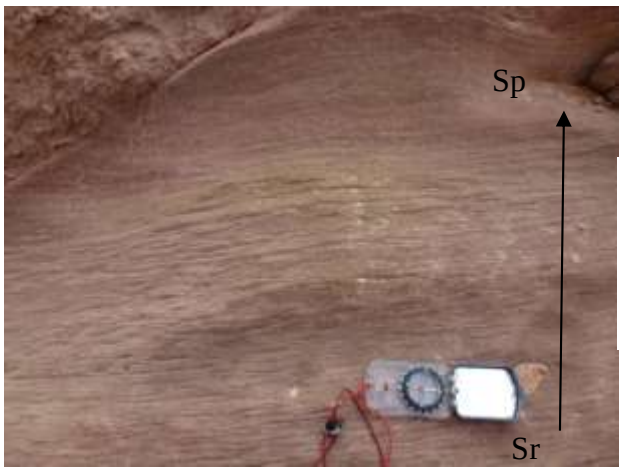

Grading from ripples to planar cross bedding

Figure 3.17 Ripples grading up to planar cross bedding
GPS: N37° 58.001', E076° 34.234'

3.5.3.2 Interpretation / Depositional Environment

The sandstone beds contain sets of planar, rippled and occasionally trough cross bedding with de-watering structures interbedded with fine silts and clays with planar and ripple cross laminations. This unit is dominated by sandy bedforms (SB), overbank fines (OF) and channelised sandstones (CH).

The large scale fine to medium red sandstone beds are typical of meandering sandy channel deposits with point bar and bar top facies and over-bank deposits indicated by thicker sets of clays and siltstones.

The finer over-bank deposits are very planar and contain oscillation ripples suggesting a long term standing body of water characteristic of a lacustrine or floodplain. Within the finer sands and silts, the grading from dunes to small ripples indicates a reduction

in flow energy or water depth. The overall depositional environment is typical of a lacustrine like floodplain being fed by large sandy channels.

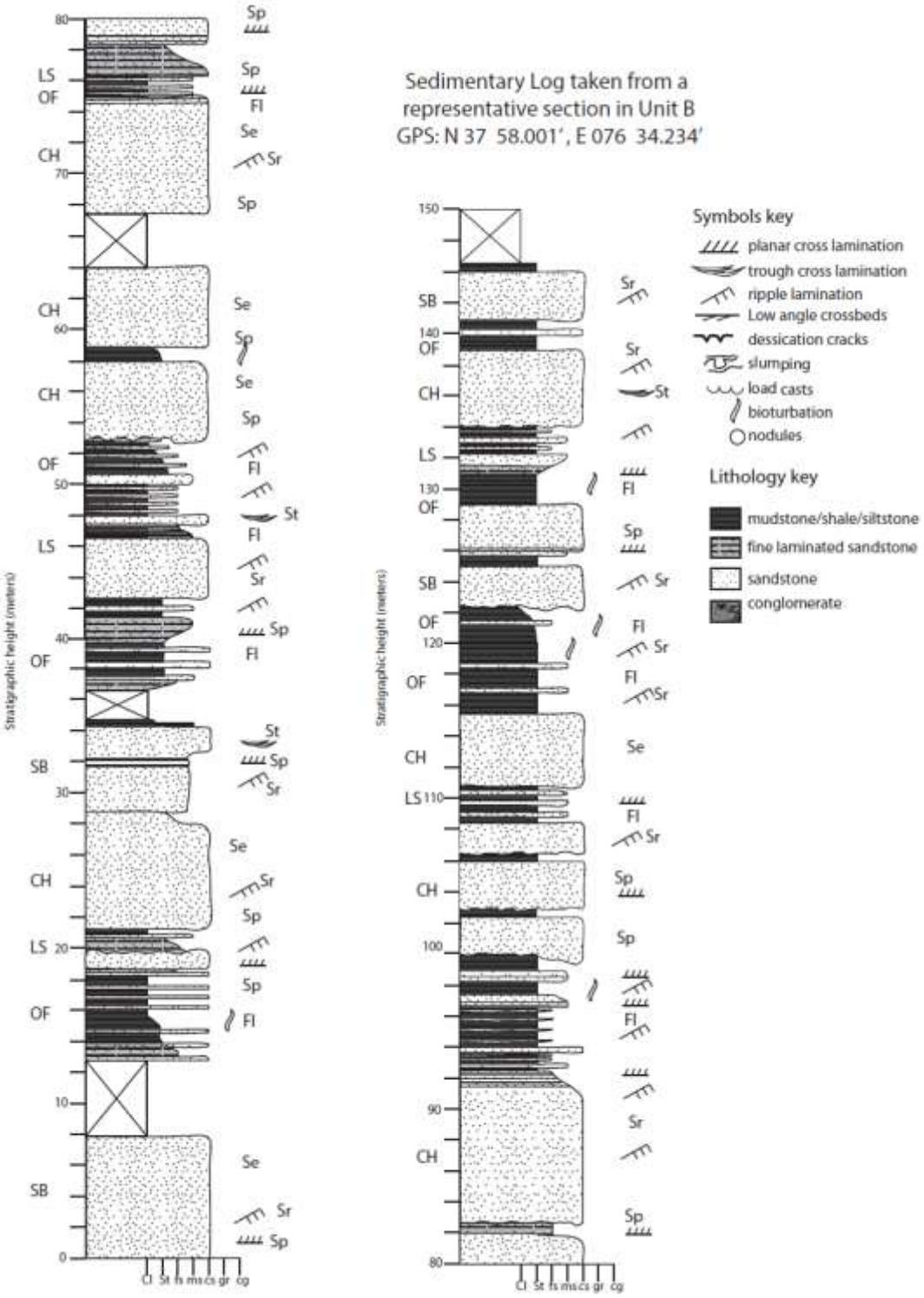

Figure 3.18 Detailed log from within unit B with facies associations (see text) GPS: N37° 58.001', E076° 34.234'

3.5.4 Unit C (~1520-2050 m): Meandering channel belts

The transition from unit B to unit C is gradual. Unit C is ca. 560 m-thick (~1490 – 2050 m) and composed of stacked sets of 2-3 m thick fining up sequences of medium to fine grained sandstones and siltstones (Figure 3.19). Each set comprises an erosional scour base (Se) with low angle cross bedding (Sl), which fines up to ripples (Sr) and planar cross laminations (Sl).

The fine material shows cm-scale rippled beds (Figure 3.21) with mm-scale mud pebbles interbedded with micro-laminated silts with clay drapes (Fl).

The fines are cut in places by dm-scale fining up sandstone beds with bioturbated tops. Occasional exposed horizons have desiccation cracks with animal footprints (Figure 3.22).

Occasionally at the top of the unit, the basal erosional surface is filled with pebbles (Se) (Figure 3.20).

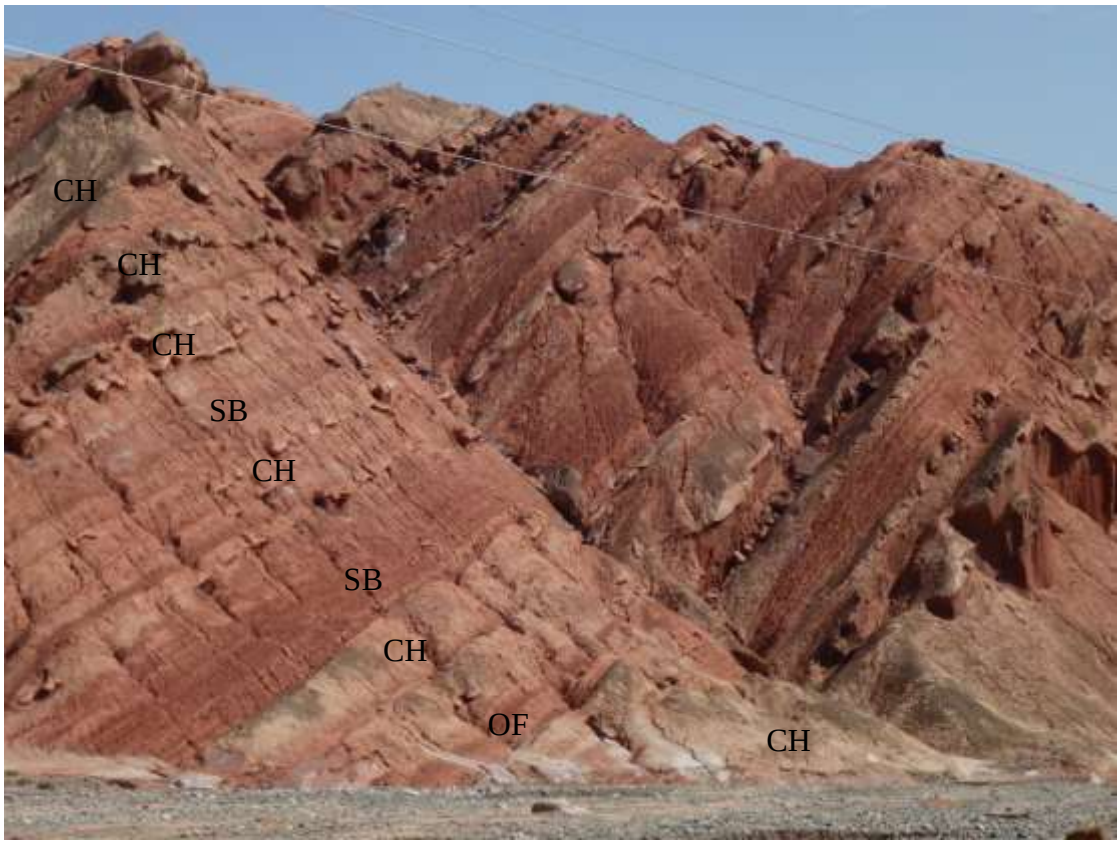

Figure 3.19 Overview of unit C stacked channels and overbank deposits.

Figure 3.20 Erosional scour filled with gravels and pebbles (Se).

Figure 3.21 Exposed surface of unit C with ripples (Sr)

Figure 3.22 Exposed surface of unit C with desiccation cracks and animal footprints.

Overall the sequence contains repeated sets of fining upwards sandstones and siltstones (Figure 3.23)

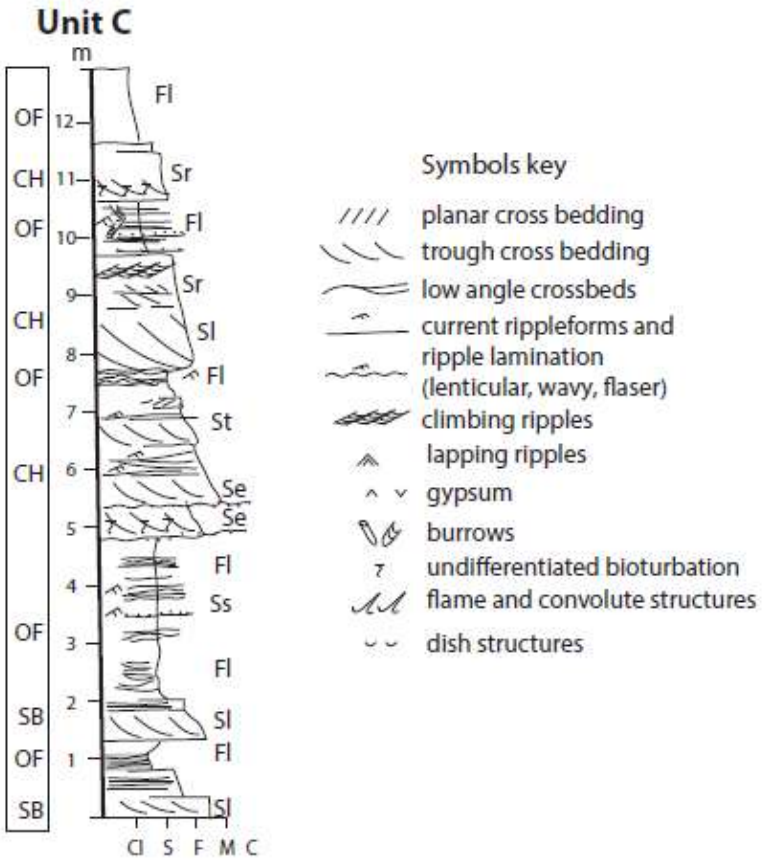

Figure 3.23 Detailed sedimentary log of a type example of unit C, GPS: N 37° 59,225, E 76° 34,515.

3.5.4.1 Interpretation / Depositional Environment

Unit C is composed of sequences of sandy bedforms (SB), overbank fines (OF) and channelised sandstones (CH). Whilst unit C is very similar to unit B, the increased frequency of channels and increase in pebble and channel lag type infills indicates an increase in energy, exposed horizons are characterised by desiccation cracks indicating an ephemeral environment.

Unit C is interpreted to be large stacks of meandering channels produced by high-energy flows within an ephemeral flood plain environment.

3.5.5 Unit C-D transition (Figure 3.20)

There is a clear transition between the stacked channel type deposits of unit C and the overlying gravel and conglomerate facies of unit D (Figure 3.24). The base of the transition is characterised by an isolated lens of large, up to 1 m clasts of limestone within a sandstone layer directly beneath the first conglomerate bed of unit D (Figure 3.25). Above this transition lay sets of planar cross bedded gravel deposits with no obvious palaeocurrent indicators or channel scours, grading is difficult to see. Cross beds are defined by finer layers of sand which pinch out along the trough.

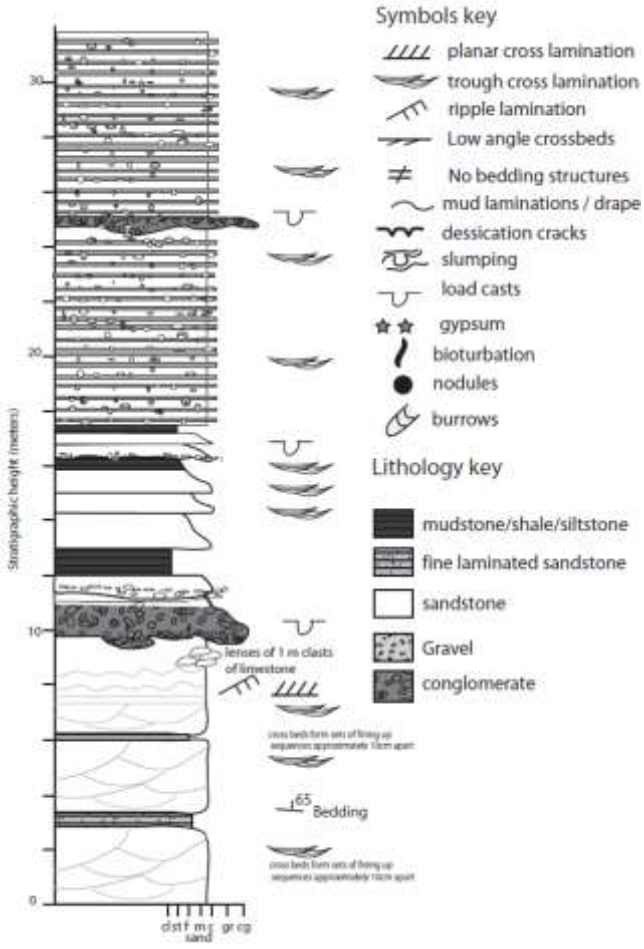

Figure 3.24 Log of the transition between units C and D with the onset of conglomerate deposition downcutting unit C in an erosional unconformity. GPS: N37°58.284' E 076°34.785'

Above the transition, gravel bedding sets are large scale, tabular and planar with each set fining up from coarse sand / gravel to medium coarse sand approximately up to 25 cm thick. Grains are sub-angular – sub-rounded and poorly sorted (Figure 3.26).

Figure 3.25 Example of a lens of large limestone clasts within a sandstone layer at the base of the transition between units C and D

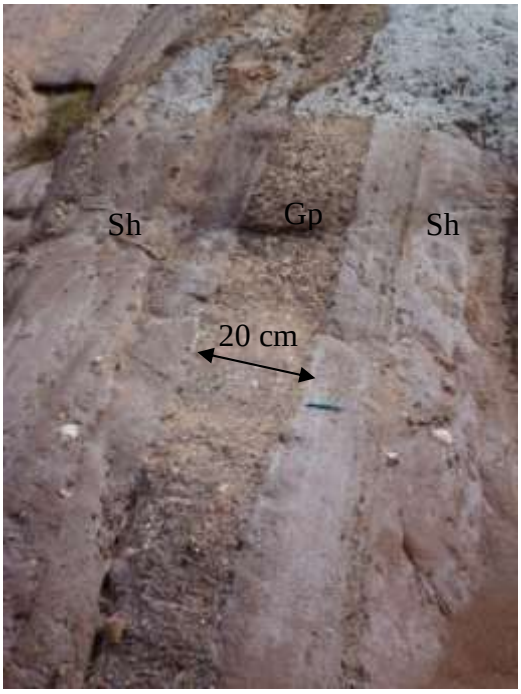

Figure 3.26 Planar gravel beds (Gp) within sandstone layers (Sh) above the transition between units C and D.

3.5.6 Unit D (2050-2790 m): Distal alluvial fan (Figure 3.27)

Unit D (log taken from GPS: N37°58.339' E076°34.910') is 740 m thick and is characterised by sequences of gravel and conglomerate beds interbedded with gravels, finer sands and silts.

3.5.6.1 Description

Following on from the contact between units C and D (described in section 3.5.5), the conglomerate beds of unit D are poorly graded and sorted with clasts ranging from 2 cm – 40 cm (with the exception of the basal conglomerate bed where limestone clasts are up to 1 m in diameter as described above). Clasts are composed of sandstone, limestone and occasional small volcanic clasts (Figure 3.27, 3.28, 3.29, 3.30 and Appendix 18 for clast count data). The conglomerates range from matrix supported (Gms) (Figure 3.30) to clast supported (Gm) (Figure 3.28) with erosive bases (Figure 3.27, 3.29) and gutter casts. In between the large conglomerate sets are thinner beds of planar gravels and sandstones (Gp) (Figures 3.26).

The gravel beds consist of planar, parallel bedding up to 20 cm in width, clast supported and with no obvious grading or bedding structures (Figure 3.26).

Interlayered between the gravel and conglomerate beds are sandstone beds ranging in grain size from fine to coarse grained with a variety of fining up, coarsening up and ungraded sequences. Many gravel 'sets' contain planar, low angle cross beds (Sp, Sl, Sh) and occasional siltstone beds with fine laminations (Fl) (Figure 3.31).

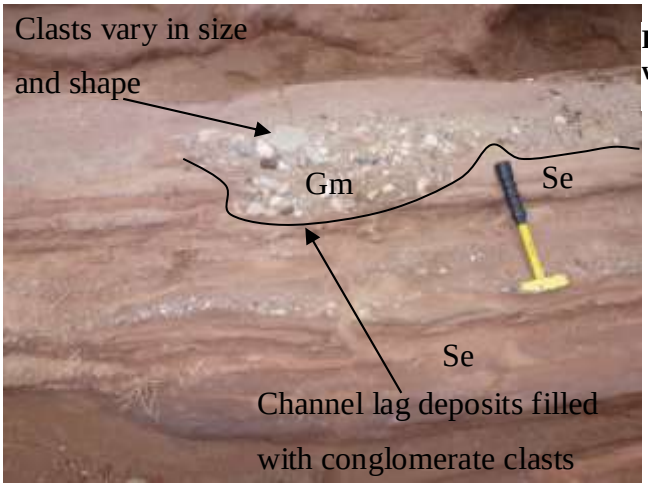

Figure 3.27 Channel lag deposit filled with conglomerate clasts.

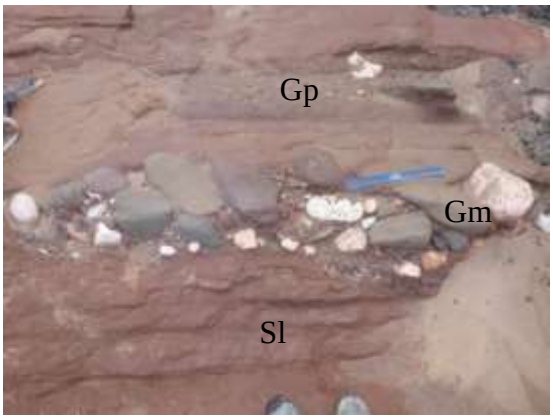

Figure 3.28 Conglomerate clasts dominated by sandstones and limestones (see 30cm ruler for scale)

A typical sequence is composed of a massive matrix supported conglomerate bed overlain by planar sets of coarse gravels sands and siltstones.

3.5.6.1 Interpretation / Depositional Environment

Unit D is composed of predominantly gravel bars and bedforms (GB), with sediment gravity flows (SG) and occasional laminated sand sheets (LS), overbank fines (OF) and channelised sandstones (CH).

The large clast size and poor sorting of the conglomerate beds indicate a high energy environment with rapidly deposited successive debris flows interpreted to be a braided river/distal alluvial fan. The increase in energy observed between units C and D suggests a transition to a more proximal source in the adjacent topography, or an increase in gradient proximal to deposition (resulting in an increase in debris flow rates and resultant clast size). However, a change in the climate resulting in an increase in precipitation and weathering cannot be ruled out without further investigation (see Chapter 6).

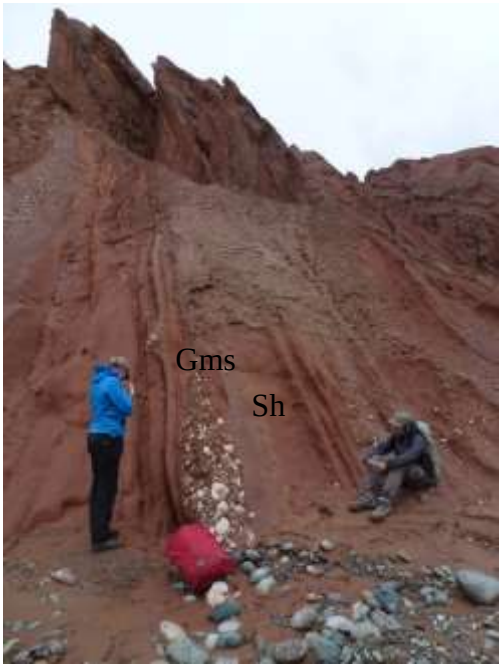

Figure 3.30 Overview of unit D conglomerates.

Figure 3.29 Conglomerate clasts of unit D in sandy / gravel matrix

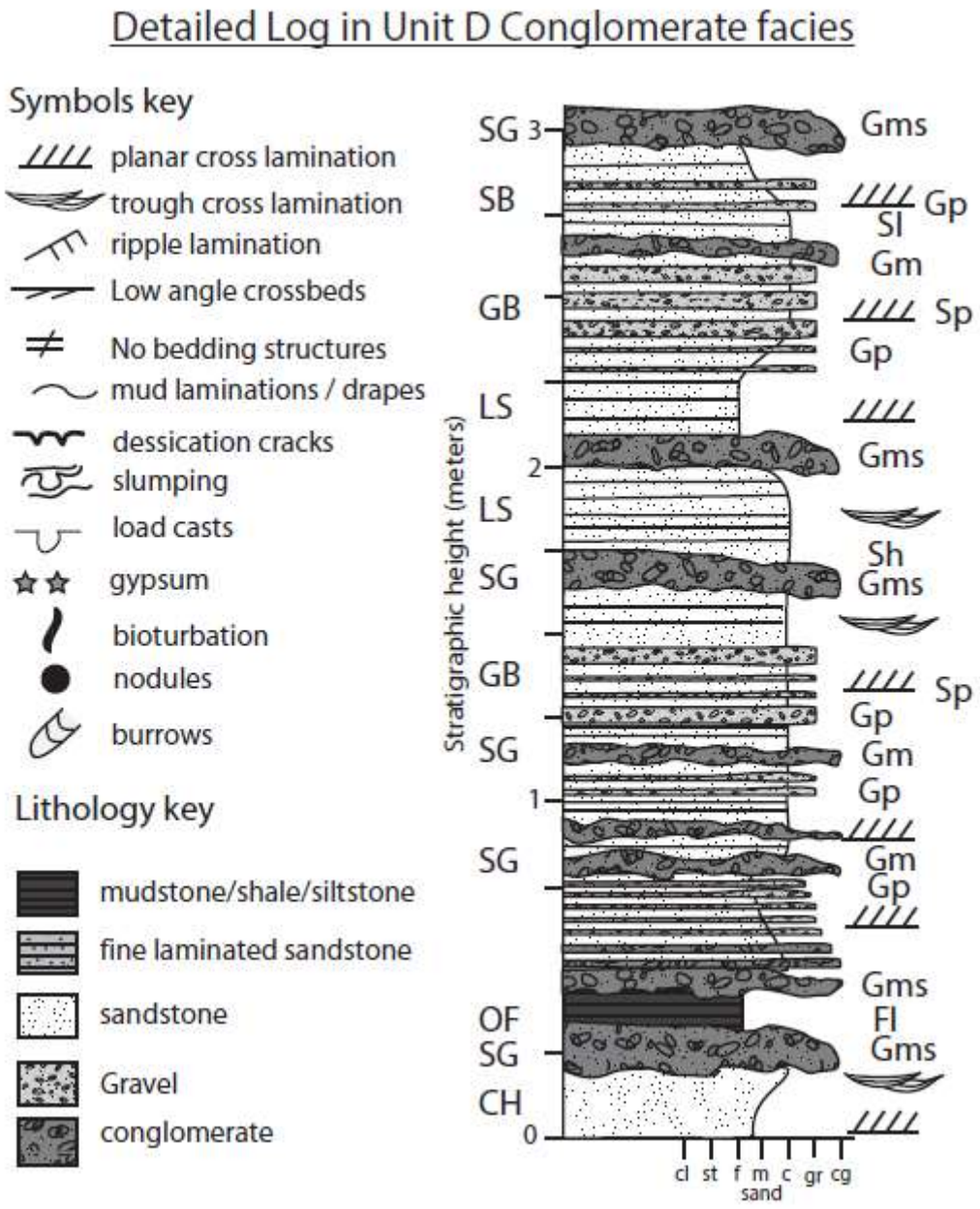

Figure 3.31 Log of a typical depositional sequence within unit D, conglomerate facies
GPS: N37°58.339' E076°34.910'

3.5.7 Unit D – E transition

The transition between unit D and E is conformable with the coarser gravelly bed of the upper unit D appearing grey in colour compared to the more orange appearance of unit E (Figure 3.32). The log in Figure 3.33 is taken from the top of the conglomerate facies at GPS: N37°58.823' E076°35.335'.

Figure 3.32 Transition from conglomerate facies to more sandy facies GPS: N37°58.823' E076°35.335'

Following on from the last conglomerate bed of unit D, the lower most part of unit E contains coarse sandstones and gravels with occasional floating clasts and lenses of gravels within finer sands and silts. These gravel and coarser beds gradually give way to increasing finer and medium sandstone beds and finely laminated siltstones of unit E. Overall, the transition appears to be conformable and gradual with no obvious unconformities.

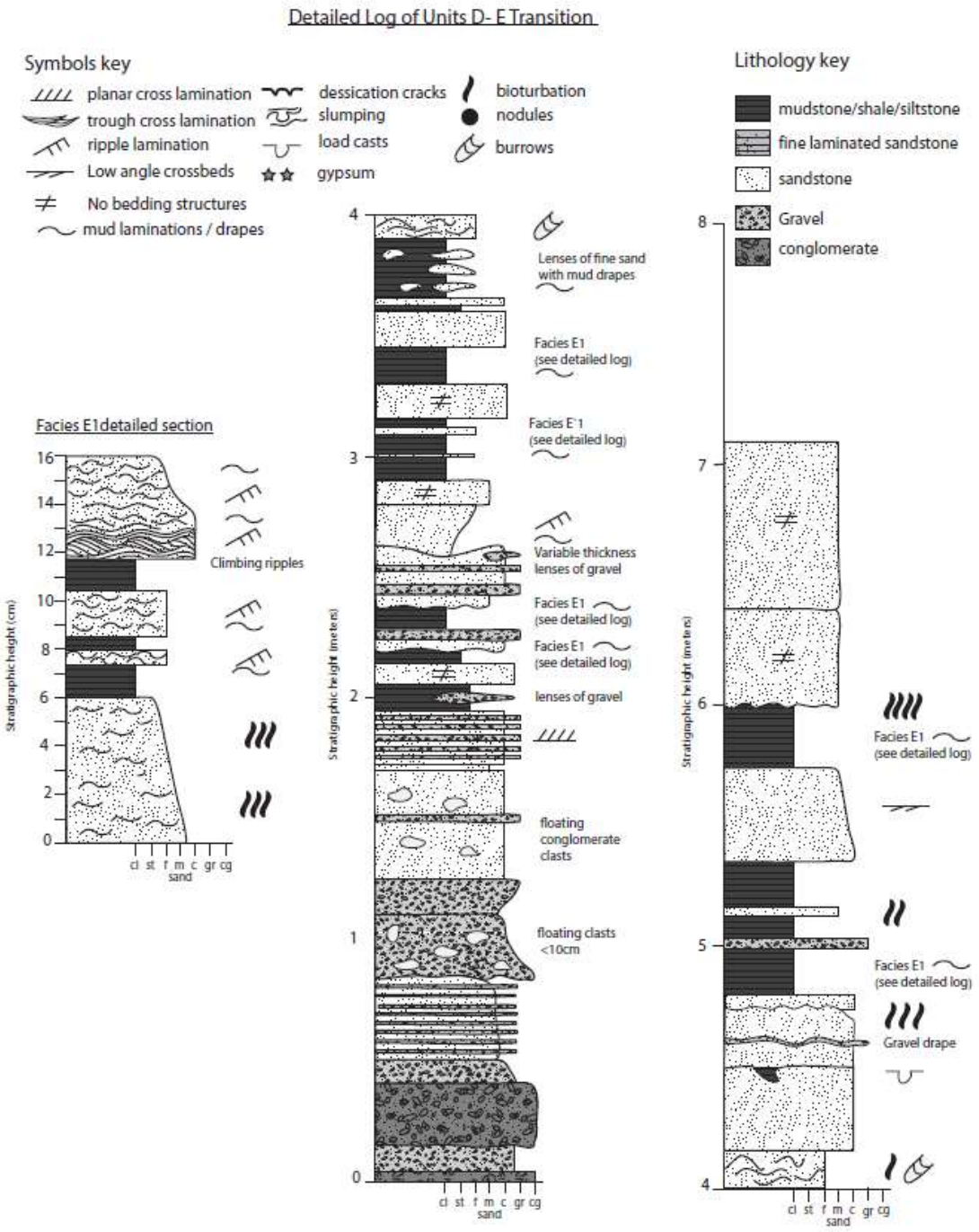

Figure 3.33 Detailed log of the unit D-E transition, GPS: N37°58.823' E076°35.335'

3.5.8 Unit E (2790-4050 m): Distal braid plain with ephemeral streams.

Overall, unit E consists of cyclical sets of thick structureless coarse sandstones separating sequences of finer sands, silts and mudstones.

3.5.8.1 Description

Unit E base is dominated by thin laterally extensive gravel beds interbedded with coarse sand with occasional 'floating' clasts which grade upwards into fining–up sequences of medium sandstones (Figure 3.33). These layers are interbedded with sets of climbing ripple bases and mud drapes fining up into fine bioturbated sands (See Figures 3.33 log E1 and 3.34). Beds range in thickness from 1 to 10 cm and are interlayered with fine clay containing small sandstone lenses (see Figure 3.33 and 3.34) Further up the sequence are occasional beds of thick medium to coarse, massive sandstones with occasional bioturbation at the base, gravel drapes and sporadic load casts with silt infills.

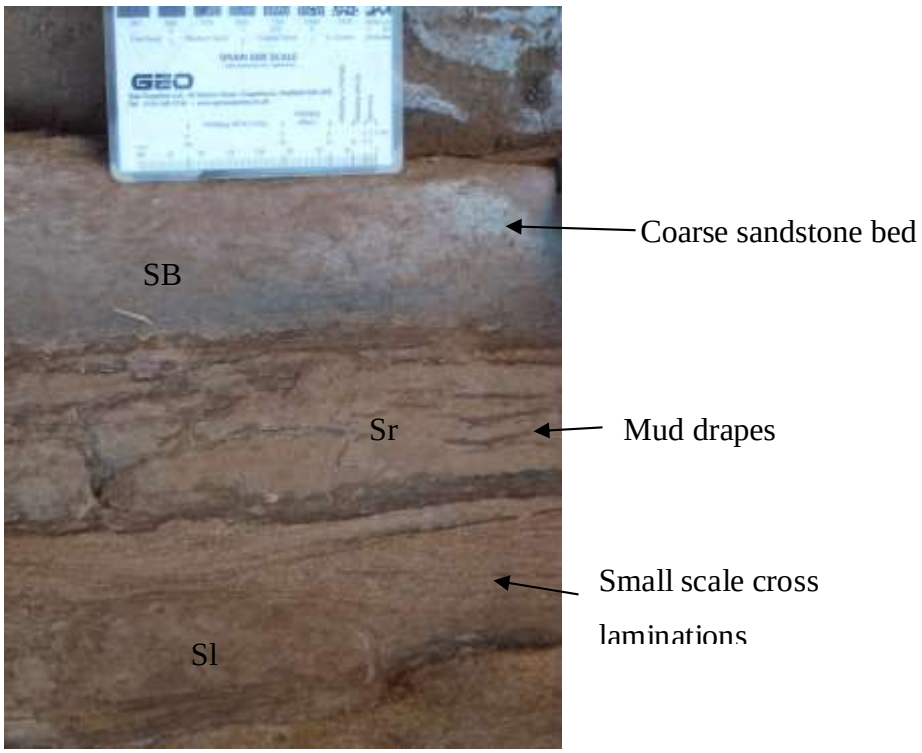

Figure 3.34 Detailed section E1 (see small scale log in Figure 3.29) with fine mud drapes, cross bedding and bioturbated sandstones GPS: N37°58.823' E076°35.335'

The upper part of unit E (Figure 3.38) is composed of metre scale structureless coarse sandstones with occasional gravel drapes, interlayered with sets of 0.2-0.7 m thick mud and fine sandstones containing ripples (Sr) and planar cross laminations (Sh) with occasional lenses of silt (Figure3.36), interbedded with very small (cm scale) lenses of fine sand.

Within the interlayered sandstones are small ripples and mud drapes (Sl) (Figure 3.35) and thin finely laminated silty layers with occasional lenses of fine – medium sands and sporadic bioturbation.

The sequence is occasionally interrupted by 0.2 – 0.5 metre scale sets of medium sandstone (Figure 3.37) with sharp basal contacts parallel to the bedding plane. These sandstones are laterally extensive and structureless. Figure 3.38 log encompasses one large cycle/set defined by two metre scale coarse beds.

Figure 3.35 Overview of unit E, GPS: N37º 58.804', E 076º 35.377'

Figure 3.36 Up close fine sets of ripples grading up to parallel laminations can be seen within the lenses of silt within unit E GPS: N37º 58.804', E 076º 35.377'

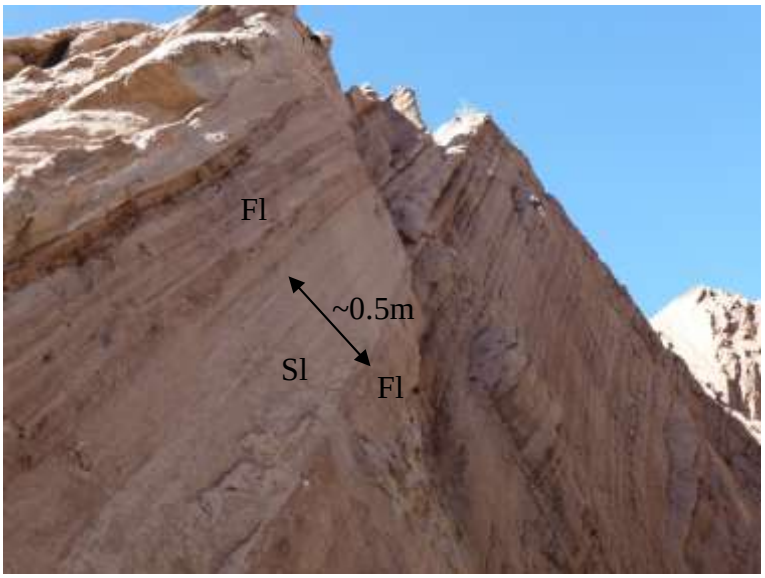

Figure 3.37 Overview of unit E GPS: N37º 58.804', E 076º 35.377'

3.5.8.2 Interpretation / Depositional Environment

Unit E is dominantly characterised by overbank fines (OF), laminated sands (LS), sandy bedforms (SB) and occasional large channels (CH)

The base of unit E consists of climbing ripples indicative of a high sediment flux with fine lenses and layers of sand and mud drapes suggesting rapidly fluctuating flow. The floating clasts are all transported with the bedload indicating a high energy / sediment flux. The low energy small channels with finely laminated muds of log E1 are interpreted to be crevasse splay facies.

The thick structureless sandstones suggest deposition from highly concentrated, laminar sediment/water flows, where sediment-laden currents were generated through

mechanisms related to flooding and mass flow. The occasional gravel drapes are likely to be channel lag deposits. These sediments indicate that deposition was rapid.

The fine silt facies with sandstone lenses are characteristic of small scale sand channels, whilst larger sandstone beds with climbing ripples appear to suggest an increase in sediment flux and energy.

The overall sequence appears to show a transition from a highly proximal braided river/distal alluvial fan facies of unit D to a more distal braided river facies with abrupt changes in flow rate and sediment flux.

Unit E is interpreted to be a high energy floodplain environment with abundant crevasse and flood deposits produced by highly efficient flow channels. The floating pebbles and coarse-grained sand with low angle laminations, suggests the predominance of ephemeral streams fed by laminar flash floods which are particularly prevalent at the base of unit E, typical of the distal part of a braid plain.

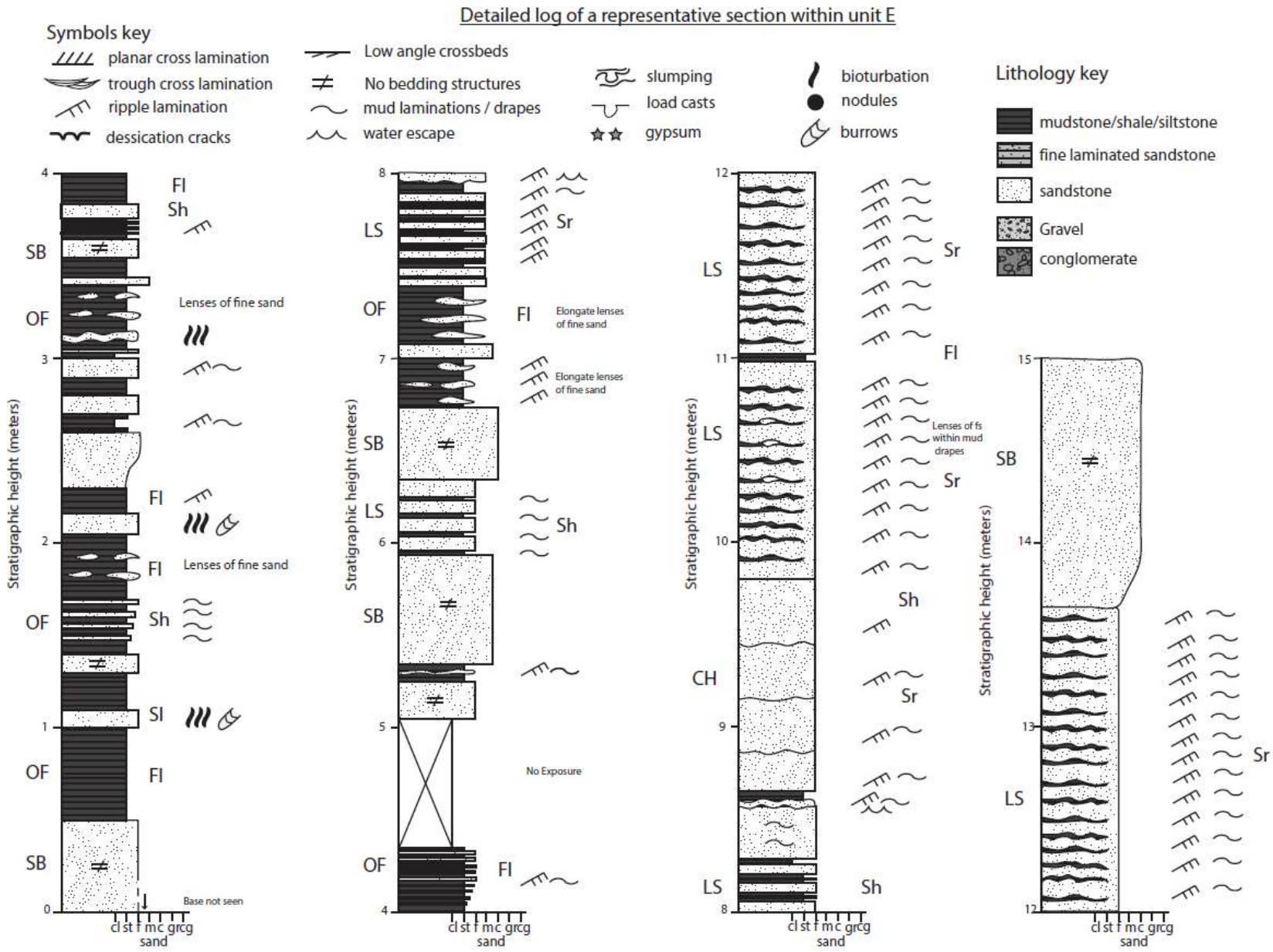

Figure 3.38 Detailed log of a representative section within unit E GPS: N37º 58.804', E 076º 35.377'

3.5.9 Unit F (>4050 m): Proximal alluvial fan

Unit F (GPS: N37° 59.240', E 076° 40.512') consists of grey coarse sandstone beds and conglomerates. The transition from unit E to F is gradual, marked by gradually increasing grey sandstone beds interlayered with finer red beds in the top 50 metres of unit E. However, the first conglomerate bed of unit F marks a key change in the Aertashi section with the onset of extensive thick cobble conglomerate deposition throughout the remainder of the section and beyond. Although in Aertashi most of this unit lays beneath a thick layer of loess cover making access limited, no log is available for this unit.

The conglomerates are clast supported with very large, well rounded clasts, ranging in size from 5–50 cm, they are poorly sorted with no clear grading (Figure 3.39). Clasts are composed of gneiss, granite with occasional large K-feldspar phenocrysts, weathered volcanics, gabbros, basalt, dolomite, serpentenite, quartzite and various metamorphic sandstones. There are no obvious signs of imbrication or palaeoflow indicators (detailed clasts list in Appendix 18).

The conglomerates are interbedded with coarse grey heterogeneous sandstone beds with undulatory cross bedding.

3.5.9.1 Interpretation

Although the transition beneath the first conglomerate bed of unit F indicates a gradual change in depositional environment, the first conglomerate bed contact is sharp alluding to an erosional unconformity. Overall, the conglomerates were deposited in a very high energy environment. Well rounded, matrix supported clasts are indicative of a change in source which is likely to be more distal than the source of clasts in unit D. The composition of the conglomerates is different to those seen in unit D, containing a much greater variety of clasts and an increase in intrusive igneous and metamorphic clasts suggesting they are derived from a previously eroded mountain source where 'deeper' facies are exposed, indicating a change in provenance from unit D.

The depositional environment of unit F is interpreted to be a proximal alluvial fan environment.

Figure 3.39: Various pictures of the unit F (Xiyu Formation) taken from an isolated exposure approximately 2000 metres above the Aertashi section, GPS: N37° 59.240', E 076° 40.512'.

3.6 Overall summary of the Aertashi continental section (Figure 3.40)

The ephemeral, high capacity fluvial flood plain of the non-marine Bashibulake Formation, deposited within an arid or semi-arid climate, marks the onset of continental deposition in Aertashi. Above this unit is a depositional hiatus marked by an unconformity recorded by Bosboom et al. (2014c) which spans the Eocene – Oligocene boundary (ca.36-33 Ma). Following this hiatus, units A and B show a progressive evolution from an arid distal environment to a more ephemeral floodplain environment, with the aeolian dune and avalanche deposits of unit A, typical of a distal floodplain, progressively grading into wetter inter-dunes and into a lacustrine delta plain environment (unit B). This lacustrine environment progrades into a more distal, muddy flood plain environment with meandering channels which amalgamate into channel belts in unit C which may be attributed to either an increase in sediment flow or decrease in accommodation rate.

A distinct erosional unconformity marks the transition between unit C and the onset of unit D, which is characterised by a distal alluvial fan to braid plain environment. The onset of conglomerate deposition marks a transition in Aertashi to a more proximal

facies with the abundance of limestone and sandstone type clasts indicating the erosion of localised sedimentary cover as a consequence of relief formation proximal to Aertashi at this time. A gradual shift from the gravelly, debris flows of unit D to the more fine – grained muddy flood plain deposits of unit E indicates a shift back to a more distal environment with a high sediment flux.

Towards the top of unit E is a progressive change in the depositional environment, with a gradual reduction in the finer red beds and increase in grey sandstone beds towards the top of the unit. However, the onset of unit F is marked by the distinct onset of large grey cobble conglomerates. Clasts are composed of metamorphic rock types indicating unroofing of a proximal source. This period marks a sharp basin-ward shift of the facies to a proximal alluvial fan environment.

Overall from units A – F there is a generally prograding system associated with a rising local/regional topography (Figure 3.40). However the finer facies of unit E indicates that this trend is not constant throughout time and is more complex than it may originally appear, see Chapters 4, 5 and 6 for further investigation of the evolution of the Aertashi section.

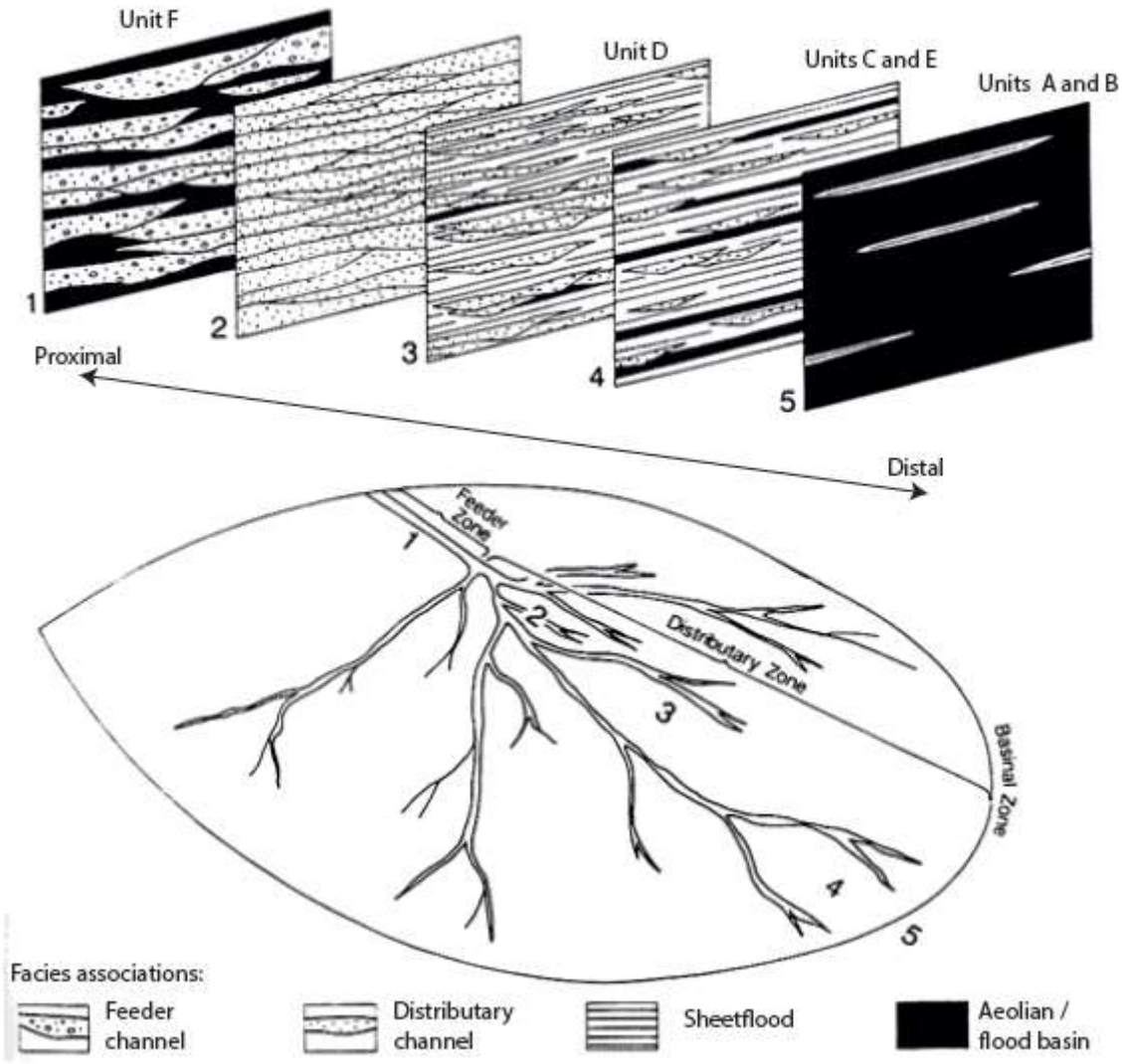

Figure 3.40 Idealised model of a terminal fan showing down-fan changes in sand body shape, lithofacies types, and architecture with units A-F of the Aertashi section labelled. 1, Feeder zone, possibly with more than one channel; 2, proximal fan zone; 3, medial fan zone; 4, distal fan zone and 5, flood basin, adapted from Kelly and Olsen (1993).

4. Indentation of the Pamir with respect to the northern margin of Tibet: constraints from the Tarim Basin sedimentary record.

Published in *Tectonics,* 35, 2016.

Tamsin Blayney[1], Yani Najman[1], Guillaume Dupont-Nivet[2,3,4], Andrew Carter[5], Ian Millar[6], Eduardo Garzanti[7], Edward R. Sobel[3], Martin Rittner[8], Sergio Andò[7], Zhaojie Guo[4], Giovanni Vezzoli[7.]

1. Lancaster Environment Centre, Lancaster University, Bailrigg, Lancaster, LA1 4YQ, UK
2. Géosciences Rennes, UMR-CNRS 6118, Université de Rennes 1, Rennes, France
3. Universitaet Potsdam, Institut für Erd- und Umweltwissenschaften, Karl-Liebknecht-Strasse 24, 14476 Potsdam, Germany
4. Key Laboratory of Orogenic Belts and Crustal Evolution, Ministry of Education, Beijing, China
5. Department of Earth and Planetary Sciences, Birkbeck College, Mallet Street, London, WC1E, 7HX, UK
6. NERC Isotope Geosciences Laboratory, BGS Keyworth, Nottingham NG12 5GG, UK
7. Laboratorio di Petrografia del Sedimentario, Dipartimento di Scienze Geologiche e Geotecnologie, Università di Milano-Bicocca, Piazza della Scienza 4, 20126 Milano, Italy
8. London Geochronology Centre, Department of Earth Sciences, University College London, Gower Street, London, WC1E 6BT, UK

Key Points

- Prior to Pamir indentation, the West Kunlun (WKL) mountain range already formed topographic relief.
- Pamir indentation commenced at ca. ~ 25 Ma with activation of the Kashgar-Yecheng Transfer System and Tiklik fault.
- It was no sooner than 14 Ma that the Pamir range had indented ≈200 kms northward.
- Establishment of the modern day Yarkand drainage pattern occurred after 11 Ma.

Abstract

The Pamir represent the indented westward continuation of the northern margin of the Tibetan Plateau, dividing the Tarim and Tajik basins. Their evolution may be a key factor influencing aridification of the Asian interior, yet the tectonics of the Pamir Salient are poorly understood. We present a provenance study of the Aertashi section, a Paleogene to late Neogene clastic succession deposited in the Tarim Basin to the north of the NW margin of Tibet (the West Kunlun) and to the east of the Pamir. Our detrital zircon U-Pb ages coupled with zircon fission track, bulk rock Sm-Nd and petrography data document changes in contributing source terranes during the Oligocene to Miocene which can be correlated to regional tectonics. We propose a model for the evolution of the Pamir and West Kunlun (WKL) in which the WKL formed topography since at least ~200 Ma. By ~25 Ma, movement along the Pamir-bounding faults such as the Kashgar-Yecheng Transfer System had commenced, marking the onset of Pamir indentation into the Tarim-Tajik Basin. This is coincident with basinward expansion of the northern WKL margin, which changed the palaeodrainage pattern within the Kunlun, progressively cutting off the more southerly WKL sources from the Tarim Basin. An abrupt change in the provenance and facies of sediments at Aertashi has a maximum age of 14 Ma; this change records when the Pamir indenter had propagated sufficiently far north that the North Pamir was now located proximal to the Aertashi region.

4.1 Introduction

Although the Pamir is an archetype of intracontinental collision and the region's topographic evolution likely played a key role in controlling regional climate, our understanding of the detailed tectonic history remains poorly constrained. The region (Figure 4.1), an indented continuation of the north-west margin of the Tibetan Plateau, consists of a number of terranes which amalgamated as the Tethys closed, culminating in the India-Asia collision most commonly quoted at ~60-50 Ma (DeCelles et al., 2014, Hu et al., 2015, Najman et al., 2010, Rowley, 1996, Wu et al., 2014). Although topography existed in both the Pamir and Tibet prior to the India-Asia collision (e.g. Cao et al., 2015, Kapp et al., 2007, Murphy et al., 2002, Robinson et al., 2004, Royden et al., 2008, Schwab et al., 2004, Volkmer et al., 2007), it is this final collision, associated with evolution of the Himalayan orogen, that resulted in the indentation of

the Pamir into the Tajik -Tarim basins to the north (e.g. Burtman and Molnar, 1993), and significant uplift of Tibet (e.g. Harrison et al., 1992)

a)

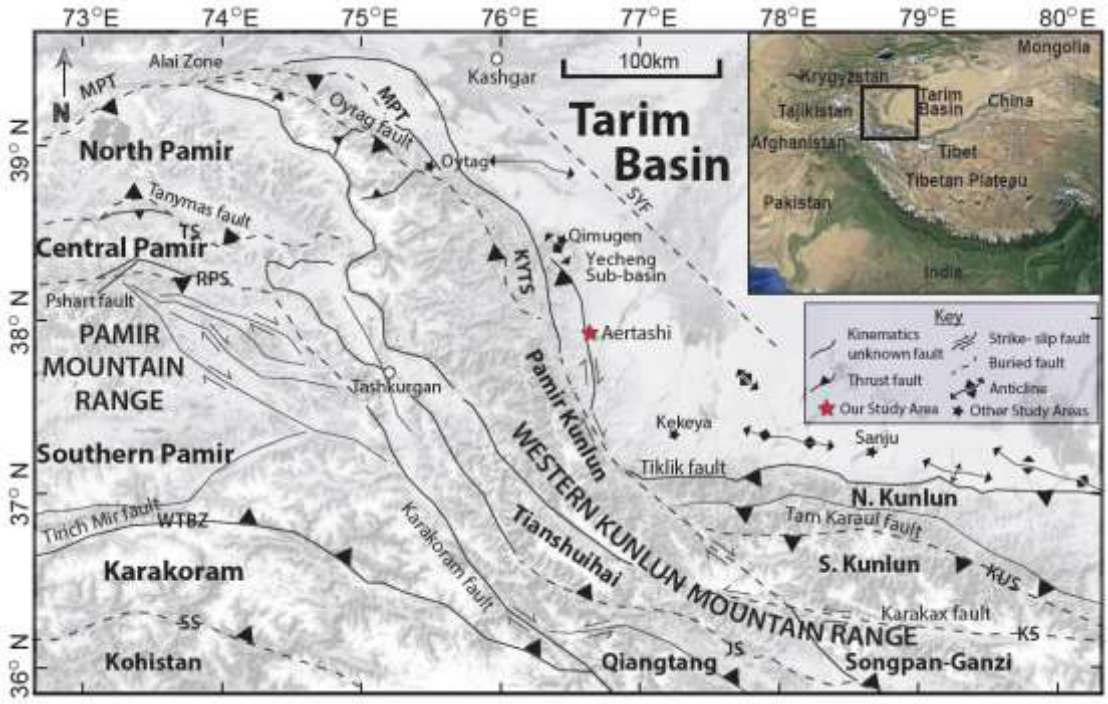

b)

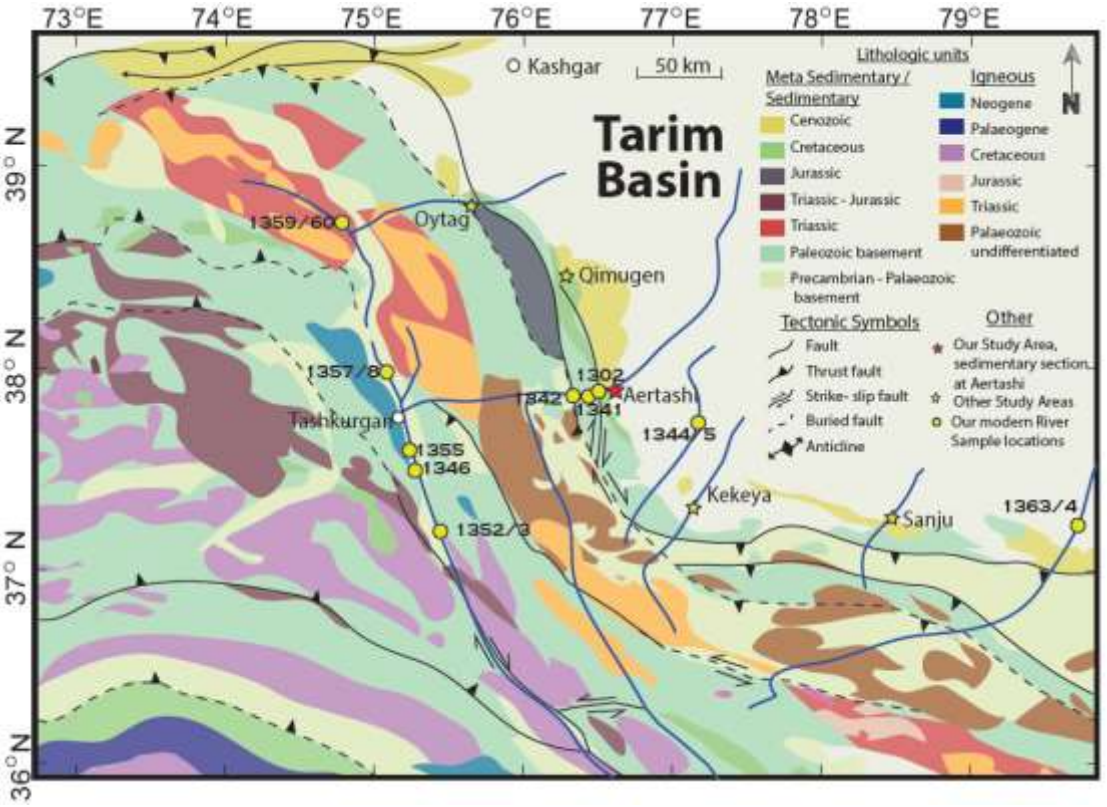

Figure 4.4.1 (a) The major terrains of the Pamir and West Kunlun in NW Tibet after Robinson et al. (2012). (b) The geology of the region after Bershaw et al. (2012) and Cao et al. (2015). Modern river sample locations shown as yellow dots, sedimentary section located at "Aertashi". TS = Tanymas suture, RPS = Rushan-Pshart suture, WTBZ = Wakhan-Tirich boundary zone, SS= Shyok suture, JS= Jinsha suture, KS= Kunlun suture, KUS = Kudi suture, MPT = Main Pamir Thrust, KYTS = Kashgar-Yecheng transfer system, SYF=Sache-Yangdaman fault.

The Pamir terranes (Figure 4.1) are an along-strike continuation of Tibetan terranes (Burtman and Molnar, 1993, Robinson et al., 2012, Schwab et al., 2004, Tapponnier et al., 1981, Yin and Harrison, 2000) that have been subjected to a higher degree of crustal shortening and metamorphism, and deeper exhumation, relative to the equivalent terrains in Tibet. Intracontinental subduction occurred along the south–dipping Alai subduction zone (e.g. Burtman and Molnar, 1993, Fan et al., 1994) with the Main Pamir Thrust and Pamir Frontal Thrusts forming the updip expression of this subduction zone (Arrowsmith and Strecker, 1999, Burtman and Molnar, 1993, Coutand et al., 2002, Hamburger et al., 1992, Sobel et al., 2013).

When and how the northern margin of Tibet evolved and the Pamir range indented and uplifted is poorly documented. Models have been proposed for a northward propagation of deformation across the Tibetan Plateau (Tapponnier et al., 2001) while there is also evidence that the northern margin of Tibet was deforming soon after India-Asia collision, by middle-late Eocene times (e.g. Clark et al., 2010, Yuan et al., 2013, Staisch et al., 2016). However that research mostly relates to the more north-eastern regions of Tibet and little has been published on the northwest margin. Significant work includes the seminal work of Burtman and Molnar (1993), who synthesized the Cenozoic geodynamic framework, Ducea et al. (2003) who considered that crustal thickening during the early stages of India-Asia collision resulted in a low relief elevated plateau since early Cenozoic, Yin et al. (2002) who similarly proposed earliest Cenozoic crustal thickening for the WKL, Sobel and Dumitru (1997) who recorded evidence for late Oligocene exhumation in the WKL, Amidon and Hynek (2010) who recorded two periods of accelerated exhumation in the middle Eocene and early Miocene and Schurr et al. (2014b), who quantified recent and active deformation.

The onset of Pamir indentation relative to Tibet has been constrained as ~25-20 Ma (Burtman and Molnar, 1993, Sobel and Dumitru, 1997, Cowgill, 2010, Bande et al., 2015), as discussed in more detail in section 4.2.1.

The evolution of both the Pamir and the Tibetan Plateau has been suggested to drive regional as well as global climate change (e.g. Bosboom et al., 2011, 2014c, Ruddiman and Kutzbach, 1989, Zhang et al., 2007c). Uplift of Tibet resulted in intensification of the monsoon and changes in atmospheric circulation patterns (Molnar et al., 2010 and references therein). The evolution of the Pamir resulted in the

removal of a major moisture source in Asia: prior to the India-Asia collision, the Tarim Sea filled the broad east-west trending Tarim Basin that extended across the location of the modern Pamir and into the Tajik depression (e.g. Bosboom et al., 2015, Mao and Norris, 1988). During the Eocene, this sea retreated west from the basin, removing a major source of moisture, thus contributing to the aridification of Asia (Ramstein et al., 1997, Zhang et al., 2007c) and the development of one of the largest sand seas in the world; dust from this desert contributes substantially to the global aerosol system that modulates global climate (Uno et al., 2009, Zheng et al., 2015a). Proposed mechanisms that caused this sea retreat range from Pamir indentation, overthrusting and associated sedimentary overfilling (Burtman and Molnar, 1993, Burtman, 2000, Coutand et al., 2002) to a eustatic regression (Dupont-Nivet et al., 2007, Sobel and Dumitru, 1997) or a combination of the two (Bosboom et al., 2011, 2014a).

This paper elucidates the evolution of this region, particularly the indentation history of the Pamir, from a study of material deposited in the Tarim Basin to the north of the NW margin of Tibet and to the east of the Pamir (Figure 4.1). We interpret our new provenance data from the Cenozoic Aertashi sedimentary section in terms of an evolving source area and the controlling tectonics which effected the changes we document.

4.2 Geological Background

To constrain the evolution of the NW margin of Tibet and the Eastern Pamir, we focus our study on the longest and best dated Cenozoic stratigraphic record in the SW Tarim Basin. The Aertashi sedimentary section (Figure 4.1) is located adjacent to the eastern side of the Pamir, to the north of the northern margin of Tibet, and at the western edge of the Tarim Basin.

4.2.1 The Pamir

The Pamir mountain range forms a prominent indenter separating the Tarim and Tajik basins and has a complex and debated formation history; intracontinental subduction, lower crustal delamination, slab rollback, subduction erosion, subduction accretion, and a marginal slab-tear have all been discussed (e.g Burtman and Molnar, 1993, Hamburger et al., 1992, Negredo et al., 2007, Replumaz et al., 2010, Sippl et al., 2013, Sobel et al., 2013).

Prior to indentation, the Pamir is thought to have had a relatively straight east-west trending northern margin aligned with the West Kunlun (WKL) and the northern margin of Tibet (Figure 4.1), forming the western continuation of these accreted terranes (Burtman and Molnar, 1993, Robinson et al., 2004, Schwab et al., 2004). Formation of the Pamir indenter may have resulted from the interaction of distributed shortening across the India–Asia collision zone with lateral heterogeneities in the Asian crust such as the Tarim Basin (England et al., 1985). The Pamir's characteristic curvature has been attributed to oroclinal bending (Yin et al., 2001), radial thrusting (Robinson et al., 2004), a hybrid model involving north-west radial thrusting with anticlockwise rotation at the western margin and transpressional right-slip transfer faulting at the eastern margin (Cowgill, 2010), or a consequence of northward rollback of the subducting slab (Sobel et al., 2013).

The Pamir region can be subdivided into three main terranes (Figure. 4.1a) separated by major sutures, which sequentially collided during progressive closure of the Tethyan Ocean (Burtman and Molnar, 1993, Robinson et al., 2012, Schwab et al., 2004). The North Pamir, bound by the Main Pamir Thrust (MPT) in the north and the Tanymas suture in the south, is composed of predominantly Palaeozoic, and Triassic (meta)sedimentary and metavolcanic rocks intruded by Triassic-Jurassic granitoids (Figure 4.1b) (Schmidt et al., 2011, Schwab et al., 2004).

The Central Pamir is bound by the Tanymas suture to the north and the Rushan-Pshart zone to the south. It consists of Palaeozoic and Triassic-Jurassic (meta)sedimentary rocks (Schwab et al., 2004) and gneiss domes of various protolith types and ages, including the Muztagh Ata dome, which were metamorphosed and exhumed during the Cenozoic (Robinson et al., 2007, Schmidt et al., 2011, Schwab et al., 2004, Stearns et al., 2015).

The South Pamir, bounded by the Rushan-Pshart suture zone to the north and the Wakhan-Tirich Boundary zone (possibly equivalent to the Bangong Nujiang suture (Robinson, 2015)) to the south, are composed of Palaeozoic, Triassic and Jurassic (meta)sedimentary rocks which have been affected by Cretaceous and Cenozoic magmatism and metamorphism (Schwab et al., 2004). It contains the giant Shakhdara dome of Cretaceous and older protolith, metamorphosed and exhumed during domal formation in the Cenozoic (Stübner et al., 2013b). In the eastern Pamir, horsetails

splaying from the northern termination of the Karakoram strike-slip fault (KKF) delineate the boundary between the South and Central Pamir (Figure 4.1a).

To the south of the Pamir lie the Karakoram and the Kohistan-Ladakh arc (Figure 4.1), separated by the Shyok suture. The former consists of deep crustal metamorphics, Cretaceous and Cenozoic intrusives and sedimentary rocks (e.g. Fraser et al., 2001); the latter consists of a predominantly Cretaceous age oceanic island arc (e.g. Tahirkheli and Jan, 1979).

The Pamir is suggested to have been translated ~300 km northward relative to the northern margin of Tibet (Burtman and Molnar, 1993) accommodated along the south dipping Alai subduction zone (Burtman and Molnar, 1993, Fan et al., 1994, Hamburger et al., 1992) with the Main Pamir Thrust (MPT) forming its updip projection (Burtman and Molnar, 1993, Hamburger et al., 1992, Roecker et al., 1980) (Figure 4.1a).

Northward motion of the Pamir salient is accommodated along the eastern and western margins by a series of strike-slip faults including, on the western side of the Pamir Salient, the sinistral Darvaz - Karakul fault system and on the eastern margin the Kashgar-Yecheng transfer system (KYTS) with an estimated offset of 280 km (Cowgill, 2010, Sobel and Dumitru, 1997). In turn, the KYTS transfers shortening to the north-vergent Tiklik fault, which bounds the northern margin of the WKL (Cao et al., 2013, 2015).

Timing of movement on the KYTS, dated as having initiated by 20 Ma from apatite fission track (AFT) data (Sobel and Dumitru, 1997), provides one of the few constraints on the timing of Pamir indentation. Cowgill (2010) used the above data and combined it with previously published sedimentological and magnetostratigraphic data from the Aertashi section (Yin et al., 2002) to further interpret the timing of movement. While the subsidence curves suggesting Eocene onset of motion have since been updated with magnetostratigraphically refined depositional ages which do not show acceleration of subsidence at this time (Bosboom et al., 2014b), Cowgill's assertion of movement along the fault at 25-18 Ma, based on the AFT data and onset of conglomeratic facies, is in agreement with other researcher results.

More recently, Bande et al. (2015) proposed that movement along both the buried Shache-Yangdaman right-slip fault in the Tarim Basin, and the Talas-Fergana fault in

the Tianshan (Figure 4.1a), dated around ~25 Ma as well as late Cenozoic counterclockwise vertical axis rotations of the Fergana Basin to the north of the Pamir, is related to Pamir indentation. Furthermore, Tang et al. (2015) used anisotropy of magnetic susceptibility data to record an increase in strain in basin sediments at 26 Ma, which they related to the onset of Pamir indentation. Dating of indentation in the late Oligocene-early Miocene is broadly consistent with the time at which contours of isopach maps for Tarim Basin sediments show truncation against the Pamir (Wei et al., 2013), taking into account the large uncertainties in formation ages at this regional scale.

The dextral Karakorum fault (KKF) is associated with intra-Pamir shortening. Active since 16-13 Ma (e.g. Phillips and Searle, 2007, Phillips et al., 2004) or ~24 Ma (e.g. Lacassin et al., 2004, Valli et al., 2008), the northern end of the KKF terminates in horsetail splays which bound some of the Central Pamir gneiss domes (Schurr et al., 2014b, Strecker et al., 1995). Most of these domes experienced N-S extensional exhumation from ~20 - ~16 Ma; this was succeeded by renewed N-S contractional deformation (e.g. Stearns et al., 2015).

4.2.2 The West Kunlun Mountain Range (WKL)

The WKL forms the northern margin of the western Tibetan Plateau, extending into the south-eastern Pamir; we refer to the latter as the Pamir Kunlun (Figure 4.1). Prior to the India–Asia collision, the WKL evolved as part of a sequence of terranes accreted onto the southern margin of Asia during the Palaeozoic–Mesozoic as a result of closure of the Paleotethys (Matte et al., 1996, Robinson et al., 2012, Xiao et al., 2002, Yin and Harrison, 2000). The West Kunlun mountain range consists of the North Kunlun, South Kunlun, our regionally-defined Pamir Kunlun, and the Songpan-Ganzi and Tianshuihai terranes (Figure 4.1a).

As illustrated in Figure 4.1b, the North and South Kunlun consist predominantly of Precambrian-Palaeozoic metasedimentary rocks, and plutons of Palaeozoic and, at its western extent adjacent to the Pamir Kunlun, Triassic age (Cowgill et al., 2003, Liu et al., 2015, Schwab et al., 2004, Xiao et al., 2003, 2002, Youngun and Hsü, 1994). The Songpan-Ganzi terrane consists of Triassic and Jurassic plutons, and Triassic (meta)sedimentary rocks (Yin and Harrison, 2000) while the Tianshuihai terrane consists predominantly of Triassic-Cretaceous (meta)sedimentary rocks overlying a

Palaeozoic basement (Cowgill et al., 2003, Liu et al., 2015, Matte et al., 1996, Robinson et al., 2012, Schwab et al., 2004). The Pamir Kunlun is composed of Precambrian and Palaeozoic (meta) sediments, a large areal extent of Palaeozoic plutons, as well as Triassic intrusions.

Cao et al. (2015) suggest that the WKL had emerged above sea level by Triassic-Early Jurassic times, supported by the presence of well-developed Triassic to Lower Jurassic magmatism; Matte et al. (1996) suggested that these resulted from north-dipping subduction of the Paleotethyan lithosphere under the Kunlun at this time. Crustal thickening along the WKL northern margin began at >46 Ma according to Yin et al. (2002). Thrusting along the northern margin of the Kunlun was considered to have initiated at ca. ~26-23 Ma by Jiang et al. (2013), Jiang and Li (2014), and Cao et al. (2015); 25-20 Ma by Sobel and Dumitru (1997) and 20 Ma by Wang et al. (2003) and Matte et al. (1996), while Jin et al. (2003), Liu et al. (2010) and Zheng et al. (2000, 2010) consider that the main phase of uplift occurred in the Pliocene.

4.2.3 The Western Tarim Basin

The Tarim Basin today forms a large intracontinental basin which preserves a stratigraphic record spanning the Late Proterozoic through the Cenozoic(e.g. Tian et al., 1989). During the Late Cretaceous through Eocene, the SW Tarim Basin hosted a series of shallow marine transgressions and regressions (Bosboom et al., 2011, Bosboom et al., 2014b, Tang, 1989, Lan and Wei, 1995, Burtman et al., 1996, Burtman, 2000). Surrounding the basin is a series of ranges that have been deformed by the successive accretion of continental terranes, which started during the Permian and ended at the Indo-Asia collision (Hendrix et al., 1992, Jia, 2004, Robinson et al., 2003, Yin and Harrison, 2000). The basin has been overthrust by the Tian Shan in the north, the Pamir in the west and the Kunlun and the Tibetan Plateau in the south (e.g. Burtman and Molnar, 1993, Cowgill, 2010, Jia, 1997, Yin and Harrison, 2000). However, the Tarim Basin itself has remained relatively undeformed (e.g. Zheng et al., 2000). In the south-western region of the basin, where our study is located, it is separated from the WKL hinterland by the Tiklik Thrust and Kashgar-Yecheng Transfer system (KYTS) (Figure 4.1).

Cenozoic depositional units of the western Tarim Basin include the Palaeogene Kashi Group, composed of the Aertashi, Qimugen, Kalatar, Wulagen and Bashibulake formations. These formations are predominantly composed of marine facies (Tang, 1989) which record a series of marine transgressions–regressions (e.g. Bosboom et al., 2011, Lan and Wei, 1995, Tang, 1989). Following the final retreat of this sea, terrestrial red clastic units named the Wuqia Group were deposited, composed of the Keziluoyi, Anjuan and Pakabulake formations. These mainly consist of fluvial facies siltstones and mudstones in the lower portion (e.g. Jia, 2004, Bosboom et al., 2011) with the upper Wuqia Group and overlying Artushi and Xiyu formations dominated by fluvial and alluvial fan facies sandstones, gravels and conglomerates (Yin et al., 2002, Zheng et al., 2006, Zheng et al., 2010, Zheng et al., 2015a and this study). Basinward thrusting by the WKL, from ~26 or ~23 Ma (Cao et al., 2015, Jiang and Li, 2014, Jiang et al., 2013) has resulted in weak deformation of these sediments.

The NW-SE trending Shache-Yangdaman right-slip fault (SYF) lies in the subsurface of the western Tarim Basin (Wei et al., 2013). This structure was active syn-depositionally with the Wuqia Group and Xiyu Formation. Facies analysis and isopach patterns suggest that a 6 km thick transtensional basin (the Yecheng subbasin) formed between the SYF and the dextral-slip KYTS. This fault possibly connects to the dextral Talas-Fergana fault (TFF) to the northwest, which experienced significant slip during the late Oligocene - middle Miocene (Bande et al., 2015).

4.3 Previous isotopic provenance studies on the Western Tarim sedimentary records.

Isotopic provenance studies in the western Tarim Basin relevant to this research have been carried out in the Oytag and Qimugen sections east of the Pamir, and the Kekeya and Sanju sections north of the NW Tibetan margin (Figure 4.1). Isotopic provenance studies in the Tian Shan and the rest of the Western Tarim Basin have also been carried out (e.g. Yang et al., 2014) but are not discussed further here as these areas do not contribute to sedimentation of the Aertashi section.

The Oytag (Wuyitake) sedimentary section is located near the Main Pamir Thrust. Today the Gez River cuts across this outcrop belt, draining the North Pamir. The Oytag section spans the Jurassic-Neogene (Bershaw et al., 2012, Sobel and Dumitru, 1997 and references therein, Sun and Jiang, 2013). The recent Paleogene chronology

proposed by Sun and Jiang (2013) should be considered with caution because it implies marine sediment depositional ages that are at odds with the rich marine biostratigraphic assemblages recorded in this and other sections (see reviews in (Bosboom et al., 2014b, 2014a)). Located south of the Oytag section is the Qimugen section (Figure 4.1). Today Qimugen is part of a drainage system which drains the North Pamir and Pamir Kunlun. The majority of the section on which isotopic provenance analyses have been undertaken is dated at <18 Ma on the basis of detrital zircons (Cao et al., 2014). Further southeast, along the south-western edge of the basin lie the Eocene to Mid-Miocene Kekeya and Early to Mid-Miocene Sanju sections (Cao et al., 2015). These sections lie along rivers that drain the North and South Kunlun terranes.

4.3.1 Oytag section

This section was studied by Bershaw et al. (2012) along the Oytag River without the use of magnetostratigraphic dating. Later application of magnetostratigraphic dating to the parallel section exposed along the Gez River (Sun and Jiang, 2013) led those authors to reinterpret Bershaw's data in light of their new age constraints. A more comprehensive provenance data set has since been produced by (Sun et al., 2016b), although we note the uncertainty in the age of this section, as summarised above.

Palaeocurrent data show a consistent direction toward the NE throughout the section (Bershaw et al., 2012), and according to Chen et al. (1992) there is little tectonic rotation.

We confine our summary of data in the Oytag section to the age range comparable with that part of the Aertashi section on which this research focusses. Noting that the magnetostratigraphic ages of Sun and Jiang (2013) should be used with caution, a provenance change is documented sometime in the interval they date between ~34 Ma and ~26 Ma (Sun et al., 2016b). Samples dated at 34 Ma and 40 Ma have distinctive zircon U-Pb age peaks at ~200-300 Ma and ~400-500 Ma, and an appreciable proportion of grains at >500-1000 Ma and >1600 Ma. Rare Late Cretaceous and Paleogene grains are also recorded. By contrast, the sample dated at ~26 Ma does not contain any Paleogene grains and there is no distinct peak at 400-500 Ma. The provenance change is also mirrored by bulk rock Sm-Nd data which show an evolving upsection decrease to less negative εNd(0) values through time. The proportion of

metamorphic lithic fragments as determined from petrography also increases over this time interval. Sun et al. (2016b) interpreted these results to indicate input into the lower part of the section, from the Karakoram and Kohistan arc south of the Pamir (located on Figure 4.1), based on the presence of Cretaceous and Paleogene grains. Later absence of such grains upsection, they interpret as due to accelerated uplift of the Pamir-Kunlun terrane blocking the input from more distal terranes. By contrast, Bershaw et al. (2012) speculated that Paleogene grains were derived from a volcanic source from the Central or southeastern Pamir (Budanov et al., 1999).

4.3.2. Qimugen section

Magnetostratigraphic dating has not been published for this section. The majority of the section over which isotopic provenance analyses have been carried out is dated by zircon U-Pb analyses at <18 Ma, and the uppermost sample analysed for zircon U-Pb lies below the Xiyu Formation, with the youngest zircon dated at 19 Ma (Cao et al., 2014). Palaeocurrents are broadly NE directed, with the exception of one south-easterly and one westerly directed data set in the lower Miocene. Clockwise rotations of 14.2 ± 11.5° in 41 to 40 Ma strata for the Qimugen section were observed by Bosboom et al. (2014b), indicating that true palaeocurrent direction lay more toward the north than north-east. Zircon populations show peaks at ~200-300 Ma, ~400-500 Ma, ~800-1000 Ma and >1500 Ma. Sporadic occurrences of Cretaceous (~100Ma) and Neogene (20 Ma) grains were also recorded throughout the section, interpreted by Cao et al. (2014) as indicating derivation from the southeast Pamir-Karakoram hinterland and transported by a palaeo-Yarkand River.

4.3.3 Sanju and Kekeya sections

In the Sanju section, proposed to be dated between ~20 and ~9 Ma on the basis of magnetostratigraphy, palaeocurrent data are NNE directed throughout the section (Cao et al., 2015). This is in keeping with a southern source that would be expected given the location of this section, located just north of the northern Tibet margin, and distant from the Pamir indenter to the west. Throughout this section, Precambrian U-Pb zircon ages show populations at ~700-1200 Ma, ~1600-2100 Ma, and >2400 Ma. Prominent peaks at 400-500 Ma, and ~200-300 Ma are also recorded, along with sporadic Cretaceous grains (~100 Ma), Paleogene grains and Neogene grains as young as 11 Ma. Such an overall age distribution is very similar to that found in both the

Songpan-Ganzi (Ding et al., 2013) and eastern North Pamir (Robinson et al., 2012). Given the palaeocurrent directions, Cao et al. (2015) interpreted a Songpan-Ganzi source for these sediments. They did note the lack of coincidence between sporadic Cenozoic zircons found in the Sanju section but not so far recorded in the Songpan-Ganzi terrane, and they considered this mismatch to be the result of incomplete characterisation of this terrane to date.

Double dating of zircon U-Pb with zircon fission track (ZFT) ages (Cao et al., 2015) indicates that the fission track ages reflect times of exhumation rather than magmatism. Three predominant fission track age populations were recorded: a Triassic–Early Jurassic (~250–170 Ma) population, a Palaeocene–early Miocene population (~60–21 Ma) and a middle Eocene–late Miocene (~39–7 Ma) population, along with a minor Early Cretaceous (~131-103 Ma) population. The data are taken to reflect that the northern margin of Tibet was above sea level and exhuming in the Mesozoic; exhumation was moderate during the Palaeogene, steady during the late Oligocene to early Miocene, and accelerated somewhat at ~15 Ma.

The Kekeya section shows near identical data over approximately the same time period, in terms of palaeocurrents (Zheng et al., 2010), and zircon U-Pb and FT data, and therefore was interpreted as also southerly derived (Cao et al., 2015). The Kekeya section does differ from the Sanju section in its lack of Neogene zircons. However, the significance of this absence is debatable given the small number of such grains recorded at Sanju, and the low number of samples (two) analysed at Kekeya.

4.4 The study area - the Aertashi section

The study area is located near the village of Aertashi east of the Pamir (Figure 4.1), adjacent to the Yarkand River, which today predominantly drains the Central and South Pamir, including the Muztagh Ata dome, and the WKL. The area forms part of the larger Yecheng Sub-basin, which has its depocenter near the town of

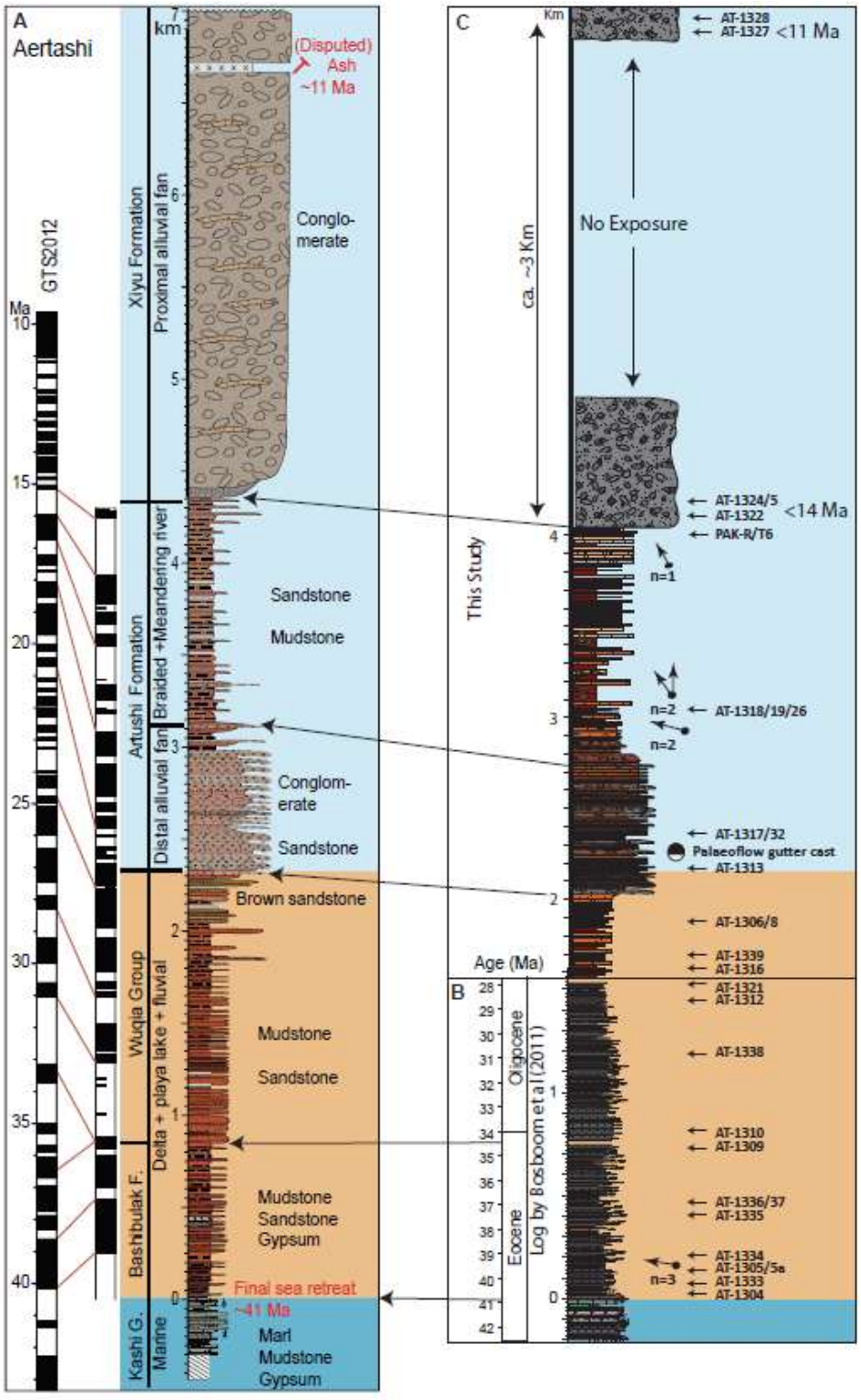

Figure 4.2 (a) A magnetostratigraphic timeline for the Aertashi section by Zheng et al. [2015a] and Bosboom et al. [2011]. (b) Sedimentary log [Bosboom et al., 2011] for the Upper Kashi Group and lower Wuqia Group with our sample locations and palaeocurrent data. (c) Sedimentary log of the Aertashi section from this study with sample locations and palaeocurrents. Figures b and c are correlated to the timeline of Zheng et al. [2015a] using facies interpretations for the upper log C and previous magnetostratigraphic dating by Bosboom et al. [2011] for log b. Colours on the logs are added to highlight our correlation to the log of Zheng et al. [2015a] and follow the format of Zheng et al. [2015a] for consistency. Colours within our sedimentary section reflect the observed colour changes for these sedimentary rocks

Yecheng (Wei et al., 2013). The Palaeogene - Neogene eastward dipping sediments, are composed of the Palaeocene to Eocene marine Kashi Group, which here comprises the Aertashi, Qimugen, Kalatar, and Wulagen formations (Figure 4.2a). These rocks record marine transgression-regression sequences preceding the final retreat of the Tarim sea (Bosboom et al., 2011). Note that the marine Bashibulake Formation, which overlies the Wulagen Formation in north-western Tarim, is not present in this area (Bosboom et al., 2011). Continental deposits overlie the Wulagen Formation in the Aertashi section. Some authors name these oldest continental deposits in the Aertashi section the Bashibulake Formation (Zheng et al., 2015a), while others name these rocks the Keziluoyi Formation (Bosboom et al., 2011). Following the stratigraphy of Zheng et al. (2015a), these sediments are overlain by thickly-bedded red sandstones and mudstones of the Oligocene to Lower Miocene continental Wuqia Group comprising the Keziluoyi, Anjuan and Pakabulake formations. These formations are interpreted to be composed of fluvial, lacustrine and delta facies. Overlying the Wuqia Group, Zheng et al. (2015a) describe thin conglomeratic deposits with sandstone and siltstone layers of the Artushi Formation as representing distal alluvial fan and fluvial deposits respectively. An abrupt change in lithofacies is recorded in the overlying Xiyu Formation containing massive cobble conglomerates interpreted to be proximal alluvial fan deposits (Zheng et al., 2015a).

Previous work conducted by (Bosboom et al., 2011, 2014c) on the lower part of the Aertashi section and Zheng et al. (2015a) for the Wuqia Group and Artushi and Xiyu formations provided a revised magnetostratigraphic timeline for the section (Figure 4.2), which supersedes lower resolution work conducted by Yin et al. (2002). The final marine regression in this section is dated as middle Eocene (Bosboom et al., 2011, 2014c), with the onset of continental deposition from ~41 Ma onward. The updated chronology provided by Zheng et al. (2015a) revises the age of the uppermost Artushi Formation as 15 Ma. The overlying Xiyu Formation was not magnetostratigraphically dated, but a new maximum constraint to its age is derived from our new detrital zircon U-Pb ages of 14 Ma from samples near the base of the Xiyu Formation (Section 4.6.4). Accordingly, the prominent onset of coarse conglomerates of the Xiyu Formation previously estimated at ca. 24 Ma by Yin et al. (2002), is now revised to be <14 Ma. Further age constraint within the Xiyu Formation is provided by a disputed ash layer in which the youngest populations of

biotites and zircons were dated at 11 Ma. This dates this horizon as either 11 Ma or <11 Ma depending on whether the horizon is interpreted as an ash layer (Zheng et al., 2015a, 2015b) or a heterolithic sediment layer (Sun et al., 2015). Although the exact outcrop location was not published by the original authors, we estimated, based on succession thickness, that our uppermost sample lies above this layer and is also therefore younger than 11 Ma. While we utilise the more conservative "younger than" 11 Ma age for our uppermost sample throughout our interpretations, we do note the presence of fresh volcanic detritus in this sample (Section 4.6.2). This indicated that the presence of penecontemporaneous volcanics in the vicinity could support the proposal of an ash layer temporally and spatially close by, in agreement with the report of 10-12 Ma granite-syenite intrusions near Tashgorgan (Jiang et al., 2012, Robinson et al., 2007).

Yin et al. (2002) conducted petrographic analysis of the Wuqia Group in Aertashi. Overall they recorded the section as mainly composed of feldspatho-litho-quartzose sandstones, dominated by monocrystalline quartz grains. They concluded that the Oligocene sandstones at Aertashi are similar to those of Middle Jurassic to Paleogene strata studied in Aertashi by Sobel (1999). From this similarity they interpreted that the source region has not changed substantially since the Middle Jurassic. They interpreted significant changes observed above their measured section to indicate the initiation of a new thrust fault in the foreland after ~24 Ma. However, the revised chronology of this section indicates that this event likely occurred after ~14 Ma.

Palaeoflow data based on flute casts (Bosboom et al., 2014c), and imbrication and ripples (Zheng et al., 2010) indicate that flow was consistently from the south throughout the Eocene–Miocene with the exception of the upper Wuqia Group where a change is recorded to flow from the west to northwest. However the latter data set are based on cross-bed foreset orientations, which when not taken in 3D can provide only apparent directions; this change in palaeocurrent direction was not observed in our data from this section, presented in section 4.6.1.

4.5 Approach, sampling and methods

4.5.1 Sampling

Characterisation of the terranes which may have sourced the Aertashi section, namely the WKL, North, Central and South Pamir, and comparison of that signature with the

rocks of the Aertashi section, is key to our provenance study. We undertook U-Pb analyses on detrital zircons from modern river sediments draining these terranes, in order to characterise their signature (see Figure 4.1 and text in Appendix 7 in the supporting information). The use of modern river sands for terrane characterisation is preferable to using bedrock samples, as it provides a more representative average of a larger area. Rivers draining the Central Pamir were not easily accessible in China, and for this terrane we therefore used published data from the western (Tajik) Pamir (Lukens et al., 2012), to characterise the source.

We collected samples from each unit in the Aertashi section, as identified by Zheng et al. (2015a), and constructed a detailed sedimentary log (Figure 4.2c). By comparison with the equivalent log from Zheng et al. (2015a) (Figure 4.2a), we were able to extrapolate the depositional ages of the Aertashi rocks. We were aided in this task by a) the fact that, unsurprisingly, the main provenance changes we see at Aertashi occur at intervals where clear facies changes occur (e.g., the onset of conglomerate stringers), making it easy to accurately correlate times of provenance change to Zheng et al. (2015a) ages on their log, and b) our own paleomagnetic data (Chapter 5), which agree with that of Zheng et al. (2015a). The Xiyu conglomerates were not subject to magnetostratigraphic analysis in either Zheng et al. (2015a) or our studies. The top of the underlying unit is dated at 15 Ma by the magnetostratigraphy and our sample from the base of the Xiyu conglomerates yielded zircons of 14 Ma U-Pb age, thus providing a maximum age constraint. Although Zheng et al. (2015a) did not provide location coordinates for their 11 Ma / <11 Ma disputed ash layer (see Section 4.4), it is located at ~2300 m stratigraphic height above the base of the conglomerates. Our uppermost Xiyu sample (above our logged section) is located at ~3000 m stratigraphic height above the base of the conglomerates (as estimated approximately from application of trigonometry to dip data), and therefore our uppermost sample is constrained at <11 Ma depositional age. All sample locations are given in Appendix 1 and 2.

By comparing our modern river U-Pb zircon data, representing the source region signatures, with the signature from Aertashi rocks, we identified the provenance and changes up section, aided by additional information, such as palaeocurrent data, Sm-Nd bulk geochemistry data, petrography, and heavy-mineral data. We also took two samples from the Yarkand River to provide the signature of the modern day Aertashi setting. Zircon fission track data were used to assess exhumation patterns, but

unfortunately only the Keziluoyi Formation, Xiyu Formation and Yarkand River sand yielded usable data, due to grain size issues. We double-dated these samples with U-Pb analyses to extract maximum provenance information. Analyses were carried out at a number of labs, and full methodologies are given in Appendix 7 in the supporting information.

4.5.2 Petrography and heavy mineral analyses.

Twelve bedrock samples from the Aertashi section and two modern river sands from the Yarkand River along with a single sample from a river draining the Muztagh Ata dome were analysed. Petrographic analysis involved the counting of 400 points per sample following the Gazzi-Dickinson method (Ingersoll et al., 1984). Heavy-mineral analysis involved the counting of 200 points of 63-355 μm size fraction transparent heavy minerals, obtained by dry sieving and heavy liquid separation. All analyses were carried out at the University of Milano-Bicocca, Italy; full methodologies are given in Appendix 7, and full data sets are given in Appendix 8.

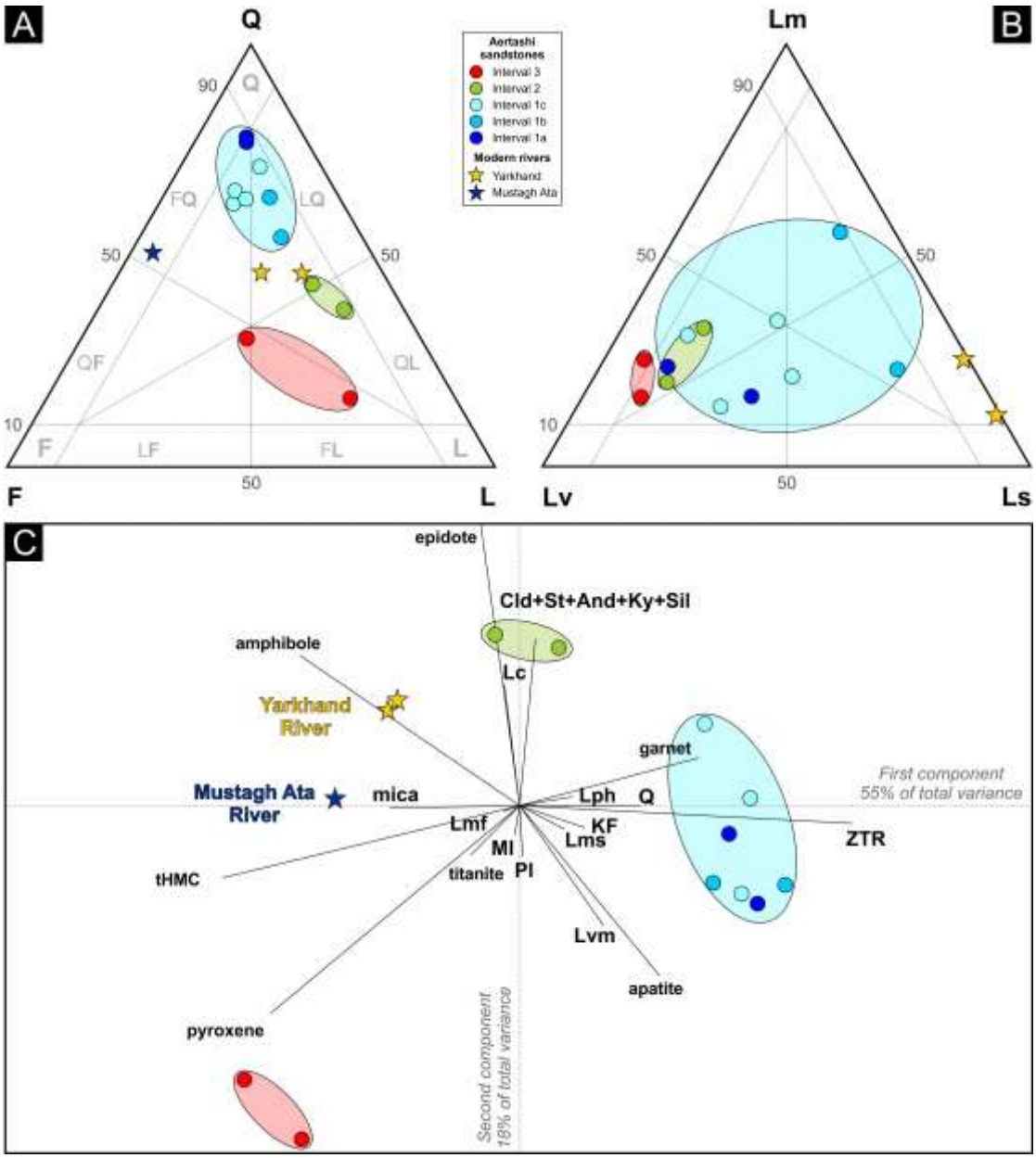

Figure 4.3 Petrography and heavy minerals in Aertashi sandstones and modern rivers draining the Pamir. (a) QFL plot (fields after Garzanti, [2015]). (b) Lithic plot; (c) Compositional biplot including all major petrographic and heavy-mineral parameters. In the biplot [Gabriel, 1971], the length of each ray is proportional to the variance of the corresponding element in the data set. If the angle between two rays is close to 0°, 90°, or 180°, then the corresponding elements are directly correlated, uncorrelated, or inversely correlated, respectively. Note sharp petrographic changes upsection, at ≤14 Ma and <11 Ma. None of the Aertashi sandstones compare well with modern Yarkand River sands. Q= quartz; F= feldspars (KF= K-feldspar; Pl= plagioclase); L= lithic fragments (Lv= volcanic; Ls= sedimentary; Lm= metamorphic; Lvm= volcanic, metavolcanic and metabasite; Lc= carbonate; Lph= pelite and chert; Lms= low-rank metasedimentary; Lmf= high-rank felsic). MI= metamorphic index [Garzanti and Vezzoli, 2003]. tHMC= transparent heavy-mineral concentration [Garzanti and Andò, 2007]; ZTR= zircon + tourmaline + rutile; Cld= chloritoid; St= staurolite; And= andalusite; Ky= kyanite; Sil= sillimanite.

4.5.3 Sm-Nd bulk analyses

Eleven mudstones from the Aertashi section and 6 modern river muds from the Yarkand, Muji, Tashkorgan, Muztagh Ata, Karakash and Tiznip Rivers were powdered in an agate ball mill. They were then leached in dilute acetic acid to remove carbonate before spiking with ^{149}Sm-^{150}Nd isotope tracers, followed by dissolution and column chemistry following the method of Makishima and Nakamura (1997). Analyses were carried out on a Thermo Scientific Triton mass spectrometer at the Natural Environment Research Council (NERC) Isotope Geoscience Laboratories. Nd isotope data are normalised to ^{146}Nd/^{144}Nd = 0.7219. Fifteen analyses of the JND-I standard gave a value of 0.512106 ± 0.000005 (9.1 ppm, 1 sigma). All other standard and sample data are quoted relative to a value of 0.512115 for this standard. Seven analyses of La Jolla gave 0.511864 ± 0.000006 (11.5 ppm, 1 sigma). Full methodologies are given in Appendix 7; full datasets are given in Appendix 6

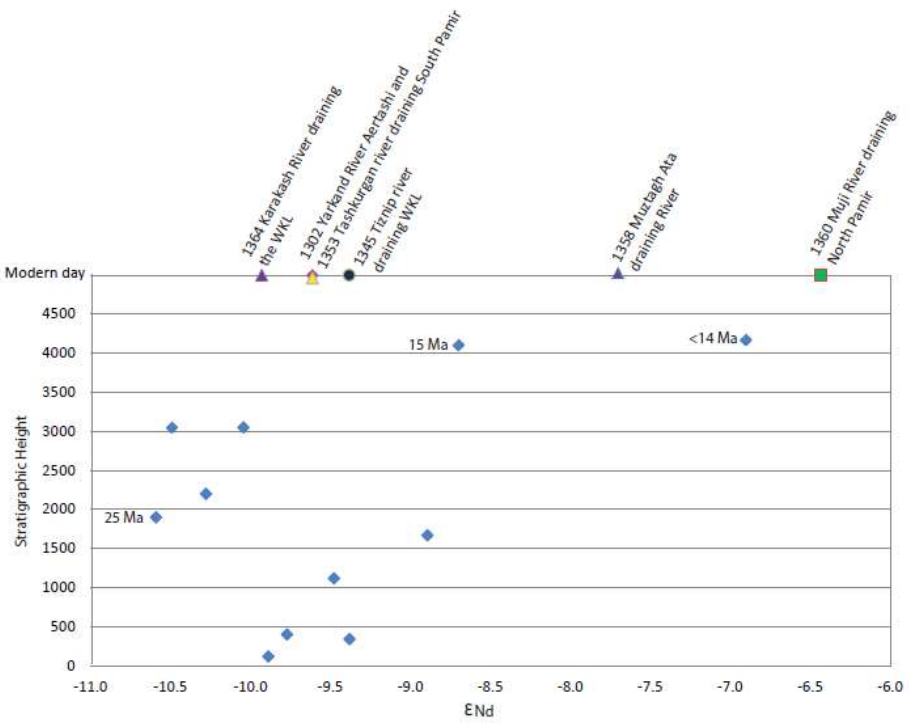

Figure 4.4 εNd bulk geochemistry data for modern river sediments draining the Yarkand River at Aertashi, the Karakash and Tiznip Rivers draining the WKL, the Muji river draining the North Pamir, a Muztagh Ata draining river and the Tashkurgan River draining the South Pamir, and from the Aertashi section, sedimentary rocks with ages in Ma for key units taken from Zheng et al. (2015a). This plot highlights two key shifts, (1) at approximately 25 Ma, corresponding to the onset of a change in facies with thin conglomerate stringers, and (2) a second shift at ≤14 Ma, corresponding to the onset of the major conglomeratic unit.

4.5.4 Zircon U-Pb and fission track analyses.

Eight modern river sands draining the North Pamir, South Pamir, Muztagh Ata drainage and WKL, and eleven rocks from the Aertashi section were used for detrital zircon U-Pb analyses. Three of the samples on which detrital zircon U–Pb analyses were undertaken were also analysed for zircon fission track analysis, all other samples having zircons unsuitable for fission track analyses due either to low yield or small grain size. Detrital zircon separation was performed following standard protocols. Heavy-mineral concentrates rich in zircon were mounted in araldite and polished for U-Pb analyses by laser ablation-inductively coupled plasma-mass spectrometry (ICP-MS). Handpicking was avoided as this can introduce bias. Zircons for ablation were selected independent of grain size by systematically scanning the grain mount. Samples for fission track analysis were selected on the basis of zircon abundance and an adequate mean grain size. Multiple Teflon grain mounts were made to enable different etch times to capture grains of different age and/or uranium concentrations. Zircon U-Pb analyses and fission track analyses were undertaken by using the London Geochronology Centre facilities at University College London. U-Pb analyses, both for single-dated zircons and zircons doubled dated with fission track were conducted by using a New Wave 193 nm excimer laser ablation system coupled to an Agilent 7700x quadrupole-based ICP-MS. Full analytical methods can be found in the Appendix 7 datasets, and more detailed descriptions of the zircon characteristics are provided in Appendix 7.

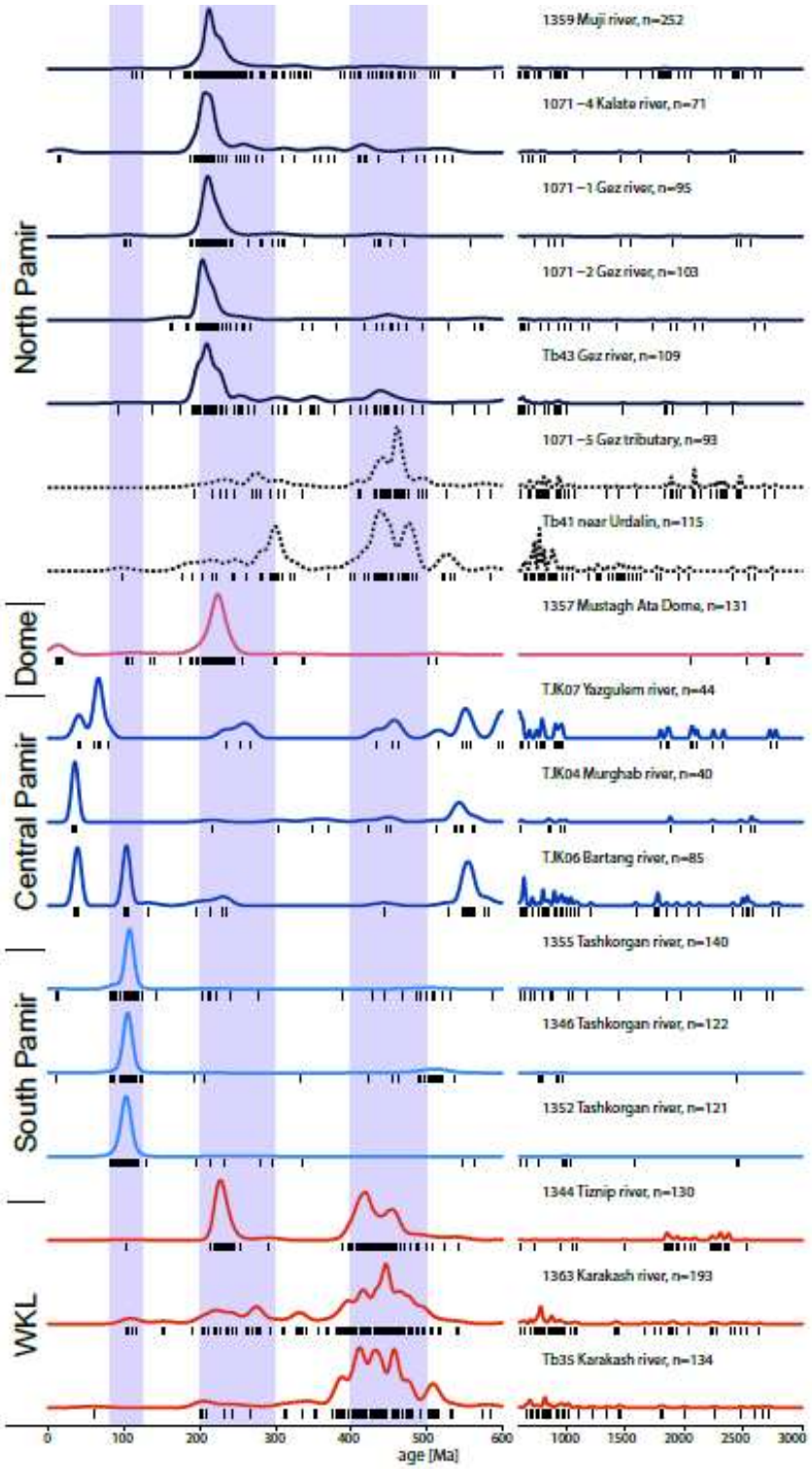

Figure 4.5 Characterisation of Pamir and WKL terrains. Normalised kernel density plots for U-Pb detrital zircon data from modern rivers draining the WKL, South, Central and North Pamir. Data are from this study except where noted (samples prefixed Tb are from Rittner et al. [2016], prefix 1071 are from Carrapa et al. [2014] and TJK are from Lukens et al. [2012]. TJK06, drains both Central and Southern Pamir. The dotted plots relate to small tributaries rather than major drainages, which may not be representative of the terrain as a whole. ~The 206/238 ages from Lukens et al. [2012] are taken for <1100 Ma, and for Carrapa et al. [2014] their "best age" is plotted. The shaded bars highlight the ~400-500 Ma and ~200-300 Ma peaks, typical of WKL provenance, and 100 Ma the peak typical of South Pamir provenance. The colour coded KDE lines reflect the different tectonic terrains.

4.6 Results

4.6.1 Sedimentology and palaeocurrent data.

Our sedimentological log recording conglomerates, sandstones and mudstones (Figure 4.2) shows the close correlation of our facies with that of Zheng et al. (2015a), as described in section 4.5. Particularly useful for correlation was the unit of thin beds of conglomeratic stringers at 2050-2700 m up-section, and the onset of the major conglomeratic unit at 4050 m up-section. Clasts in the lower, thin conglomerate stringer facies are up to 5 cm in diameter, and of predominantly sedimentary origin, with a few isolated limestone clasts at the base of the unit which are up to 50 cm diameter. Basement and volcanic clasts were recorded in the upper, major conglomeratic unit, clasts of which were up to 30 cm diameter. We were unable to replicate the palaeocurrent data previously recorded by Zheng et al. (2010), as described in section 4.5. Reliable palaeocurrent indicators, predominantly flute marks, were measured throughout the section up to the base of the Xiyu conglomerates and have been restored to account for tectonic rotation in accord with the work of Bosboom et al. (2014b) and Chapter 5. Bosboom et al. (2014b) recorded clockwise rotations of 21.6±4.2° in 41 to 36 Ma strata for the Aertashi section and 17.1±6.5° rotation recorded in 33 to 28 Ma strata Chapter 5 of this study recorded a 15° ± 4.3° clockwise rotation in 27-15 Ma strata. A consistent NW directed palaeoflow is recorded throughout (Figure 4.2).

4.6.2 Petrography and heavy mineral data.

The Aertashi succession displays a very sharp compositional trend from base to top. Quartz decreases progressively up-section while, conversely, feldspars, rock fragments, micas and heavy minerals all progressively increase. Selective diagenetic dissolution of the least chemically stable minerals partly contributed to this trend. Deep corrosion features and even skeletal outlines (Andò et al., 2012) were observed on garnets, staurolite and epidote. The transparent heavy-mineral concentration (tHMC); (Garzanti and Andò, 2007) increases up-section by nearly 2 orders of magnitude, and the proportion of stable heavy minerals zircon, tourmaline, and rutile (ZTR index) (Hubert, 1962) correspondingly decreases. Nevertheless, provenance signals are very clearly preserved (Figure 4.3).

From the base of the section until 15 Ma (petrologic intervals 1a-1c), rocks include litho-feldspatho-quartzose to feldspatho-litho-quartzose sandstones, yielding extremely low heavy-mineral assemblages including tourmaline, apatite, garnet, zircon and rutile. Provenance trends are subtle in this lower part of the succession most affected by diagenetic dissolution. Petrologic interval 1c sandstones (i.e., from ~25 Ma, just below the lower conglomerate "stringers") become more enriched in phyllite, schist, metasandstone and dravitic tourmaline grains relative to the petrologic intervals 1a and 1b below, suggesting increasing supply from very low grade to low-grade metasedimentary rocks. An abrupt provenance change is documented in petrologic interval 2 (≤14 Ma, at the start of the major conglomerates), with a marked increase in very low to low-grade felsic to mafic metavolcanic rock fragments and epidote-dominated heavy-mineral suites. Such a metavolcanic source was also present but much less prominent during the deposition of the underlying rocks, as testified by the constant presence of a few metavolcanic grains although epidote has been largely dissolved. Stratigraphically higher up the conglomeratic unit (petrologic interval 3, <11 Ma), significant input from penecontemporaneous volcanic sources are documented by quartzo-feldspato-lithic to quartzo-litho-feldspathic sandstones with mafic to intermediate volcanic rock fragments and frequently zoned plagioclase. Commonly fresh zoned green augitic clinopyroxene represents nearly a third of the sand fraction and is associated with apatite and minor titanite, hornblende, and oxy-hornblende.

Comparison with modern fluvial sands yields a poor match. Evidence of erosion from the hinterland gneiss domes was not recorded in any of the Aertashi sandstones, which are sharply distinct from the feldspatho-quartzose sand, with abundant granitoid rock fragments and rich hornblende-dominated suites, carried by the modern river draining Muztagh Ata. The Yarkand modern river sand also bears little similarity to any of the Aertashi section sandstones, having much more abundant carbonate rock fragments and no volcanic or metavolcanic rock fragments. Quartz is much more abundant in the Yarkand River samples compared to petrologic interval 3 and much less abundant than in petrologic intervals 1a-1c. Feldspars and metamorphic indices (Garzanti and Vezzoli, 2003) tend to be higher in the Yarkand River sand, indicating a different source area and erosion of a deeper tectono-stratigraphic level compared to Aertashi sandstones

4.6.3 Sm-Nd data.

Previous works on Sm-Nd for the Pamir and WKL are limited (Robinson et al., 2012, Schwab et al., 2004). Therefore, we analysed modern muds from rivers draining the North, Central and South Pamir, and WKL in order to gain a better averaged characteristic signature for these terranes (Figure 4.4) which is used to interpret our data from the Aertashi sedimentary section.

In the Aertashi section, the times of provenance change seen in the petrographic data, as described above, are mirrored by the Sm-Nd data. A shift to more negative, crustal, εNd values is seen just below the onset of the unit containing thin conglomeratic stringers at ~25 Ma, synchronous with the petrographic record of greater input from very low grade and low-grade metamorphic rocks. A second major shift, to more juvenile, less negative values, is seen at ≤14 Ma, synchronous with the petrographic change to a major increase in felsic and mafic metavolcanics at this time. Fine-grained material was not present higher up the succession, and therefore the still later petrographic addition of substantial fresh volcanic input was not recordable by our Sm-Nd bulk analyses. Similar to the petrographic signal, the modern Yarkand River displays an εNd value very different from that of the rocks at ≤14 Ma.

4.6.4 Zircon U-Pb data.

4.6.4.1. Source terrains:

The North, Central, South Pamir and WKL each have characteristic signatures as illustrated in Figure 4.5 (see also Supplementary Item 5). We were not able to access modern rivers draining the Central Pamir in China. Published data only are available from the western Central Pamir, draining west in Tajikistan, from catchments principally draining the gneiss domes (Lukens et al., 2012); these may not be representative of the eastern regions.

The North Pamir is considered to be the along strike equivalent to the WKL, the WKL being composed of both the North/South Kunlun terranes (e.g. Burtman and Molnar, 1993) and Songpan-Ganzi terrane (Schwab et al., 2004). Therefore, unsurprisingly, the zircon spectra of some rocks from the North Pamir and WKL, when looking at, for example, Mesozoic metasedimentary rocks, can be very similar (for example, compare spectra in Figure 5 of Robinson et al. (2012) for the North Pamir with the

Songpan-Ganzi data of Ding et al. (2013), compiled in Figure 7 of Cao et al. (2015)). However, there is considerable along-strike variation; in particular, the Palaeozoic igneous rocks that are prevalent in the South Kunlun and Pamir Kunlun of the WKL are sparse in the North Pamir (Figure 4.1b). Instead, the North Pamir are dominated by Triassic igneous and metasedimentary lithologies, as already noted by Robinson et al. (2012). This along-strike variation expresses itself in differences in the zircon spectra of modern river sediments draining the two regions, since modern river sediments from large catchments better depict the average signature of a terrane compared to individual bedrock samples. In Figure 4.5, it can be seen that the WKL, unlike the Pamir terranes, has a very distinctive and characteristic "double peak" of U-Pb zircon ages, at ~200-300 Ma and 400-500 Ma, a subordinate peak at ~800 Ma, and an appreciable population at >1800 Ma. Our modern river data from the North Pamir, and published modern river data from Carrapa et al. (2014) and Rittner et al. (2016) (Figure 4.5) show that the significant populations aged ~400-500 Ma, 800 Ma and >1800 Ma in the WKL are much less prevalent in the North Pamir. Instead, in the North Pamir, the 200-300 Ma peak dominates, consistent with the igneous outcrop pattern (Figure 4.1b). A Triassic 200-300 Ma peak also dominates our modern river sample draining the Muztagh Ata Dome, along with an appreciable ~15 Ma peak.

The only available data from the Central Pamir are from Lukens et al. (2012); these are from river samples draining west which may not be applicable for comparison with sediment deposited in the Tarim Basin. Note that one of the samples (TJK06) is from a river that drains both South and Central Pamir, and therefore is of mixed provenance. Samples are characterised by a zircon peak at ~500-600 Ma, as well as the presence of Paleogene grains. The South Pamir is dominated by an ~100 Ma peak, reflecting grains sourced from batholiths of this age which dominate this unit (Robinson et al., 2012).

4.6.4.2 Aertashi Sedimentary Section Data

Detrital zircon data from the Aertashi section can be compared to the modern river potential source signatures (compare Figures 4.5 and 4.6). In comparison with the modern river data, key points to note in the Aertashi rocks follows:

1. The >1800 Ma population and the 200-300 Ma and 400-500 Ma double peak, characteristic of the WKL (see Figures 4.5, and section above) are well

represented in the lower part of the Aertashi section. However, two changes occur upsection. First, the >1800 Ma population, although prevalent in the lowest samples at Aertashi, decreases in prominence upsection by ~29-27 Ma. Second, the distinctive 200-300 Ma and 400-500 Ma "double peak" is characteristic of the Aertashi rocks until 15 Ma, after which time the 400-500 Ma peak becomes considerably less prominent.

2. The ~100 Ma peak seen in the South Pamir and Yarkand Rivers, is recorded in the Aertashi detritus by sparse ~100 Ma grains in the <11 Ma sample.
3. The Aertashi rocks contain uncommon Paleogene aged grains in the section until 26 Ma, and then again in samples dated 15 Ma and ≤14 Ma. Grains of such age are not recorded in any of the modern river samples draining to the Tarim Basin, bar one grain in a Kunlun modern river sample from Rittner et al. (2016). However, grains of such age are recorded in the west draining Central Pamir Rivers (Lukens et al., 2012; Figure 4.5) .
4. The 15 Ma zircon peak that is prevalent in the modern Muztagata drainage, is represented by a few grains, in the <11 Ma sample in the Aertashi section.
5. The modern Yarkand River shows elements of similarity with the WKL (400-500 Ma peak), South Pamir (100 Ma peak), and the Cenozoic domes (Neogene grains).

To gain a more robust comparison of the zircon U-Pb age spectra, the data were plotted as a Multidimensional Scaling (MDS) Map (Figure 4.7), which is a configuration of points based on calculated Kolmogorov-Smirnov distances between age spectra (Vermeesch, 2013). Points to note are that the Aertashi rocks >14 Ma plot in close correspondence to rivers from the WKL. Data from Aertashi samples <14 Ma and younger are displaced from the WKL pole toward the rivers of the North Pamir. The modern Yarkand River today drains upland regions of the WKL, North Pamir, South Pamir and gneiss domes, reflected in its position on the plot.

4.6.5 Zircon fission track data, double dated with U-Pb ages.

Data are presented in Figure 4.8 and Appendix 9, 10 and 11. The majority of our samples were not suitable for zircon fission track (ZFT) dating due to their small grain size. About 60% of grains from the Yarkand River sample have Cenozoic ZFT ages. Double dating shows that some of the Cretaceous population and a minority of the Cenozoic grains are of volcanic or shallow intrusive origin, as indicated by their U-Pb

age and ZFT age overlapping within error. By contrast, the grains from the samples collected from the Xiyu conglomerate (≤14 Ma) and from near the base of our studied section (~37 Ma) are near-exclusively (bar one grain in the Xiyu Formation) pre-Cenozoic in age, with double dating indicating that the ages are exhumational rather than magmatic.

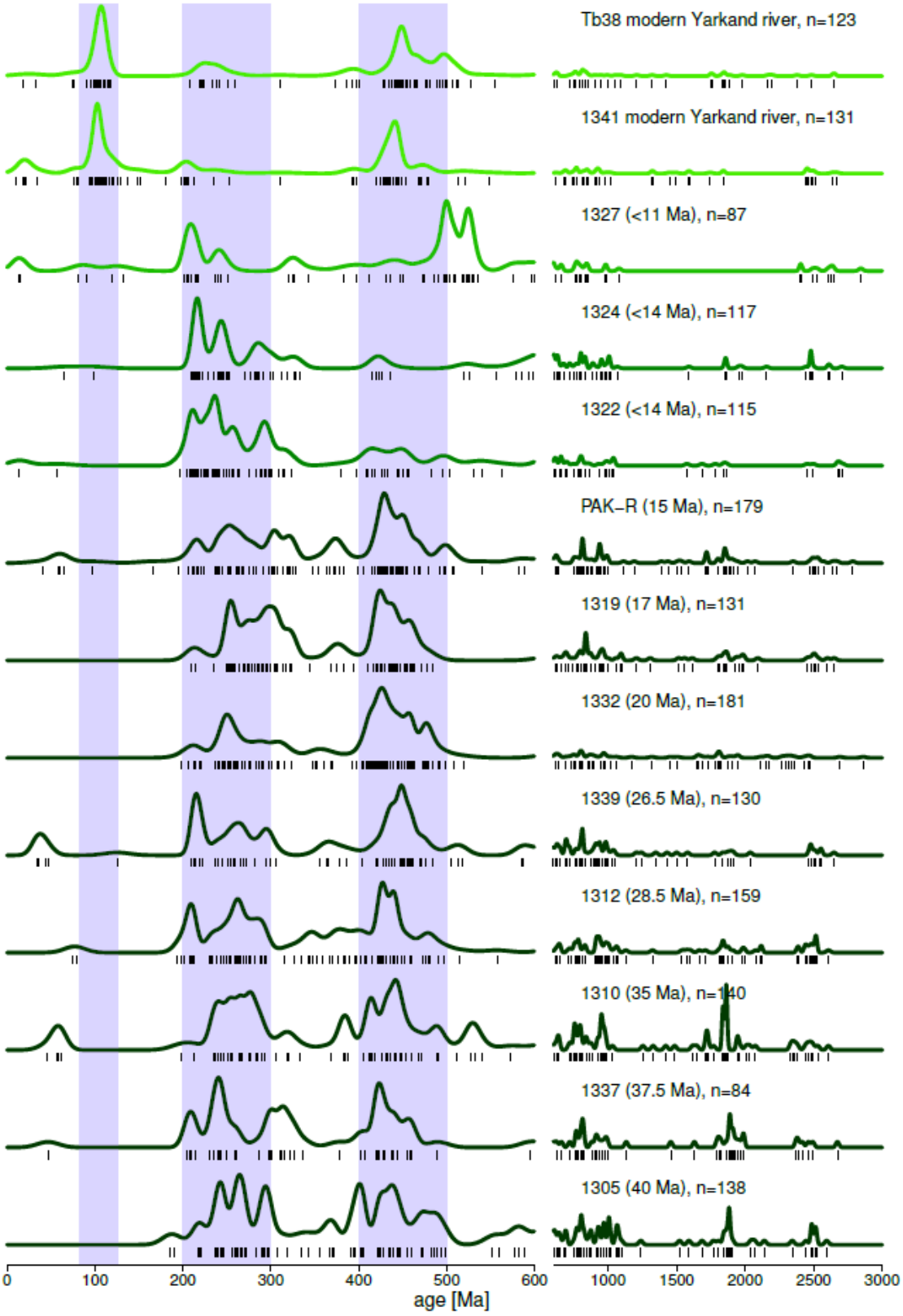

Figure 4.6 U-Pb detrital zircon data shown as normalised kernel density plots for rocks from the Aertashi section. The shaded bars represent the populations diagnostic of WKL provenance (200-300 Ma and 400-500 Ma), with the 100 Ma bar typical of South Pamir provenance. Ma in brackets provides the depositional age of the sample. The colour coded KDE plots relate to samples of similar provenance.

4.6.7 Summary of provenance changes

- A subtle shift in provenance is detected at ~25 Ma, just below the start of the lower conglomerate stringers. This is evidenced by a declining importance of the >1800 Ma zircon population, a shift to more negative εNd values, and a subtle petrographic/mineralogical shift to greater input from very low grade / low-grade metamorphic sources. Paleogene grains appear to become less prominent, but the low numbers of such grains throughout the section in total make such an assessment tentative.
- At ≤14 Ma, at the start of the major conglomeratic unit, there is a drastic change in provenance. There is a shift in εNd signature to more juvenile values, petrography and heavy minerals show an increase in input from metavolcanic rocks, and the 400-500 Ma zircon population loses its prevalence. The MDS plot shows the poles starting to pull toward the North Pamir, although there is still considerable similarity with the WKL.
- At <11 Ma, petrography and heavy minerals show dominant influx from a penecontemporaneous volcanic unit. The sample at <11 Ma shows an increased resemblance to the modern Yarkand River, in terms of the first sparse occurrence of Cretaceous aged zircons, yet the petrography remains distinct.

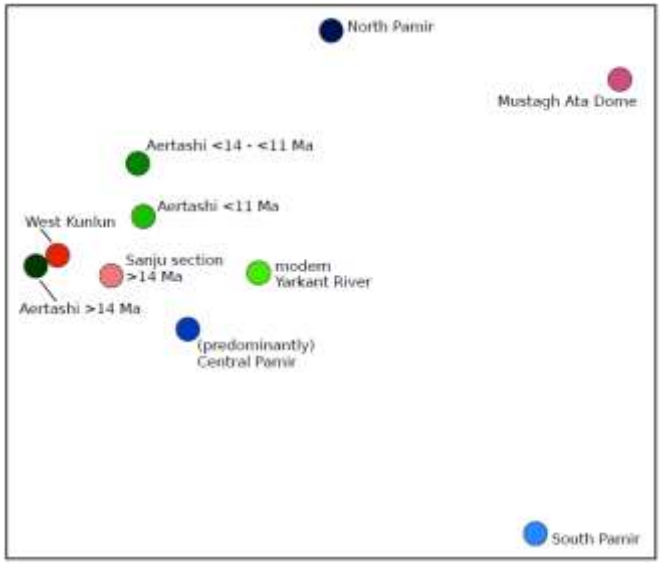

Figure 4.7 A multidimensional scaling map (Vermeesch, 2013) displays the similarities/dissimilarities between the individual sample age spectra. Aertashi at >14 Ma and WKL samples plot together because they have similar age distributions. Aertashi samples at ≤14 Ma and younger, pull away from the WKL pole, toward the North Pamir, indicating additional contribution from this region at this time.

4.7 Interpretations

4.7.1 Pre-Cenozoic and early Cenozoic times

We interpret our oldest samples (from 40 Ma) as southerly-derived, deposited by rivers draining the WKL, based on the combination of the palaeocurrent data, and the presence of the distinctive ~200-300 Ma and 400-500 Ma double peak and conspicuous ~ 800 Ma and >1800 Ma populations in these rocks. While, as noted in section 6.4.1, such zircon age spectra can be found in individual metasedimentary bedrocks from both the North Pamir and WKL, the spectrum is typical of the larger "averaged" drainage basins of the WKL but dissimilar to that of the North Pamir (Figures 4.5 and 4.9).

This southerly sourced interpretation is consistent with the fact that the U-Pb age spectrum for these samples is very similar to that of the southerly derived detritus from the coeval Sanju section (Figure 4.9). This section is located on the southern fringe of the Tarim Basin (Figure 4.1), distant from the Pamir to the west, and is thus clearly southern (WKL) rather than western (Pamir) derived, as also evidenced by palaeocurrent data (Section 4.3.3). The provenance of Sanju has previously been compared to a southern WKL source (the Songpan-Ganzi section 4.3.3) with which it correlates very well (Cao et al., 2015; their figure 7).

The source of the Paleogene grains remains unresolved. Although Sun et al. (2016b) ascribe such grains in the Oytag section to derivation from the Kohistan island arc and Karakoram, we note that similar aged grains are found in the Miocene Sanju section which is far removed from the Kohistan island arc. Bershaw et al. (2012) suggested that the source of the Paleogene grains lay in the Central/South Pamir (Section 4.3.1). This is an attractive idea in view of the documentation of such grains in the western part of the Central Pamir by Lukens et al. (2012), section 4.6.4.1 and Figure 4.5), and documentation of igneous rocks of suitable age in the Central Pamir by Budanov et al. (1999) and Ratschbacher (unpublished data) as quoted in Bershaw et al. (2012). Similar aged igneous bodies are recorded in the northern part of the Qiangtang terrane (Long et al., 2015) which is potentially correlated with the Central Pamir (Cowgill, 2010, Robinson et al., 2012, Schwab et al., 2004). Such a source would be more suitable than a Kohistan arc source for the southerly derived grains of the Sanju section, since the Qiangtang terrane, or its correlatives, lies south of the WKL (Figure

4.1a) and in some correlations the Central Pamir is correlated with the Songpan-Ganzi of the WKL (see Cowgill (2010) and references therein). This would be consistent with the suggestion of Cao et al. (2015) that such grains in the Kekeya and Sanju sections (deposited <25 Ma) are derived from regions to the south which are currently incompletely characterised (Section 4.3.3). A single Paleogene grain has been recorded by Rittner et al. (2016) in a modern river sediment draining the WKL (Tb35), but more data would be required before such a source could be robustly confirmed in the region.

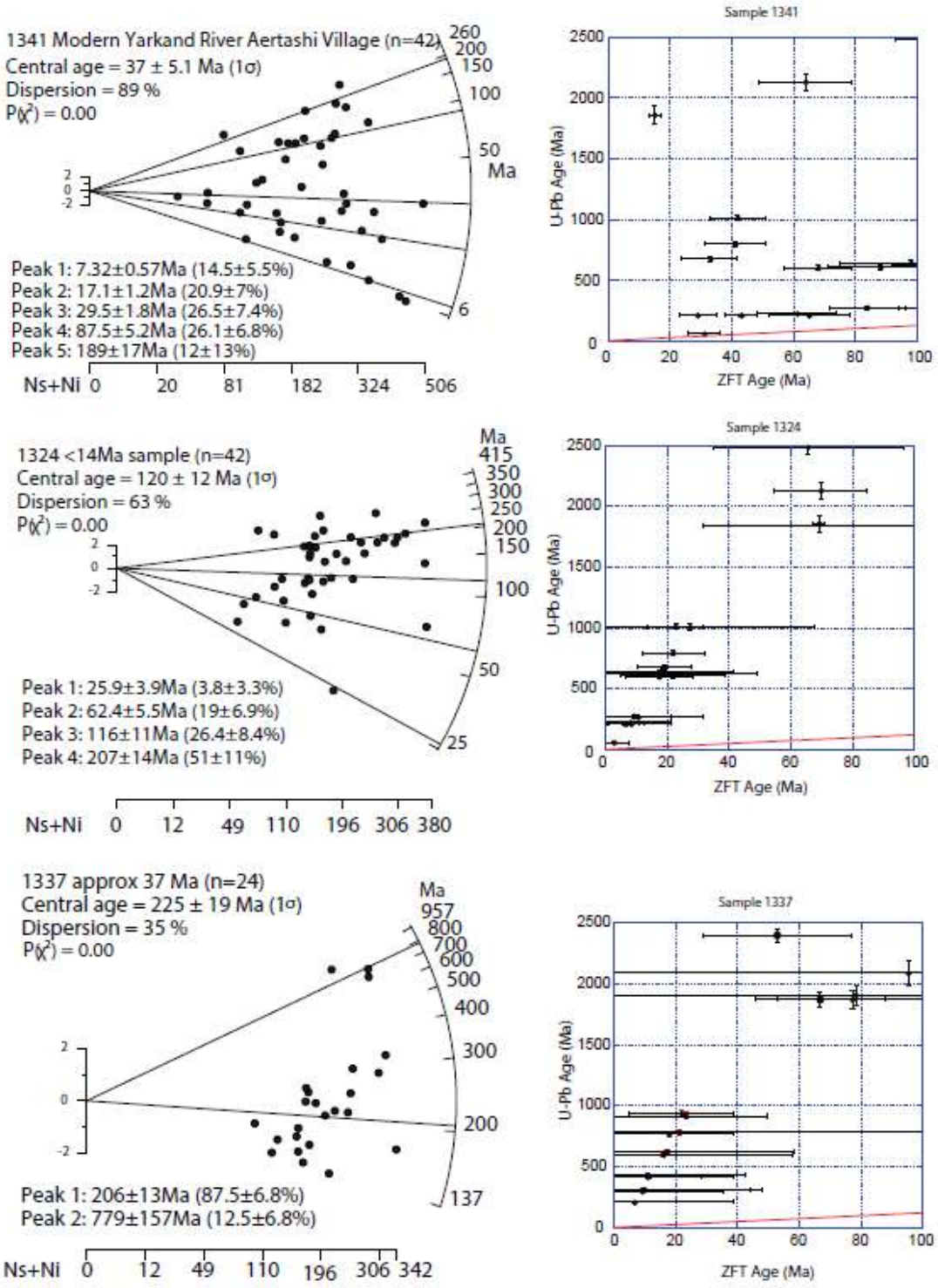

Figure 4.8 Zircon fission track radial plots and ZFT-U-Pb age double dating plots for zircons from the Aertashi section rocks and from the modern Yarkand River at Aertashi.

The prominent ZFT population with exhumational ages of ~200 Ma is similar to that recorded in Cenozoic sedimentary sections along the southern margin of the Tarim Basin at Sanju and Kekeya, and like Cao et al. (2015) we interpret the northern margin of Tibet to have been an emergent exhuming area at ~200 Ma, subsequent to subduction and closure of the palaeo-Tethys which was occurring at this time (Cao et al., 2013, Liu et al., 2015, Zhang et al., 2015, Pullen et al., 2008, Meng and Zhang, 1999).

The ZFT data for the sample deposited at ~37 Ma show only pre-Cenozoic ages. This indicates that rocks of this age do not show any evidence for source region exhumation sufficient to exhume rocks from depths below the zircon partial annealing zone to surface. This is consistent with the conclusion of Cao et al. (2015) from their much more extensive ZFT data set. Apatite fission track (AFT) data from similar-aged strata at Aertashi also show old, albeit partially reset, AFT ages (Sobel and Dumitru, 1997), confirming the lack of evidence for strong exhumation in the source area at this time.

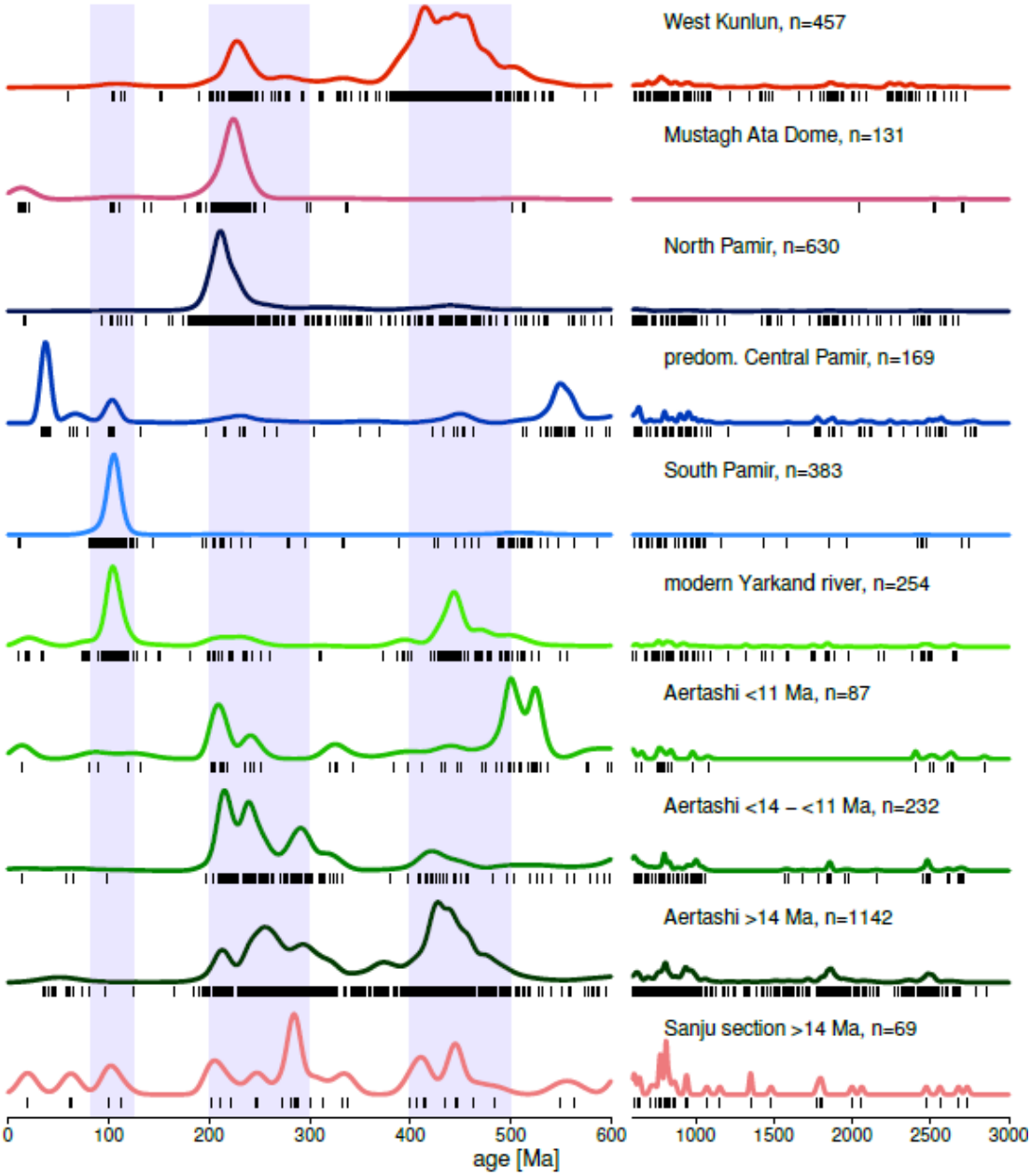

Figure 4.9 A summary of U-Pb KDE plots for Aertashi divided into age bins of documented provenance change, compared to data from the Sanju sedimentary section and pooled data from the various source regions (WKL, North, South, Central Pamir and gneiss domes). The colour scheme aligns with Figs 5 and 6.

4.7.2 Late Oligocene (~25Ma)

The provenance shift occurring at ~25 Ma, just below the facies change recorded by the lower conglomerate stringers, is subtle; the dominant signature remains that of the WKL regions to the south, as evidenced by the zircon U-Pb data (Figures 4.7 and 4.9) and palaeocurrents (Figure 4.2). The shift is recorded most clearly in the move to more negative εNd bulk rock values but is also reflected in the increasing input of very low grade and low-grade metamorphic detritus, decreasing prominence of the >1800 Ma zircon population, and perhaps a reduction of the Paleogene zircon population (2 samples contain no Paleogene grains, but the youngest sample in the interval before the next provenance change, at 15 Ma, again contains these uncommon grains). The disappearance of the Paleogene zircon population also occurred in the Oytag section around this time, but not in the Sanju and Kekeya sections where grains of such age continue to be recorded up-section (Section 4.6.4). A provenance change is also recorded by changing Sm-Nd bulk rock data and petrography in the Oytag section around this time (Section 4.3.1).

This period is proposed to be the time of initiation of the bounding faults along the Kunlun's northern margin, with movement of the KYTS and Tiklik faults (Section 4.2.2) and consequent basinward expansion of the northern margin of Tibet and initiation of indentation of the Pamir salient. We propose that changes in the provenance signature at both Oytag and Aertashi reflect this tectonism. Uplift of the North and South Kunlun may have progressively, but not completely cut off the more southerly, Palaeogene zircon bearing, source of the Songpan-Ganzi/Central Pamir terranes. A greater effect of the uplift of these terranes may have been felt farther west, closer to the Pamir salient, as reflected in the elimination (at Oytag) and reduction (at Aertashi) of the Palaeogene zircon population in the more western areas only. Proximity to the now moving KYTS may also explain the more proximal conglomerate stringer facies observed at Aertashi at this time.

4.7.3 After the Early–Mid-Miocene (≤ 14 Ma)

At ≤14 Ma, the ~400-500 Ma U-Pb zircon age peak is no longer prominent in the sedimentary section, leaving the ~200-300 Ma peak dominant. While the zircon age spectrum still reflects dominance of a WKL-like source, Figure 4.7 shows that samples of this age and younger are pulling away from the WKL pole toward the

North Pamir. Input from the North Pamir is also reflected in the shift in εNd values to become more similar to the North Pamir than the WKL signature at this time (Figure 4.4); this change to more positive values is consistent with the increase of metavolcanic detritus recorded in this interval). Cretaceous, Paleogene and Neogene (14 Ma) zircons are sparse. The overwhelming majority of the ZFT ages are pre-Cenozoic. This indicates that either the source regions were still undergoing predominantly thin-skinned exhumation or that not enough time had elapsed to exhume young zircons to the surface.

The major reduction in prominence of the ~400-500 Ma zircon U-Pb population (Figure 4.9) is significant. As discussed above, while the North Pamir and WKL are correlated (Section 4.2.2), and thus broadly share similar lithological characteristics, Palaeozoic igneous intrusions comprise a considerably higher proportion of lithologies in the WKL compared to the North Pamir (Figure 4.1) as reflected in the modern river data draining these terranes (Figure 4.9). We therefore interpret the considerable reduction in the 400-500 Ma zircon population in Aertashi rocks at ≤14 Ma, coupled with the shift in εNd values toward a signature more similar to the North Pamir, to reflect the time when the Pamir indenter had propagated sufficiently far north that the North Pamir began to contribute detritus to the Aertashi region, i.e., ~200 km north of the northern margin of Tibet. Such proximity to the salient is supported by our palaeocurrent data and change in facies; while the NW-directed palaeocurrents prior to 14 Ma indicate a lack of topography to the west of the basin during this period, the onset of major conglomerates after ≤14 Ma documents a proximal exhuming hinterland at this time.

Recurrence of rare Paleogene grains, from 15 Ma, now accompanied by sparse Cretaceous grains, may hint at limited derivation from the Central/South Pamir at this time. The uncommon Neogene zircon grains hint at a possibility of minor input from the gneiss domes, such as the Shatput and Muztagh Ata, which had begun to exhume by this time (Robinson et al., 2007, Stearns et al., 2015, Thiede et al., 2013). Any domal input was not prominent however, as shown by the petrography, and such zircons could also be ascribed to volcanic sources. The occurrence of magmatism in this region, albeit of a mafic composition, is evidenced by the major influx of fresh mafic volcanic detritus in the samples at <11 Ma. This mafic detritus may be sourced

from the 13-8 Ma Tashkorgan igneous complex, which outcrop in the eastern central Pamir (Stearns et al., 2015 and references therein).

Between <11 Ma and modern day, the provenance signal changes again. A minor ~100 Ma peak, characteristic of the South Pamir is first recorded in the <11 Ma sample but only becomes prominent in the modern Yarkand River (Figures 4.6 and 4.9). Thus, although a palaeo-Yarkand may have been identified earlier in the sedimentary record in other regions (Cao et al., 2014 and section 4.3.2), we see no evidence of it following its current drainage pattern until very recently. In contrast to samples from the Aertashi sedimentary record (youngest sample analysed for ZFT has a depositional age <14 Ma), there is also a substantial population of Neogene ZFT ages from the modern Yarkand River sample indicating exhumation from depth in the source region; 30% of the double-dated grains have Neogene ZFT ages and double dating with U-Pb shows these ages to be exhumational rather than magmatic.

The petrographic signature of the Yarkand River indicates a mixed input from a number of terranes, consistent with the modern day drainage pattern. Likewise, the shift back to a more negative εNd signature in modern times at Aertashi reflects expansion of the Yarkand drainage basin, with values consistent with input from upland regions of the Yarkand catchment draining the South Pamir, Central Pamir, and gneiss domes today (Figure 4.4).

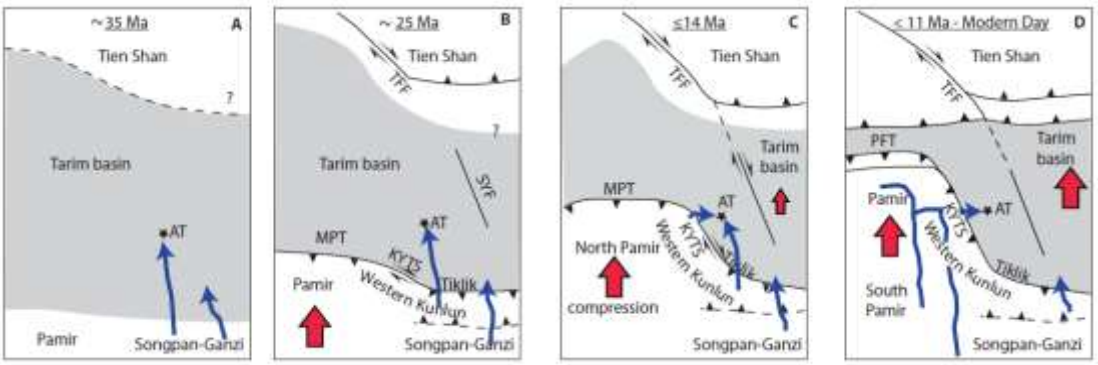

Figure 4.10 Model of the evolution of the Pamir salient (modified from Bande et al. (2015)) and palaeodrainage pattern (in blue) interpreted from the sedimentary record at Aertashi. The Red arrows indicate the direction of movement. (a) The Songpan- Ganzi terrane forms raised topography such that the Aertashi section receives sediment from northward flowing rivers. (b) Basinward expansion of the NW margin of Tibet, and initiation of Pamir indentation as the North and South Kunlun terranes exhume as the KYTS and Tiklik Thrusts initiate. This results in a subtle shift in the drainage to Aertashi, with abundance of material from more distal sources declining as the more proximal Kunlun terranes are exhumed. (c) Indentation of the Pamir Salient was now sufficiently proximal to Aertashi that a new North Pamir source contributed to the Aertashi drainage and the proximal location to the new source resulted in a major sequence of conglomerate deposition in Aertashi. However, the southern palaeodrainage from the Kunlun was not yet cut off. (d) The catchment area of the modern Aertashi River. The embryonic establishment of the modern drainage initiated after 11 Ma (Figure 4.10d).AT = Aertashi section, KYTS = Kashgar Yecheng Transfer System, SYF =Shache–Yangdaman fault, TFF= Talas–Fergana fault, MPT= Main Pamir Thrust, PFT = Pamir Frontal Thrust

4.8 Summary and conclusions: The palaeogeographic model

Based on our results in the context of the regional review presented above, we propose a conceptual model of palaeogeographic evolution, as follows:

At ~35 Ma (Figure 4.10a), the WKL is a topographic feature which is likely to have been elevated since ~200 Ma; its early uplift was associated with closure of the palaeo-Tethys. Prior to the indentation of the Pamir with respect to Tarim, the WKL and the North Pamir likely formed an east-west trending belt with higher topography than the basin to the north. The resulting paleotopographic gradient resulted in northward flowing rivers as our provenance data indicates.

At ~25 Ma (Figure 4.10b), movement along the WKL bounding faults such as the Tiklik fault and KYTS accommodated northward basinward expansion of the range and the beginning of Pamir indentation. Uplift of the northern plateau margin changed the palaeodrainage pattern within the Kunlun, progressively cutting off the more distal southerly hinterlands of the rivers draining north to Aertashi. The western region, closer to the Pamir salient and KYTS, was more affected than the eastern region.

It was not until after 14 Ma (Figure 4.10c), that an additional new, westerly, North Pamir source was provided to the basin, as attested to by the provenance data and the abrupt change to proximal facies. Nevertheless, a WKL source continued to contribute detritus from the south (Figure 4.7).

Thus, although the KYTS was active since ~25 Ma (Figure 4.10b), accommodating northward indentation of the Pamir, we interpret that it is not before 14 Ma that the indenter had propagated sufficiently far north, ≈200 km, that the North Pamir was now located proximal to the Aertashi region and supplied sediment to the basin lying to the east.

The modern day drainage (Figure 4.10d) clearly reflects the input from the internal regions of the Pamir, as evidenced by the significant population of South Pamir-derived Cretaceous zircons, and zircons with Neogene exhumational fission track ages, both found in the modern Yarkand River sample but not in the <11 Ma Aertashi sample. A small population of Cretaceous grains in the <11 Ma Aertashi sample hints at embryonic development of a Yarkand River system starting to cut back into the internal regions of the orogen. However, the Yarkand River in its current form, with a drainage basin encompassing an extensive area of the southern Pamir, as recorded by a significant Cretaceous zircon peak in the modern river sand, and flowing over a region exhuming from greater depth, as evidenced by the Neogene ZFT ages in zircons from the modern river sand, are attributes not present in the <11 Ma sample, indicating such drainage was not established until closer to the modern day.

Acknowledgements:

This work was funded by a NERC PhD Studentship to Blayney (grant number NE K501001-1), and by a VIDI grant from the Netherlands Organization for Scientific research (NWO), an ERC consolidator grant MAGIC, and support from the Alexander von Humboldt to Dupont-Nivet. We would like to thank Annabelle Bernard and Laura Fielding and our Guides Kasim and Khader for their contributions in the field. We thank reviewers Alex Robinson, Dr. Bihong Fu, and a third anonymous reviewer for their thorough and constructive reviews. Supporting data are included as five tables and a detailed method summary in the supporting information.

5. Pamir tectonic evolution recorded in the western Tarim Basin: a combined magnetostratigraphic and sedimentological analysis of the Aertashi sedimentary section (China)

Tamsin Blayney[1], Guillaume Dupont-Nivet[2,3,4], Jean-Noël-Proust[2], Yani Najman[1], Pierrick Roperch[2], Niels Meijer[2], Edward R. Sobel[3], Ian Millar[5,] Zhaojie Guo[4]

1. Lancaster Environnent Centre, Lancaster University, Bailrigg, Lancaster, LA1 4YQ, UK
2. Géosciences Rennes, UMR-CNRS 6118, Université de Rennes 1, Rennes, France.
3. Institut für Erd- und Umweltwissenschaften, Universitaet Potsdam, Potsdam, Germany.
4. Key Laboratory of Orogenic Belts and Crustal Evolution, Ministry of Education, Beijing, China.
5. NERC Isotope Geosciences Laboratory, BGS Keyworth, Nottingham NG12 5GG, UK

Abstract

In response to the India-Asia continental collision, the northward indentation of the Pamir salient into the Tarim Basin links deep lithospheric processes to surface and atmospheric processes; however, poor temporal constraints for this indentation precludes evaluation of regional geodynamic, geomorphic and climatic models. Here we reconstruct the Pamir tectonic evolution from the most complete sedimentary record of the western Tarim Basin (the Aertashi section) flanking the Pamir and based on sedimentologic analysis and magnetostratigraphic dating complemented by previously published provenance data. Increased tectonic subsidence and a shift from marine to continental fluvio-deltaic deposition at 41 Ma indicate that deformation started propagating into the Tarim from the distal India-Asia collision. A depositional hiatus from 24.3 to 21.6 Ma followed by the deposition of proximal conglomerates until 18.6 Ma is interpreted as the expression of a major dextral strike-slip system linking the Kunlun to the Tian Shan and propagating ahead of the Pamir northward indentation. This may be related to coeval Indian slab break off and the onset of south dipping continental subduction and roll back of the Eurasian slab. From 18.6 to 15.0

Ma, increasing accumulation of fine clastics with a distal source is interpreted as further thrust loading of the Kunlun and Tian Shan focusing the Tarim Basin depocenter near Aertashi. At 15.0 Ma, the appearance of conglomerates with a distinct proximal Pamir source from the west is coeval with the onset of growth strata and clockwise vertical-axis rotation associated with the activation of the regional east-verging Qimugen thrust wedge comprising the Aertashi section, indicating that the Pamir indentation and associated deformation reached the study location at this time. This, along with the detrital occurrence of diagnostic 11 Ma volcanics from the Central Pamir, provide kinematic constraints on Pamir indentation that are more consistent with proposed tectonic models involving continental subduction rather than delamination. The timing of the Pamir indentation since 25-20 Ma progressively shielded the Tarim Basin from the influence of the westerlies which also provides constraints for associated Asian desertification.

5.1 Introduction

The indentation of the Pamir salient in response to the India-Asia continental collision links deep lithospheric processes of slab break off and roll back, continental subduction and delamination (e.g. Sobel et al., 2013, Küfner et al., 2016), to surface processes of the Pamir Plateau orogeny and central Asian climate evolution (e.g. Thiede et al., 2013, Caves et al., 2015). However, the poor temporal resolution for this indentation precludes evaluation of regional geodynamic, geomorphic and climatic models.

It is generally considered that the Pamir penetrated into Asia and acquired its arcuate configuration as a response to the northward propagation of deformation from the India-Asia collision through indentation (Cowgill, 2010, Tang et al., 2015, Sobel and Dumitru, 1997, Bande et al., 2015, Blayney et al., 2016). Prior to indentation, the Pamir is thought to have formed a relatively straight east-west margin aligned with the Western Kunlun mountain range and the northern margin of Tibet; what is now the Tarim and Tajik basins lay to its north (Burtman and Molnar, 1993, Robinson et al., 2012, Schwab et al., 2004, Robinson, 2009). The Pamir are therefore considered the now indented, western continuation of these ranges although little evidence for an originally straight margin exists.

Beneath the Pamir is a double subduction zone, with the north dipping Hindu-Kush slab of the Indian lithospheric indentor and the south dipping 300 km long arcuate Alai slab roughly following the shape of the Pamir range forming the overriding Eurasian plate (e.g. Küfner et al., 2016, Sobel et al., 2013). There are two key models proposed to explain Pamir uplift and indentation; the "subduction model" (Sobel et al., 2013) suggests that the Pamir indented as a result of subduction induced processes along with uplift and exhumation resultant from back arc extension linked to roll back of the southward dipping Alai plate. The "delamination model" (Bird, 1979, Küfner et al., 2016, Rutte et al., 2017a,b) suggests that the Pamir formed from the underthrusting of the Indian plate beneath the Pamir, which resulted in delamination of the Alai plate forcing its rollback. Both of these models make specific predictions regarding the timing and evolution of the Pamir indentation. The subduction model requires subduction roll back of the Alai plate coeval with the 22-12 Ma dome exhumation within the Pamir coincident with the 300 km indentation, whilst the delamination models suggests thickening within the Pamir propagated from the south with limited Pamir indentation into the Tarim Basin before 10 Ma. Improved constraints on the timing of Pamir indentation would provide a key tool in distinguishing between these two models.

A distinctive feature of the Pamir is its unique arcuate structure the cause and mechanism of which has been the subject of much debate. A number of models have been proposed to explain this, ranging from oroclinal bending or radial thrusting, which is associated with extensive vertical-axis rotations (Yin et al., 2001, Robinson et al., 2004, Strecker et al., 1995), transfer faulting induced by shear faults along the eastern and western margins associated with limited rotation (Burtman and Molnar, 1993, Searle, 1996), to a hybrid model involving north-west radial thrusting with anticlockwise rotation at the western margin and transpressional right-slip transfer faulting at the eastern margin (Cowgill, 2010). All with specific predictions regarding the extent of vertical axis rotations and strike – slip faulting along the margins of the Pamir and its neighbouring basins.

Understanding the evolution of Pamir range is not only key to our understanding of geodynamic and tectonic processes; it also provides a unique location in which to examine the complex interactions between tectonics and climate. Prior to India – Asia collision the western Tarim Basin was occupied by a vast continental sea known

locally as the Tarim Sea, which formed the eastern extent of the Para-Tethys (Bosboom et al., 2011 and references therein). By ~37 Ma (Bosboom et al., 2011) this internal sea retreated from the Tarim Basin removing a critical moisture source from central Asia. The driving factor for the sea retreat, whether eustatic or tectonic, remains to be determined (Bosboom et al., 2014c). Subsequent indentation of the Pamir range effectively cut off the Tarim Basin from the westerlies moisture input and probably drove further aridification in the Asian interior, transforming the Tarim Basin into one of the largest deserts in the world, the Taklimakan (Caves et al., 2015). Confirming the relationship between Pamir indentation and Tarim Basin desertification remains speculative due to the poor age control on both the indentation and the desertification.

To reconstruct the tectonic history of the Pamir, we focus here on the western Tarim Basin where a >10 km sedimentary record exists (Jia, 1997), which records the evolution of the Pamir indentation into the Basin (Figure 5.1). It is therefore an excellent location to reconstruct the tectonic history of the Pamir (e.g. Yang and Liu, 2002). However, age control and depositional environments along the western Tarim Basin are still poorly defined. In order to better constrain the Pamir evolution recorded in the Tarim Basin, we carried out a sedimentological and palaeomagnetic study on the Cenozoic Aertashi sedimentary section of the Yecheng sub-basin, incorporating magnetostratigraphy, anisotropy of magnetic susceptibility (AMS), magnetic susceptibility and determination of vertical-axis rotations. These results are discussed in light of our parallel study of provenance data (Blayney et al., 2016 and Chapter 4 of this study), and the regional evolution of the western Tarim Basin.

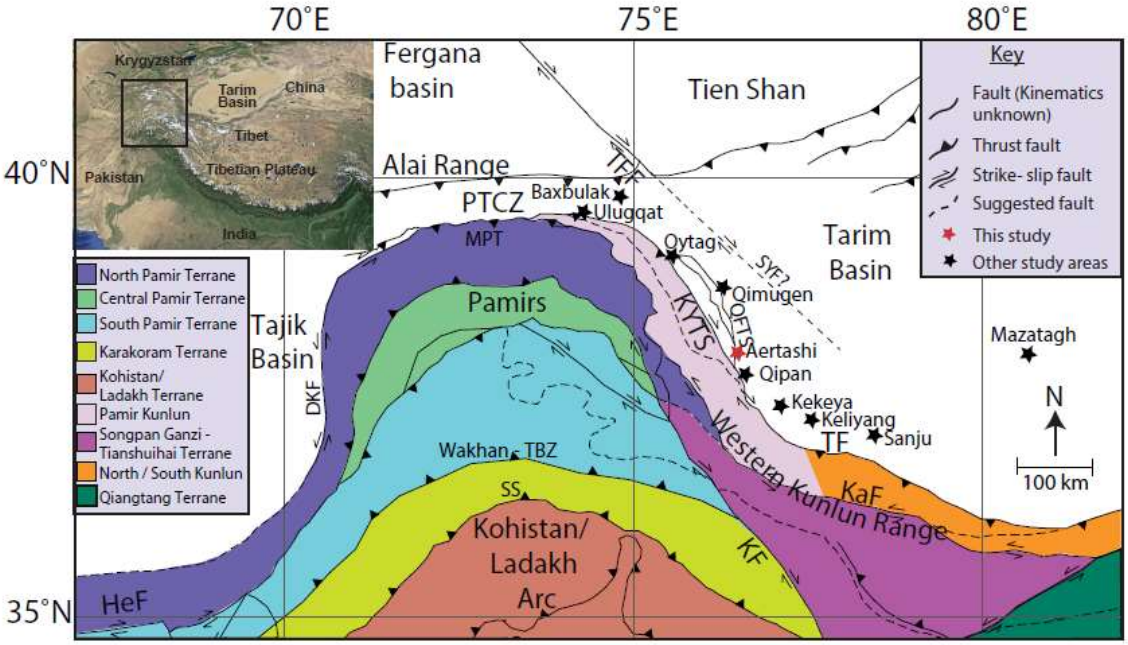

Figure 5.1 Adapted from Sippl et al. (2013) HeF = Herat fault, SS Shyok suture, DKF = Darvaz-Karakul Fault System, MPT = Main Pamir Thrust, PTCZ = Pamir – Tian Shan Convergence Zone, TFF = Talas Ferghana fault, SYF = Sache-Yangdaman fault, KYTS = Kashgar-Yecheng Transfer System, KF = Karakorum fault, TF – Tiklik fault, KaF = Karakax fault, QFTS = Qimugen Fold Thrust System. Our study section Aertashi is highlighted with a red star with other study sections highlighted with a black star, insert shows the location of the Pamir range in its broader region.

5.2. Geological background

5.2.1 The Pamir and Western Kunlun

Located directly north of the western syntaxis of the India-Asia collision, the Pamir forms a high elevation protrusion extending north from the Kunlun ranges to the Tian Shan and flanked by the Tarim Basin to its east and the Tajik Basin to its west (Figure 5.1). The eastern limb of the arcuate Pamir range is often referred to as the "Western Kunlun" as it is regarded as a continuation of the east-west trending Kunlun range that forms the northern boundary of the Tibetan Plateau (Burtman and Molnar, 1993).

The Pamir is highly seismic with intermediate-depth events interpreted to represent the breaking off of the north dipping Hindu-Kush slab and the continental subduction and roll back of the Alai slab based on deep seismic imaging and tomography (Burtman and Molnar, 1993, Fan et al., 1994, Hamburger et al., 1992, Negredo et al., 2007, Roecker et al., 1980). Recent kinematics inferred from GPS and fault activity indicates (Jay et al., 2017 and references therein) north-south compression is mainly

accommodated directly north of the Pamir and south of the Tian Shan (Ischuk et al., 2013, Zubovich et al., 2016) (Figure 5.1) and east-west extension accommodated by low angle normal faults and domes within the Pamir and possibly by westward gravitational extrusion (e.g. Argand, 1924, Brunel et al., 1994, Schurr et al., 2014b, Robinson et al., 2004, Thiede et al., 2013).

The Pamir structure is bounded by the Main Pamir Thrust (MPT) and Pamir Frontal Thrusts (PFT) in the northern Pamir and by strike slip systems along its margins. These include the dextral Kashgar-Yecheng Transfer System (KYTS) along the eastern side and the sinistral Darwaz-Karakul fault system to the west (Burtman and Molnar, 1993, Cowgill, 2010) (Figure 5.1). The structural activity of the latter is still poorly constrained in age and slip magnitude although structural reconstructions have indicated that sinistral indentation is facilitated by vertical-axis counter-clockwise crustal rotations in the Tajik Basin (Thomas et al., 1996, Bourgeois et al., 1997).

Of particular interest here, the dextral KYTS on the eastern side of the Pamir is better constrained. Its activation is suggested by thermochronology of detrital Apatite Fission Track (AFT) to have initiated around 25-20 Ma (Sobel and Dumitru, 1997). Slip estimates on the KYTS have been reviewed by Cowgill (2010) and proposed to be ~280 km based on the offset between current thrust traces of the MPT to the north and the Kunlun to the south. However, no definitive piercing point has yet been established. Cessation of slip since Pliocene times (~5-3 Ma) has been suggested by Sobel et al. (2011) based on thermochronologic exhumation ages of geological features which are not offset by the KYTS, and has been related to the northward motion of Tarim along with the Pamir since that time. Note that GPS data shows that Pamir and Tarim are currently moving coherently and that northward Tarim motion is accommodated within the Tian Shan through strike slip faulting and further north of the Tian Shan, while Pamir northward motion it is accommodated mostly south of the Tian Shan (Ischuk et al., 2013, Zubovich et al., 2016).

The KYTS may be related to the Karakoram fault system that extends from the Gurla Mandhata detachment or the Indus-Yarlung suture in the south (McCallister et al., 2014) to the Muji fault, in the north and divides into a series of horsetail splays towards the northern extent (e.g. Chevalier et al., 2015) (Figure 5.1). The role of the Karakoram fault during Pamir indentation is hindered by uncertainties in its initiation

age and offset (Murphy et al., 2002). Estimates for initiation range from 25-22 Ma (Lacassin et al., 2004, Valli et al., 2008, Sen et al., 2014), <18 Ma (Searle et al., 1998), 13.7 ± 0.3 to 15.7 ± 0.5 Ma (Phillips et al., 2004), <13 Ma (Murphy et al., 2002), ≥11 Ma (Matte et al., 1996) to <5 Ma (Searle, 1996). Associated offset is similarly controversial as it is highly dependent on the fault activation age, although a recent review of estimates suggests an offset ca. 150 km decreasing towards the north and south end of the fault as the slip is accommodated into splays (Robinson, 2009). The KYTS may also relate to the Talas Fergana fault (TFF) to the north of the Tarim in the southwestern Tian Shan as part of a large dextral system allowing transfer of deformation to the Tian Shan by ~25 to 15 Ma (see Bande et al., 2015 and references therein).

The Pamir evolution is also recorded in its geology constituted by the Cimmerian accreted terranes (comprising the north, central and south Pamir terranes respectively) that are proposed to be the western continuation of the Tibetan Plateau terranes (the Songpan-Ganzi, Qiangtang and Lhasa terranes respectively) with varying interpretations (e.g. Cowgill, 2010, Robinson, 2015). However, the Pamir 'appear' very different from the rest of the Tibetan Plateau. The latitudinal extent of the Pamir Plateau (~300 km) is smaller than the Tibetan Plateau (~500 km) suggesting the former has been subject to more contraction and that it is rheologically stiffer (Jay et al., 2017). Large portions of the Pamir Plateau exhibit exhumation of deep crustal levels through a set of core-complex domes (Rutte et al., 2017a, b, Stübner et al., 2013a, b) suggesting a very different deformation regime and history compared to the Tibetan Plateau which is still exposing mostly upper crustal levels. In the Pamir, thickening of the continental crust forming the Pamir Plateau is documented to have occurred since before ~37 Ma based on the timing of prograde metamorphism and compression, which continued until 22 Ma as documented in the Pamir terranes (Rutte et al., 2017a, b, Stübner et al., 2013a, b). This is followed from 22 to 12 Ma by the formation of bivergent N-W extensional core-complex domes interpreted as extensional collapse of the thickened crust following Indian slab break off around 25-20 Ma (Rutte et al., 2017a,b, Carrapa et al., 2014, Thiede et al., 2013). Since 12 Ma, N-S compression resumed, as indicated by inverted dome structures in the Pamir. In addition, compression and exhumation in the Tian Shan is also recorded at this time (e.g. Heermance et al., 2007, Liu et al., 2017, Sobel et al., 2006, Käßner et al., 2016,

Charreau et al., 2006). Since 12 Ma, Pamir extension is concentrated mostly along the E-W Kongur Shan graben (Argand, 1924, Brunel et al., 1994, Robinson et al., 2007) and has been associated with volcanic eruptions of deep material such as the Dudelick volcanics (Kooijman et al., 2017).

Recently two models have been proposed for the formation and indentation of the Pamir range. The continental subduction model (Sobel et al., 2013) proposes that slab break off of the western end of the Indian slab at ~25 Ma (Mahéo et al., 2002, Replumaz et al., 2010, Amidon and Hynek, 2010, Wilke et al., 2012) led to the onset of a new, south-dipping intra-continental subduction system, with the Pamir forming the overriding plate. Continental subduction driven by Indian indentation and trench suction along with slab rollback of the narrow, south dipping Alai slab led to the unique curvature of the Pamir salient. This drove the northward motion of the Pamir into central Asia facilitated by a series of subduction- transform edge propagator (STEP) faults such as the KYTS (Govers and Wortel, 2005, Sobel et al., 2013). Back arc extension within the Pamir is recorded by the exhumation of a series of gneiss domes in the central and southern Pamir (as discussed above). Thermochronologic data (Sobel et al., 2013) from the northernmost Pamir indicates that the North Pamir has experienced limited late Cenozoic cooling driven by exhumation implying that the bulk of the shortening accommodated during Pamir indentation is facilitated by large scale under-thrusting and subduction erosion during the middle Miocene. In the latest Miocene – present, an influx of syn-tectonic sediments resulted in increased coupling and promoted subduction accretion as the Main Pamir Thrust (MPT) and Pamir Frontal Thrust (PFT) propagated northwards creating an accretionary wedge.

A more recent model, referred to here as the 'delamination model', has been proposed based on new seismic tomographic data. Küfner et al. (2016) suggest that the buoyant northwestern salient of cratonic India drives into cratonic Asia, forcing delamination and rollback of its lithosphere. India's thinned western continental margin then separates from India and subducts beneath Asia, forming a prominent anomaly down to the mantle transition zone. The Pamir salient is under-thrust by the Indian plate resulting in uplift and exhumation of the Pamir. This model implies much later, ca ~10 Ma, northward motion of the Pamir salient, with crustal thickening driven from the south by the motion of the Indian plate into Asia. In this model, Central Pamir gneiss domes form as a result of gravitational collapse initiated by Indian slab breakoff

around 22 Ma. Both models have different predictions about the spatial and temporal pattern of deformation and exhumation that have been recorded in the sediments of the basins adjacent to the Pamir. The continental subduction model requires subduction roll back coeval with the 22-12 Ma dome exhumation and at the same time as the 300 km indentation and associated slip on the indentor bounding strike slip faults. The delamination model suggests limited Pamir indentation into Tarim before 10 Ma and most of it afterwards.

5.2.2 The western Tarim Basin

The western margin of the Tarim Basin holds a record of the Pamir evolution and indentation. The Tarim Basin forms part of a relatively un-deformed crustal block of Archean and Proterozoic crystalline metamorphic gneisses (Zheng et al., 2010) overlain by Palaeozoic, Mesozoic and Cenozoic marine to continental sedimentary rocks and sediments and Permian intrusives.

During the northward motion of India into Asia subsequent to continental collision at ca 60-55 Ma (Hu et al., 2016 and references therein), the Tarim Basin has been subjected to marginal over-thrusting by the Tian Shan in the north, the Kunlun Shan and Altyn Tagh in the south and the Pamir in the west (e.g. Burtman and Molnar, 1993, Cowgill, 2010, Jia, 1997, Yin and Harrison, 2000) with suggestions that the Altyn Tagh fault acts as an oblique plate boundary with the lithosphere of the Tarim Basin 'plunging' beneath the north-western edge of the Tibetan Plateau (Wittlinger et al., 1998).

Cenozoic sedimentation in the western Tarim Basin includes deposition of the Palaeogene Kashi Group, composed of the Aertashi, Qimugen, Kalatar, Wulagen and Bashibulake formations. These formations are predominantly composed of marine facies providing reliable markers for regional lithostratigraphic correlations with relatively good age control from biostratigraphy (Tang, 1989, Lan and Wei, 1995, Mao and Norris, 1988, Bosboom et al., 2011, Bosboom et al., 2014a). During the late Eocene to Pliocene, after final sea retreat, the Tarim Basin was filled by a series of thick terrestrial red sandstones known as the Wuqia Group, composed of the Keziluoyi, Anjuan, Pakabulake and Artushi formations (Yin et al., 2002). These mainly consist of sandstone, interbedded with clay and siltstones (Zhou, 2000, Zheng et al., 2015a, Yin et al., 2002). These are dominated by continental fluvial deposits

ranging from meandering stream facies through to braided river deposits and lacustrine and floodplain deposits. Some occasional aeolian deposits have also been reported and attributed to desertification (Kekeya and Mazatagh sections, see Zheng et al. (2015a)), however, there are no aeolian deposits currently reported at Aertashi in this interval. The overlying Xiyu Formation is dominated by thick successions of grey to brown conglomerates typical of alluvial fan environments (Zheng et al., 2006, 2015a, Teng et al., 1996). The Xiyu Formation is highly time transgressive. Its base has yielded various ages at different locations, from 16 Ma to < 1 Ma (Heermance et al., 2007, Yang et al., 2015, Zheng et al., 2000, Teng et al., 1996, Charreau et al., 2006, Sun et al., 2004, Sun et al., 2007). Rare volcanic horizons have been recently dated at around 11 Ma at two locations providing additional age control (Zheng et al., 2015a).

Basinward thrusting and sedimentary infilling of the Tarim bounding ranges (Kunlun Shan, Pamir, Altyn Shan and Tian Shan) has resulted in exhumation and tilting of these sediments. However, the details of the basin tectonics are poorly known, in part due to the difficulties associated with basin-scale correlation of the various formations which are poorly dated and of continental facies, thus prone to rapid facies change along and across strike. Both Yang and Liu (2002) and Wei et al. (2013) used subsurface data to propose basin-wide overviews. Yang and Liu (2002) reconstructed the deformational history of the basin's basement by a backstripping and modelling approach. They concluded that the majority of basement flexure could be accounted for by sedimentary loading, with additional tectonic loading required near major depocenters. Evidence of tectonic loading can be linked to hinterland evolution; however the authors acknowledge that poor dating constraints on the sedimentary rocks preclude accurate temporal interpretations. The data from Wei et al. (2013) suffer from the same limitations regarding temporal interpretations. In contrast to Yang and Liu (2002), Wei et al. (2013) focus more on the importance of strike slip faulting to basin evolution in some areas. They divide the basin into various sub-basins, and the Yecheng sub-basin, as described in section 5.2.3 below, is proposed to be a pull-apart basin between two right-lateral strike-slip faults, for part of its history.

5.2.3 The Yecheng sub-basin and the Aertashi section

The study area is located near the village of Aertashi which is situated to the west of Yarkand River along the margin of the West Kunlun Shan thrust belt (Figure 5.1 and Figure 1.4). It is located in the Yecheng sub-basin, with its depocenter near the town of Yecheng (Wei et al., 2013).

The Yecheng sub-basin has been interpreted by Wei et al. (2013) as a transtensional 'pull apart' basin, formed in the Miocene as a result of the synchronous activity of the Sache-Yangdaman Fault (SYF) in the Tarim Basin and the Pamir and Western Kunlun bounding KYTS dextral strike slip fault. Wei et al. (2013) as well as Wang and Wang (2016) provide seismic data from the Pamir margin Qimugen frontal thrust belt (QFTS), located adjacent to Aertashi (Figure 5.1). This shows growth faulting in the upper conglomeratic series which they correlate to the Xiyu Formation of Zheng et al. (2000). Re-dating of the Xiyu Formation by Zheng et al. (2015a) and by the current study indicates that the QFTS was active by ca. 15 Ma.

Within the Aertashi section, Paleogene - Neogene eastward dipping sedimentary rocks are well exposed along the Yarkand River and the roadside between the villages of Aertashi to Poskam (38° 11'29.56"N, 77°16'18.11"E) and provide a continuous record of the transition from marine facies of the Kashi Group to a continental fluvial system in the Wuqia Group. Within the sampled 4000m (true thickness) section (Figure 5.2), there is no evidence of major faulting or folding.

Previous work on sedimentology at this section identified the underlying Kashi Group as a series of marine successions including the Aertashi, Qimugen, Kalatar and Wulagen formations which record marine transgression-regression cycles of the Tarim Sea (Bosboom et al., 2011). Overlying these rocks is the Wuqia Group, present at the Aertashi section as a series of terrestrial red sandstones, siltstones and mudstones interpreted to be fluvial, lake and delta facies. An abrupt change in lithofacies is recorded in the overlying Xiyu Formation, which contains massive cobble conglomerates interpreted to be proximal alluvial fan deposits (Zheng et al., 2010, 2015a).

In a previous paper, Blayney et al. (2016) provided a constraint on the timing of indentation of the Pamir from provenance analysis of the Aertashi section. They recorded a subtle change in provenance at ~25 Ma, using the published

magnetostratigraphic dating of the section by Zheng et al. (2015a). They ascribed this provenance change to initiation of indentation of the Pamir at this time.

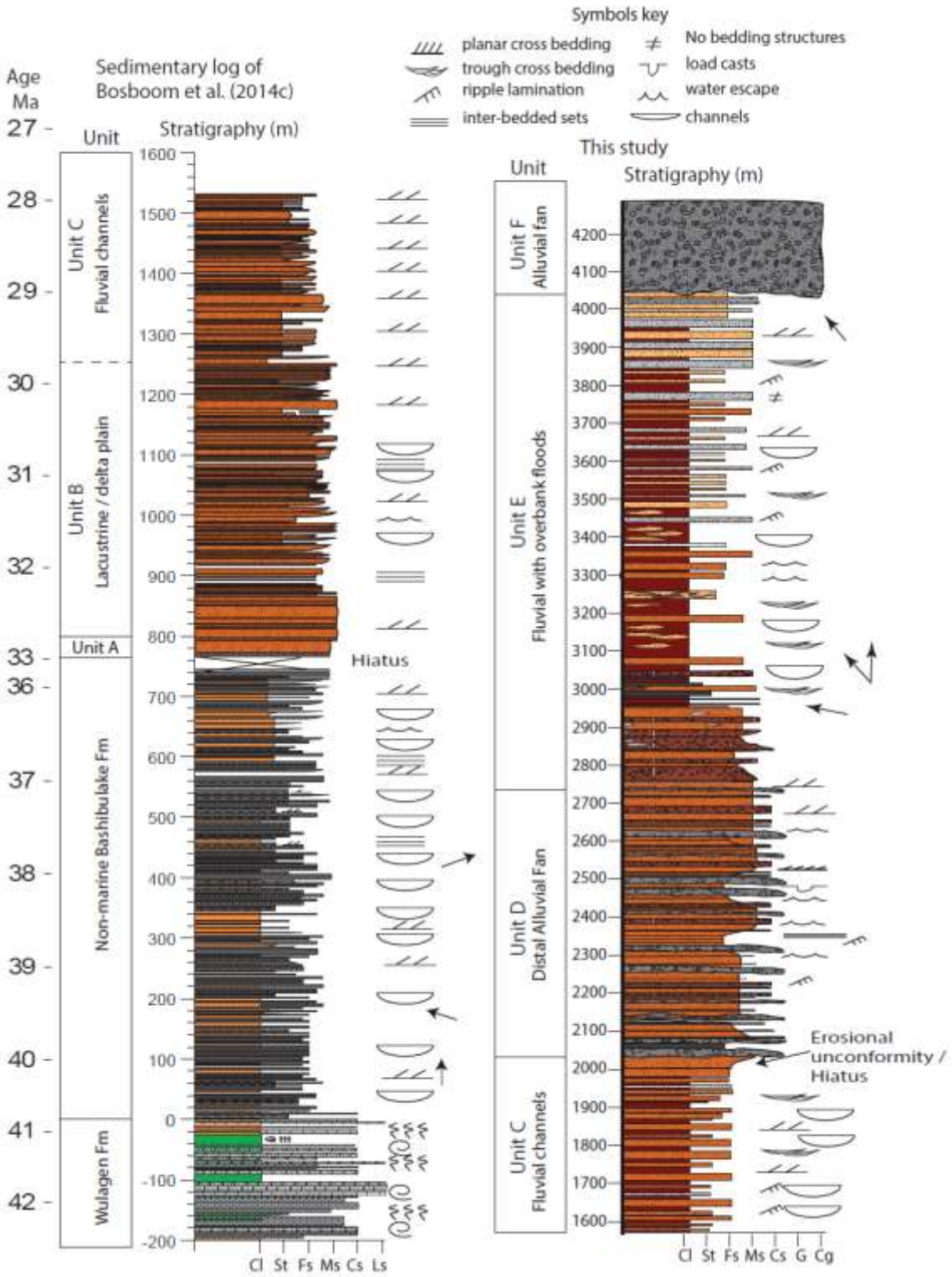

Figure 5.2 A complete grain scale log of the Aertashi section with previous work by Bosboom et al. (2014c) colours used represent the colour changes observed in the section. Palaeocurrent indicators are taken from Blayney et al. (2016) and Bosboom et al. (2014c). The non-marine Bashibulake Fm is also referred to as the Kezilouyi Fm by Bosboom et al. (2014c), see Section 5.5.1 for further discussion on nomenclature. The hiatus at the base of unit D was originally suggested by Zheng et al. (2015a) and is further defined in this study.

5.3. Sedimentological analyses

We conducted a full sedimentology analysis on the section at Aertashi. This record contains vital clues to the evolution of the Western Tarim Basin and indentation of the Pamir range. By studying these sediments in detail we can not only understand the changes in tectonic regime but also explore the relationship between complex tectonics and the resulting depositional environment.

The lithological section was described in the field at a 1/100-scale while sampling for magnetostratigraphy. Any major changes in facies were logged in more detail at the 1/40-scale. Observations include lithology, grain size, sedimentary and biogenic structures and palaeocurrent measurements. We use the Miall (1985) approach for facies analysis and depositional environment interpretations, with full facies descriptions and associations provided in Table 1a and b and facies identification labelled in Figure 5.3. The stacking pattern of the successive depositional environments is interpreted in term of changes in base level and accommodation space.

The onset of extended continental deposition in Aertashi commenced at the 4th marine regression at ~ 41 Ma (Bosboom et al., 2014a), with the last marine beds defining the 0 metre-level of our section. The lower part of the stratigraphic section, from 0 to 760 m is characterised by red siltstones to medium sandstones with cross stratification and incised channel fills interbedded with gypsiferous mudstones. These facies are interpreted by (Bosboom et al., 2014a) to represent dominantly alluvial floodplain deposits with occasional (brackish) lacustrine intervals. This part is dated from ~ 41 to ~36 Ma in age, with a marked hiatus at ca. 760 m, dated from ca. 36 to 33 Ma. This hiatus has been interpreted to result from a base level drop at the Eocene-Oligocene transition (Bosboom et al., 2014a, 2014c) . Our lithological study begins just above this hiatus (Figure 5.2). We subdivided the studied ca. 2200 m-thick sediment section into six units based on their main lithological characteristics (Figure 5.3).

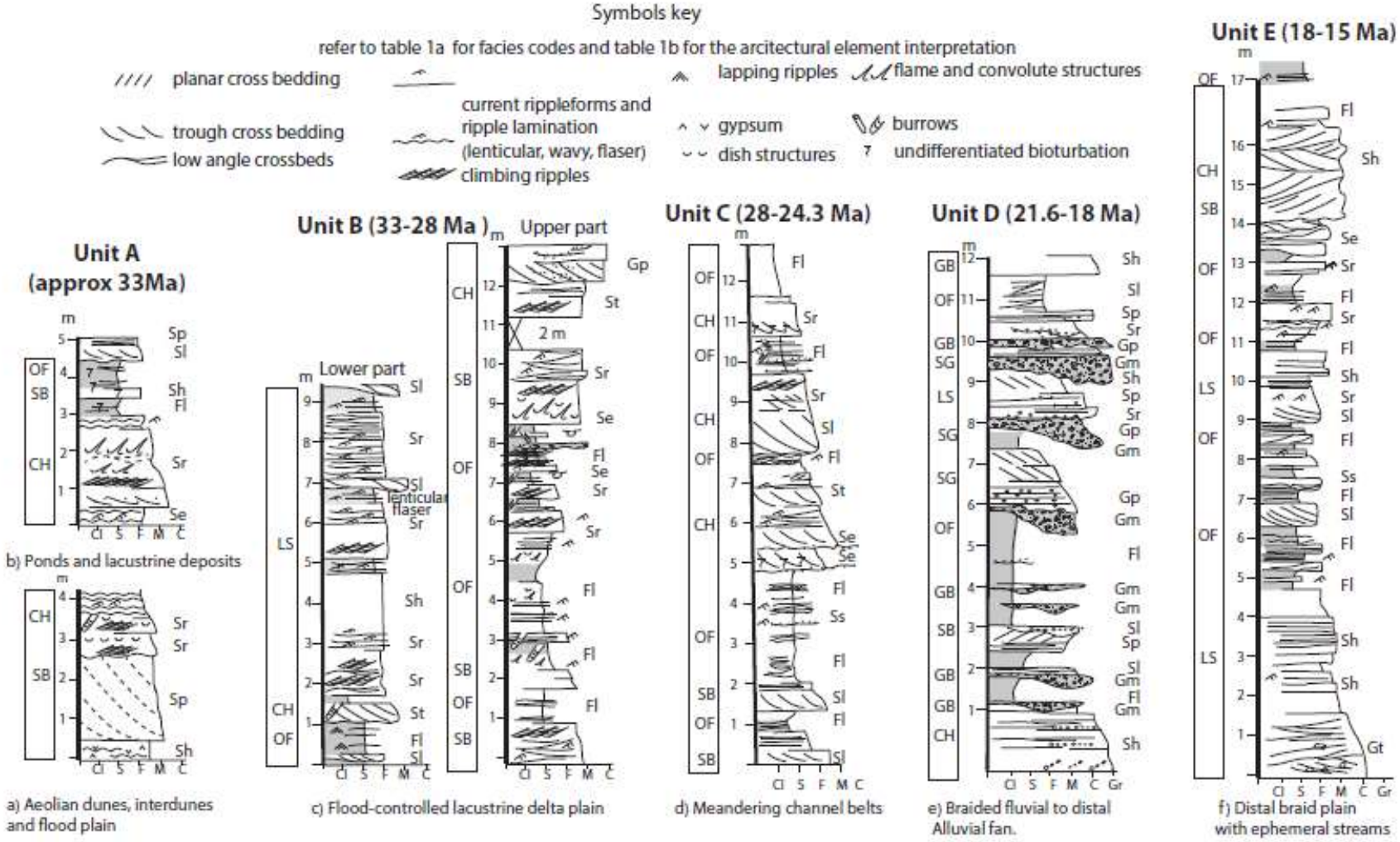

Figure 5.3 Detailed sedimentary logs taken from representative intervals of the units of the Aertashi section. Facies interpretations along the left hand column include depositional models for all with tectonic interpretations. For facies description see table 1a and 1b and text in Chapter 5.

a) Unit A, Aeolian dune, interdunes and floodplain

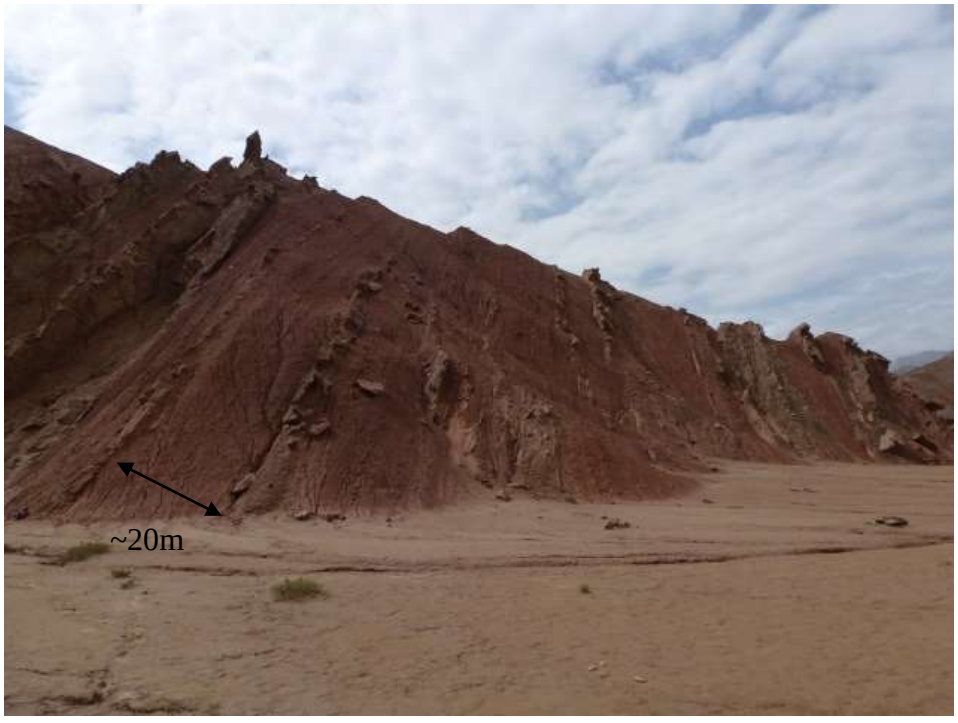

b) Unit B overview

c) Unit C gravel bedding

d) Unit D base with limestone channel lag clasts

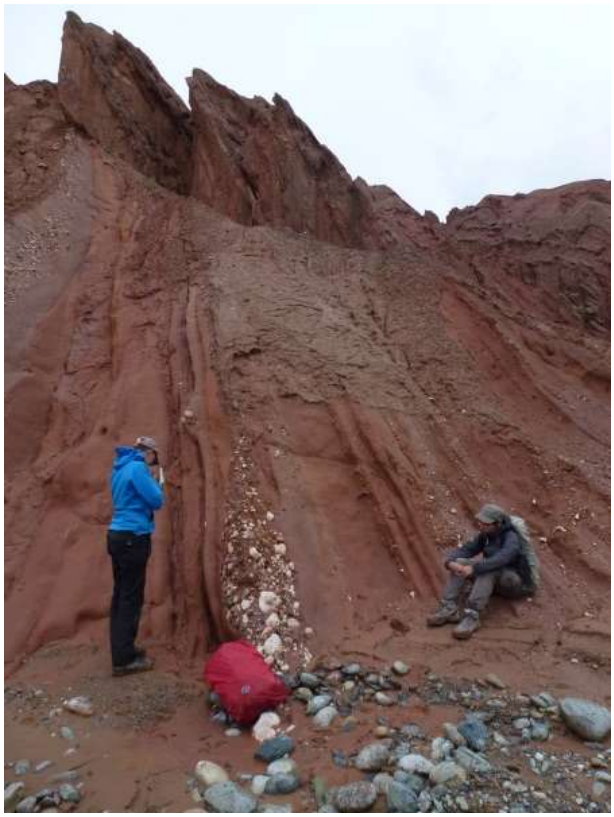

e) Close up of unit D conglomerate clasts with large limestone clasts within a gravel matrix

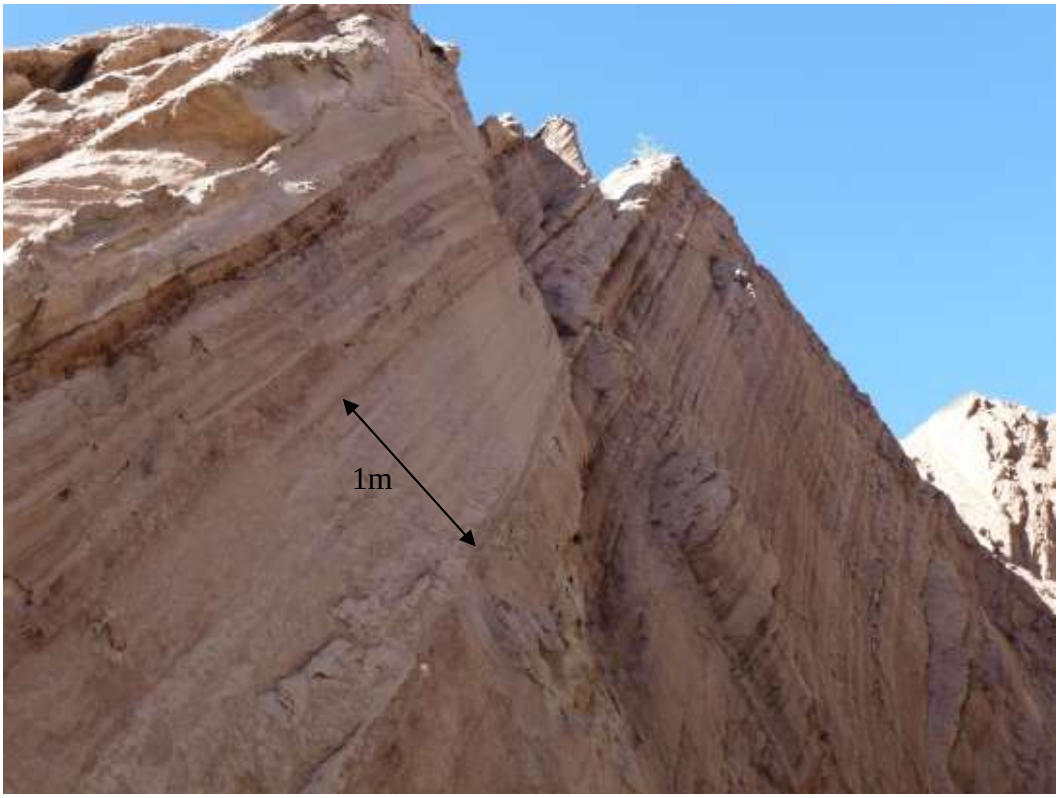

f) Unit E overview of sand channels and mud inter-bedding

g) Unit E close up of mud drapes within the finer sandy fraction

h) Overview of unit F conglomerates interbedded with medium grey sandstones with abundant ‘fresh’ volcanics

i) Unit D matrix supported conglomerate clasts at Yarkand

j) Unit D clast supported conglomerate at Yarkand

Figure 5.4 Images of the main sedimentological units in the study section a) overview of unit A aeolian dune, interdune and floodplain facies, b) an overview of unit B showing large scale cycles of medium - coarse sandstone, interbedded with siltstones and clays, c) Unit C gravel bed showing planar gravels interbedded with coarse sandstones and occasional siltstones, d) Unit D base with typical conglomerate beds containing abundant large limestone clasts interbedded with medium to fine sandstones and siltstones, e) Close up of the conglomerate clasts within unit D showing large clasts of limestone within a gravel matrix, f) Overview of unit E, g) close up image of unit E showing cross bedding overlain by mud drapes and sandstone beds, h) overview of unit F conglomerates interlayered with grey sandstones, geological hammer used for scale, i) image of the unit D conglomerates from Yarkand section showing clast supported structure and j) matrix supported structure.

Table 3 Architectural elements of the Aertashi section a) modified from Miall (1985) with facies classification b) from Miall (1977).

a) Architectural elements in fluvial deposits.

Element	**Symbol**	**Principal lithofacies assemblage**	**Geometry and relationships**
Channels	CH	any combination	finger, lens or sheet; concave-up erosional base; sale and shape highly variable; internal concave-up 3rd order erosion surfaces common
Gravel bars and bedforms	GB	Gm, Gp, Gt	lens, blanket; usually tabular bodies; commonly interbedded with SB
Sandy bedform	SB	St, Sp, Sh, Sl, Sr, Se, Ss	lens, sheet, blanket, wedge, occurs as channel-fills, crevasse splays, minor bars
sediment gravity flow	SG	Gm, Gms	sheet, typically interbedded with GB
laminated sand sheet	LS	Sh, Sl, minor Sp, Sr	sheet, layered
Lateral accretion deposits	LA	St, Sp. Sh, SI, Sr, Se, Ss; less commonly Gm, Gt, Gp	wedge, sheet, lobe; characterised by internal lateral accretion surfaces
Overbank fines/ flood plain	OF	Fm, Fl, Fsc	thin to thick layers; commonly interbedded with SB; may fill abandoned channels

b) Lithofacies classification

Facies codes	**Lithofacies**	**Sedimentary Structures**	**Interpretation**
Gms	massive, matrix supported gravel	grading	debris flow deposits
Gm	massive or crudely bedded gravel	horizontal bedding, imbrication	longitudinal bars, lag deposits, sieve deposits
Gt	gravel, stratified	trough cross beds	minor channel fills
Gp	gravel, stratified	planer cross beds	longitudinal bars, deltaic growths from older bar remnants
St	sand, medium to very coarse, may be pebbly	solitary or grouped trough cross beds	aqueous dunes (lower flow regime)
Sp	sand, medium to very coarse, may be pebbly	solitary or grouped planar cross beds	linguoid, transverse bars, sand waves (lower flow regime)
Sr	sand very fine to coarse	ripple cross lamination	ripples (lower flow regime)
Sh	sand, very fine to very coarse may be pebbly	horizontal lamination parting or streaming lineation	planar bed flow (upper flow regime)
Sl	sand, very fine to very coarse may be pebbly	low angle (<10˚) cross beds	scour fills, washed-out dunes, antidunes
Se	erosional scours with intra-clasts	crude cross bedding	scour fills
Ss	sand, fine to very coarse, may be pebbly	broad, shallow scours	scour fills
Fl	sand, silt, mud deposits	fine lamination, very small ripples	overbank or waning flood

5.3.1 Unit A (33 Ma): Aeolian dune, interdune and arid flood plain deposits (Figure 5.3 a, b and 5.4 a))

Unit A lies directly above the identified hiatus at the 760 m stratigraphic level. This hiatus is dated to span 33-36 Ma including the Eocene - Oligocene transition (Bosboom et al., 2014c). Unit A is 40 m-thick (760-800 m) and made up of two parts.

The lower part is ~20 m-thick and comprised of massive, well-sorted, pinkish, medium-grained sandstones. The sedimentary structures show alternations of m-scale, trough cross bedding and cm-scale rippled and low angle planar laminated beds. The upper part of the large cross beds exhibits inverse grading typical of avalanche deposits when their lower part wedge out in mm scale wind-ripple laminae (Figure 5.3 a, b).

The upper part is 25 m-thick and comprised of 3 to 5 m-thick sequences of pinkish to reddish brown medium-grained locally coarse sandstones, siltstones and minor gypsiferous mudstones alternations (Figure 5.3b). The mudstone content increases up section. At the base, the sequences are comprised of thick sandstone beds with large cross-beds, as described above, alternating with dm-scale, fining-upward sandstone and siltstone beds with climbing ripples, dish structures and bioturbation structures at the top (Table 1 and Figure 5.3b). Up section, the large cross-stratified beds disappear while rippled beds with convolute and dish structures interbedded with bioturbated red siltstone and mudstone become predominant (Table 1 and Figure 5.3 a, b). The main facies interpretations for unit A consist of channelised sandstones (CH), overbank fines (OF) and sandy bedforms (SB) (Table 1 and Figure 5.3 a, b)

The large cross-beds in the lower part of unit A are interpreted to be aeolian dune deposits. These are interbedded up section with waterlain rippled deposits deposited rapidly in shallow ponds or interdune environments. Up section, the aeolian dune deposits disappear, giving rise to larger ponds or lakes in a muddy flood plain environment with occasional crevasse splays.

5.3.2 Unit B (33-28 Ma): Flood-controlled lacustrine sandy delta plain deposits (Figure 5.3c and 5.4b)

The contact between units A and B is gradual. Unit B is ca.670 m-thick (820-~1490m) and made up of fine to medium-grained sandstones alternating with minor red silts and clays (Figure 5.4 b).

The lower part is comprised of 10 m-scale fine to medium-grained, reddish brown, clayey sandstones, which alternate with dm-scale red muddy siltstones. The sandstones show fining upward cm to 50 cm-thick beds. In the most complete sequences, the beds comprise high energy planar and climbing ripple (flaser to lenticular) laminations capped by low energy planar laminations or a cm-scale clay drape (Figure 5.3c, table 1). In places, these rippled sandstones are cut by fining upward, cm-thick and 10 m-large, flat channels of medium to coarse sandstones with low angle lamination, overlain by bioturbated red silty mud with flaser and lenticular bedding and lapping ripples (Figure 5.3c, table 1). The upper part is more heterolithic with a few m-thick fine-grained sections alternating with well-sorted sandstone bars and gravelly sandstone channels. The fine-grained sections show fining upward sequences of rippled sandstone and bioturbated siltstones with intervening pebbly gutter casts. The sandstone sections show large rippled cross-bedding with dewatering structures where gravelly channels exhibit trough bedding. Unit B consists of mainly sandy bedforms (SB), overbank fines (OF), and channelised sandstones (CH) (Table 1 and Figure 5.3c).

The rippled fining upward sequences in unit B are interpreted as flood deposits (splays) in a highly efficient laminar flow fluvial system of a lacustrine delta plain. At the base of unit B, during the dry season, small, shallow crevasse splay channels overlain by muddy ponds incise the delta plain. At the top of the unit, the fine red mud brought by the successive flood events in the flood plain is more abundant. The muds reduce channel wandering leading to an increase in channel size in order to drain the flood plain and build large rippled, cross-bedded bars along their main conduits. In places, the top of the channel fills and crevasse splays are filled by pebbly to gravelly material during flash floods.

5.3.3 Unit C (28-24.3 Ma): Stacked, fluvial meandering channel belts (Figure 5.3 d, 5.4 c)

The transition from unit B to unit C is gradual. Unit C is ca. 560 m-thick (~1490 – 2050 m) and made up of 10's m-thick alternations of red siltstones /fine sandstones and medium to coarse-grained sandstones (Figure 5.3d, Table 1). The fine material shows cm-scale rippled beds with mm-scale mud pebbles interbedded with micro-laminated silts with clay drapes. The fines are cut in places by dm-scale fining up sandstone crevasse channels with bioturbated tops. The sandstones show a channelised erosive base overlain by fining and thinning upward stacks of beds with trough cross laminations and ripple laminations at the top. Occasionally at the top of the unit, the basal erosional surface is filled with pebbles and cobbles of carbonate, sandstones and occasional basement rocks. Unit C is mainly composed of sequences of sandy bedforms (SB), channelised sandstones (CH) and overbank fines (OF) (Table 1 and Figure 5.3 d and 5.4 c).

We interpret the cross-bedded sandstones are large stacks of channels filled by sinuous crested bedforms produced by high-energy flows. These channel belts are bounded by thin layers of fine-grained material settled in a flood plain environment, which is frequently flooded as shown by the varve-like silt-clay couplets, the scarcity of crevasse splay deposits and pedogenesis horizons.

5.3.4 Unit D (21.6–18.6 Ma): Braided fluvial to distal alluvial fan (Figure 5.3e and 5.4 d, e)

Unit D is a wedge shaped unit, 740 m-thick (2050 – 2790m) at Aertashi, the contact between unit C and D is marked by an erosional unconformity (Figure 5.2). Unit D is a gravelly unit with interbedded medium red sandstones, siltstones and clays (Figure 5.3e, 5.4 d and Table 1). The basal beds contain large 'floating' limestones clasts of up to 0.5 m in diameter within a cross-bedded sandy matrix (Figure 5.3e). Unit D is typically made up of stacked, m-scale, fining upward sequences with an overall fining upward trend and increasing upward proportion of red, fine-grained material. Clasts are predominantly composed of limestones and sandstones with rare 'basement' clasts observed.

A typical and complete sequence is comprised of a massive, matrix (sand) supported, coarse gravel beds, overlain by pebbly (and occasionally cobble) sized sand (Figure

5.4c) with planar horizontal lamination and trough cross-bedded sands. The sequence is capped by planar horizontal lamination in sandy silt and massive red silts with occasional floating pebbles (Figure 5.4 e). The latter show thinning and fining upward successions of planar and trough cross stratified, cm-scale sand beds with normal and reverse grading. Unit D is composed of predominantly gravel bars and bedforms (GB) with sediment gravity flows (SG) and occasional laminated sand sheets (LS), overbank fines (OF) and channelised sandstones (CH) (Table 1 and Figure 5.3e).

Unit D is interpreted to represent the toe of an alluvial fan with ephemeral braiding streams feeding a semi-arid flood plain. The proximity of the fan break-in-slope is indicated by the presence of oversized blocks, the abundance of debris flows and the floating pebbles in the red mudstones. The conglomerates of unit D extend over a horizontal (along strike) distance of approximately 40 km ((Figure 5.4 i, j and supplementary item 2) as mapped in the field and using Google Earth. They disappear towards the north but thicken towards the south as observed at the Yarkand section. There the measured thickness of the unit is estimated at ~1050 m between the upper (N37 48’02.1’’ E076 37’33.9’’) and lower (N37 47’52.1’’ E076 36’29.4) contacts with an average bedding attitude of 042/62 (dip direction and dip). This is clearly thicker than the measured 690 m at the Aertashi section showing that these conglomerates thicken substantially to the south. In addition, the conglomerates at Yarkand contain clasts of up to 30 cm diameter (Figure 5.4 g, h), predominantly composed of limestone, sandstones, quartzite with occasional mafic volcanics and exhibit both clast supported and matrix supported structures (Figure 5.4 i, j). Clasts are generally larger and denser than at Aertashi further suggesting a more proximal position with respect to the source.

5.3.5 Unit E: (18.6-15.0 Ma): Distal braid plain with ephemeral streams (Figure 5.3 f and 5.4 f, g)

There is a gradual transition from coarse to fine between unit D and unit E observed by a reduction in gravel beds and an increase in sandstone and mudstone beds. Unit E is 1260 m-thick (2790 – 4050m) and composed of a coarser lower sub-unit Ea and a finer sub-unit Eb, arbitrarily separated at the highest observed gravelly conglomerate bed in unit E at 3020m. Typical successions of unit E are composed of ca. 10’s of m-scale thinning and fining upward then thickening and coarsening upward packages of

gravelly sands, sands, silts and red mudstones. The base of these individual facies successions are marked by erosion surfaces (Se), in places scoured (Ss) that display the morphology of 1m-deep and 10's m-large and smooth shallow channels. The channels are filled with trough cross-bedded sands with some floating pebbles organised into low angle lateral accretion bedding (LA). The overlying sandstone beds that fill up the channels are predominantly low angle to horizontally laminated (Sh) with occasional trough cross-laminations (St) while red silts and clays drape their top. The fine grained part which makes up the most part of the facies succession is composed of sets of 1-2 m fining up sequences with thick medium to fine sandstones with low angle cross bedded bases. These grade into ripple laminations (Sr) with fine laminated clays and silts (Fl) at the top of the sequence (Figure 5.4g). Unit E has four facies associations, predominantly laminated sand sheets (LS) and overbank fines (OF) with occasional sandy bedforms (SB) and channelised sandstones (CH) (Table 1 and Figure 5.3f and 5.4f).

Unit E is interpreted to be distal alluvial with abundant crevasse and flood deposits produced by very highly efficient shallow, meandering channels. The presence of floating pebbles and coarse-grained sand, the low angle lamination and lateral accretion bedding, points to a predominance of ephemeral streams fed by laminar flash floods at the distal part of the coarse alluvial fan or braid plain. The gradual fining upwards throughout unit E reflects increasingly distal alluvial fan depositions.

5.3.6 Unit F (<15.0 Ma): Proximal alluvial fan (Figure 5.4 h).

Unit F (4050m) is dominated by large clast-supported cobble conglomerates (Figure 5.4h). A gradual change precedes the onset of unit F within the top 50 metres of unit E where grey gravelly beds are occasionally interlayered within the finer red beds. The composition of these gravels is similar to that observed in the clasts of the overlying conglomerates of unit F. Clasts of unit F are well rounded and up to 30 cm in diameter. These conglomerates contain basement rocks and volcanic pebbles, they are clast-supported and clasts are generally much larger and more rounded than those observed in the lower conglomerates of unit D.

The unit exposure is discontinuous and predominantly covered by loess, however, Zheng et al. (2010, 2015a) were able to estimate a total thickness for unit F of >6 km

based on bedding measurements and mapping relationships. These conglomerate beds are interpreted to be a proximal alluvial fan facies.

5.3.7 Evolution of the depositional environments through time (Figure 5.5).

Three major changes marked by depositional shifts interrupt the studied section: one at the base of unit A, including the Eocene – Oligocene transition (EOT); one at the base of unit D; and one at the base of unit F. These surfaces correspond to periods of relief rejuvenation and/or regional deformation and are bound by depositional megasequences that provide insights into the overall development of the landscape through time.

The first megasequence boundary is marked by a disconformity at ca. 760 m, dated from ca. 36 to 33 Ma. It has been interpreted to result from a base level drop at the Eocene-Oligocene transition (Bosboom et al., 2014a). Above this, units A, B and C show evolution from a very dry environment with large aeolian dune deposits (unit A) passing upward into wet inter-dunes and ponds to a lacustrine delta plain (unit B base) with highly efficient flows which transport a large volume of sandy material. The lacustrine delta plain dries upward and evolves progressively into a distal, muddy flood plain with isolated meandering channels (unit B top). These channels progressively amalgamate into channel belts in unit C, as the accommodation space decreases sharply below the onset of the unit D defining the next megasequence boundary. The distal alluvial fan to braid plain deposits of unit D sharply overly distal fluvial, meandering channels belts of unit C. The onset of unit D corresponds to a long depositional hiatus as shown from the magnetostratigraphic result presented below and Figure 5.2. This, and the sharp facies change indicate a drastic basinward shift of the facies belts and depositional environments as a consequence of relief formation. The sediments above the unconformity show an increasing subsidence with an evolution from proximal to more distal environments. Gravelly, debris flows dominated alluvial fan deposits in unit D shift up-section in unit E to fine-grained, muddy flood plain deposits, with sands fed by ephemeral streams and flash floods during rainy periods in more distal alluvial fan environment. The sharp increase in grain size to cobble conglomerates at the base of unit F signals another period of sharp basinward shift of the facies belts, with a large set of proximal alluvial fans forming part of a distal braid plain. However, it has been suggested by Wang et al. (2003) that

unit F, referred to as the Xiyu Formation by Wang et al, may have been formed by large rivers draining the western highlands (ie West Kunlun) and are the result not of tectonic activation, but from climate change as a result of increased humidity and varying temperature between cold and warm, leading to increased precipitation and erosion. This interpretation is based on previous studies by Molnar and England (1990) and Zhang et al. (2001),who recorded increasing sedimentation and erosion rates worldwide at ~2-4 Ma which they suggest accounts for the increase in grain size of these sediments. However this study is based on previous age control for the Xiyu conglomerates which placed the onset of these large conglomerates at Plio-Pleistocene time. Subsequent revision of the age control of these sediments as discussed in section 5.4 has resulted the age on onset of unit F being reassigned the mid-Miocene ~15 Ma (Zheng et al., 2015a). We therefore rule out worldwide climate in the Plio-Pleistocene as the cause of deposition of unit F.

In addition, provenance analysis in Aertashi by Blayney et al. (2016) and Chapter 4.8 of this study, records a critical provenance change at the onset of unit F with the first recorded instance of northern Pamir derived material in Aertashi. Although changes in paleo-drainage patterns may result in changes in source catchments, a tectonic origin for these changes remains the most likely interpretation at this time (see Chapter 4.8 for full provenance analysis and Chapter 6 for full discussion of the climate in Aertashi).

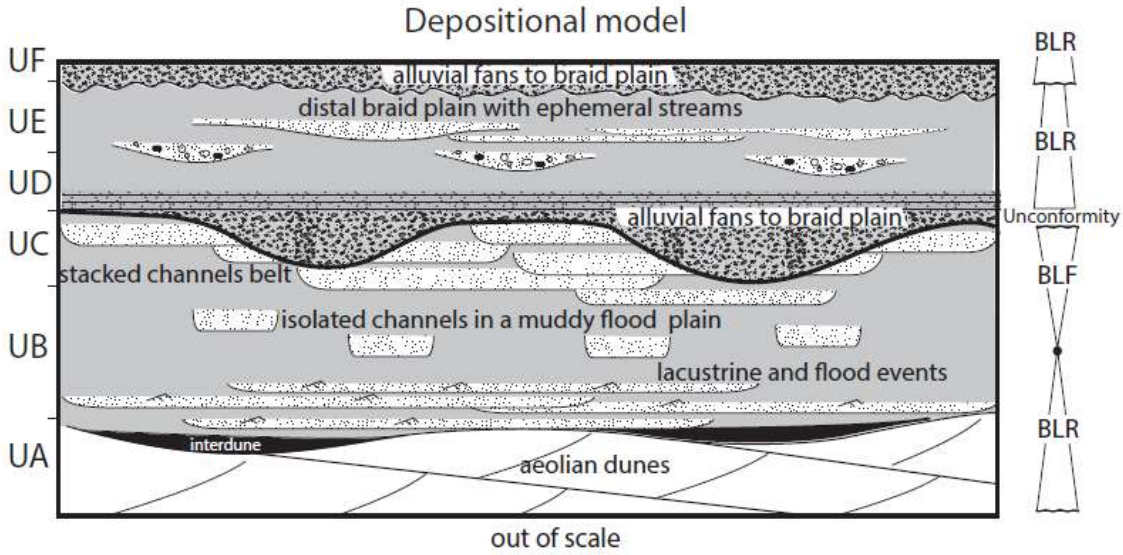

Figure 5.5 Depositional model for the Aertashi section UA-F refers to the unit allocation used in this study, BLF = base-level fall, BLR = base-level rise.

On a broader scale, the evolution of the depositional environments from the base to the top of the studied section shows an overall progradation and an evolution of the Aertashi section towards a more proximal location with respect to the rising regional relief. But in detail, it is a different story with a protracted evolution involving the proximal activation of deformation, relief and subsidence varying over time, interpreted to be a proximal alluvial fan facies.

5.3.8 εNd provenance analysis

The Sm-Nd values of a mudstone largely reflect its provenance, in terms of more crustal (negative ƐNd) vs. more mafic (more positive ƐNd) nature of the source rock. In this paper we use this technique to build upon previous research carried out by Blayney et al. (2016) to further constrain the provenance of the Aertashi sediments. A further 11 bedrock samples from throughout the measured section (See Figure 5.6 with new samples indicated in red and Appendix 1 for full sample names and locations) were added to the previous dataset (Blayney et al., 2016) using the same methods described in Blayney et al. (2016) Figure 6 (Figure 4.4 in this document), with the exception of JNd-i values which yielded a value of 0.512106 ± 0.000003 (6 ppm) for the additional samples. A shift to more negative, crustal, εNd values is seen starting at the base of unit D, immediately after the hiatus in the section and dated at 21.6 Ma as presented below (Figure 5.6). A second major shift, to more juvenile, less negative values, is seen at the top of unit F and dated between ~15.5-14 Ma.

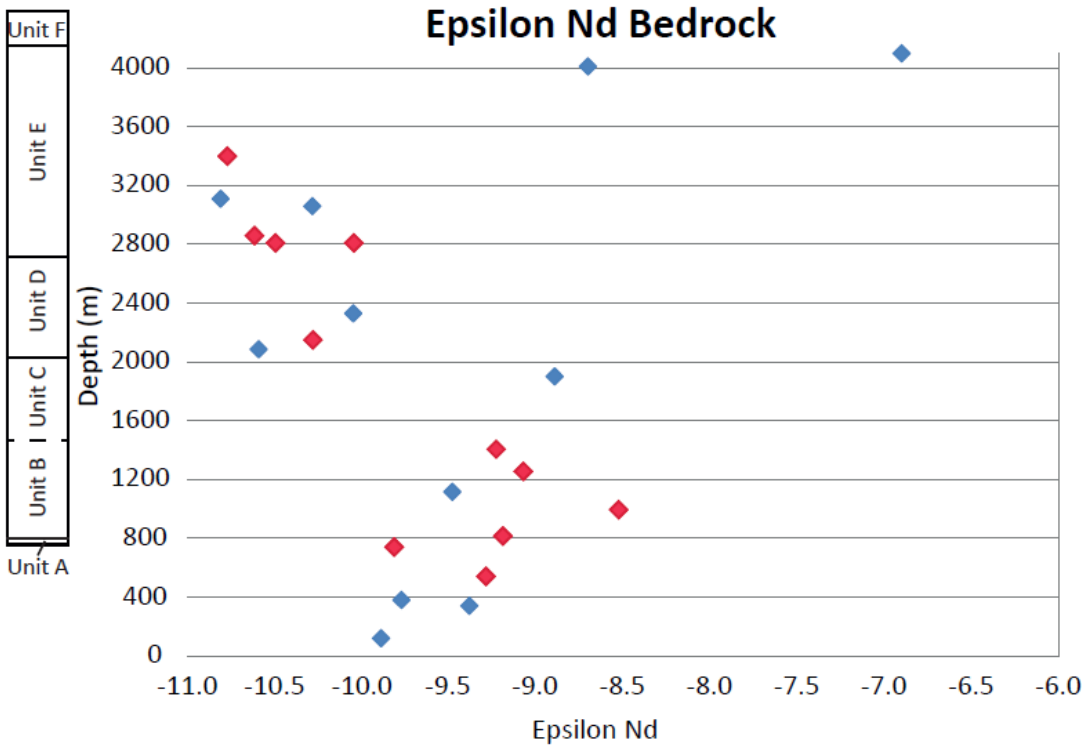

Figure 5.6 εNd plotted by stratigraphic height and unit divisions used in this study. An additional 11 samples indicated in red which have been added to our previous study (Blayney et al., 2016) along with revised stratigraphy.

5.4. Paleomagnetic analyses

5.4.1 Existing age control in Aertashi

A low resolution magnetostratigraphic study in Aertashi was conducted by Yin et al. (2002). However, given the low sampling resolution of 22.5 m, this study was insufficient to make an accurate correlation with the geomagnetic polarity timescale (GPTS). It thus yielded a number of possible correlations from 31-24 Ma or from 20-15 Ma for the section under study, with a high level of ambiguity.

Bosboom et al. (2014a,c) co-ordinated biostratigraphic and magnetostratigraphic analyses of the Aertashi section. They recognized the last marine deposits at Aertashi as belonging to the Wulagen Formation with a late Eocene age constrained by bivalves, calcareous nanofossils and dinoflagellate cysts. Based on magnetostratigraphy they further indicated that the start of the continental section lies at the base of C18.r (ca. 41 Ma) and dated through to C9.n (ca. 27 Ma). More recently, this section has been dated by Zheng et al. (2015a) using magnetostratigraphy combined with constraints of the base from Bosboom et al. (2014c), and an upper constraint, above the level of their magnetostratigraphic dating, provided by Ar-Ar

age control from a volcanic ash layer located at ~6700 m stratigraphic height (See Blayney et al., 2016 for a comparison of this study with Zheng et al. 2015a.).

This ash layer, suggested to be formed during an eruption possibly related to the Tashkorgan Alkali complex, provides a depositional age of 11 Ma for this location, although there is some dispute as to whether this dated layer is a volcanic ash deposit as suggested by Zheng et al. (2015a, b), or a reworked sedimentary deposit (Sun et al., 2015) which would allow interpreting the depositional age of this layer to be younger than 11 Ma. Nevertheless, Zheng et al. (2015a) provided a revised age for the upper Aertashi section (1600 – 4300 m) of 40-~15 Ma and associated interpretations of sedimentological content with focus on the climate significance.

To quantify and understand the tectonic significance of the observed sedimentological changes presented above, we have conducted paleomagnetic analyses on the section including magnetostratigraphy, bulk magnetic susceptibility, vertical-axis tectonic rotations and anisotropy of magnetic susceptibility. Our study continues up-section from the point where the work of Bosboom et al. (2014c) terminates (ca. 1450 metre-level dated ca. 27 Ma; 37°58.284'E, 076° 34.785 N). We therefore provide a complete and revised paleomagnetic analysis from the final sea retreat recorded by Bosboom et al. (2014c) all the way through to the onset of alluvial fan facies of unit F.

5.4.2 Magnetostratigraphic analysis

We conducted detailed paleomagnetic sampling and analysis at the Aertashi section; 662 samples were collected over 2500 m of section at a resolution of 0.4-5 m (average 3.7 m). Sampling gaps are minimal due to the exceptionally continuous outcrop and by the use of digging trenches in less well-exposed parts. Following fieldwork, samples were cut into cores of 2.2 cm in length. Analysis was performed in the magnetically-shielded room at the archeo-palaeomagnetic laboratory at the University of Rennes 1.

A full description of sampling methods, analysis and data reduction is provided in Appendix 17. Following verification of the primary origin of the magnetization, polarity zones identified in Aertashi could be correlated with the GPTS (Gradstein et al. (2012); (Figure 5.7). Polarity zones were defined by at least two consecutive VGP latitudes of identical polarity, leaving any isolated directions within a polarity interval of opposing polarity rejected. Polarity zones were numbered from N12 to N28

following on from the numbering scheme defined by Bosboom et al. (2014c) for the lower part of the Aertashi section, from which this work is a continuation.

A basal constraint is provided for the Aertashi section by Bosboom et al. (2014c) who defined a correlation between N12 to C9.n (41.2-27.2 Ma). Following on from the basal correlation, the next normal zone of N13 can be correlated directly with C8.n, however polarity zones from N14 through to N20 cannot be correlated without ambiguity. We therefore start from the upper part of the section where the longest normal polarity zones are found. There, given that the record must be above C8.n, a unique correlation of the observed polarity pattern can be readily identified as follows. Chrons C5B.r and C5D.r correspond respectively to R28 and R25 of this study and are separated by the peculiar suite of three normal chrons of C5C corresponding to N27, N26 and N25 respectively. It follows upwards that N28 corresponds to C5B.2n and downwards that R24 corresponds to C5D.n, N23 to C5D.n.1n and N22 and N21 to C5E.n and C6.n (Figure 5.7). These constraints provide clear age determination for the bottom and top of the sampled section respectively at 27.2 and 15.0 Ma. This fits well with the independent 14.05 ± 0.85 Ma youngest U/Pb ages from detrital zircons from the conglomerates directly overlying the sampled section (Blayney et al., 2016). However, the correlation remains ambiguous between N21 and N13 where too few polarity zones must be correlated to the period between C7 and C6AA.n characterised by a large number of short chrons. This indicates that there must be one or more depositional hiatii present, of which multiple correlations may be proposed. A good correlation in this interval has been identified by continuing up from the basal section using the accumulation rate defined by the lowermost correlations, thus linking N15 to C7A.n and N16 to C7.n. The same procedure was applied to the upper section by following the accumulation rate down the section correlating N19 with C6A.n and N17 and N18 with the short normal chrons of C6AAn which points to a single hiatus between C7 and C6AA (24.3 to 21.6 Ma, 2050 metre-level). This corresponds precisely to the major change in depositional environments between the fluvio-lacustrine facies of unit C below to the conglomeratic braided facies of unit D above. Alternative viable correlations in this interval are found less likely because they would involve multiple large variations in accumulation rates and/or depositional hiatii that do not correspond to the observed changes in depositional environments.

From these age constraints, sediment accumulation rates can be determined using thicknesses between identified polarity zones of known age throughout the section (Figure 5.8). Accumulation rates for the basal part of the section from 41.2 to 24.3 Ma are fairly constant around 15 cm/kyr on average. However, following the hiatus recorded at the unit C – D transition, accumulation rates increase dramatically from ~18.6 cm/kyr between 21.6-18.6 Ma to 34.5 cm/kyr between 18.6 Ma and 16.5 Ma. Rates continue to increase towards the top of the section with a rate of 50.7 cm/kyr from 16.5 Ma to 15.0 Ma before the onset of the proximal alluvial fan conglomerate deposition of unit F (Figure 5.8).

Accumulation rates of the overlying Xiyu conglomerates can be roughly estimated based on the minimum 11 Ma deposition age provided by volcanic U/Pb zircons (Zheng et al., 2015a) stratigraphically positioned ca. 3 km above the onset of the conglomerates. This suggests rates on the order of 75 cm/kyr for the conglomerates between 15 and 11 Ma and therefore implies a significant increase associated with the conglomerate deposits. Furthermore, we can estimate the age of the top of the Xiyu conglomerates at 6 Ma by extrapolating this accumulation rate above 11 Ma, in the remaining 3 km conglomeratic section, given the estimated total thickness of the conglomerates of ~6 km (Zheng et al., 2010, 2015a).

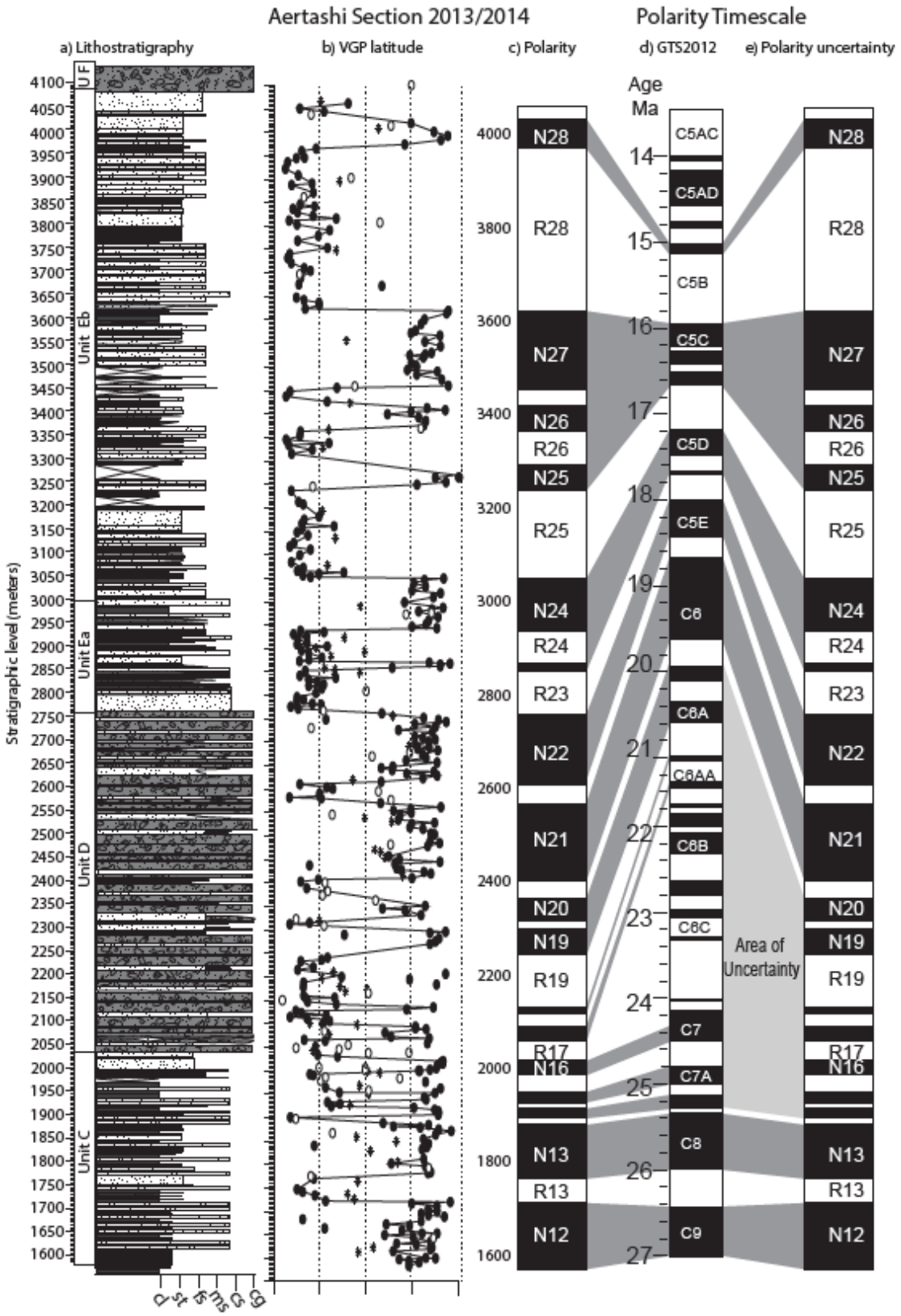

Figure 5.7 Aertashi log with interpreted magnetostratigraphic correlation. a) lithostratigraphic log (height in metres), b) Virtual Geomagnetic Pole (VGP) latitudes derived from the paleomagnetic ChRM directions, c) interpreted polarity zones with preferred correlation to the geomagnetic polarity timescale of Gradstein et al. (2012) d), e) interpreted polarity zones showing area of uncertainty for the magnetostratigraphic correlation

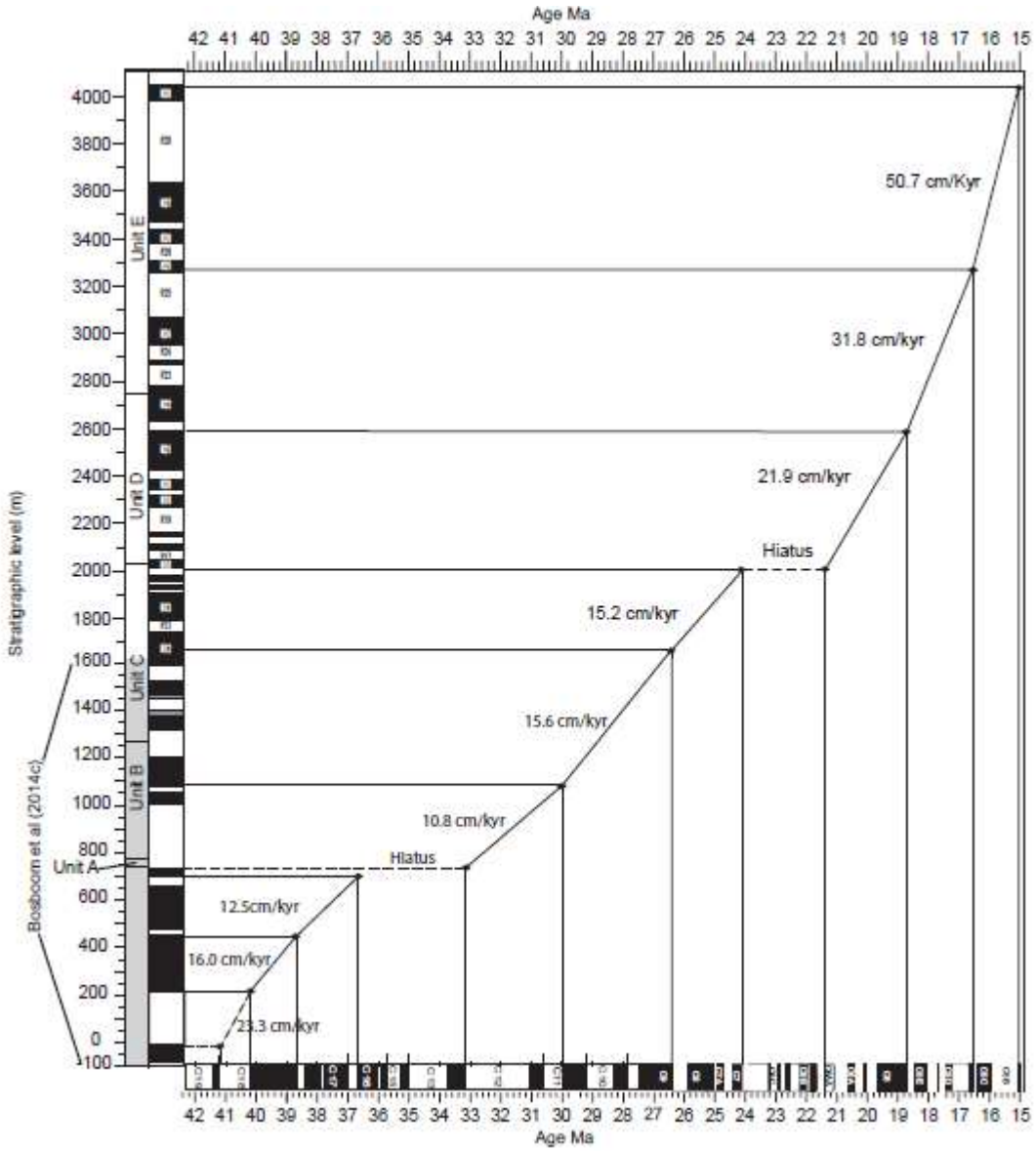

Figure 5.8 Accumulation rate diagram for the Aertashi section, grey shaded area indicates the work of Bosboom et al. (2014c) for the lower Aertashi sediments combined with the magnetostratigraphy of this study.

5.4.3 Tectonic rotation

For our rotational analysis we followed methodologies reported in Bosboom et al. (2014b) using our magnetostratigraphic datasets that passed the reversals test (Appendix 3). This provides average normal and reversed directions unbiased by secondary overprints. Antipodal reversed directions were rotated into normal and combined with normal directions to obtain, for the sampled section between 27.2 and 15.0 Ma, an overall average direction with associated α95 (95% confidence angle) calculated according to Fisher (1953). This averaged direction was compared to the expected directions for the Eurasian continent derived from the Eurasian apparent

polar wander path (APWP) at 20 Ma from Torsvik et al. (2008) to derive a 14.0° ± 3.9° clockwise vertical-axis rotation following the methods of Demarest (1983). We compared our results with those of Bosboom et al. (2014b) and identified a systematic trend of decreasing clockwise rotation continuing throughout the section from 21.2° ± 4.2° between 41 to 36 Ma decreasing to 18.3° ± 6.4° between 33 and 27 Ma and our observed 14.0° ± 3.9° from 27.2 to 15.0 Ma (Appendix 5). This indicates that most of the clockwise rotation (14° ± 4°) occurred after 15.0 Ma and only a small part of the rotation (6 ± 4°) occurred between 41.2 and 15.0 Ma. This is at variance with previous work which proposed that most tectonic rotation ceased by the end of the Oligocene on the eastern side of the Pamir (Bosboom et al., 2014b and references therein), with implications for models of the salient evolution (see discussion in section 5.5).

5.4.4 Anisotropy of Magnetic Susceptibility (AMS)

In weakly deformed sediments, the analysis of the AMS usually reflects the regional stress field and therefore enables the establishment of tectonic regime at the time of deposition (Tarling and Hrouda, 1993). From the Aertashi section 345, samples were selected for AMS analysis at regular intervals throughout the section (the lowermost 82 samples were collected by Bosboom et al. (2014c)). This analysis was conducted using a KLY3 – CS Kappabridge instrument. For each sample, we obtained principal susceptibility axes (Kmax, Kint and Kmin), used to infer the fabric variations throughout the section. After tilt correction, we corrected the AMS directions for the observed vertical-axis rotation recorded in section 5.4.3 (Figure 5.9).

The minimum anisotropy axes (Kmin) observed throughout the section are nearly vertical in tilt-corrected coordinates indicating a clear sedimentary fabric obtained in response to gravity strain acquired at or near the time of deposition. However, the magnetic lineation (Kmax), aligns broadly in an E-W direction in tilt-corrected coordinates between 41.2-17.3 Ma. In the uppermost unit Eb between 17.3 – 15.0 Ma, the magnetic lineation shifts to roughly N-S (Figure 5.9).

Early laboratory depositional experiments have indicated a link between, slope, grain size, shape and sediment transport directions (Rees, 1965). However, in most tectonic belts, anisotropy of low field magnetic susceptibility of sedimentary rocks display triaxial AMS ellipsoids mainly controlled by compaction and tectonic strain (Borradaile and Henry, 1997). Upon deformation, the lineation Kmax quickly aligns

along the direction of maximum extension or, equivalently, perpendicular to maximum compression. In a compressional setting, a lineation perpendicular to the compressional direction is typically acquired during the early stages of diagenesis and deformation (Parés et al., 1999, Frizon de Lamotte et al., 2002). The magnetic lineation, usually known as Layer Parallel Shortening (LPS), develops parallel to fold axes and thus perpendicular to the principal strain direction (Kissel et al., 1986, Robion et al., 1995, Sagnotti and Winkler, 1999, Soto et al., 2009, Roperch et al., 2010, Poblete et al., 2014). If not reset by strong subsequent deformation, the initial LPS of this early acquired magnetic fabric usually behaves as a passive marker recording early deformation and subsequent tectonic rotations (Roperch et al., 2011). This results in a hybrid triaxial fabric with the Kmin perpendicular to bedding as observed in the Aertashi sediments.

Because no significant relative rotations are recorded within the section (most of it occurs after 15 Ma), the striking change from E-W magnetic lineation through the section (41.2-17.3 Ma) to N-S lineation in the uppermost unit (17.3 – 15.0 Ma) is interpreted to reflect a change in principal strain direction from mostly N-S to mostly E-W occurring after 17.3 Ma (Figure 5.9).

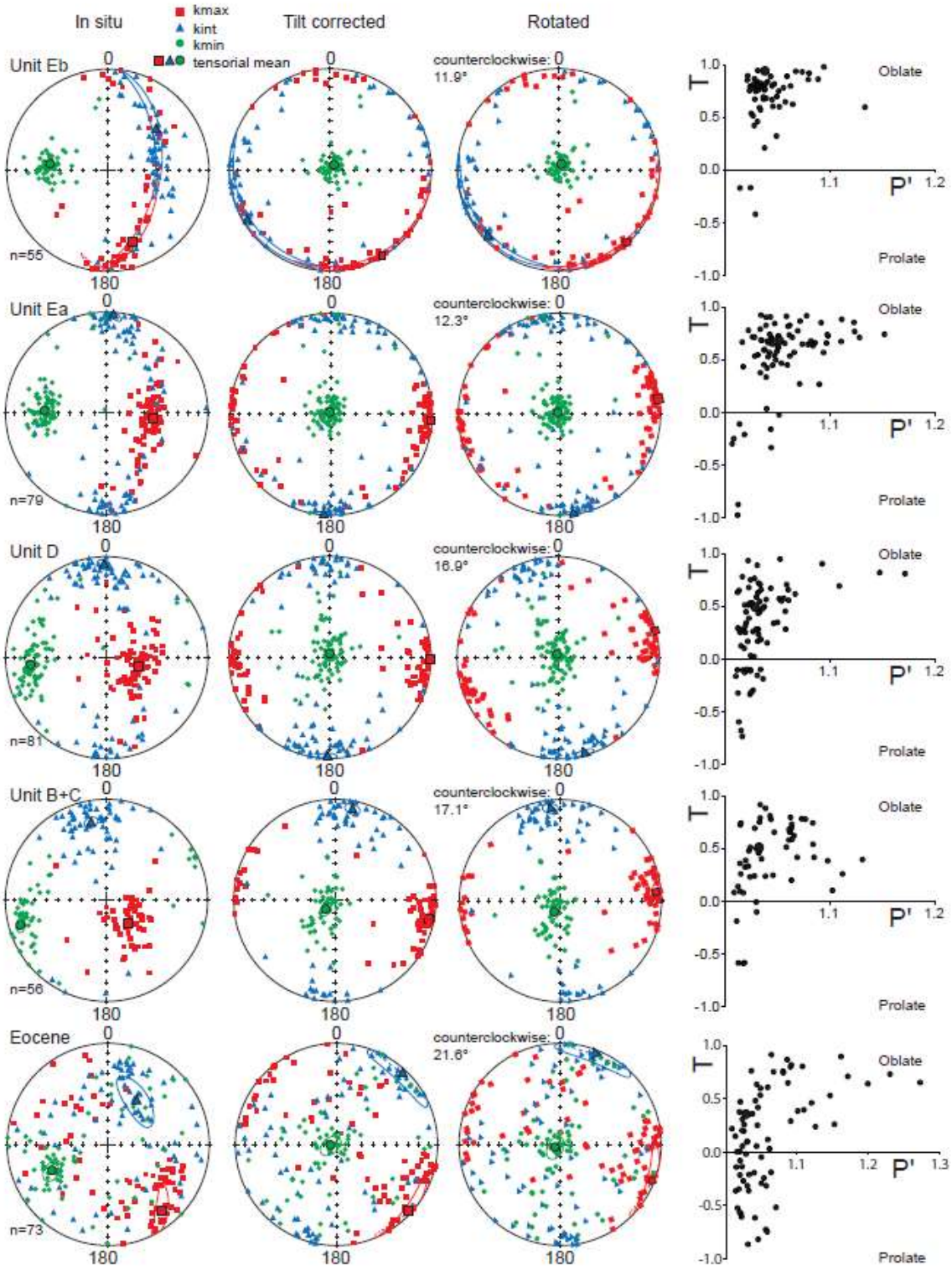

Figure 5.9 AMS principal directions are plotted on stereographic projections. Diagrams of anisotropy parameters T (shape parameter) and P' (corrected anisotropy;(Jelinek, 1981) indicate dominantly oblate fabrics. The samples are subdivided in six groups: Units B&C, Unit D and Unit Ea (~2800 – 3020 m) and Eb (3020 - ~4060 m). The lower section below the EOT is combined to form one 'Eocene' group

5.4.5 Backstripping analysis

We conducted modelling of the tectonic subsidence of the Aertashi section using the published data by Sobel (1999) with updated stratigraphy and age control by Bosboom et al. (2011, 2014c) and this paper. Backstripping was performed with the Macintosh program, Backstrip (Cardozo, 2012), which is based on the methods of Van Hinte (1978) and Steckler and Watts (1978). We assigned a lithology-dependent density to every layer for density distribution within our sediments. Factors for different lithologies were chosen in order to approximate porosity–depth relationships. Two hiatuses are recorded at 33.5-36.1 Ma (Bosboom et al., 2014c) and a second at 24.3 to 21.6 Ma (this study) which were included in our model.

Our results identify the prominent onset of tectonic subsidence (subsidence which is not caused by weight of sediments) at the base of the continental sediments at ~41 Ma. This marks the transition from the last marine sequence in Aertashi and the onset of subsequent continental deposition which continued to increase incrementally throughout the remainder of the section (Figure 5.10).

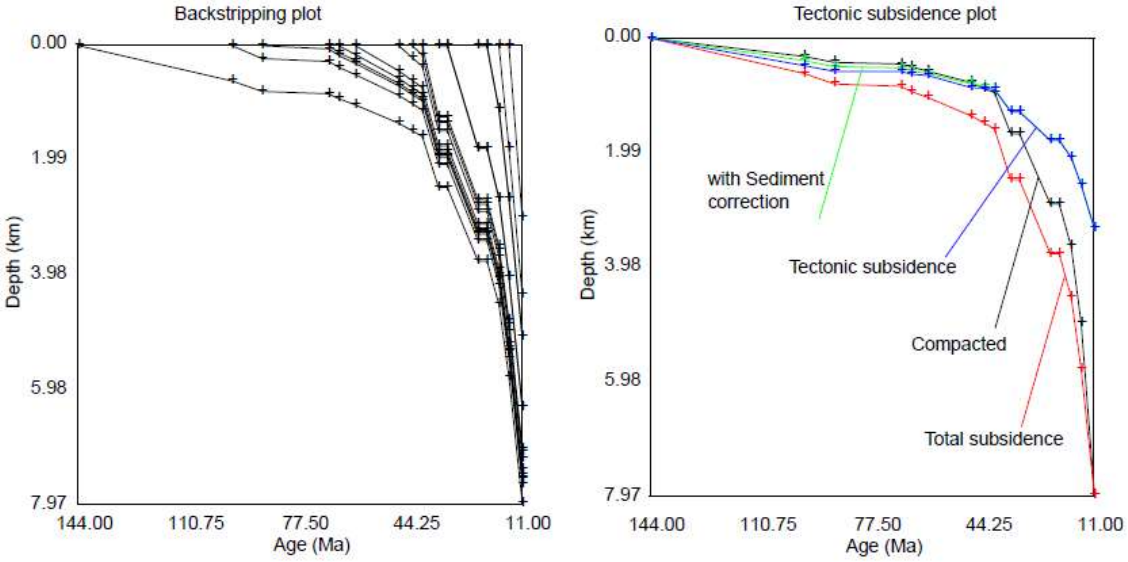

Figure 5.10 Backstripping model indicating tectonic subsidence for the Aertashi section using revised age control and formation thickness data from Sobel (1999), Bosboom et al. (2014c) and this study.

5.5. Discussion

5.5.1. Regional stratigraphic review of western Tarim Basin

5.5.1.1 Correlation of defined stratigraphic units to regional formations

We correlate the various units defined in this study to published formations of the western Tarim Basin as follows:

The last marine formation at Aertashi is recorded in the Wulagen Formation at 41.2 Ma (Bosboom et al., 2011, 2014c). The overlying unit made of continental fluvial red beds extends from 41.2 to 36.3 Ma. As such it is time equivalent to the Bashibulake Formation, which is an alternation of marine and non-marine deposits where it was defined in the northwest Tarim Basin (e.g. Hao and Zeng, 1984, Wang, 1990, 1992, Sobel, 1995). However, the marine incursions of the Bashibulake Formation in northwest Tarim did not reach as far south as the Aertashi region where time-equivalent deposits are exclusively continental (Bosboom et al., 2014a,c). At Aertashi this unit has thus been assigned either to the Bashibulake Formation by Zheng et al. (2015a) or the Keziluoyi Formation by Bosboom et al. (2014a,c). To avoid misunderstanding on this issue we here attribute this unit to the "non-marine time-equivalent of the Bashibulake Fm". The unit division of this study begins above the Eocene – Oligocene transition and is marked by a facies change to coarser lithologies. We assign our units A-C to the Kezilouyi, Anjuan and Pakabulake formations and units D and E to the Artushi (also known as the Artux) Formation following Zheng et al. (2015a). Overlying the Artushi Formation are the extensive conglomerates of unit F assigned to the Xiyu Formation as described by Zheng et al. (2015a) but contrary to the regional geologic map (Wang and Peng, 2013) where this conglomeratic formation is labelled as the Artux Formation. (N1a).

5.5.1.2 Compilation of previous magnetostratigraphic records of western Tarim Basin

Several Cenozoic sections have been dated using magnetostratigraphy along the western margin of the Tarim Basin with variable reliability as described below (Figure 5.1). The best dated and most complete section is the Aertashi section reported here. It therefore constitutes a reference section for comparison with the other sections in the region.

Kekeya section (South Tarim): The dating of this section by Zheng et al. (2000) was re-interpreted as much older in Zheng et al. (2015a) due to the discovery of a volcanic ash layer which allowed re-calibration of the magnetostratigraphy. Zheng et al. (2015a) provided two alternative magnetostratigraphic correlations, one which they proposed fitted the magnetostratigraphic data better, the other which they proposed fitted the field and stratigraphic correlation better, in particular their view that the Xiyu Formation conglomerates which are well dated at Aertashi at ca 15 Ma, are coeval with the Xiyu conglomerates at Kekeya. This led them to choose the latter as their preferred correlation. However, given that the Xiyu conglomerates have been shown to be extremely time transgressive (Charreau et al., 2009, Heermance et al., 2007), and that the Xiyu conglomerates at Aertashi are derived from the Pamir to the West (Blayney et al., 2016 and Chapter 4 of this study), it seems unlikely that the Xiyu Formation at these two locations, affected by different tectonics at that time, are co-eval. We therefore take the alternative correlation of Zheng et al. (2015a) which is stronger in terms of correlations of observed polarity zones to the GPTS, and propose yet an alternative correlation for the lower part of the section. Using this strongest correlation, a hiatus is present in the sedimentary record in the interval from 25 to 20 Ma (See Figure 5.11). This portion of the stratigraphy corresponds to the onset of growth strata documented in the nearby Qipan seismic section (Wang and Wang, 2016) and therefore most likely corresponds to sediment accumulation disturbed by 'continuous unconformity' of the growth strata. This correlation also fits much better with the record of the nearby Sanju section which also shows conglomerate deposition starting as early as 20 Ma (Cao et al., 2015).

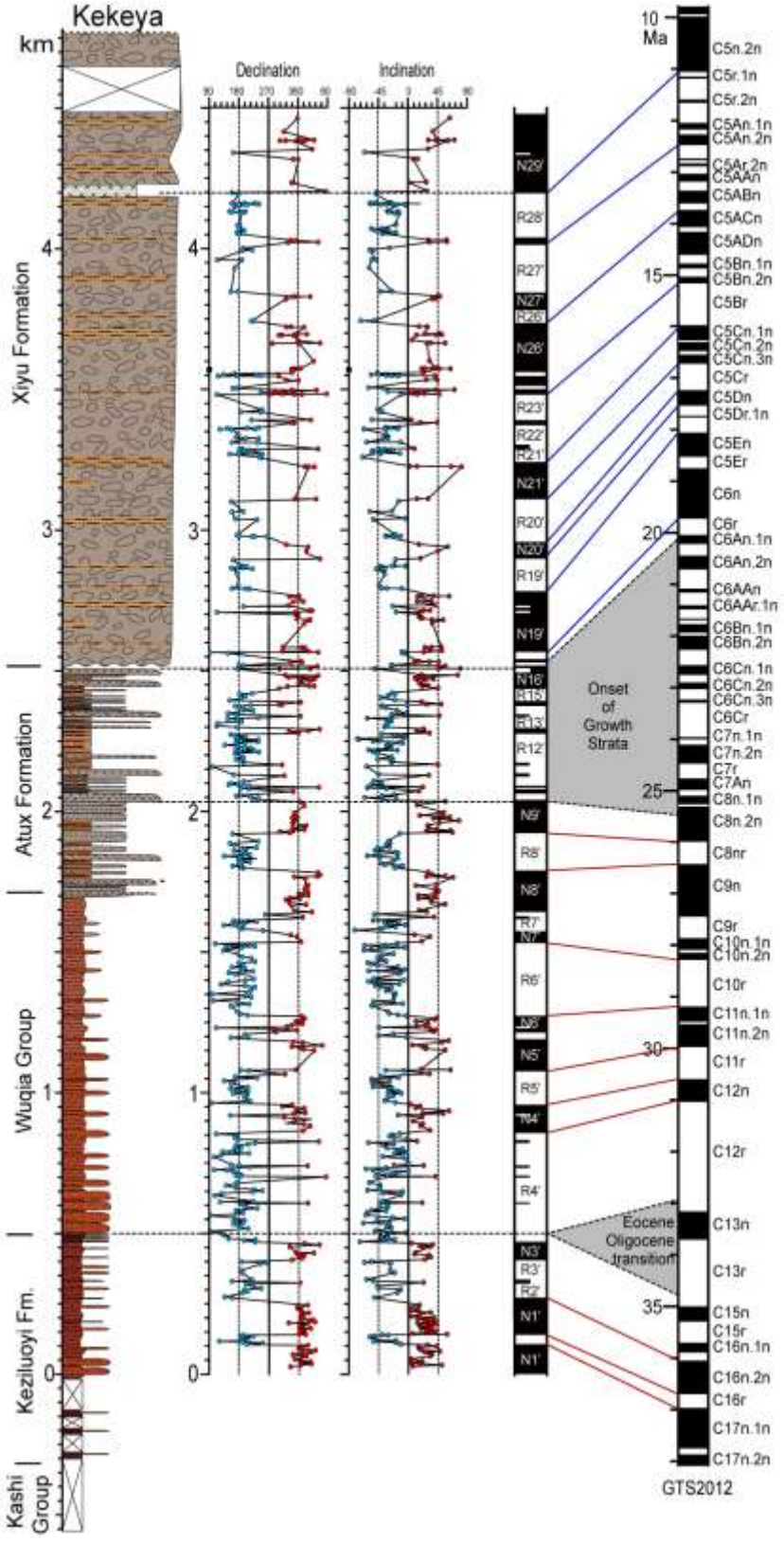

Figure 5.11 Paleomagnetic results and correlations with GTS2012 for the Kekeya section (modified from Zheng et al. (2015a)). The blue and red correlation lines represent the 2 originally proposed correlations of Zheng et al. (2015a) combined here into a single unified correlation based on the recognition of an expected zone of poor correlation (shaded grey) that correlates with the onset of growth strata identified by Wang and Wang (2016). See Zheng et al. (2015a) for explanatory legend of lithologic log and paleomagnetic results.

Sanju section (South Tarim). Sun and Liu (2006) provide a very young Pliocene age for the mostly conglomeratic deposits in this section. However, these ages have been re-interpreted by (Cao et al., 2015) as much older, from about 20 to 10 Ma, based on detrital zircon U-Pb and fission track ages. Here we follow the ages proposed by (Cao et al., 2015) but we re-interpret that the section actually comprises the same conglomerates as found starting also at 20 Ma in the Kekeya section (see above). This seems reasonable, given that both locations are along strike and most likely governed by the same tectonics along the northern margin of the northern Tibetan Plateau. This would imply that the Sanju section comprises only the Xiyu Formation and not the Pakabulake Fm as defined in the Kekeya section. The onset of conglomeratic deposition is actually not reported in the Sanju section and is probably lower, below the logged outcrop.

Ulugqat (Mine) section (Northwestern Tarim): Here, Yang et al. (2015) report a reliable magnetostratigraphy partly constrained by detrital apatite fission track ages. The onset of continental clastic deposition is found at 20.8 Ma above a very large hiatus on the marine Priabonian Bashibulake Formation. This study also reports an onset of coarse clastics and conglomerates between 15 and 14 Ma. The provenance of this section is the Tian Shan to the North as indicated by detrital zircon U-Pb age distributions (Yang et al., 2014).

Other magnetostratigraphic results have been reported, in particular at Keliyang (Sun et al., 2016a), from the Mazatagh (Sun et al., 2009, Sun et al., 2011) or at Oytag (Sun and Jiang, 2013) but we prefer to omit reinterpreting them here because the ages are found to be not sufficiently reliable due to the lack of acceptable magnetostratigraphic correlations, dubious biostratigraphy, and/or insufficiently described lithologies to make valid and useful stratigraphic correlations in the scheme of the present study.

Our compilation and re-interpretation highlights at around 25-20 Ma growth strata and conglomerates were deposited in the south (Kekeya and Sanju sections) which coincides with the onset of continental deposition in the north (Ulugqat section). This suggests regional subsidence and tectonic activity in this time frame although the records can be time-transgressive as previously evidenced for northern Tarim and around the Tian Shan range (Heermance et al., 2007, Charreau et al., 2009).

5.5.3 Implications of the post-15 Ma 14° clockwise rotation; constraints on Pamir arc formation models

Part of the observed rotation as documented at Aertashi may relate to wholesale clockwise rotation of the Tarim Basin. Previous paleomagnetic studies from the nearby Qimugen section but also from central and southern Tarim have also documented ca. 15° clockwise rotation in loosely dated Miocene sediments (Dupont-Nivet et al., 2002, Gilder et al., 2001, see review in Bosboom et al., 2014b). However, these rotations may also be related to local structures, such that the long term Tarim rotation remains poorly quantified. Nevertheless, based on geometric considerations, Avouac et al. (1993) first estimated a maximum 7.0 ± 0.25° of clockwise rotation of the Tarim Basin about an axis at the eastern end of the basin (96°E; 43.5°N). This would explain the shortening in the Tian Shan increasing to ca. 203 ± 50 km at the western end of the Tarim Basin (see also Van Hinsbergen et al., 2011). This has been substantiated by GPS measurements indicating present clockwise rotation of the Tarim Basin about an axis at its eastern end at rates of 11 ± 1 nrad/yr (Shen et al., 2001) or 0.6 ± 0.06°/Myr assuming this rate has been steady and can be extrapolated far back in time. At this rate it would take at least ~12 Myrs to rotate 7° which is consistent with the post 15.0 Ma rotation that we find and therefore suggests that up to half of the recorded rotation may have been accommodated by wholesale Tarim rotation. This also indicates that at least half of this rotation must be attributed to more local processes directly associated with Pamir indentation.

The distribution of vertical-axis rotations within the Pamir salient in response to various models of indentation has been well described by Cowgill (2010). Indentation is associated with rotations when accommodated by radial thrusting or oroclinal bending (or buckling). It is non-rotational if indentation is accommodated by transfer faulting on both sides of the salient. Based on the observations that counter-clockwise rotations are large (20 to 40°) and pervasive west of the Pamir in Cretaceous to Miocene sediments in the Afghan-Tajik Basin (Thomas et al., 1996, Bourgeois et al., 1997) but that clockwise rotations were not recorded to the east in the Tarim Basin. Cowgill (2010) proposed a model in which the Pamir indentation has been accommodated by radial thrusting to the west and transfer faulting to the east. However, Bosboom et al. (2014b) later reported results showing systematic clockwise rotations at the Aertashi and Kezi (near Qimugen) sections that seemingly ceased by

the end of the Oligocene (Bosboom et al., 2014b and references therein). On this basis, those authors supported the model of Cowgill (2010) for the evolution of the Pamir salient but from Miocene times onward, counter-clockwise rotation continued in the Tajik Basin but ceased in the Tarim Basin. The cessation of rotation in the Tarim Basin has been previously interpreted to have been the result of activation of movement on the KYTS, and thus transfer of indentation movement to dextral strike-slip motion along the eastern margin, with limited distributed shear. However, our new data indicate that most of the rotation occurred sometime after 15.0 Ma, with a small amount prior to this time. The rotation is therefore likely related to the change to indentation and proximal deformation documented in Aertashi after 15 Ma. This age also corresponds to the time when the east-propagating Qimugen Thrust System (QFTS; Figure 5.1), including the Aertashi study area, became active based on growth strata in the Xiyu Formation now dated by this study at 15 Ma (Wei et al., 2013, Wang and Wang, 2016). This suggests that before that time, the study area lay within the footwall in the Tarim Basin and was only slightly affected by the deformation. It is only when the study area became part of the QFTS that it rotated clockwise as described in the radial thrusting model.

Radial thrusting and generally oroclinal bending implies, due to lateral expansion, some along strike extension (Cowgill, 2010) that has been proposed (Strecker et al., 1995, Yin et al., 2001) to explain the 34 km of EW extension since 9-7 Ma in the Kongur Shan of the north eastern Pamir (Robinson et al., 2004, Robinson et al., 2007; Figure 5.1). However, as discussed in Robinson et al. (2004) and Cowgill (2010), the E-W observed extension is perpendicular to the extension directions expected by radial thrusting. Radial thrusting is therefore not the cause for the extension. The observed clockwise rotation of the eastern limb of the Pamir may, however, relate to previously proposed mechanisms of extension associated with the northward propagation of the dextral Karakoram fault along a right-step releasing bend (Ratschbacher et al., 1994, Murphy et al., 2000). The post 15 Ma clockwise rotation of the eastern Pamir limb with the coeval motion on the Karakoram fault is consistent with the formation of a releasing bend. However, further structural investigations are necessary to assess this releasing bend model, in particular the accommodation of the strike-slip motion further north of the bend. Whatever the contribution of the rotation and releasing bend, a large part of the extension is most likely to be related to post-

thickening gravitational collapse of the Kongur Shan (Robinson et al., 2004, Rutte et al., 2017b, Brunel et al., 1994, Thiede et al., 2013).

5.5.4. Synthesis of Basin evolution and its relationship to Pamir tectonics.

41.2-24.3 Ma: The distal effects of India-Asia collision, crustal thickening in the Pamir hinterland and deposition in the foreland basin.

The depositional environments shift at 41.2 Ma from shallow marine to continental deposits with an increase in tectonic subsidence. From then on until 24.3 Ma, the section is characterised by no significant change in depositional environment, accumulation rate, sediment source, or strain direction. Sediment source is from the distant WKL to the south (Blayney et al., 2016). The strain direction from AMS is consistent with NS compression.

The marine to continental facies change has previously been explained as a combination of eustatic sea level fall with the influence of tectonics (Bosboom et al., 2014c). The increase of tectonic subsidence at 41 Ma, followed by its continued increase and exclusively continental clastic deposition favour the proposal that this subsidence is predominantly the result of the distal effects of the India-Asia collision, which had propagated to this region by this time (e.g. Amidon and Hynek, 2010, Rutte et al., 2017a).

The data suggest a distal foreland basin environment (Figure 5.12A) that can be linked to northward thrust loading of thickened Tibetan crust onto Tarim and Pamir since at least 40 Ma (Cao et al., 2014, Rutte et al., 2017b, Jolivet et al., 2001). Regionally, a number of studies suggest a tectonic event at this time, which would be consistent with our suggestion of a collisional cause. It coincides in time with prograde metamorphism in the Pamir which began before ~35 Ma (Rutte et al., 2017b, Stübner et al., 2013b). More generally, tectonism is well-established in northern Tibet between ~50-40 Ma (e.g. Zhao et al., 2016, Clark et al., 2010, Staisch et al., 2016, Duvall et al., 2011).

24.3-18.6 Ma: Propagation of strike slip into the foreland

A long hiatus (24.3-21.6 Ma) is recorded in the Aertashi section, associated with a change from distal foreland basin deposits below, to proximal conglomerates at the

toe of an alluvial fan, deposited above the hiatus from 21.6 to 18.6 Ma. Our new higher resolution Sm-Nd data (Figure 5.6) pick out a change in provenance with increased clarity compared to our previous work (Blayney et al., 2016). Recognition of the disconformity between 24.3-21.6 Ma from our magnetostratigraphic data allow us to place this change precisely above the disconformity at 21.6 Ma. The conglomeratic rocks, which are composed predominantly of sedimentary clasts, require a shallowly exhuming proximal source. This hiatus and change in facies and provenance is synchronous with exhumation recorded by Apatite Fission Track (AFT) ages at the base of the Aertashi section a few kilometres to the west (Sobel and Dumitru, 1997). We discuss the likely origin of this change below.

At the sampled section the 2.7 Myr disconformity (24.3-21.6 Ma), is estimated to represent about 400-metres of sediment lacking given the measured accumulation rate of 150 m/Myr, although some degree of erosion of the underlying sediments is expected given the coarse nature of the overlying unit. This disconformity is most likely linked to the coeval exhumation event reported from Cretaceous strata at the base of the section recorded by Apatite Fission Tracks (AFT) which indicate a minimum of 20.0 ± 3.1 Ma age for the time of cooling below 120-100°C (Sobel and Dumitru, 1997). According to Sobel and Dumitru (1997) the partially annealed tracks and non-uniform age distribution indicates that grains have not been fully reset and are therefore interpreted to have resided near the minimum 120-100°C track annealing temperature before exhumation.

This exhumation from shallow depth is supported by the composition of the overlying conglomerate clasts made principally of shallow cover deposits indicating little unroofing (mainly sandstones and limestone). It is also consistent with the ca. 2-km stratigraphic thickness measured between the marine limestone deposits and the disconformity (Figure 5.2).

The combination of the documented nearby exhumation to the west, and the hiatus overlain by the onset of conglomeratic deposition, together indicate a proximal tectonic structure uplifted to the west of the study site in this time period. Therefore bedrock, provenance and subsurface data together indicate a change which could be interpreted as a shift from southern to western local sourcing at this time.

This exhumed structure resulted in the exposure of ca. 2-km deep Cretaceous strata in the west, and resulted in the ca. 400-metre hiatus at the location of the section, whilst accumulation would continue further eastwards. We believe this structure represents a local manifestation of the India – Asia stress field that had propagated as far north as the Tian Shan by 25 Ma (Sobel et al., 2006) rather than indentation of the Pamir to the Aertashi region by this time, for reasons we outline below.

More regionally, growth strata are indicated from ca. 25-20 Ma from seismic investigations at the Qipan seismic section near Kekeya further south along the KYTS (Wang and Wang, 2016). At this southern location these growth strata are directly followed by the onset of conglomeratic deposits starting around 20 Ma as indicated by dating at the nearby stratigraphic Kekeya section (see Section .5.5.1 above).

At Aertashi, a thick succession of fine sediments is found after the hiatus and lower conglomerates and before the Xiyu conglomeratic arrival at 15.0 Ma. This continuous deposition from 21.6 to 15.0 Ma suggests that the nearby structure at Aertashi did not evolve into a thrust belt propagating eastwards during this time interval or the section would have recorded a coarsening upwards succession, been overthrust and/or fully exhumed.

The continuously increasing subsequent deposition of fine clastics near to the site of exhumation more likely suggests that the structure has a mainly strike-slip component that did not propagate significantly eastwards into the basin. This strike-slip hypothesis is supported by the previously reported synchronous exhumation along the dextral strike-slip system along the western margin of the Tarim Basin (KYTS), which is based on AFT data (ca. 20 Ma exhumation at Kulisaf location; Sobel and Dumitru (1997)), the reported strike-slip flower structure in the subsurface (Wei et al., 2013), and with the N-S trending fold hinges of the growth-strata identified in the Qipan seismic profile by Wang and Wang (2016). Such strike-slip structures have also been mapped in the region by Cowgill (2010).

Therefore, rather than being a direct response to Pamir indentation reaching this location at this time, for which provenance data provide no evidence (Blayney et al., 2016 and Chapter 4 of this study), we interpret the transpressional deformation to the west of Aertashi to be part of the wider regional deformation that was occurring at the time. This includes a dextral transpressional system that stretched from the Kunlun to

the south to as far north as the Tian Shan by 25 Ma where fast exhumation (Sobel et al., 2006), activation of the right-lateral TFF and associated counter-clockwise rotation of the Fergana Basin with exhumation in the horsetail Chatkal ranges (Thomas et al., 1996, Bande et al., 2015, 2017 and references therein) and basin accumulation (Yang et al., 2015) initiated. More regionally, this period coincides with a major change in the geodynamics of the Pamir, from crustal thickening to extension and possible crustal collapse (Amidon and Hynek, 2010, Rutte et al., 2017a,b, Sobel et al., 2013, Stübner et al., 2013a,b) and to a slowing down of India, indicated at 20±2 Ma from 57 to 44 km/Myr (Molnar and Stock, 2009, Iaffaldano et al., 2013).

This change in tectonic regime has been proposed to be effected by either initiation of movement on the Karakoram fault at the time, or a second slab break off of the Indian plate (Amidon and Hynek, 2010, Sobel et al., 2013, Rutte et al., 2017a,b) which occurred at ca 25-20 Ma (e.g. Replumaz et al., 2010, Mahéo et al., 2009, Stearns et al., 2013, DeCelles et al., 2011 and references therein).

In the intracontinental subduction model, Sobel et al. (2013) propose that following slab break-off, the build-up of stress due to continued northward convergence from India to the south, resulted in inception of continental subduction of a south-dipping slab beneath the Pamir (e.g. Replumaz et al., 2010). Subsequent stress release and roll-back of the south-dipping slab resulted in the exhumation in the Central Pamir. The timing of prograde metamorphism in the Pamir was not available when the model of Sobel et al. (2013) was published; therefore this model should be revised to suggest that south-dipping subduction started shortly after the second Indian-plate break-off.

By contrast, in the delamination model, Rutte et al. (2017a,b) propose that the slab break off led to a change from subduction to underthrusting of the Indian plate beneath Asia. In this model, the ~22 Ma collapse documented in the Pamir could relate to the foundering, delamination and roll-back of its lithospheric mantle in response to the northward motion of the thicker continental Indian lithosphere from 22 to 12 Ma under the Pamir terranes. Part of this collapse has been proposed to be accommodated by westward as well as northward thrusting of Pamir terranes towards Tarim during this time (Rutte et al., 2017a,b). Either of these mechanisms, northward collapse or subduction roll-back, is potentially responsible for the northward compression and the onset of crustal Pamir indentation into Tarim at this time.

18.6-15.0 Ma: Increasing tectonic subsidence in the Tarim depocenter around Aertashi.

From 18.6 to 15.0 Ma, fine clastics accumulated at Aertashi with drastically increasing rates. Despite the nearby structural activity described above, the grain size remained fine and the source remains unchanged with no sign of contribution from the Pamir or deeper crustal levels. In the same time interval, mostly conglomerates are deposited along the southern margin of Tarim with exhumation associated with northward thrusting of the Kunlun hinterland (see Section 5.5.1 above; (Cao et al., 2015). To the north along the north-western Tarim margin, increasing accumulation rates and southward propagation of conglomerates suggest southward migrating foreland deformation associated with continuing southwestern Tian Shan exhumation (Yang et al., 2015, Heermance et al., 2007).

Reconstructed isopach maps of formations corresponding to this time interval (see Wei et al. (2013) and Figure 5.3d where the Anjuan Fm is interpreted as Pakabulake Fm. here and Figure 5.3e where the Pakabulake Fm is interpreted as the Artux Fm here, see Section 5.5.1) indicate the Tarim depocenter is situated around the Aertashi-Qimugen area towards the middle of the western Tarim margin at this time. We therefore consider that the increasing subsidence and accumulation at Aertashi may relate to a regional signal of deformation of the entire Tarim Basin due to regional loading and overthrusting by the basin margins, although the nearby strike slip structure may also have influenced the location of the depocenter and local stress field in the area. Bande et al. (2015) proposed a pull-apart basin for the region, bounded by the KYTS to the west and the Sache-Yangdaman fault (SYF) (a southern continuation of the TFF) to the east.

In post-17 Ma sediments, AMS fabric records a change in the strain orientation from generally N-S to E-W compression. Because the timing of acquisition of this AMS strain fabric is post-depositional, the timing of the observed shift can only be determined as sometime after 17 Ma. It could be a late manifestation of the effects of the KYTS dextral transpressional deformation, or an early response to the Pamir indentation approaching the latitude of Aertashi, as discussed below.

15 Ma to recent: Pamir indentation reaches and exceeds the latitude of Aertashi

At ~15.0 Ma a major shift to proximal alluvial fan grey conglomerates is recorded with a provenance from the North Pamir terrane to the west, suggesting that the North Pamir was proximal to Aertashi by this time (Blayney et al., 2016). The transition occurs within a few tens of metres (Figure 5.2) but is gradual with increased occurrences of grey gravelly beds within continuing red clastic beds suggesting no large hiatus. Between 15.0 and ca. 11 Ma a doubling of accumulation rates is estimated by available time constraints from this dominantly conglomeratic section (see Section 5.4.2). The occurrence of fresh volcanic detritus (Blayney et al., 2016) in the section at 11 Ma in the Aertashi record, conspicuously corresponds to the age of the 11 Ma Dudelick volcanics (Hacker et al., 2005) from the Central Pamir terrane recently re-analyzed by Kooijman et al. (2017). These volcanics constitute the only known source for a volcanic component in the Aertashi sediments and leads us to propose here that the volcanic-rich detritus is sourced from these Dudelick volcanics. This suggests that the Aertashi sediments are recording the northward motion of the North Pamir terrane at 15 Ma and then Central Pamir terrane at 11 Ma. This age also corresponds to the clockwise rotation (see above) and the suggested onset of the Qimugen thrusting (Wei et al., 2013). This together indicates the tectonic setting changed drastically at 15 Ma in response to east-verging thrusting of the Pamir onto Tarim. The post 15 Ma clockwise rotation and the presence of the North Pamir terrane nearby the location of the Aertashi section at 15 Ma and Central Pamir terrane at 11 Ma provides important kinematic constraints on the timing and position of the Pamir indentation into Tarim.

In the Pamir, this period corresponds to resumed shortening documented at ~12 Ma with opposite-sense thrusting and folding focused along the dome margins. This also corresponds to the further decrease in Indian northward velocity from 44 to 34 km/Myr estimated at 11 ± 2 Ma (Molnar and Stock, 2009). This resumption of crustal thickening has been interpreted, in the subduction-driven model of Sobel et al. (2013), to a change in the degree of coupling between the down-going and over-riding slab resulting in renewed crustal thickening. In the delamination model of Küfner et al. (2016), it is interpreted to result from the underthrusting of cratonic India reaching the latitude of, and impinging on “cratonic” Asia since 10 Ma. In the latter model, the northern edge of cratonic India is retro-positioned 350 km to the south (Molnar and

Stock, 2009) suggesting the onset of Pamir indentation at 10 Ma with delamination accounting for the entire ca. 300 km northward indentation since that time. However, our data imply that indentation was already underway by 15 Ma, with about half of the 300 km consumed when the northern Pamir reached the latitude of Aertashi. Furthermore, the KYTS activity and regional deformation at 25-20 Ma suggests that indentation had started at this time. In contrast, these geologic constraints are not inconsistent with the timing and evolution of the subduction model. We note that if the northward Pamir indentation into the Tarim and Tajik basins started only after 10 Ma (Küfner et al., 2016), the proposed coeval westward gravitational collapse and extrusion of Pamir into the Tajik Basin (Rutte et al., 2017a,b) becomes problematic.

Since 15 Ma, the rest of the 300 km indentation is accounted for by the subduction model to until about 5-3 Ma when the KYTS becomes mostly inactive (Sobel et al., 2011, 2013). According to the delamination model and Indian plate velocities (Küfner et al., 2016, Molnar and Stock, 2009), the position of the northern edge of the Indian lithospheric indentor can be estimated to reach the present position of Aertashi only around 5 Ma. This is not consistent with our observations of Pamir detritus and thrusting at 15 Ma at Aertashi. In addition, in the delamination model a large part of the Pamir indentation into Tarim remains to be accommodated after 5 Ma although the slip on the KYTS has mostly stopped by then.

Sobel et al. (2011) suggested that the KYTS may have become inactive due to the northward motion of Tarim moving coherently with the Pamir similar to today (Ischuk et al., 2013, Zubovich et al., 2016). Taking into account the northward motion of Tarim also has implications for the delamination model. Assuming a maximum of 200 km northward motion since 12 Ma (as predicted by Avouac et al. (1993) based on maximum Tian Shan shortening, see Section 5.5.2) would imply Aertashi may have been positioned as much as 200 km further south at this time. Interestingly, it can be estimated that this position would have been reached by the Indian lithospheric indentor around 11±2 Ma based on Indian plate velocities (Molnar and Stock, 2009). Only in this extreme scenario could the delamination model account for some of our observations at Aertashi, assuming the 15 Ma onset of Pamir source and deformation preceded the arrival of Indian lithospheric indentor by a few million years. In this view the post 15 Ma indentation of Pamir moving northward slightly faster than Tarim would be driven by the Indian lithospheric indentor.

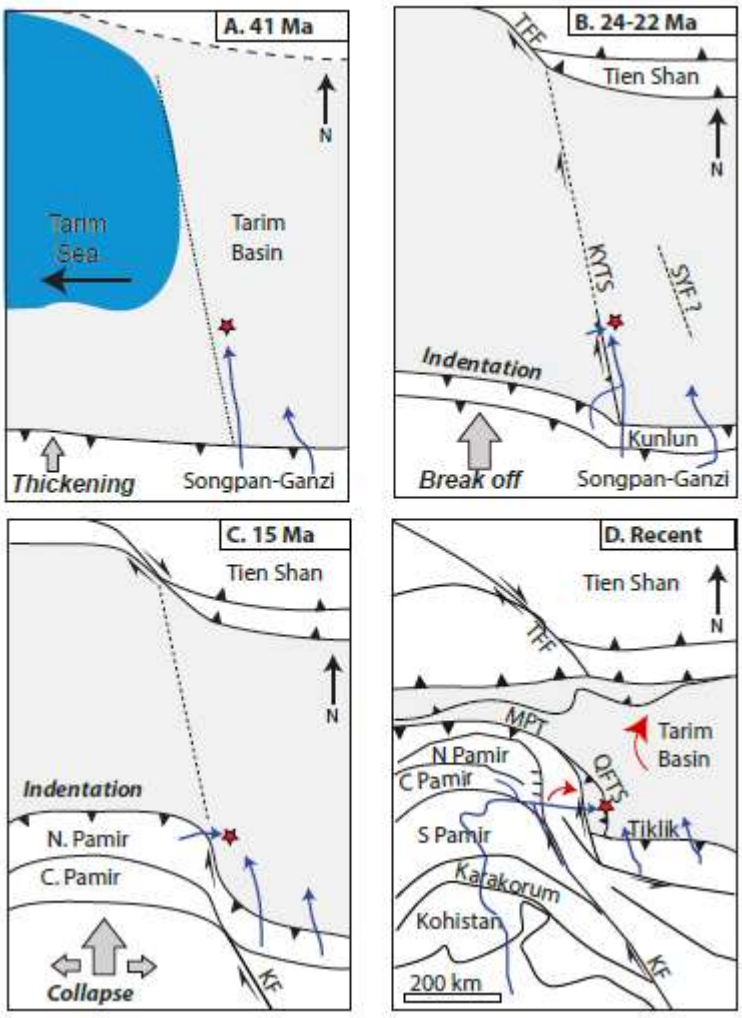

Figure 5.12 Model of the evolution of the Pamir salient (modified from Bande et al. (2015) and Blayney et al. (2016)) and palaeodrainage pattern (in blue) interpreted from the sedimentary record at Aertashi. The grey arrows indicate the direction of movement. (a) 41 Ma The Songpan-Ganzi terrane forms raised topography such that the Aertashi section receives sediment from northward flowing rivers, Tarim sea retreat from Aertashi recorded by Bosboom et al. (2011)(b) Basinward expansion of the NW margin of Tibet, and initiation of Pamir indentation as the North and South Kunlun terranes exhume and the KYTS and Tiklik Thrusts initiate. Activation of strike slip faulting, growth strata and exhumation along the KYTS (and possibly the SYF system) resulting in the deposition of Unit D from a proximal source near Aertashi. (c) 15 Ma Indentation of the Pamir Salient now proximal to Aertashi marked by the onset of a major sequence of conglomerate deposition and source change. (d) Recent; the catchment area of the modern Aertashi River. The embryonic establishment of the modern drainage initiated after 11 Ma. Red star = Aertashi section, KYTS = Kashgar Yecheng Transfer System, SYF = Shache-Yangdaman fault, TFF = Talas-Fergana fault, MPT = Main Pamir Thrust, PFT = Pamir Frontal Thrust, QFTS = Qimugen Frontal Thrust System, KF = Karakorum fault.

5.6. Conclusions

Our results from the Tarim Basin Aertashi section provide the most complete sedimentary record of the Pamir indentation, revealing the following accurately-dated sequence of tectonic events (Figure 5.12).

41.2-24.3 Ma. The transition of marine to continental facies recorded in Aertashi and increased clastic sediment accumulation is related to an increase in tectonic subsidence. This is interpreted as a response to crustal thickening in northern Tibet and Pamir further south which is ascribed to the northward propagation of the effects of India - Asia collision (Figure 5.12A).

24.3-18.6 Ma. A depositional hiatus (24.3-21.6 Ma) and subsequent first influx of conglomerates at Aertashi is related to nearby exhumation and uplift associated with dextral transpressional deformation along the KYTS (Sobel and Dumitru, 1997). This is linked to the regional propagation of deformation from the Kunlun to the Tian Shan ranges through the dextral strike slip system which implies onset of Pamir indentation into the southern margin of the Tarim (Sobel et al., 2006, Jolivet et al., 2001, Cao et al., 2015). This is coincident with a slowing down of the northward indentation of the Indian plate, the initiation of movement on the Karakoram fault and slab break-off of the Indian plate (e.g. Molnar and Stock, 2009, Mahéo et al., 2009) (Figure 5.12B).

18.6-15.0 Ma The increasing accumulation of fine clastic deposition is interpreted, in combination with the local influence of KYTS, as increasing tectonic subsidence in the Aertashi region that constitutes, by this time, the Tarim Basin depocenter in response to regional deformation from thrust loading of the Kunlun and Tian Shan (Wei et al., 2013) (Figure 5.12B).

15.0 Ma – recent; Proximal alluvial fan conglomerates sourced from the North Pamir Terrane appear at ~15 Ma in Aertashi, suggesting the Pamir indentor had reached this location. Since 15 Ma a 14° clockwise rotation is associated with the activation of the east verging Qimugen thrust sheet indicated by growth strata observed on nearby seismic lines (Wang and Wang, 2016). In addition, diagnostic 11 Ma volcanics from central Pamir are found higher in the conglomeratic sequence (Hacker et al., 2005, Kooijman et al., 2017). This together suggest that Pamir indentation detritus and deformation reached Aertashi at 15.0 Ma and moved northward until at least 11 Ma (Figure 5.12 C, D).

These kinematic constraints on Pamir indentation are not inconsistent with proposed tectonic models involving continental subduction since 25 Ma (Sobel et al., 2013) and are inconsistent with delamination driven roll back models that imply indentation since ca. 10 Ma (Küfner et al., 2016, Rutte et al., 2017a). The timing of the Pamir indentation since 25-20 Ma progressively shielded the westerlies providing constraints for the associated Asian desertification. Gradual aridification since 41 Ma due to sea retreat and increased orographic effects from the Tibetan Plateau is expected (Bosboom et al., 2015, Bougeois et al., 2014), but most of the environmental changes should be linked to the Pamir indentation shielding the westerlies in addition to Tian Shan uplift (Bougeois et al., Submitted, Caves et al., 2015 and Chapter 6 of this study). This indentation driven aridification probably started around 25-20 but should have really influenced strongly only since 15 Ma and increasing until recently as the indentation of Pamir reached the uplifting Tian Shan to fully close the influence of the moisture source from the west.

Acknowledgements

This work was funded by a NERC PhD Studentship to Blayney (grant no NE K501001-1), and by a VIDI grant from the Netherlands Organization for Scientific research (NWO), an ERC consolidator grant MAGIC, ANR DSP-Tibet and support from the Alexander von Humboldt to Dupont-Nivet. We would like to thank Annabelle Bernard, Laura Fielding, Chris Kneale, and our guides Kasim and Khader for their contributions in the field, and Guangsheng Zhuang for his considerable efforts in getting our samples safely back to the UK. We thank Sofia Küfner for enlightening discussions on deep processes.

6. The Climate Evolution of the Western Tarim Basin during Pamir indentation

Tamsin Blayney[1], Yani Najman[1], Guillaume Dupont – Nivet[2,3,4], Simon J Kemp[5], Peter Wynn[1].

1. Lancaster Environment Centre, Lancaster University, Bailrigg, Lancaster, LA1 4YQ, UK
2. Géosciences Rennes, UMR-CNRS 6118, Université de Rennes 1, Rennes, France, and Department of Earth and Environmental Sciences, Potsdam University, Germany, and Key Laboratory of Orogenic Belts and Crustal Evolution, Ministry of Education, Beijing, China
3. Institut für Erd- und Umweltwissenschaften, Universitäet Potsdam, Potsdam, Germany.
4. Key Laboratory of Orogenic Belts and Crustal Evolution, Ministry of Education, Beijing, China.
5. British Geological Survey, Environmental Science Centre, Nicker Hill, Keyworth, Nottingham NG12 5GG, UK

Abstract

The formation of the Himalayas and surrounding mountain ranges is one of the most significant tectonic events of the Cenozoic, with far reaching impacts on both regional and global climate. Prior to the India–Asia collision, central Asia was home to the Tarim Sea which provided a critical moisture source to central Asia. During the Eocene at ~ 41 Ma, the Tarim Sea retreated from the Tarim Basin, marking the onset of aridification throughout central Asia and culminating in the formation of the Taklimakan Desert. Aridification continued in a stepwise fashion throughout the Cenozoic. However, it is difficult to deconvolve the influence of tectonics from global climate change in central Asia. Previous climate studies are hampered by poor age control within central Asia and in particular the Tarim Basin. Here we present a detailed stable isotopic, geochemical and clay mineralogical study from a well-dated sedimentary section along the western margin of the Tarim Basin (Aertashi). These analyses are used as climate proxies in order to better understand the timings and mechanisms relating to the climatic evolution of this region in the Cenozoic. We observe the appearance of kaolinite between 17.6 and 15 Ma, accompanied by

increased total organic carbon (TOC) and a decrease in magnetic susceptibility χ which may be related to the Mid Miocene Climatic Optimum (MMCO). A shift to more positive $\delta^{13}C_{org}$ values at 18.5 Ma may be an early manifestation of the effects of the MMCO. However, this could also reflect onset of C_4 vegetation in the area driven by increased aridity. Onset of smectite occurrence between 30 and 28 Ma may relate to a climatic shift due to the onset of an early Oligocene aridification event, to an increase in aridity related to eustatic sea level fall, or a facies change recorded at this time. Comparison of signals in different sedimentary sections, achieved through improved age control, is required to distinguish between these factors.

6.1 Introduction

The inter-relationship between orogeny and global climate change in effecting the progressive aridification of Asia during the Cenozoic is highly debated and complex. One of the key drivers in climate change during the Cenozoic has been linked to the collision of India with Asia and the resultant formation of the Himalayan and surrounding mountain ranges (Zhang et al., 2007b, Raymo et al., 1988, Ruddiman and Kutzbach, 1989, Harris, 2006, Zachos et al., 2001, Caves et al., 2014). Asian monsoonal climate and desertification in central Asia is attributed in a large part to these orogenies; this is due to the resultant creation of orographic barriers, removal of moisture sources and alteration of atmospheric circulation (Molnar et al., 2010, Wu et al., 2012, Liu et al., 2012b, Dupont-Nivet et al., 2007, Bosboom et al., 2011). However, a highly seasonal, semi-arid environment in Asia and Mongolia has been reported as early as the Cretaceous (Jiang et al., 2008, Hasegawa et al., 2009, Chen et al., 2013), indicating that these orogenies may only have accelerated aridification and are not likely to be causal.

In addition, during the Cenozoic global climate also changed drastically. This creates difficulties deconvolving localised effects from global ones.

The global climate in the Paleogene, is marked by a key shift in tectonics with the opening of seaways surrounding Antarctica. This resulted in the thermal isolation of the Antarctic continent, leading to the formation and expansion of extensive ice sheets and a reorganisation of ocean currents (e.g. Livermore et al., 2005, Barker et al., 2007, Barker, 2001, Lagabrielle et al., 2009, Scher and Martin, 2006, Kennett, 1977, Exon et al., 2004). In addition, during the mid-Eocene, large amounts of carbon were removed

from the ocean/atmosphere system through increased siliceous plankton productivity and marine carbon burial (Pearson and Palmer, 2000). In addition, silicate weathering of the uplifting Himalaya and Tibetan Plateau in the Paleogene (Raymo et al., 1988, Ruddiman and Kutzbach, 1989) affected additional CO_2 draw down, resulting in a reduction of the greenhouse effect. These effects combined drove a long term change in the climate from 'greenhouse' to 'icehouse' conditions. Thus the deconvolution of the influence of global climate change versus regional tectonics on the climate of central Asia is an ongoing research question.

Today, central Asia is located far from the ocean, cut off from the effects of the Asian monsoonal systems to the east and south and from the westerly air flow from the west by the surrounding mountain ranges. What was once a vast internal sea is now home to the Taklimakan Desert, China's largest, driest and hottest desert.

Dust from the Taklimakan Desert contributes substantially to the global aerosol system, allowing it to play a significant role in modulating global climate (Uno et al., 2009). Yet in spite of its importance, the time of its formation is debated with onset of desertification proposed to have occurred any time between ~26.7 Ma (Zheng et al., 2015a) and ~3.4 Ma (Sun et al., 2011).

Regionally, a highly seasonal climate has been recorded in the Western Tarim Basin since at least the Eocene (Licht et al., 2014, Huber and Goldner, 2012, Caves et al., 2014, Zhang et al., 2012, Zhang et al., 2007b, Bougeois et al., Submitted, Sun et al., 2010). This has been progressively subjected to continued aridification in a stepwise manner throughout the Cenozoic (e.g. Harzhauser et al., 2016).

This paper seeks to provide further constraints on the timing and mechanisms of climate shifts in the western Tarim Basin. A range of proxies are applied to a sedimentary section from a strategically selected sample site, Aertashi, in order to better understand the development of central Asian climate.

6.2 Geological background

6.2.1 Global climate during the Cenozoic

The regional context of climatic change in central Asia is superimposed on a global cooling trend from the mid-Eocene to the early Oligocene, which marked a key shift from a relatively ice-free world to the formation of continental ice sheets in Antarctica

(Zachos et al., 2001). These ice sheets remained a substantial feature of the global climate system throughout the Oligocene (DeConto and Pollard, 2003, Miller and Mountain, 1996, Zachos et al., 1994).

By the late Oligocene, commencing ~28 Ma, a global warming trend began (Wright and Miller, 1993, Zachos et al., 2001). This is known as the Late Oligocene Warming Event (LOWE) and continued throughout the early Miocene. During this time, global ice volume remained low (Zachos et al., 2001 and references therein) with the exception of a number of short glacial periods known as Miocene isotope (Mi) events (Wright and Miller, 1993). The general warming trend in the early Miocene culminated in the Mid Miocene Climate Optimum (MMCO) at around 18-15 Ma (Flower and Kennett, 1994, Zachos et al., 2001, Wright and Miller, 1993, Sun and Zhang, 2008). The MMCO was characterised by a warmer, wetter climate with mid-latitude warming as much as 6°C higher than today (Savin et al., 1975, Shackleton and Kennett, 1975). The MMCO ended at ~15 Ma with the onset of a global cooling event (Mi3/4), which has been related to an expansion of the East Antarctic Ice-Sheet (EAIS) (Flower and Kennett, 1994, Zachos et al., 2001, Miller and Mountain, 1996).

An extensive cool and dry period followed, known as the 'Middle Miocene climate transition'. This drop in global temperature coincides with a reduction in CO_2 levels (Zachos et al., 2001, Tipple and Pagani, 2007, Pagani et al., 2005) which played a significant role in the evolution of C_4 plants globally (e.g. Tipple and Pagani, 2007, Ehleringer et al., 1997). A gradual rise in $\delta^{18}O$ of benthic foraminifera throughout the late Miocene (~10 Ma) until the early Pliocene was marked by additional cooling and ice sheet expansion in Antarctica and the development of ice sheets in the Arctic (Zachos et al., 2001).

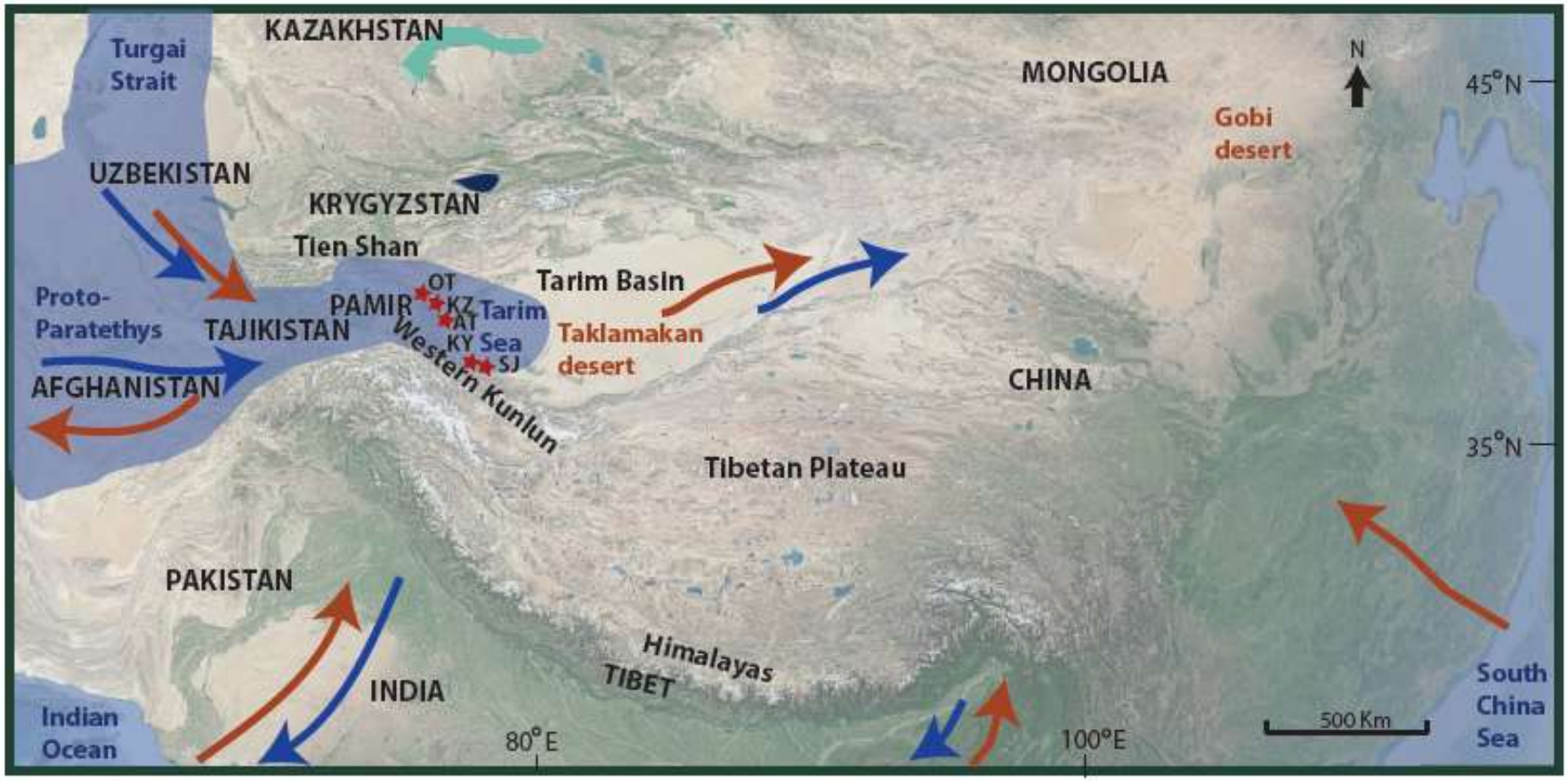

Figure 6.1 Overview of central Asia with the Westerlies and South Asian wind patterns during the Eocene imposed on the modern day geography of central Asia. Blue Proto-Para-Tethys and Tarim Sea indicates the extent of the 4th marine incursion into the Tarim sea in the early Eocene at ~41 Ma (Bosboom et al., 2014a). The dry summer wind patterns are illustrated with red arrows and the 'wetter' winter wind patterns in blue, key study sites are indicated with red stars OT=Oytag, KZ = Kezi, AT = Aertashi, KY= Keliyang and SJ = Sanju. This figure is based on palaeoreconstructions by Bosboom et al. (2014a) and Bougeois et al. (Submitted) .

6.2.2 Regional climate of central Asia, in particular the Western Tarim Basin, during the Cenozoic

Prior to the India–Asia collision, central Asia was home to a vast internal sea; the Tarim Sea which formed the easternmost extent of the Para-Tethys and provided a critical moisture source to central Asia from the Cretaceous to Eocene (Figure 6.1). However, throughout this time the Tarim Sea progressively retreated from the Tarim Basin in a series of five steps with the last major retreat at ~41 Ma, as recorded at Aertashi (Bosboom et al., 2014c), followed by a minor advance and retreat at ~37 Ma, only recorded at the north-western most edge of the Tarim Basin (Bosboom et al., 2011, 2014c). The retreat of the Tarim Sea coincided with a marked aridity shift in central Asia at ~40 Ma based on lithofacies and pollen records from the Kezi, Aertashi and Keliyang sections (Bosboom et al., 2011, 2014c) (Figure 6.1). This aridification trend continued through to the present day, eventually leading to the formation of the Taklimakan Desert (Uno et al., 2009, Zheng et al., 2015a). Aridification is thought to have advanced in a stepwise manner, punctuated by wetter periods (Harzhauser et al., 2016), and with spatial as well as temporal variation. Seasonality in Asia was already established in the early Paleogene (Sun and Wang, 2005, Licht et al., 2014, Bougeois et al., Submitted) (Figure 6.1). However, the seasonality in the western Tarim Basin was dominated by the Westerlies, while the South or East Monsoon controlled seasonality further east and south (Caves et al., 2015). From at least Eocene times, the Westerlies carried moisture from the Para-Tethys and Atlantic into Tarim and contrary to modern conditions, this seasonality was controlled by higher precipitation in the winter and a dry summer. A reorganization of the climate system must have occurred in the Oligocene to Miocene before the establishment of the modern inverted seasonality in the Tarim Basin with recycled limited moisture (Bougeois et al., submitted). Little information is available for the Western Tarim Basin for the Eocene and Oligocene when this change must have occurred (Figure 6.1).

The summary below incorporates the recent re-dating of many of the sections presented in chapter 5 (Figure 6.2), with revised inferences. This includes the Aertashi section studied by Kent-Corson et al. (2009) with age control revised by Zheng et al. (2015a) and chapter 5 of this study, the Qimugen section studied by Wang et al. (2013) with age control revised by Cao et al. (2014) and the Sanju section studied by

Sun et al. (2009, 2013a) and Sun and Liu (2006) with age control revised by Cao et al. (2015).

Clay mineralogy recorded in the Qimugen section (Figure 6.2) along the Western Tarim Basin by Wang et al. (2013) indicates that the Tarim Basin underwent a distinct change from a warm and humid climate to a cold and dry climate during the late Eocene (41 Ma revised age). This is marked by an absence of kaolinite in this part of the section, which coincides with the transition from marine to continental deposits. Kaolinite reappears towards the top of the section sometime between ~18-15 Ma (revised age), although age control for this section is poorly constrained. In the lower part of the section, smectite is recorded in the uppermost marine sediments, disappearing just prior to the onset of continental deposition and reappearing in the upper Kezilouyi Formation (the Kezilouyi Fm is estimated to be ~28 Ma in Aertashi by Bosboom et al. (2014c)) . Although age control for this part of the section is below the revised age control of Cao et al. (2014), we estimated the reappearance of smectite to be sometime in the mid-Oligocene.

Kent-Corson et al. (2009) analysed stable $\delta^{18}O$ and $\delta^{13}C$ of inorganic carbonate from the Aertashi sedimentary section and further east in the Tarim Basin and central Asia, in order to assess the tectonic, topographic and climatic evolution of the region (see supplementary material 4 for a comparison of this study with the work of Kent-Corson et al. (2009)). They noted that for many of the sections, there was a decrease (i.e. an increase in ^{16}O:^{18}O) in average oxygen isotope values during the Paleogene which they ascribed to a change in water source from low lying regions to more integrated, high altitude drainages as the Tibetan Plateau uplifted to the south. Uplift of the Tarim-bounding ranges or retreat of the Para-Tethys Sea was also ascribed by Bershaw et al. (2012) to explain a similar trend they documented in the region. In contrast, Kent-Corson et al. (2009) recorded that both oxygen and carbon isotope values increase in many of the sections in the Neogene, which they ascribed to a regional increase in aridity and temperature. However, it should be noted that the Aertashi section does not follow this trend with respect to oxygen isotopes. At Aertashi, oxygen isotope values continue to decrease (Kent-Corson et al., 2009); perhaps, we suggest, due to the local effects of the Pamir immediately to the west of the region which over-rode the regional climatic signal.

Zheng et al. (2015a) place initial desertification in the Tarim Basin as early as ~26.7 Ma based on magnetostratigraphy, grain size distribution and SEM imagery from the Aertashi and Kekeya sections, whilst studies from the Sanju section based on stable isotopes and magnetic susceptibility place the onset of desertification at ~15 Ma (based on revised age control as previously discussed) (Sun and Liu, 2006, Sun et al., 2013).

Additional studies of the Mazatagh and KT2 sections (Sun et al., 2011) and the Lop Nor, Sanju, Kuza and Korla sections (Liu et al., 2014) (Figure 6.2) use lithology, grain size analysis, SEM and magnetic susceptibility to place the onset of desertification at ~7-3.4 Ma, although the age control (as discussed above) for these sections contain a range of revised and uncertain ages.

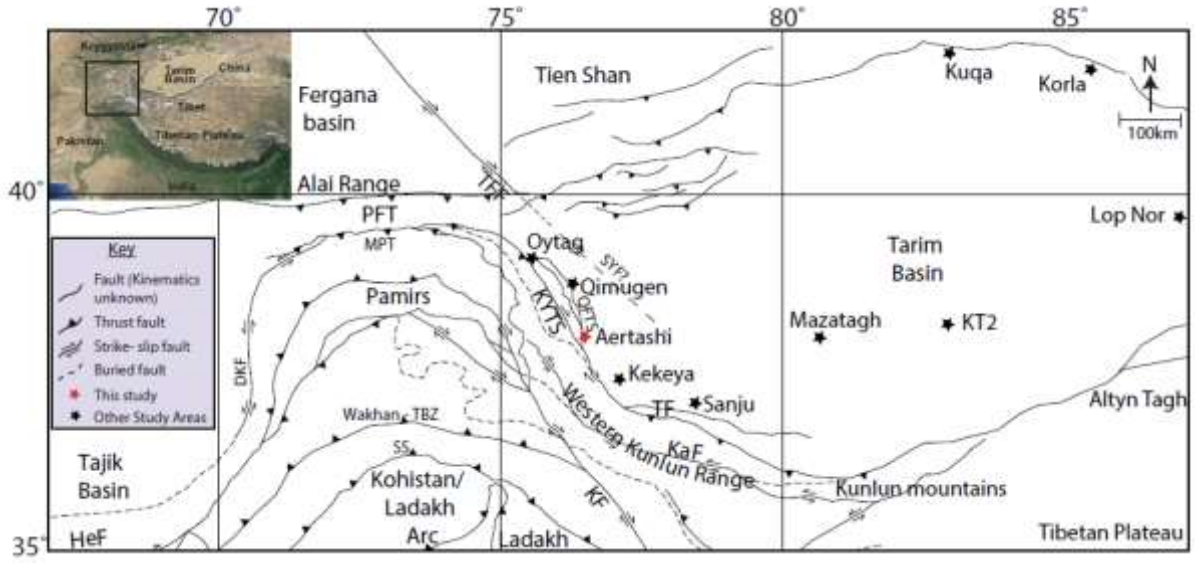

Figure 6.2 Adapted from Sippl et al. (2013) and Sun et al. (2011); summary of the sample locations for the Tarim Basin and surrounding areas. HeF = Herat fault, SS Shyok suture, DKF = Darvaz- Karakul fault System, MPT = Main Pamir Thrust, PTCZ = Pamir – Tian Shan Convergence Zone, TFF = Talas Ferghana fault, SYF = Sache-Yangdaman fault, KYTS = Kashgar-Yecheng Transfer System, KF = Karakorum fault, TF – Tiklik fault, KaF = Karakax fault, QFTS = Qimugen Fold Thrust System. Our study section Aertashi is highlighted with a red star, with other study sections highlighted with a black star; insert shows the location of the Pamir range in its broader region

6.3 Approach and methods

6.3.1 The Aertashi section

The study area is located on the western edge of the Tarim Basin, near the village of Aertashi east of the Pamir (Figure 6.2). The Palaeogene - Neogene section (Figure 6.3c) is composed of the Palaeocene to Eocene Kashi Group, which here comprises the Aertashi, Qimugen, Kalatar, and Wulagen formations and records a series of marine transgression-regression sequences preceding the final retreat of the Tarim Sea (Bosboom et al., 2011). Overlying these are the continental sequences of the Wuqia Group comprising the Keziluoyi, Anjuan, Pakabulake and Artushi formations. These formations are composed of fluvial and lacustrine delta facies (Zheng et al., 2015a, Yin et al., 2002, Blayney et al., 2016 and Chapter 5). Some gypsum is present in the Kezilouyi Formation but is not recorded in any of the later formations at Aertashi (Chapter 5). The Wuqia Group formations are overlain by the Xiyu Formation, which is marked by an abrupt change in lithofacies to kilometres of massive grey sandstones and cobble conglomerates interpreted to be proximal alluvial fan.

Magnetostratigraphic dating was carried out by Zheng et al. (2015a) and in Chapter 5 of this study, complementing the previous work of Yin et al. (2002) and Bosboom et al. (2014c). Blayney et al. (2016) showed the correlation between the magnetostratigraphic dating and the

formations, as well as documenting provenance changes up-section using a variety of techniques. In summary, the section stretches from 41.2 to 15.0 Ma, with depositional hiatuses between 36-33 Ma and 24.3-21.6 Ma. Provenance changes are recorded just above the second hiatus at 21.6 Ma, and just above the top of the magnetostratigraphically dated section at 15.0 Ma.

In this study, we predominantly used core samples collected over 2500 m of section for the magnetostratigraphic study presented in Chapter 5. Sampling was targeted at the finest lithologies available at sampling intervals of 0.4-5m. The resultant cores were divided into samples used for paleomagnetic analysis, with the remaining sample being utilised for organic carbon, X-ray fluorescence (XRF) and S-ray diffraction (XRD) analysis. An additional set of 26 mudstones were also collected (see Figures 3.5 and 3.6 and Appendix 1 for sample names and locations).

6.3.2 X-ray diffraction (XRD)

Clay minerals may be formed as a by-product of weathering of a protolith, or as a result diagenetic alteration and metamorphosis. The resultant clay mineral formed is determined by the type of weathering mechanism, morphological environment and the composition of a source rock.

Different clay mineral species form under different climatic conditions; for example, a very cold or hot-dry climate leads to the formation of clays dominated by illite and chlorite, whereas temperate climates tend to lead to the formation of exfoliated illite and chlorite, irregular mixed layers, vermiculite and degraded smectite with changing proportions which reflect the local petrography, level of precipitation, drainage and temperature. A semi-arid environment favours the formation of well-crystallised Fe-smectite, particularly in warm and poorly drained regions with a long dry season, whereas a hot and wet climate leads to the formation of kaolinite and goethite and of gibbsite under very intense leaching (Chamley, 1989).

Highly crystalline illite and chlorite clays are associated with the physical weathering processes of erosion and alteration of aluminosilicates in the host rock (Chamley, 1989, Huyghe et al., 2011). By contrast, clays formed by chemical weathering processes provide information about climatic conditions during their formation. As temperature and moisture levels increase, chemical reactions are enhanced. Both smectite and kaolinite can form from

the weathering of chlorite and illite during chemical weathering processes (Hong et al., 2007, Vicente et al., 1997). In general a semi-arid to highly seasonal environment favours the formation of well-crystallised smectite particularly in warm, mildly alkaline and poorly drained regions with a long dry season (Chamley, 1989), whilst kaolinite is typically associated with a warm and humid climate due to intense hydrolysis and chemical leaching. As a result, clay minerals can provide a good proxy for palaeoclimate, however the type of source rock, transportation mechanisms and post-depositional environments may also have a marked impact on the clay mineral formed.

Provenance changes in particular can have a significant impact on clay mineralogy. Changes in river drainage patterns can result in changes in the source rock. This is likely to affect the availability of particular ions and minerals required for clay formation, as well as changes in transportation conditions prior to deposition. Shifts in clay mineralogy may therefore be the result of not only climatic conditions, but also changes in provenance. As such, in any climate study utilising clay mineralogy the source rock composition, any provenance changes and post-depositional conditions must also be considered.

XRD analysis was conducted on 20 mudstone samples collected from the Aertashi section (See Figure 3.5 and 3.6 and Appendix 1 for sample locations and Figure 6.3 e for analysis results). Sample preparation was conducted following the methods of Moore and Reynolds (1997). Samples were gently broken down into smaller pieces using a standard agate pestle and mortar before disaggregation in an industrial Waring Blender and rinsed using deionised water into 250 ml glass beakers. Samples were then put onto a low temperature (50˚C) hotplate to remove the excess water without drying down the samples. Samples were then decalcified using 1M acetic acid, allowed to react overnight and then rinsed.

Following decalcification the samples were wet sieved on a 63 μm aperture sieve and the <63 μm fraction transferred to 250 ml cylinders and re-suspended. After standing for a period of ~4 hours as determined from Stokes' Law, the suspended material containing the <2 μm fraction was removed.

Slide mounts of <2 μm material were made using the 'smear' method as outlined in Moore and Reynolds (1997). Analysis was conducted at Lancaster University using a Rigaku Smart Lab 9kW XRD using a Dtex detector in OD mode. Parallel beam optics were used with incident slit and receiving slits configured to 1 mm. The slides were scanned from 2 to 35°2θ

at 1°2θ/min after air-drying, ethylene glycol-solvation (room temperature for 4 days) and heating at 550°C (2 h).

Clay mineral species were then identified from their characteristic XRD peak positions and intensities and their reaction to the three diagnostic conditions (air dry, ethylene glycated and heated), which are outlined in Moore and Reynolds (1997) using the software program Newmod-for-Windows™ (Reynolds and Reynolds, 1996). The relative proportions of clay minerals in each assemblage were determined from their characteristic peak area measurements and the application of corrective multipliers to determine semi-quantitative estimates following the method of (Biscaye, 1965). The results of this method yield precision estimates of around ±5-10% of the 'true' value in compositional percentages >15% (Schultz, 1964). XRD peak width measurements (full width at half maximum, FWHM, Δ°2θ) were made for illite (d001, ~10 Å) and chlorite (d002, ~7.1 Å) in order to assess their relative degree of crystallinity. Note that these measurements cannot be regarded as strict illite (Kübler Index, KI) and chlorite (Árkai Index, AI) crystallinities senso stricto, as the diffractometer had not been calibrated with the Crystallinity Index Standards (CIS, e.g. Warr and Rice (1994); Guggenheim et al. (2002)).

6.3.3 Stable isotopes ($\delta^{13}C_{org}$)

The $\delta^{13}C$ value of a plant is strongly influenced by its environment; the significance of an environmental factor will often depend on the degree to which it limits photosynthesis. Variations in light, nutrients, temperature, atmospheric pCO_2 and water availability are the primary factors (Farquhar et al., 1989, Tieszen, 1991, O'Leary, 1995, Diefendorf et al., 2010, Kohn, 2010, Ehleringer et al., 1997, Cerling et al., 1997, Beerling and Royer, 2002, Beerling, 1996, Tcherkez et al., 2006). Of the two main plant types, C_3 plants typically have highly negative $\delta^{13}C$ values of −33 to −22‰ (O'Leary, 1988, Bender, 1971, Hatch et al., 1967) and comprise plant varieties such as woody and round leaf plants including wheat, rye, and oats, whilst C_4 groups have $\delta^{13}C$ values of −20 to −10‰ (Hatch et al., 1967) and include plants such as Sudan grass, pearl millet, corn and sugarcane.

C_3 plants are highly sensitive to temperature, aridity and high light intensity changes (Hatch, 1987, Ehleringer and Monson, 1993). However, the effects of temperature on $\delta^{13}C$ are inconsistent and both positive and negative correlations have been reported (Schubert and Jahren, 2012 and references therein). C_4 plant types are far more efficient in 'water stressed', intense light and low pCO_2 conditions (Tipple and Pagani, 2007), and as a result, all C_4 plants

have a significant advantage over C_3 plants in hot, high-light, and dry environments (Tipple and Pagani, 2007, Sage et al., 1999).

A total of 78 samples were analysed for organic $\delta^{13}C$ at Lancaster University. Samples were crushed and milled using a planetary ball mill and decalcified by acid digestion using 10% dilution of 1M HCl before being rinsed repeatedly using de-ionised water and centrifugation. The dried sample was then reground to ensure homogeneity before being weighed into 100-200 mg tin foils for analysis.

Analysis for $^{13}C/^{12}C$ ratios (expressed as $\delta^{13}C$ values) of bulk organic matter was conducted using a vario micro elemental analyser, linked to a VisION continuous flow isotope ratio mass spectrometer. Each prepared sample was combusted within tin capsules at 960 °C to yield CO_2 for determination of $\delta^{13}C_{org}$. $\delta^{13}C$ values were corrected against V-PDB standard using internal reference materials calibrated to international standards. Within-run $\delta^{13}C$ replication (1σ) was <0.2 ‰ for standards and <0.25 ‰ for samples.

6.3.4 X-ray Fluorescence (XRF)

Traditional weathering indices such as the chemical index of alteration (CIA, $Al_2O_3/ (Al_2O_3 + CaO + Na_2O)$, the chemical index of weathering (CIW, $Al_2O_3/ (Al_2O_3 + CaO + Na_2O + K_2O)$ and K/Si may be strongly grain-size dependent (Garzanti and Resentini, 2016). Sediment transport and deposition results in changes in the grain size of deposited sediments which affects the chemical composition of the sample (Lupker et al., 2013).

Lupker et al. (2012, 2013) suggested that grain size and sorting effects can be eliminated by normalising mobile to immobile ratios (X=Si) to a common Al/Si, which is a proxy for grain size. This model assumes that the coarse-grained end member composition can be assigned to the low Al/Si mixing end-member and that the weathering signature is mainly carried by the finer clay fraction. Chemical weathering preferentially removes more mobile elements such as K and would lower the relative K/Si ratio relative to Al/Si during increased chemical weathering.

In total, 70 samples were submitted for XRF analysis from the Aertashi section. These samples were milled into powders at Lancaster University using an agate planetary ball mill before being analysed at the University of Plymouth CORIF ISO9001 facility. Samples were prepared as fused beads using the PANalytical Eagon 2 fusion system with a lithium tetraborate flux. Fused beads were then analysed for major elements using a PANalytical

Wavelength Dispersive X-ray Fluorescence Spectrometer (WD-XRF) (Axios Max) instrument. Loss on ignition (LoI) was determined independently by heating to 1050˚C for 1 hour and calculated using the formula:

$$LoI\ (\%) = (Ws - WA)/(Ws - Wc) \times 100$$

Where Ws = Crucible + sample dried at 105℃ (g), WA = Crucible + ignited sample (g) and Wc = Preconditoned crucible (g).

6.3.5 Magnetic susceptibility (MS, χ)

In sedimentary deposits the formation of pedogenic magnetic minerals is dependent on the concentration, grain size distribution and mineralogy of magnetic minerals present (Sun et al., 2011).

Variations in these values are dependent on the composition of the source material, fractionation of detrital magnetic minerals during transport and deposition and post-depositional alteration (Garzanti and Resentini, 2016, Sun et al., 2011).

Source rock variations in diamagnetic minerals (e.g. quartz, calcite) and paramagnetic minerals (e.g. clay minerals) may affect the MS, particularly if the sediment magnetic mineral content is low (Sun et al., 2011).

The depositional facies of the sediment also plays a key role in affecting the MS; for example, Sun et al. (2011) observed that MS was highest in loess deposits when compared with other sedimentary facies, attributed to the increased presence of magnetic minerals of pedogenic origin. Maher and Thompson (1995) also noted a higher MS signal as a result of an increase in the concentration of ultra-fine ferromagnetic grains (≤0.03μm), making loess deposits particularly useful for interpreting the paleoclimate, especially rainfall signals.

Sun et al (2011) observed that the lowest MS signal was identified in aeolian sands due to their coarser grainsize and weaker pedogenesis. Lacustrine sediments also produced a very low MS signal (less than $5*10^{-8}$SI) whilst fluvial sand and clay had slightly higher values.

Tectonic processes also play a role in affecting MS; for example, sources that contain magnetic particles with both magnetite and haematite are transported to their sinks more rapidly during increased tectonic phases (Sun et al., 2005), resulting in higher MS values. Conversely, during periods of tectonic quiescence, source materials undergo more prolonged in-situ chemical weathering resulting in an increase in the oxidation of magnetite to haematite. This leads to an abundance of haematite in the sink relative to the original source

and lower relative MS values. In general, if all other factors (grain size, facies and provenance) are equal, an increase in high susceptibility magnetic minerals can be attributed to a relative decrease in the production of oxic forms of magnetic minerals which is the result of more rapid burial of the sediment, or alternatively to a change in the climate to more humid conditions (Gilder et al., 2001, Lu and Xiong, 2009). However in nature these conditions are rarely met.

Bulk MS (χ) was measured on 495 core samples throughout the sampled section. Analysis was performed in the magnetically-shielded room at the archeo-palaeomagnetic laboratory at the University of Rennes, where measurements were made at room temperature using a Bartington MS2 magnetic susceptibility meter.

6.4 Results

All samples were plotted by age in Ma using the magnetostratigraphically and biostratigraphically dated timeline of Bosboom et al. (2014c) and Chapter 5 of this study for the Aertashi section.

6.4.1 XRD

The clay-mineral assemblage composition varies with time within the Aertashi section (Figure 6.3e). The oldest part of the section, from 41 to 31 Ma, is dominated by illite- and chlorite-rich assemblages. There is a change sometime between 31 Ma and 28 Ma, after which time the section is characterised by the additional presence of varying proportions of smectite. From ~17.6 to ~15 Ma, there is a limited appearance of kaolinite which is then absent again in the uppermost sample at ~14 Ma. Overall, illite and chlorite crystallinity values decrease linearly for the lowermost part of the section from 41- ~25 Ma, whilst from ~ 21.6 Ma the degree of variability increases up section. However, values remain low <0.6 throughout the section (Figure 6.3f).

6.4.2 $\delta^{13}C_{org}$

The $\delta^{13}C_{org}$ for the Aertashi section has been plotted in Figure 6.3(g). In the lowermost part of the section between 41 to ~18.5 Ma, $\delta^{13}C$ remains relatively stable. A marked positive shift in organic carbon is recorded at the onset of unit E, at ~18.5 Ma and continues until the top of the section. This shift coincides with a reduction in data variability, and is shortly followed by a subtle increase in total organic carbon (TOC) (Figure 6.3(h)) at ~17.6 Ma.

A subtle reduction in TOC is recorded at ~16 Ma, which is superseded by a marked increase in TOC recorded by the topmost datapoint at ~14 Ma.

To determine if there was a significant difference between mean $\delta^{13}C$ determined from the lower part and the upper part of the section, a Shapiro-Wilk test for normality was performed on both datasets. This resulted in *p* values greater than 0.18, showing that the data was normally distributed within each category. A test for equality of variance, the Levene's test for means, was then performed yielding a *p* value of <0.001, determining that the variances were significantly different from each other. Based on these analyses, an unpaired t – test was undertaken assuming equal variances yielding t (76) = 5.297, $p = <0.001$. The mean $\delta^{13}C$ for the lower section is -25.56‰. The less negative shift in the upper dataset yielded a mean of -23.36‰ (note this mean is for the whole of the upper section from 18.5 Ma to 15 Ma (Figure 6.3g)).

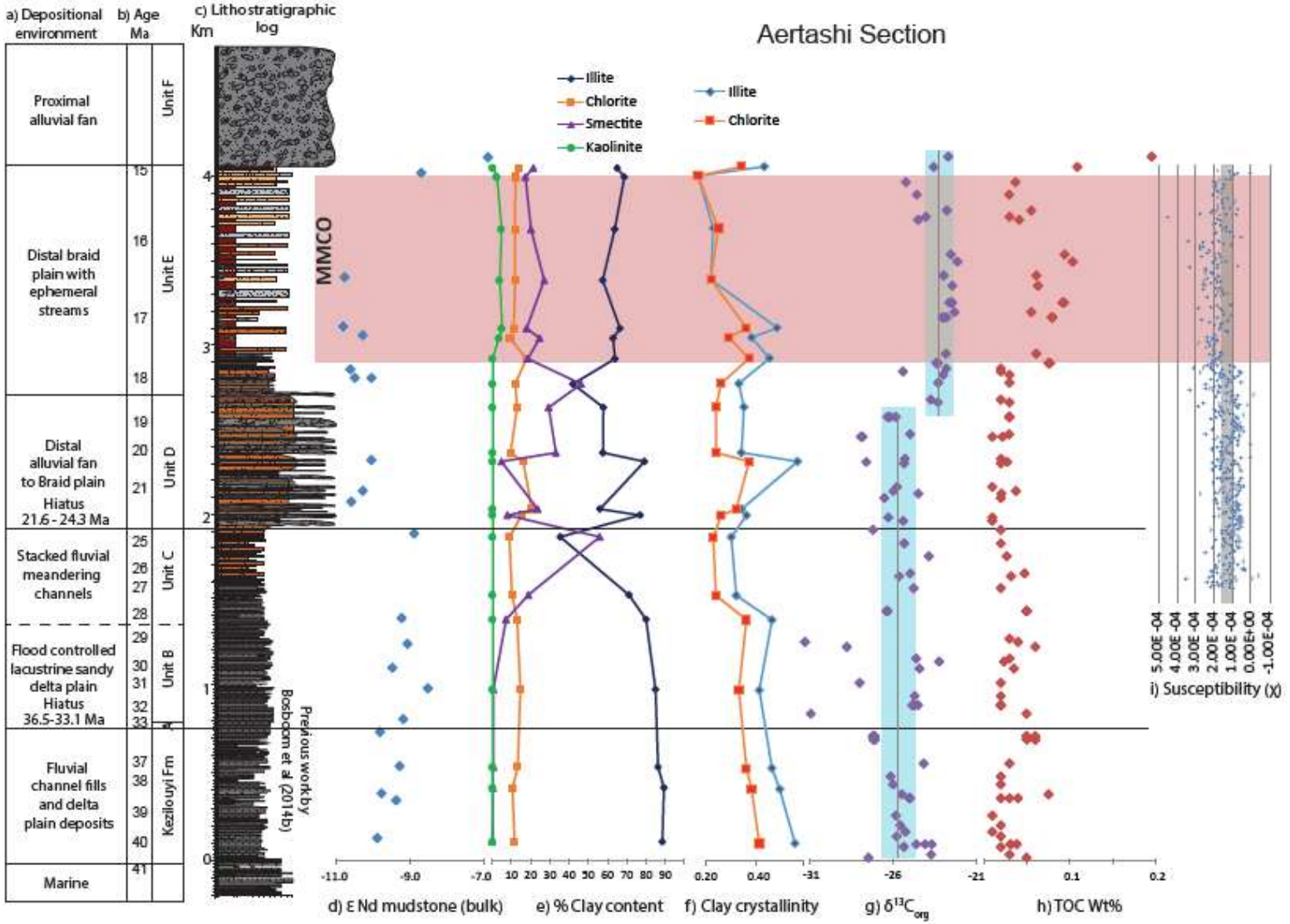

Figure 6.3 Summary of results from the Aertashi section including:
(a) depositional environment,
(b) stratigraphic age control both from Blayney et al., Chapter 5 of this study,
(c) lithostratigraphic log,
(d) provenance epsilon Nd by Blayney et al. (2016) and Chapter 4 and 5 of this study,
(e) % clay content,
(f) Clay crystallinity,
(g) $\delta^{13}C_{org}$ with average values for the upper and lower section indicated with 2σ values indicated in pale blue,
(h) TOC and
(i) magnetic susceptibility.

6.4.3 XRF

Due to the grain size dependency of traditional weathering proxies, we illustrate the degree of chemical weathering of the Aertashi section here by using ratios of mobile to immobile elements (Lupker et al., 2013) (Figure 6.4). Linear regression plots of K/Si vs Al/Si were produced following the method of Lupker et al. (2013). The Aertashi section was divided into pre- and post-28 Ma (Figure 6.4a) to determine if any changes in weathering could be detected at the onset of the appearance of smectite in the section (section 6.4.1), with a second divide at pre- and post-18.5 Ma (Figure 6.4b) to determine if there was any change in weathering at the onset of unit E, where a shift to more positive $\delta^{13}C_{org}$ is observed (Figure 6.3g). Linear regression lines were plotted through each dataset along with 0.95 confidence intervals for each regression line, to assess the significance of inferred changes in the degree of weathering over time. There is no observable increase in weathering at the onset of smectite appearance at ~28 Ma, however a subtle but statistically significant increase in weathering is observed in the uppermost 18.5-14 Ma section when compared with the lower 18.5-41 Ma section (Figure 6.4b).

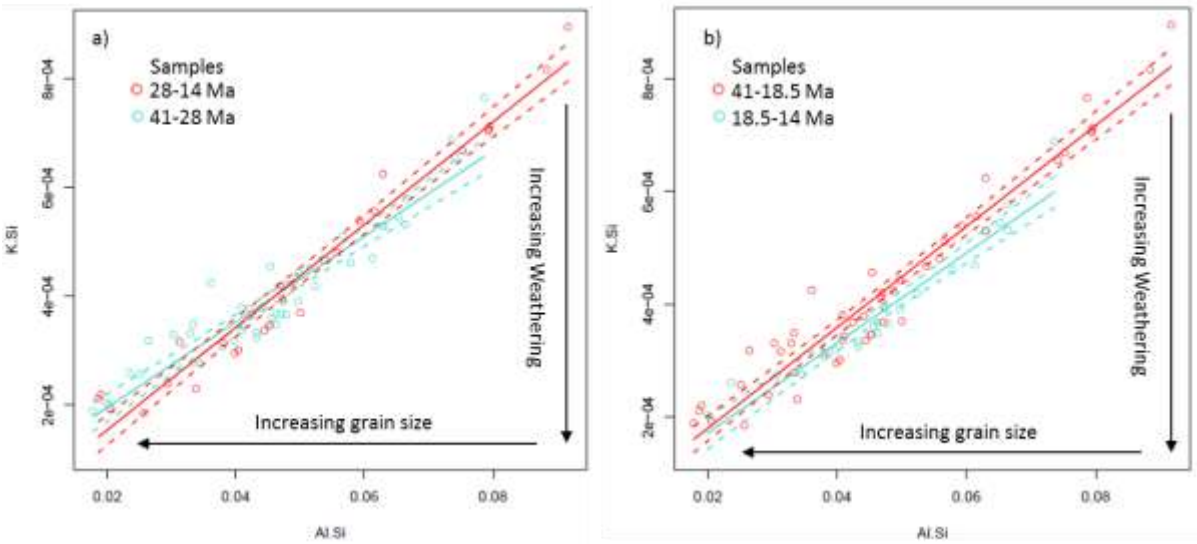

Figure 6.4 Plot of Al/Si vs K/Si mol:mol for the Aertashi section divided at (a) 28 Ma and (b) 18.5 Ma to determine any change in the degree of weathering for these intervals in the section at these times. Best-fit regression lines through the datasets are indicatedas solid lines and dotted lines represent the

6.4.4 Magnetic susceptibility

We plotted bulk magnetic susceptibility as a function of depth and time (Figure 6.3i and Supplementary item 1) where Susceptibility (χ) ranges from -1.00 – 5.00 $x10^{-4}$ SI. The data were divided at 17.85 Ma into an upper group and a lower group for statistical analysis, based on a broad shift to more positive values at ~17.85 Ma.

To determine if there was a significant difference between mean magnetic susceptibility values in the lower part of the section and the upper part, a Kolmogorov-Smirnov test for normality was performed. Resulting p values are smaller than 0.02, showing that the data are not normally distributed. Based on this, an unpaired t–test assuming unequal variances was undertaken yielding t(287) = -9.468, p = <0.001, indicating that the mean of the two sections was significantly different. The calculated mean for the upper section is $1.32744x10^{-4}$ and for the lower section $1.86x10^{-4}$.

6.5 Interpretation

Previous work has shown that in the Aertashi section and elsewhere in central Asia, high seasonality and aridity were already in evidence in the Paleogene (Licht et al., 2014, Huber and Goldner, 2012, Caves et al., 2014, Zhang et al., 2012, Zhang et al., 2007b, Bougeois et al., Submitted, Sun and Wang, 2005). This is in agreement with Eocene facies at Aertashi which represent fluvial and lacustrine red beds. The presence of gypsum provides evidence of periodic drying. Seasonality is confirmed by the presence of smectite in the clay assemblage that characterises all but the base of the succession, and there is little change in our climate proxies until the Mid Miocene. At this time, between ~17.3 and 15 Ma, a small proportion of kaolinite is recorded, and at 17.6 Ma, there is a subtle change in $\delta^{13}C$. Interpretations are discussed below.

6.5.1 Onset of smectite sometime between 30 and 28 Ma

The bulk of the section, from 28 Ma to the top of the section at 14 Ma, is characterised predominantly by illite, smectite, and chlorite. Illite and chlorite are typically the products of a physical weathering regime (Chamley, 1989), whilst smectite may be formed in a chemical weathering regime.

Although smectite is typically considered to be a by-product of the chemical weathering of mafic volcanic rock types, in a number of central Asian locations, both

semi-arid (e.g Mongolia; Dill et al. (2005)) and monsoonal (e.g. the south slopes of the Himalaya; Huyghe et al. (2011)) smectite is recorded in considerable proportions with no apparent mafic volcanic source. Smectite provides a unique indicator of a highly seasonal environment due to the requirement of poorly drained mildly alkaline environments, typical of highly seasonal, tropical climates with a very long dry season (Chamley 1989, Righi and Meunier, 1995, Bergaya et al., 2006). We thus discuss the presence of smectite in terms of seasonality.

The record of smectite at Aertashi indicates a seasonal climate from ~ 28-31 Ma to the top of the studied section at 14 Ma. However, seasonality and semi-aridity were already established in the western Tarim Basin since at least the Eocene (~41Ma) (Licht et al., 2014, Bosboom et al., 2011, 2014c, Bougeois et al., Submitted) whilst aridity in central Asia has been evidenced since as early as the Cretaceous (Sun and Wang, 2005, De Pelsmaeker et al., 2017). This climate deterioration continued in a stepwise fashion throughout most of the Cenozoic (see Section 6.2.2). The lack of the smectite signal in the lowermost part of the Aertashi section may be due to diagenesis, facies variations or climatic changes which we discuss further, below.

Diagenetic changes: The smectite-illite transition zone lies between 58-92 °C for transition onset and 88-142 °C for transition completion of the process, depending on a number of variables (Freed and Peacor, 1989). In a sedimentary basin with typical geothermal gradient (~30°C/km^{-1}), the transition would correlate to burial depths of ~3.5-4 km (Merriman and Kemp, 1996).

In the Aertashi section, the period from ~ 30-41 Ma when no smectite was detected, corresponds approximately to the lower Wuqia Group and Bashibulake Formation of Zheng et al. (2015a), correlated to our section using Blayney et al. (2016). Apatite fission track (AFT) data from the Wuqia Group and Bashibulake Formation in the Aertashi section (Sobel and Dumitru, 1997) shows that the samples have not been strongly annealed within the AFT partial annealing zone (60-120 °C) post-burial, and were subjected to temperatures in the range of 50-90 °C. This corresponds to a burial depth of ~2-3 km, assuming a geothermal gradient of 30 °C/km. Independent estimation of depth of burial from the sedimentary section is difficult to determine due to limited knowledge of the time of exhumation of the Basin. However, if we take exhumation at the Aertashi location to have commenced at the earliest during deposition of the lower Artushi Formation and at the latest during deposition of the

lower Xiyu Formation (Wang and Wang, 2016), then overburden was of the order of <3 km.

Also mitigating against a diagenetic explanation for the lack of smectite below 31 Ma in the section is the fact that no mixed layer smectite-illite clays were observed, and that the trend of the illite crystallinity is consistent with a detrital origin for the illite, shed into the basin from a thrust belt eroding to higher metamorphic grade through time.

Facies change: A gradual facies change recorded ~28 Ma, between 'Unit B' playa lake, lacustrine delta plain and 'Unit C' meandering facies with thick-bedded sandstones (Chapter 5 of this study), coincides with the onset of smectite detection and may therefore provide an explanation for this change. In order to assess the importance of facies changes on the appearance of smectite, comparison is made with the neighbouring Qimugen section. As noted above (Section 6.2.2), the Qimugen section is the only sequence for which a clay record exists in the Tarim Basin (Wang et al., 2013, 2014, 2016). Detailed correlation between the sections is hazardous due to the lower level of depositional age control at Qimugen. Nevertheless, there is a change from no smectite to smectite within the lowest part of the Wuqia Group (units A-C of this study) which, in the Qimugen section, appears without a facies change in the sedimentology. This suggests that the appearance of smectite is not facies dependent. Additionally, data from the Qimugen section were collected to lower levels compared to Aertashi and show the reappearance of smectite lower in the section, coincident with the marine to non-marine transition. Wang et al. (2013) attribute the absence of smectite in this interval (between the marine to non-marine transition and the lowest part of the Wuqia Group) to be the result of a climate change from warm and humid to cold and dry during this time, which we investigate further below.

Climate change: a stepwise aridification of the central Asian climate is widely accepted (e.g. Harzhauser et al., 2016, Wang et al., 2014). Detailed regional stratigraphic compilations have shown that westward retreat of the Para-Tethys ocean from the Tarim Basin occurred in stages, which influenced the aridification of central Asia due to withdrawal of this moisture source (Ramstein et al., 1997, Bosboom et al., 2015). Sobel and Dumitru (1997) invoked the 30 Ma eustatic sea level fall as being responsible for final retreat of the ocean, whilst Bosboom et al. (2011), (2014a) argued that both eustatic sea level falls, particularly at 34 Ma and 30 Ma, as well as tectonics,

caused retreat of the Para-Tethys Sea. Bosboom et al. (2011) further noted that overall, the times of stepwise retreat of the sea corresponded reasonably well to the long-term eustatic sea level curve. Further afield, tentative support for an aridification step at this time is recorded in Mongolia at ~31 Ma (Harzhauser et al., 2016, Richoz et al., 2017).

Globally, an increase in temperature is also recorded by $\delta^{18}O$ at ~28 Ma marking the onset of the late Oligocene Warming Event (LOWE) (Zachos et al., 2001). However, records of this event in central Asia are limited. Chi et al. (2013) alluded to a possible link between the LOWE and an increase in gymnosperms from the Xining Basin in northern China. In order to test whether local factors (e.g. facies change) or regional factors (e.g. climatic influence) caused the reappearance of smectite in this section, more sedimentary sections should be studied in the region.

6.5.2 Kaolinite between 17.6 and 15 Ma: an expression of the Mid Miocene Climate Optimum?

Kaolinite may be formed by extreme chemical weathering, and when co-occurring with smectite, may suggest formation under a savannah climate (Thiry, 2000). The coeval occurrence of kaolinite at 17.6 Ma and the timing of the warmer, wetter period of the MMCO at ~18-15 Ma (see Section 6.2.1); suggest a causal relationship. A subtle but statistically significant increase in weathering at this time is recorded in our geochemical data (see Section 6.4). However, it has been observed by Thiry (2000) that kaolinite clay horizons take at least 1 Myr to form, which may place the onset of kaolinite formation at this facies change between units D and E, which occurs at ~18.5 Ma (Figure 6.3c).

In order to determine if the occurrence of kaolinite is a response to a regional climatic event rather than a locally driven tectonic event, comparison with other sections in the western Tarim Basin must be made.

The Qimugen section has been studied for clay mineralogy (Wang et al., 2013), but its more limited constraint of depositional age control precludes precise correlation as previously discussed. In spite of this, a similar change is seen to that recorded at Aertashi, in as much as there is an appearance of kaolinite sometime in the mid-Miocene in Qimugen without a corresponding change in facies. This suggests that the

appearance of kaolinite is not likely to be facies dependent and implies a link to a more regional event.

In spite of the paucity of previous research using clays to investigate the MMCO in the Tarim Basin, elsewhere in central Asia the MMCO has been recognised using clays and by the other proxies we utilise in this paper. In the South China Sea, Clift et al. (2014) report increased kaolinite along with a sharp decrease in K/Rb, K/Al and the Chemical Index of Alteration (CIA) corresponding to the MMCO at 17.2-15.5 Ma. Studies from the Xining Basin in northern China report changes in magnetic susceptibility to lower and more variable values of (χ) (Zan et al., 2015), whilst organic carbon values show a peak in $\delta^{13}C_{org}$ values at 17-18 Ma (Chi et al., 2013). However, no changes in climate proxies are observed over a similar time period in the Junggar Basin or the Sanju section of the Tarim Basin (Sun et al., 2013).

Similarly to the Xining Basin, our magnetic susceptibility also shows lower (χ) values beginning at ~17.85 Ma, along with an increase in total organic carbon (TOC) corresponding to the time of the MMCO. Furthermore, organic carbon $\delta^{13}C$ values also show a statistically significant increase, at 18.5 Ma, which may be an early manifestation of the MMCO. Indeed, Sun and Zhang (2008) propose that changes in the pollen record of the Taxihe section south of the Junggar Basin from 18 Ma are associated with MMCO-related climate change. The increase in TOC could be ascribed to increased productivity associated with the more humid and warmer climate. However, other factors may also be responsible for the organic carbon data, as discussed below.

6.5.3 Increase in δ^{13}Corg values at ~18.5 Ma

From ~18.5 Ma onwards there is a clearly defined shift to less negative $\delta^{13}C_{org}$ values which continues throughout the remainder of the section. The $\delta^{13}C$ of organic carbon in sediments reflects the partial pressure of atmospheric CO_2 at the time of growth of the vegetation, the degree of aridity of the region during vegetation growth, and vegetation type. The drivers of the less negative shift at 18.5 Ma are likely to be a response by organic plant matter to either a decrease in atmospheric pCO_2 ascribed by Tipple and Pagani (2007), or to an increase in 'water stress' resulting from a climatic shift to increased aridity (Farquhar et al., 1989, Tieszen, 1991, O'Leary, 1995, Diefendorf et al., 2010, Kohn, 2010, Ehleringer et al., 1997, Cerling et al., 1997,

Beerling and Royer, 2002, Beerling, 1996, Tcherkez et al., 2006). However, the jump to more positive $\delta^{13}C_{org}$ values at Aertashi cannot be explained by any change in atmospheric pCO_2 as atmospheric pCO_2 values at this time are low, and either considered to be invariant, or rising slightly over this period (Beerling and Royer, 2011, Foster et al., 2012, Zhang et al., 2013). Interestingly, the shift in $\delta^{13}C_{org}$ appears to be unaffected by the more humid period (Section 6.1) between ~17.6 and 15 Ma (Figure 6.3g), which would suggest a scenario in which vegetation crossed a threshold which was insensitive to this later more humid climate.

A change in vegetation explaining the rise in $\delta^{13}C_{org}$ values in the Tarim Basin is also consistent with $\delta^{13}C_{org}$ values from the South China Sea. Jia et al. (2003b) propose a rise in C_4 vegetation in regions of eastern Asia sourcing the sediment in the South China Sea, since 18-20 Ma, to explain their data. Supporting a change in plant type are the results of Sage (2003) who documented five centres of origin relating to the regions and habitats in which C_4 photosynthesis evolved. These centres are located in the arid tropics, subtropics and warm temperate regions. One such centre is located in central Asia, which is characterised by vast interior basins and dry salinized soils. The ten origins in the Chenopodiaceae are centred here. In the Chenopodiaceae, members of the Salsoleae diverged at 21.6-14.5 Ma (Kadereit et al., 2003). Expansion occurred in warm temperate deserts and zero-saline habitats with zero water (Ehleringer et al., 2006). Any diachroneity between regions can be ascribed to local variations in habitat.

Similar studies of terrestrial records in the region are sparse. Two studies in the Tianshui Basin (Hou et al., 2015, Hui et al., 2011) and Linxia Basin, NE Tibet (Fan et al., 2007) include organic carbon isotopic data, but average values as positive as those for the Aertashi section are not recorded in either sedimentary section in the Miocene. However, neither of these sections go back as far as 19 Ma (although the Tianshui site goes back to 17 Ma, thus partially overlapping the Aertashi age of interest). In the Junggar Basin and the Xining Basin, $\delta^{13}C$ values for inorganic carbonate are intermediate between values typical of C_3 and C_4 vegetation (Charreau et al., 2012, Sun et al., 2013), which are linked to the onset of C_4 vegetation and increased aridity in the region.

Interestingly, a marked decrease in $\delta^{13}C_{org}$ at ~18 Ma from the Xining Basin in northern China is consistent with a reduction in gymnosperm populations and an

increase in angiosperms which has been related to the Mi-1b glacial event at this time (Chi et al., 2013).

If a shift to C_4 vegetation in the Aertashi region is suggested to be the cause of the positive change in $\delta^{13}C_{org}$, the cause of this shift is likely to be resultant from an increase in plant stress conditions as discussed in section 6.3. Given that C_4 plants typically flourish in hot, high-light, and dry environments (Tipple and Pagani, 2007, Sage et al., 1999), the driver of this change, we suggest, is likely to be resultant from an increase in aridity given the general aridification trend recorded in central Asia at this time (see Section 6.2.2).

Recent redating of the Sanju section (Cao et al., 2015 and discussion in Chapter 5) places the base of this section at ~19.0 ±0.2 Ma, based on zircon U-Pb and fission track data from syn-depositional volcanism. This predates our observed shift in $\delta^{13}C_{org}$ at 18.5 Ma. If this basal age is correct then the absence of any changes in $\delta^{13}C$ around 18.5 Ma indicates that the shift observed at Aertashi is diachronous within the basin. Diachroneity of signal may rule out increased aridity as the cause of the change, since such a change might be expected to be synchronous, basin-wide. However, it should be noted that the $\delta^{13}C_{org}$ data at Sanju for the lowermost 100 m is based on just four datapoints and may not extend down sufficiently to identify a less negative shift in this part of the section.

Appealing to increased aridity to explain the change is consistent with the fact that increased aridity is considered to have occurred, in a stepwise manner, throughout the Cenozoic in central Asia (Harzhauser et al., 2016, Wang et al., 2013, 2014). Indeed, the relative proximity to local landmasses such as the Pamir and Tibet may have influenced the signal differently in Sanju (closer to the northern margin of Tibet) compared to Aertashi (closer, today, to the eastern margin of the Pamir), which is evidenced by the conglomeratic facies throughout the studied section at Sanju (Chapter 5) compared to the range of facies described at Aertashi.

Whilst a change in vegetation in this region is an attractive argument to explain the data, due attention must be paid to the potential influence of petrogenetic (inherited) carbon. At very low levels of total organic carbon (TOC) in basin samples, the influence of petrogenetic carbon will be greater than average (e.g. Galy et al., 2008). Whilst Sun et al. (2013) did not publish their TOC values at Sanju, our data from

Aertashi showed very low TOC. Thus, $\delta^{13}C_{org}$ values in the Tarim Basin sediments may reflect the signature of the source rock rather than contemporaneous vegetation. Mitigating against the influence of changes in rock type and hence associated change in petrogenetic carbon as the cause of the jump in $\delta^{13}C_{org}$ values in the Aertashi section is the lack of any evidence for co-eval change in provenance, as determined by bulk rock εNd values (Figure 5.3 (d) in Chapter 5) and petrography (Blayney et al., 2016). Analyses of rocks from the potential source areas would need to be undertaken in order to investigate this argument further.

We also note that the shift in $\delta^{13}C_{org}$ values coincides with a facies change, from conglomeratic to finer-grained facies, which may have influenced pedogenesis (Melillo et al., 1989, Connin et al., 2001, Boström et al., 2007). However, we note that similar high values of $\delta^{13}C_{org}$ are not found in fine-grained facies (albeit not *as* fine-grained) further down section at Aertashi, and that the high values recorded in the Sanju section in the Tarim Basin and studies in the Junggar Basin occur in facies dominated by conglomerates and gravels.

6.6 Conclusions

A change at 17.6 Ma, with the occurrence of kaolinite until 15 Ma, accompanied by increased TOC and decrease in magnetic susceptibility may be related to the mid-Miocene climatic optimum, which is recorded globally at ~18-15 Ma. However, a direct response to the facies change in this interval may also explain the data; a subtle increase in weathering suggests a shift to a slightly 'wetter' climate at this facies change which may be linked to the early onset of the MMCO. However, the shift to more positive $\delta^{13}C_{org}$ values at 18.5 Ma may be linked to the onset of C_4 vegetation in the area driven by an overall regional and climatic trend towards increased aridity. The coincident facies change at 18.5 Ma may also have affected this change, making the distinction between regional climatic trends and local tectonics difficult to deconvolve. The onset of smectite occurrence between 30 and 28 Ma might relate to the global eustatic sea level fall which led to a greater distance between the Westerlies moisture source and the Tarim Basin, a climate shift as a result of the Early Oligocene Aridification Event or a facies change. The limited availability of comparative studies in the western Tarim Basin along with poor age constraints on the available sections makes distinction between localised events and regional trends difficult. In order to

distinguish between these various options, more climate data from well dated sections around the western Tarim Basin are needed.

Acknowledgements

This work was funded by a NERC PhD Studentship to Blayney (grant number NE K501001-1). We would like to thank Chris Kneale, Annabelle Bernard and Laura Fielding and our guides Kasim and Khader for their contributions in the field. We would also like to thank Professor Will Blake and Dr Alex Taylor from Plymouth University for the use of their facility and technical assistance, and Dr Nathan Halcovitch and David Hughes of Lancaster University for their technical support.

7. Discussion and Conclusions

The aim of this research is to gain a greater understanding of the Cenozoic evolution of the Pamir mountain range, constrain the timing of Pamir indentation, and examine the effects of Pamir formation on regional climate. This is achieved by focusing on the Aertashi sedimentary record in western Tarim Basin, which is located along the eastern margin of the Pamir. This project incorporates a variety of techniques to date and interpret observed variations in terms of provenance, tectonism and climate, the results of which are presented here.

7.1 Evolution of the Pamir mountain range throughout the Cenozoic

7.1.1 41.2-24.3 Ma Tarim sea retreat and onset of aridification in central Asia

Deposition at Aertashi is characterised by a transition at 41.2 Ma from shallow marine to continental red beds (Bosboom et al., 2014c). A marked increase in tectonic subsidence at this time provides evidence of a dominantly tectonic cause for this sea retreat. However, a coincident global eustatic sea level fall suggests that the retreat of the Tarim Sea is likely to be resultant from a combination of the two mechanisms.

The provenance in this time frame is dominated by Western Kunlun sourced material. U-Pb zircons are characterised by >1800 Ma populations along with a double peak of U-Pb zircon ages at ~200-300 Ma and 400-500 Ma, with a subordinate peak at ~800 Ma. Palaeocurrent data indicates a south-westerly source from the western Kunlun and Songpan Ganzi terranes along the northern margin of Tibet. The strain direction from anisotropy of magnetic susceptibility (AMS) data is consistent with N-S compression at this time, indicating a distal foreland basin environment that can be linked to the northward thrust loading of thickened Tibetan crust onto Tarim and Pamir since at least 40 Ma (Cao et al., 2014, Rutte et al., 2017a, Jolivet et al., 2001)

A high seasonality and arid climate was already established by the Eocene in the facies at Aertashi, which are dominated by waterlain red beds. These beds show evidence of periodic drying as shown by the presence of gypsum throughout the Eocene. Above the Eocene – Oligocene transition, sediments indicate a dry environment with large aeolian dune deposits (unit A) passing upward to wet interdunes and ponds to a lacustrine delta plain (unit B base). These flows are highly efficient and transport a large volume of sandy material. Clays are dominated by illite

and chlorite at the basal part of the section up to ~30-28 Ma indicating a physical weathering regime was prominent at this time.

The appearance of smectite at ~30-28 Ma may be related to a gradual facies change recorded between the playa lake, lacustrine delta plain facies of unit B and meandering fluvial facies of unit C. However, the appearance of smectite in the neighbouring Qimugen section is recorded at a similar time without any record of facies change. This may indicate that the onset of smectite formation was regionally extensive and not facies dependent.

A coincident reduction in global eustatic sea level at ~34 and 30 Ma has been linked to aridification steps in the Tarim region by Bosboom et al. (2011). However, an increase in temperature recorded globally at ~28 Ma, marking the onset of the late Oligocene warming event (Zachos et al., 2001), also corresponds to the onset of smectite formation. In order to delineate regional and global climatic signals from facies changes, more studies from this region would need to be conducted along well-dated sections.

7.1.2 24.3 – 18.5 Ma Activation of transtensional deformation.

Aertashi records a long depositional hiatus (24.3-21.6 Ma), associated with a change from distal foreland basin deposits below, to locally derived conglomerates above the hiatus.

A distinctive provenance change is recorded at this transition by a shift in εNd to more negative crustal values and an associated increase in input of very low grade and low-grade metamorphic detritus. A decrease in prominence of the >1800 Ma zircon population is noted; however, the detrital signature remains dominated by Western Kunlun sourced material.

Exhumation local to Aertashi is recorded by partially reset apatite fission track (AFT) data in the Cretaceous strata at the base of the section (Sobel and Dumitru, 1997) which indicate a minimum of 20.0 ± 3.1 Ma age for the time of cooling below 120-100°C. The composition of the overlying conglomerate clasts of unit D are made principally of shallow cover deposits suggesting a link between exhumation and deposition. The ca.2 km stratigraphic thickness between the marine limestone deposits stratigraphically below the disconformity suggest little unroofing.

Although the provenance shift at this time may indicate a change from southerly-derived sedimentation to a more westerly source, the dominant regional stress direction, as evidenced by the AMS data, remains in a N-S orientation. The combination of the documented nearby exhumation to the west, and the hiatus overlain by the onset of conglomeratic deposition, provides further evidence of a tectonic structure uplifted proximal to the study area in this time period.

Continuous deposition and a fining upwards of the facies above the conglomerates (see next section), indicates that exhumation did not evolve into a thrust belt and has a mainly strike – slip component. A transpressional setting is supported by coeval exhumation and strike slip structures reported along the eastern margin of the Pamir at this time (Sobel and Dumitru, 1997, Wang and Wang, 2016, Wei et al., 2013, Cowgill, 2010). Bande et al. (2015) proposed a pull-apart basin for the region, bounded by the Kashgar-Yecheng Transfer System (KYTS) on the western side and the Sache-Yangdaman fault (SYF) to the east (a southern continuation of the Talas Ferghana fault (TFF)) between ~25-20 Ma, in which the Aertashi region forms the depocenter. However, evidence for the SYF is limited to one seismic study site and remains contentious. This structure likely represents a local manifestation of the stress field associated with India – Asia collision, with far-field affects recorded as far north as the Tian Shan by ~25 Ma (Sobel et al., 2006, Jolivet et al., 2010), rather than indentation of the Pamir to this region by this time.

Regionally, tectonic activation along the Pamir and northern margin of Tibet corresponds to the onset of activation along the Main Pamir Thrust (MPT) (Sobel et al., 2006). This shift in tectonic regime is recorded in the northern margins of the Tarim and Tian Shan mountain range by activation of the right-lateral TFF and associated counter-clockwise rotation of the Fergana Basin with exhumation in the horsetail Chatkal ranges (Thomas et al., 1996; Bande et al., 2015, 2017 and references therein).

Within the Pamir, a major change from crustal thickening to exhumation and possible crustal collapse is recorded (Amidon and Hynek, 2010, Rutte et al., 2017a, b, Sobel et al., 2013, Stübner et al., 2013a, b). This coincides with a slowing down of the Indian plate at 20±2 Ma from 57 to 44 km/Myr (Molnar and Stock, 2009, Iaffaldano et al., 2013). The change in tectonic regime has been proposed to be resultant from either initiation of movement on the Karakoram fault, or a second slab break off of the

Indian plate (Amidon and Hynek, 2010, Sobel et al., 2013, Rutte et al., 2017a, b) which occurred at ca. 25-20 Ma (e.g. Replumaz et al., 2010, Mahéo et al., 2009, Stearns et al., 2013, DeCelles et al., 2011 and references therein).

To the south of Aertashi, movement along the Western Kunlun bounding faults, such as the Tiklik fault and the KYTS system, accommodated northward expansion of the Western Kunlun range and the early onset of Pamir indentation. Uplift of the northern plateau margin altered the paleodrainage pattern within the Western Kunlun effectively cutting off the more distal hinterlands such as the Songpan Ganzi terrain, draining north to Aertashi.

There is little evidence of climatic change recorded in Aertashi at this time. This suggests that the seasonality established since the Eocene continues throughout this timeframe, which is supported by the presence of smectite in the illite-chlorite-smectite assemblage since ~28-30 Ma and throughout the remainder of the studied section. However, a generally increasing aridity trend is well documented in published works for central Asia (Wang et al., 2013, 2014, Harzhauser et al., 2016, Dupont-Nivet et al., 2007, 2008) suggesting that the seasonality required for smectite formation was overprinted on a regional climatic evolution towards increased aridity.

7.1.3 18.5 – ~15Ma Changing facies at Aertashi, changing tectonics and climate evolution

At ~18.5 Ma, there is a conformable but rapid transition in facies at Aertashi, from the proximal alluvial fan facies of unit D, to distal alluvial fan or braid plain facies with abundant crevasse and flood deposits of unit E. Gradual fining upwards throughout unit E reflects increasingly distal alluvial fan depositions. This transition coincides with a marked increase in sedimentation rate (see Figure 5.2 in Chapter 5).

The provenance of the Aertashi section throughout this time remains dominantly Western Kunlun sourced with no provenance changes defined.

At this time, along the southern margin of the Tarim Basin, conglomerate deposition and exhumation are associated with northward thrusting of the Kunlun hinterland (Cao et al., 2016 and Chapter 6). Whilst in the north, southward migrating foreland deformation is associated with southwestern Tian Shan exhumation (Yang et al., 2015, Heermance et al., 2007). The Aertashi – Qimugen section lies towards the middle of the Western Tarim margin between these two exhuming forelands in the centre of the

Tarim Basin depocenter. We therefore interpret the increasing subsidence and accumulation in Aertashi to be related to a regional signal of deformation along the western margin of the Tarim Basin. Although a local strike-slip structure discussed in section 7.1.2 is likely to have influenced the location of this depocenter and local stress conditions.

After ~17 Ma, results from AMS suggest a change in the strain orientation from generally N-S to E-W compression. This may indicate a response to the effects of dextral transpressional deformation, or an early manifestation of Pamir indentation approaching the latitude of Aertashi.

Climatically, the change in facies at 18.5 Ma coincides with a shift in $\delta^{13}C_{org}$ to less negative values. This may be linked to the onset of C_4 vegetation in the area, driven by an overall trend towards increased aridity. However, a change in facies coincident with this shift along with the potential influence of petrogenetic (inherited) carbon cannot be ruled out as a potential cause. Further analyses of potential source rocks would need to be undertaken in order to investigate this argument further.

At 17.6 Ma, a change in a number of climate proxies at Aertashi is recorded, marked by the limited appearance of kaolinite clay between 17.6-15.0 Ma. This is accompanied by a subtle increase in total organic carbon (TOC) and a decrease in magnetic susceptibility. These shifts are suggestive of a 'wetter climate', resulting in an increase in chemical weathering which may be linked to the onset of the Mid-Miocene Climatic Optimum (MMCO) in central Asia.

The MMCO is characterised by increasing temperature and precipitation and observations of its occurrence in Aertashi indicate that the general aridification trend recorded throughout central Asia from the Cretaceous onwards was interrupted by periods of increased precipitation as suggested by Harzhauser et al. (2016).

However, a delayed response to the facies change at ~18.5 Ma cannot be ruled out. Again further studies from additional well-dated sections in central Asia would allow the distinction between localised tectonic effects and regional climatic signals.

7.1.4 ~15. - ca. 6 Ma: Pamir indentation reaches and exceeds the latitude of Aertashi, with renewed crustal shortening in the hinterland

Around 15 Ma marks a critical change in Aertashi. The distal braid plain facies of unit E are gradually replaced by grey gravelly beds interlayered within finer red beds, preceding the onset of unit F. Unit F is dominated by large grey clast-supported cobble conglomerates which contain basement rocks and volcanic pebbles and is estimated to be >6 km thick (Zheng et al., 2010, 2015a).

A provenance change at the onset of unit F is marked by a major reduction in the prominence of the ~400-500 Ma zircon U-Pb population, which is characteristic of the Western Kunlun terrane. This change is also recorded by a shift in ƐNd values towards less negative more juvenile values and a major petrographic change to increasing felsic and mafic metavolcanic input. Tectonically, these changes reflect the onset of input from the North Pamir terrane indicating that the Pamir salient had propagated sufficiently far north that the North Pamir terrane was proximal to, and influencing deposition in the Aertashi region.

Between 15-11 Ma, a doubling of accumulation rates is estimated (see Chapter 5.5) and by ~11 Ma petrography in Aertashi records a significant input from penecontemporaneous volcanic sources with large quantities of mafic to intermediate volcanic rock fragments. This volcanic input is linked to the Dudelick volcanics from the Central Pamir terrane (11 Ma) (Kooijman et al., 2017, Hacker et al., 2005).

This evidence, along with the presence of a 15 Ma U-Pb zircon peak, characteristic of the modern day Mustagh Ata drainage and input of Paleogene aged zircon grains common in Central Pamir drainages (Lukens et al., 2012), indicates that Central Pamir derived material was contributing to Aertashi by this time.

Our provenance data therefore indicates that the Aertashi sediments are recording the northward motion of the North Pamir terrane at ~15 Ma and then Central Pamir terrane at ~11 Ma, the distal effects of which are also recorded in the Tian Shan at this time through increased exhumation (Charreau et al., 2006).

Changes in climate signals at this time are overprinted by marked changes in provenance, making climatic interpretations in this interval highly speculative. Further work on climate indicators from ~15 Ma onwards would be needed in order to draw conclusions on the evolution of the Asian climate at this time.

7.1.5 Implications for Pamir indentation

Locally, the tectonic setting changed significantly at ~15 Ma with the onset of Qimugen thrusting, as observed by Wei et al. (2013). Our paleomagnetic results at Aertashi indicate that the majority of clockwise rotation recorded in this section (14 ± 4°) occurred after 15 Ma. Around half of this may relate to wholesale clockwise rotation of the Tarim Basin as recorded by Avouac et al. (1993). However, this suggests that at least half must also be attributed to more local processes directly related to Pamir indentation.

Various models of indentation have been proposed for the Pamir Salient, dependent on the extent and distribution of vertical – axis rotation within the Pamir. Indentation is associated with rotations when accommodated by radial thrusting or oroclinal bending (or buckling) (Yin et al., 2001, Robinson et al., 2004, Strecker et al., 1995). It is non-rotational if accommodated by transfer faulting on both sides of the salient which accommodate the indentation (Burtman and Molnar, 1993, Searle, 1996). More recently Cowgill (2010) proposed a hybrid model for the evolution of the Pamir salient from Miocene times onward in which counter-clockwise rotation continued in the Tajik Basin but ceased in the Tarim Basin. This was interpreted to be the result of activation along the KYTS. However, this model assumes that rotation in the Tarim Basin ceased by the late Oligocene (Bosboom et al., 2014b).

Our new data indicates that rotation continued throughout the Miocene in the Tarim Basin with most of this rotation occurring after 15.0 Ma. The rotation is therefore likely related to the change to proximal deformation documented in Aertashi after 15 Ma (see Section 7.1.4). This also corresponds to estimates of the timing of activation along the Qimugen frontal thrust system (QFTS) (Wei et al., 2013, Wang and Wang, 2016). This implies that before this time, Aertashi was located within the footwall in the Tarim Basin. Rotation and deformation in Aertashi therefore only commenced when it became part of the QFTS, resulting in the clockwise rotation as described in the radial thrusting model.

A notable problem with the rotation model is the E-W observed extension which is perpendicular to the extension directions expected by the radial thrusting. Therefore, the rotation recorded in Aertashi may relate to previously proposed mechanisms of extension, connected to the northward propagation of the dextral Karakoram fault

along a right-step releasing bend (Ratschbacher et al., 1994, Murphy et al., 2000). However further structural investigations are necessary to assess this releasing bend model, in particular, the accommodation of the strike-slip motion further north of the bend. Whatever the contribution of the rotation and releasing bend, a large part of the extension is most likely to be related to post-thickening gravitational collapse of the Kongur Shan (Robinson et al., 2004, Rutte et al., 2017b, Brunel et al., 1994, Thiede et al., 2013)

7.1.6 Implications for Pamir formation models

The two key models for Pamir formation and evolution; the subduction model (Sobel et al., 2013) and the delamination model (Bird, 1979, Küfner et al., 2016, Rutte et al., 2017a,b), make specific predictions regarding the timing of Pamir indentation and mechanisms involved in its evolution.

In the subduction model, following slab breakoff at ~25 Ma, a build-up of stress due to the northward convergence from India resulted in the onset of continental subduction of a south-dipping slab beneath the Pamir (e.g. Replumaz et al., 2010). This stress build up was subsequently released, resulting in roll-back of the south dipping Alai slab and leading to exhumation of the Central Pamir through back-arc extensional processes.

Conversely, in the delamination model, slab break off led to a change from subduction to under-thrusting of the Indian plate beneath Asia (Rutte et al., 2017a,b). In this model, the 22 Ma collapse documented in the Pamir could relate to the foundering, delamination, and roll-back of its lithospheric mantle in response to the northward indentation of the thicker continental Indian lithosphere from 22 to 15 Ma under the Pamir terranes. Part of this collapse has been proposed to be accommodated by westward as well as northward thrusting towards Tarim during this time (Rutte et al., 2017a,b).

The change in tectonic regime recorded in Aertashi from 24.3 Ma onwards coincides with the timing of activation of the KYTS and regional deformation at 25-20 Ma, which has been related to the early onset of Pamir indentation (Chapter 5.6). There is also a major change in the geodynamics of the Pamir, from crustal thickening to extension and possible crustal collapse (Amidon and Hynek, 2010, Rutte et al., 2017a,b, Sobel et al., 2013, Stübner et al., 2013a,b).

This change in tectonic regime coincides to a slowing down of India, indicated at 20±2 Ma from 57 to 44 km/Myr (Molnar and Stock 2009; Iafaldano et al., 2013) and marks a time of regional deformation throughout central Asia, with the onset of strong exhumation in the western Kunlun and southern Tian Shan (Sobel and Dumitru, 1997), the eastern Kunlun (Yuan et al., 2006), the west Qilian Shan and Xining Basin (Xiao et al., 2012a) and as far east as the northern Qinling margin (Liu et al., 2013).

Subsequent post-15 Ma clockwise rotation and the presence of the North Pamir terrane nearby the location of the Aertashi section at 15 Ma, and Central Pamir terrane at 11 Ma, provides important kinematic constraints on the timing and position of the Pamir indentation into Tarim.

Within the Pamir, shortening and crustal thickening resumed at ~12 Ma, coincident with a further decrease in Indian northward velocity from 44 to 34 km/Myr at ~11 ± 2 Ma (Molnar and Stock, 2009).

This resumption of crustal thickening has been interpreted, in the subduction model (Sobel et al., 2013), to a change in the degree of coupling between the down-going and over-riding slab resulting in renewed crustal thickening. Whilst in the delamination model (Rütte et al 2017), it is interpreted to result from the underthrusting of 'cratonic' India reaching the latitude of -, and impinging on 'cratonic' Asia since 10 Ma (Küfner et al 2016). However the delamination model suggests that the onset of Pamir indentation commenced at 10 Ma with delamination accounting for the entire ca. 300 km northward indentation since that time.

Our results show that the Pamir salient had already indented significantly into the Tarim Basin by 15 Ma, with probably half of the 300 km total indentation consumed when the Northern Pamir reached the latitude of Aertashi.

We note, that if the northward Pamir indentation into the Tarim and Tajik basins started only after 10 Ma (Küfner et al., 2016), the proposed coeval westward gravitational collapse and extrusion of Pamir into the Tajik Basin (Rutte et al., 2017a,b) becomes problematic.

Since 15 Ma, the rest of the 300 km indentation is accounted for by the subduction model, which continued until about 5-3 Ma when the KYTS becomes mostly inactive (Sobel et al., 2011, 2013). According to the delamination model and Indian plate velocities (Küfner et al., 2016, Molnar and Stock, 2009), the position of the northern

edge of the Indian lithospheric indentor can be estimated to reach the present position of Aertashi only ~5 Ma. This is not consistent with our observations of Pamir detritus and thrusting at 15 Ma at Aertashi. In addition, in the delamination model a large part of the Pamir indentation into Tarim remains to be accommodated after 5 Ma, although the slip on the KYTS has mostly ceased by then.

Sobel et al. (2011) suggested that the KYTS may have become inactive due to the northward motion of Tarim moving coherently with the Pamir similar to observations made in the present day (Ischuk et al., 2013, Zubovich et al., 2016). Taking into account the northward motion of the Tarim Basin also has implications on the delamination model. Assuming a maximum of 200 km northward motion since 12 Ma (as predicted by Avouac et al. (1993) based on maximum Tian Shan shortening, see Section 3.5.2) would imply Aertashi may have been positioned as much as 200 km further south at this time. Interestingly, it can be estimated that this position would have been reached by the Indian lithospheric indentor around 11±2 Ma based on Indian plate velocities (Molnar and Stock, 2009). Only in this extreme scenario, could the delamination model account for some of our observations at Aertashi assuming the 15 Ma onset of Pamir source and deformation preceded the arrival of Indian lithospheric indentor by a few million years (Figure 3.11). According to this view the post 15 Ma indentation of Pamir moving northward slightly faster than Tarim, would be driven by the Indian lithospheric indentor.

7.2 Limitations and further work

In this study, great effort has been made to carefully choose a variety of methods and approaches in order to achieve the set aims of this project. Nevertheless, all analytical methods are subject to limitations which are discussed in detail in each Chapter of this Thesis. Here we present some key limitations that apply to this study as a whole.

7.2.1 Provenance study

All detrital provenance studies rely on detailed terrane characterisation which in this case is achieved by a combination of published material. This includes sampling from modern river catchments and individual sampling of exposed bedrock, and our own sampling of modern river catchments throughout the Pamir and western Kunlun regions. However, this sampling method assumes that the petrography and isotopic

values obtained from that terrane in the modern day have remained similar throughout its exhumational history, which may not be true.

Terrane characterisation often reveals similar ages, and isotopic, or petrographic characteristics, as is evidenced when comparing the North Pamir Terrane, Western Kunlun Terrane and Songpan Ganzi Terranes in this study. In an attempt to minimise this overlap, a variety of provenance techniques are utilised. However, it is often not possible to determine distinct provenance terranes without some degree of overlap as in this case.

Access to sample locations for source characterisation in this region was hampered by a number of political and legal borders; the study region itself borders the countries of Tajikistan, Afghanistan, Pakistan, Kyrgyzstan, Tibet and China, many of which have dangerous and politically sensitive borders. Therefore, we were only able to access the Chinese Pamir and the eastern margin of the Tarim Basin making full source characterisation of the Pamir mountain range limited to a few available published works. This was particularly the case for the Central Pamir Terrane where access was limited to sampling from the main Tashkurgan River, and the Northern Pamir Terrane where access was limited due to the boarder with Tajikistan.

In the Western Kunlun, access was limited to the Chinese region due to the politically sensitive boarder with Tibet which limited our access to the Songpan Ganzi and Tianshuihai terranes. As a result, this project and future work would benefit from access to more source river drainages currently residing in neighbouring countries in order to obtain a fuller picture of the source characterisation which can be utilised to examine sedimentary sections for provenance.

7.2.2 Age control limitations

The majority of studies from around the Tarim Basin have been limited by poor age control and interpretations that are based on this. Concerted efforts more recently have been made to revise this age control along the western margin of the Tarim Basin as discussed in Chapter 5, which has resulted in re-evaluation of many studies from this region. However, a combination of more recent studies with revised age control and older studies based on older uncertain age control makes correlative comparisons from this region difficult.

To address this issue, continued work to update the age control on existing study sites and new sites needs to be undertaken in order to provide the foundation upon which more accurate studies can be conducted in the future.

7.2.3 Climate studies.

One of the key limitations of our climate study was the ability to distinguish between provenance derived signals, facies change variations and climate signals. The use of a number of different climate proxies did allow some distinction of these factors; however, final conclusions on the evolution of the climate in central Asia are limited by the use of only one study site and the limited availability of well-dated published work. In order to determine if changes in climate proxies observed in the Aertashi section are the result of regional climatic shifts or localised tectonic events, further work on a number of well dated study sites around the Tarim Basin and from elsewhere in the region is required.

Our organic carbon study yielded extremely low values of total organic carbon for the Aertashi section, which is typical for sandstone red beds. As a result of this, the influence of inherited petrogenetic carbon (at least 30% of the total signal may be derived from detrital organic carbon) as discussed in Chapter 6.2.3 can have a significant effect on the organic carbon signal. In order to investigate the influence of detrital organic carbon on the total organic C signal, further analyses of potential source rocks and their $\delta^{13}C$ signature would need to be undertaken.

Our climate study extended up to ~14 Ma, which is now shown to be a critical transitional time in the tectonic evolution in the Pamir and Tarim Basin. Our study stopped here due to time and access constraints and the lack of viable sediments for magnetostratigraphic analysis. Our study examining the relationship between tectonics and climate in Aertashi is limited by the absence of data collected above this transitional point, therefore further work is suggested to investigate the impact and changes in climate for the Aertashi region and central Asia post 14 Ma by continuing this study in the <14 Ma sediments.

7.2.4 Models for Pamir evolution

Constraining the tectonic evolution of the Pamir was limited by the use of a single study site, even though it was coupled with a review of regional studies. Further

constraints on the tectonic evolution of the Pamir salient would benefit by continuing the tectonic examination of sedimentary sections from both sides of the Pamir where, at present, stratigraphic studies are limited.

Examination of the rotation recorded in the Aertashi section was limited by the absence of analysis above 15 Ma. Our conclusion that most of the rotation occurred after this time can be further constrained by continuing analysis in sediments <15 Ma in this region. This would also allow further investigation into how well the data from Aertashi fits into the model of thrust activation recorded in the Qimugen frontal thrust fault by Wang and Wang (2016) and Wei et al. (2013).

8. References:

AITCHISON, J. C., ALI, J. R. & DAVIS, A. M. 2007. When and where did India and Asia collide? *Journal of Geophysical Research: Solid Earth,* 112.

ALI, J. R. & AITCHISON, J. C. 2006. Positioning Paleogene Eurasia problem: Solution for 60–50 Ma and broader tectonic implications. *Earth and Planetary Science Letters,* 251**,** 148-155.

ALLEGRE, C. O., COURTILLOT, V., TAPPONNIER, P., HIRN, A., MATTAUER, M., COULON, C., JAEGER, J., ACHACHE, J., SCHÄRER, U. & MARCOUX, J. 1984. Structure and evolution of the Himalaya–Tibet orogenic belt. *Nature,* 307**,** 17-22.

AMIDON, W. H. & HYNEK, S. A. 2010. Exhumational history of the north central Pamir. *Tectonics,* 29**,** TC5017.

ANDÒ, S., GARZANTI, E., PADOAN, M. & LIMONTA, M. 2012. Corrosion of heavy minerals during weathering and diagenesis: a catalog for optical analysis. *Sedimentary Geology,* 280**,** 165-178.

ARGAND, E. La tectonique de l'Asie. Conférence faite á Bruxelles, le 10 août 1922. Congrès géologique international (XIIIe session)-Belgique 1922, 1924. 171-372.

ARNAUD, N., BRUNEL, M., CANTAGREL, J. & TAPPONNIER, P. 1993. High cooling and denudation rates at Kongur Shan, eastern Pamir (Xinjiang, China) revealed by 40Ar/39Ar alkali feldspar thermochronology. *Tectonics,* 12**,** 1335-1346.

ARROWSMITH, J. R. & STRECKER, M. 1999. Seismotectonic range-front segmentation and mountain-belt growth in the Pamir-Alai region, Kyrgyzstan (India-Eurasia collision zone). *Geological Society of America Bulletin,* 111**,** 1665-1683.

AVOUAC, J. P., TAPPONNIER, P., BAI, M., YOU, H. & WANG, G. 1993. Active thrusting and folding along the northern Tien Shan and Late Cenozoic rotation of the Tarim relative to Dzungaria and Kazakhstan. *Journal of Geophysical Research: Solid Earth,* 98**,** 6755-6804.

BALSAM, W. L., ELLWOOD, B. B., JI, J., WILLIAMS, E. R., LONG, X. & EL HASSANI, A. 2011. Magnetic susceptibility as a proxy for rainfall: worldwide data from tropical and temperate climate. *Quaternary Science Reviews,* 30**,** 2732-2744.

BANDE, A., SOBEL, E. R., MIKOLAICHUK, A. & ACOSTA, V. T. 2015. Talas–Fergana Fault Cenozoic timing of deformation and its relation to Pamir indentation. *Geological Society, London, Special Publications,* 427**,** SP427. 1.

BANDE, A., SOBEL, E. R., MIKOLAICHUK, A., SCHMIDT, A. & STOCKLI, D. F. 2017. Exhumation history of the western Kyrgyz Tien Shan: Implications for intramontane basin formation. *Tectonics,* 36**,** 163-180.

BARKER, P. F. 2001. Scotia Sea regional tectonic evolution: implications for mantle flow and palaeocirculation. *Earth-Science Reviews,* 55**,** 1-39.

BARKER, P. F., FILIPPELLI, G. M., FLORINDO, F., MARTIN, E. E. & SCHER, H. D. 2007. Onset and role of the Antarctic Circumpolar Current. *Deep Sea Research Part II: Topical Studies in Oceanography,* 54**,** 2388-2398.

BEERLING, D. 1996. 13 C discrimination by fossil leaves during the late-glacial climate oscillation 12-10 ka BP: measurements and physiological controls. *Oecologia,* 108**,** 29-37.

BEERLING, D. & ROYER, D. 2002. Reading a CO2 signal from fossil stomata. *New Phytologist,* 153**,** 387-397.

BEERLING, D. J. & ROYER, D. L. 2011. Convergent Cenozoic CO_2 history. *Nature Geoscience,* 4**,** 418-420.

BENDER, M. M. 1971. Variations in the 13C/12C ratios of plants in relation to the pathway of photosynthetic carbon dioxide fixation. *Phytochemistry,* 10**,** 1239-1244.

BERNET, M. 2009. A field-based estimate of the zircon fission-track closure temperature. *Chemical Geology,* 259**,** 181-189.

BERNET, M., BRANDON, M. T., GARVER, J. I. & MOLITOR, B. 2004. Downstream changes of Alpine zircon fission-track ages in the Rhône and Rhine Rivers. *Journal of Sedimentary Research,* 74**,** 82-94.

BERNET, M. & GARVER, J. I. 2005. Fission-track analysis of detrital zircon. *Reviews in Mineralogy & Geochemistry,* 58**,** 205-238.

BERSHAW, J., GARZIONE, C. N., SCHOENBOHM, L., GEHRELS, G. & TAO, L. 2012. Cenozoic evolution of the Pamir plateau based on stratigraphy, zircon provenance, and stable isotopes of foreland basin sediments at Oytag (Wuyitake) in the Tarim Basin (west China). *Journal of Asian Earth Sciences,* 44**,** 136-148.

BIRD, P. 1979. Continental delamination and the Colorado Plateau. *Journal of Geophysical Research: Solid Earth,* 84**,** 7561-7571.

BISCAYE, P. E. 1965. Mineralogy and sedimentation of recent deep-sea clay in the Atlantic Ocean and adjacent seas and oceans. *Geological Society of America Bulletin,* 76**,** 803-832.

BISKE, Y. S. & SELTMANN, R. 2010. Paleozoic Tian-Shan as a transitional region between the Rheic and Urals-Turkestan oceans. *Gondwana Research,* 17**,** 602-613.

BLACK, L. P., KAMO, S. L., ALLEN, C. M., ALEINIKOFF, J. N., DAVIS, D. W., KORSCH, R. J. & FOUDOULIS, C. 2003. TEMORA 1: a new zircon standard for Phanerozoic U–Pb geochronology. *Chemical Geology,* 200**,** 155-170.

BLAYNEY, T., NAJMAN, Y., DUPONT-NIVET, G., CARTER, A., MILLAR, I., GARZANTI, E., SOBEL, E. R., RITTNER, M., ANDÒ, S., GUO, Z. & VEZZOLI, G. 2016. Indentation of the Pamirs with respect to the northern margin of Tibet: Constraints from the Tarim basin sedimentary record. *Tectonics,* 35**,** 2345-2369.

BOLLE, M.-P. & ADATTE, T. 2001. Palaeocene-early Eocene climatic evolution in the Tethyan realm: clay mineral evidence. *Clay minerals,* 36**,** 249-261.

BORRADAILE, G. & HENRY, B. 1997. Tectonic applications of magnetic susceptibility and its anisotropy. *Earth-Science Reviews,* 42**,** 49-93.

BOSBOOM, R., DUPONT-NIVET, G., GROTHE, A., BRINKHUIS, H., VILLA, G., MANDIC, O., STOICA, M., KOUWENHOVEN, T., HUANG, W. & YANG, W. 2014a. Timing, cause and impact of the late Eocene stepwise sea retreat from the Tarim Basin (west China). *Palaeogeography, Palaeoclimatology, Palaeoecology,* 403**,** 101-118.

BOSBOOM, R., DUPONT-NIVET, G., HUANG, W., YANG, W. & GUO, Z. 2014b. Oligocene clockwise rotations along the eastern Pamir: Tectonic and paleogeographic implications. *Tectonics,* 33**,** 2013TC003388.

BOSBOOM, R., DUPONT-NIVET, G., GROTHE, A., BRINKHUIS, H., VILLA, G., MANDIC, O., STOICA, M., HUANG, W., YANG, W. & GUO, Z. 2014c. Linking Tarim Basin sea retreat (west China) and Asian aridification in the late Eocene. *Basin Research,* 26**,** 621-640.

BOSBOOM, R., MANDIC, O., DUPONT-NIVET, G., PROUST, J.-N., ORMUKOV, C. & AMINOV, J. 2015. Late Eocene palaeogeography of the proto-Paratethys Sea in Central Asia (NW China, southern Kyrgyzstan and SW Tajikistan). *Geological Society, London, Special Publications,* 427**,** SP427. 11.

BOSBOOM, R. E., ABELS, H. A., HOORN, C., VAN DEN BERG, B. C. J., GUO, Z. & DUPONT-NIVET, G. 2014d. Aridification in continental Asia after the Middle Eocene Climatic Optimum (MECO). *Earth and Planetary Science Letters,* 389**,** 34-42.

BOSBOOM, R. E., DUPONT-NIVET, G., HOUBEN, A. J. P., BRINKHUIS, H., VILLA, G., MANDIC, O., STOICA, M., ZACHARIASSE, W. J., GUO, Z., LI, C. & KRIJGSMAN, W. 2011. Late Eocene sea retreat from the Tarim Basin (west China) and concomitant Asian paleoenvironmental change. *Palaeogeography, Palaeoclimatology, Palaeoecology,* 299**,** 385-398.

BOSTRÖM, B., COMSTEDT, D. & EKBLAD, A. 2007. Isotope fractionation and 13C enrichment in soil profiles during the decomposition of soil organic matter. *Oecologia,* 153**,** 89-98.

BOUGEOIS, L., DE RAFÉLIS, M., REICHART, G.-J., DE NOOIJER, L. J., NICOLLIN, F. & DUPONT-NIVET, G. 2014. A high resolution study of trace elements and stable isotopes in oyster shells to estimate Central Asian Middle Eocene seasonality. *Chemical Geology,* 363**,** 200-212.

BOUGEOIS, L., GUILLAUME DUPONT-NIVET, MARC DE RAFÉLIS, JULIA TINDALL, JEAN-NOËL PROUST, GERT-JAN REICHART, LENNART DE NOOIJER, ZHAOJIE GUO & ORMUKOV., C. Submitted. Asian monsoons and aridification in response to Cenozoic sea retreat and westerly shielding.

BOURGEOIS, O., COBBOLD, P. R., ROUBY, D., THOMAS, J. C. & SHEIN, V. 1997. Least squares restoration of Tertiary thrust sheets in map view, Tajik depression, central Asia. *Journal of Geophysical Research: Solid Earth,* 102**,** 27553-27573.

BRUNEL, M., ARNAUD, N., TAPPONNIER, P., PAN, Y. & WANG, Y. 1994. Kongur Shan normal fault: Type example of mountain building assisted by extension (Karakoram fault, eastern Pamir). *Geology,* 22**,** 707-710.

BUDANOV, V., VOLKOVA, N. & DRONOV, V. 1999. Petrochemistry of a rhyodacite-trachyte series in a Paleogene volcanoplutonic belt in the Southeastern Pamirs. *RUSSIAN GEOLOGY AND GEOPHYSICS C/C OF GEOLOGIIA I GEOFIZIKA,* 40**,** 648-654.

BURTMAN, V. & MOLNAR, P. 1993. Geological and Geophysical Evidence for Deep Subduction of Continental Crust Beneath the Pamir. *Geological Society of America Special Paper 281,* 281**,** 76.

BURTMAN, V. S. 2000. Cenozoic crustal shortening between the Pamir and Tien Shan and a reconstruction of the Pamir–Tien Shan transition zone for the Cretaceous and Palaeogene. *Tectonophysics,* 319**,** 69-92.

BURTMAN, V. S., SKOBELEV, S. F. & MOLNAR, P. 1996. Late Cenozoic slip on the Talas-Ferghana fault, the Tien Shan, central Asia. *Geological Society of America Bulletin,* 108**,** 1004-1021.

BUTLER, R. F. 1992. *Paleomagnetism: magnetic domains to geologic terranes,* Blackwell Scientific Publications Boston.

CAO, K., WANG, G.-C., BERNET, M., BEEK, P. V. D. & ZHANG, K.-X. 2015. Exhumation history of the West Kunlun Mountains, northwestern Tibet: Evidence for a long-lived, rejuvenated orogen. *Earth and Planetary Science Letters,* 432**,** 391-403.

CAO, K., WANG, G.-C., VAN DER BEEK, P., BERNET, M. & ZHANG, K.-X. 2013. Cenozoic thermo-tectonic evolution of the northeastern Pamir revealed by zircon and apatite fission-track thermochronology. *Tectonophysics,* 589**,** 17-32.

CAO, K., XU, Y., WANG, G., ZHANG, K., VAN DER BEEK, P., JIAO, Y., WANG, C., JIANG, S. & BERSHAW, J. 2014. Neogene source-to-sink relations between the Pamir and Tarim Basin: insights from stratigraphy, detrital zircon geochronology, and whole-rock geochemistry. The Journal of Geology.

CARDOZO, N. 2012. *OSX Backstrip* [Online]. www.ux.uis.no/nestor/work/programs: Nestor Cardozo. [Accessed 15/05/2017].

CARRAPA, B., MUSTAPHA, F. S., COSCA, M., GEHRELS, G., SCHOENBOHM, L. M., SOBEL, E. R., DECELLES, P. G., RUSSELL, J. & GOODMAN, P. 2014. Multisystem dating of modern river detritus from Tajikistan and China: Implications for crustal evolution and exhumation of the Pamir. *Lithosphere,* 6**,** 443-455.

CARTER, A. 1999. Present status and future avenues of source region discrimination and characterization using fission track analysis. *Sedimentary Geology,* 124**,** 31-45.

CAVES, J. K., SJOSTROM, D. J., MIX, H. T., WINNICK, M. J. & CHAMBERLAIN, C. P. 2014. Aridification of Central Asia and uplift of the Altai and Hangay Mountains, Mongolia: Stable isotope evidence. *American Journal of Science,* 314**,** 1171-1201.

CAVES, J. K., WINNICK, M. J., GRAHAM, S. A., SJOSTROM, D. J., MULCH, A. & CHAMBERLAIN, C. P. 2015. Role of the westerlies in Central Asia climate over the Cenozoic. *Earth and Planetary Science Letters,* 428**,** 33-43.

CERLING, T. E., HARRIS, J. M., MACFADDEN, B. J., LEAKEY, M. G., QUADE, J., EISENMANN, V. & EHLERINGER, J. R. 1997. Global vegetation change through the Miocene/Pliocene boundary. *Nature,* 389**,** 153-158.

CHAMLEY, H. 1989. Clay formation through weathering. *Clay sedimentology.* New York: Springer.

CHARREAU, J., GILDER, S., CHEN, Y., DOMINGUEZ, S., AVOUAC, J.-P., SEN, S., JOLIVET, M., LI, Y. & WANG, W. 2006. Magnetostratigraphy of the Yaha section, Tarim Basin (China): 11 Ma acceleration in erosion and uplift of the Tian Shan mountains. *Geology,* 34**,** 181-184.

CHARREAU, J., GUMIAUX, C., AVOUAC, J.-P., AUGIER, R., CHEN, Y., BARRIER, L., GILDER, S., DOMINGUEZ, S., CHARLES, N. & WANG, Q. 2009. The Neogene Xiyu Formation, a diachronous prograding gravel wedge at front of the Tianshan: Climatic and tectonic implications. *Earth and Planetary Science Letters,* 287**,** 298-310.

CHARREAU, J., KENT-CORSON, M. L., BARRIER, L., AUGIER, R., RITTS, B. D., CHEN, Y., FRANCE-LANNORD, C. & GUILMETTE, C. 2012. A high-resolution stable isotopic record from the Junggar Basin (NW China): Implications for the paleotopographic evolution of the Tianshan Mountains. *Earth and Planetary Science Letters,* 341**,** 158-169.

CHEN, J., ZHAO, P., WANG, C., HUANG, Y. & CAO, K. 2013. Modeling East Asian climate and impacts of atmospheric CO 2 concentration during the Late Cretaceous (66Ma). *Palaeogeography, Palaeoclimatology, Palaeoecology,* 385**,** 190-201.

CHEN, Y., COGNÉ, J.-P. & COURTILLOT, V. 1992. New Cretaceous paleomagnetic poles from the Tarim Basin, northwestern China. *Earth and Planetary Science Letters,* 114**,** 17-38.

CHEN, Y., GILDER, S., HALIM, N., COGNÉ, J. P. & COURTILLOT, V. 2002. New paleomagnetic constraints on central Asian kinematics: Displacement along the Altyn Tagh fault and rotation of the Qaidam Basin. *Tectonics,* 21.

CHERNIAK, D. J. & WATSON, E. B. 2001. Pb diffusion in zircon. *Chemical Geology,* 172**,** 5-24.

CHEVALIER, M. L., LI, H., PAN, J., PEI, J., WU, F., XU, W., SUN, Z. & LIU, D. 2011. Fast slip-rate along the northern end of the Karakorum fault system, western Tibet. *Geophysical Research Letters,* 38.

CHEVALIER, M. L., PAN, J., LI, H., LIU, D. & WANG, M. 2015. Quantification of both normal and right-lateral late Quaternary activity along the Kongur Shan extensional system, Chinese Pamir. *Terra Nova,* 27**,** 379-391.

CHI, Y., FANG, X., SONG, C., MIAO, Y., TENG, X., HAN, W., WU, F. & YANG, J. 2013. Cenozoic organic carbon isotope and pollen records from the Xining Basin, NE Tibetan Plateau, and their palaeoenvironmental significance. *Palaeogeography, Palaeoclimatology, Palaeoecology,* 386**,** 436-444.

CHUNG, S.-L., LO, C.-H., LEE, T.-Y., ZHANG, Y., XIE, Y., LI, X., WANG, K.-L. & WANG, P.-L. 1998. Diachronous uplift of the Tibetan plateau starting 40 Myr ago. *Nature,* 394**,** 769-773.

CLARK, M., SCHOENBOHM, L., ROYDEN, L., WHIPPLE, K., BURCHFIEL, B., ZHANG, X., TANG, W., WANG, E. & CHEN, L. 2004. Surface uplift, tectonics, and erosion of eastern Tibet from large-scale drainage patterns. *Tectonics,* 23.

CLARK, M. K., FARLEY, K. A., ZHENG, D., WANG, Z. & DUVALL, A. R. 2010. Early Cenozoic faulting of the northern Tibetan Plateau margin from apatite (U–Th)/He ages. *Earth and Planetary Science Letters,* 296**,** 78-88.

CLIFT, P. D., WAN, S. & BLUSZTAJN, J. 2014. Reconstructing chemical weathering, physical erosion and monsoon intensity since 25Ma in the northern South China Sea: a review of competing proxies. *Earth-Science Reviews,* 130**,** 86-102.

CONNIN, S. L., FENG, X. & VIRGINIA, R. A. 2001. Isotopic discrimination during long-term decomposition in an arid land ecosystem. *Soil Biology and Biochemistry,* 33**,** 41-51.

COPELAND, P., HARRISON, T. M., KIDD, W. E. A., RONGHUA, X. & YUQUAN, Z. 1987. Rapid early Miocene acceleration of uplift in the Gangdese Belt, Xizang (southern Tibet), and its bearing on accommodation mechanisms of the India-Asia collision. *Earth and Planetary Science Letters,* 86**,** 240-252.

COUTAND, I., STRECKER, M. R., ARROWSMITH, J. R., HILLEY, G., THIEDE, R. C., KORJENKOV, A. & OMURALIEV, M. 2002. Late Cenozoic tectonic development of the intramontane Alai Valley, (Pamir-Tien Shan region, central Asia): An example of intracontinental deformation due to the Indo-Eurasia collision. *Tectonics,* 21**,** 1053.

COWGILL, E. 2010. Cenozoic right-slip faulting along the eastern margin of the Pamir salient, northwestern China. *Geological Society of America Bulletin,* 122**,** 145-161.

COWGILL, E., YIN, A., HARRISON, T. M. & XIAO-FENG, W. 2003. Reconstruction of the Altyn Tagh fault based on U-Pb geochronology: Role of back thrusts, mantle sutures, and heterogeneous crustal strength in forming the Tibetan Plateau. *Journal of Geophysical Research: Solid Earth,* 108**,** 2346.

COWGILL, E. S. 2001. *Tectonic evolution of the Altyn Tagh-Western Kunlun fault system, northwestern China.* PhD, University of California.

DE PELSMAEKER, E., JOLIVET, M., LABORDE, A., POUJOL, M., ROBIN, C., ZHIMULEV, F. I., NACHTERGAELE, S., GLORIE, S., DE CLERCQ, S. & BATALEV, V. Y. 2017. Source-to-sink dynamics in the Kyrgyz Tien Shan from the Jurassic to the Paleogene: Insights from sedimentological and detrital zircon U-Pb analyses. *Gondwana Research*.

DECELLES, P., KAPP, P., GEHRELS, G. & DING, L. 2014. Paleocene-Eocene foreland basin evolution in the Himalaya of southern Tibet and Nepal: Implications for the age of initial India-Asia collision. *Tectonics,* 33**,** 824-849.

DECELLES, P., KAPP, P., QUADE, J. & GEHRELS, G. 2011. Oligocene–Miocene Kailas basin, southwestern Tibet: Record of postcollisional upper-plate extension in the Indus-Yarlung suture zone. *Geological Society of America Bulletin,* 123**,** 1337-1362.

DECONTO, R. M. & POLLARD, D. 2003. Rapid Cenozoic glaciation of Antarctica induced by declining atmospheric CO2. *Nature,* 421**,** 245-249.

DEMAREST, H. H. 1983. Error analysis for the determination of tectonic rotation from paleomagnetic data. *Journal of Geophysical Research: Solid Earth,* 88**,** 4321-4328.

DEWEY, J. F., SHACKLETON, R. M., CHENGFA, C. & YIYIN, S. 1988. The tectonic evolution of the Tibetan Plateau. *Philosophical Transactions of the Royal Society of London A: Mathematical, Physical and Engineering Sciences,* 327**,** 379-413.

DICKINSON, W. R. 1985. Interpreting provenance relations from detrital

modes of sandstones. *In:* ZUFFA, G. G. (ed.) *Provenance of arenites.* Dordrecht: Reidel.

DIEFENDORF, A. F., MUELLER, K. E., WING, S. L., KOCH, P. L. & FREEMAN, K. H. 2010. Global patterns in leaf 13C discrimination and implications for studies of past and future climate. *Proceedings of the National Academy of Sciences,* 107**,** 5738-5743.

DILL, H., KAUFHOLD, S., KHISHIGSUREN, S. & BULGAMAA, J. 2005. Discovery and origin of a Palaeogene smectite-bearing clay deposit in the SE Gobi (Mongolia). *Clay Minerals,* 40**,** 351-368.

DING, D., WANG, D., LIU, W. & SUN, S. 1996. The western Kunlun orogenic belt and basin. *Geological Publishing House, Beijing,* 36**,** 1-224.

DING, L., YANG, D., CAI, F. L., PULLEN, A., KAPP, P., GEHRELS, G. E., ZHANG, L. Y., ZHANG, Q. H., LAI, Q. Z., YUE, Y. H. & SHI, R. D. 2013. Provenance analysis of the Mesozoic Hoh-Xil-Songpan-Ganzi turbidites in northern Tibet: Implications for the tectonic evolution of the eastern Paleo-Tethys Ocean. *Tectonics,* 32**,** 34-48.

DUBEY, A. K. 2014. *Understanding an orogenic belt,* Heidelberg, Springer International Publishing Switzerland.

DUCEA, M. N. 2011. Fingerprinting orogenic delamination. *Geology,* 39**,** 191-192.

DUCEA, M. N., LUTKOV, V., MINAEV, V. T., HACKER, B., RATSCHBACHER, L., LUFFI, P., SCHWAB, M., GEHRELS, G. E., MCWILLIAMS, M., VERVOORT, J. & METCALF, J. 2003. Building the Pamirs: The view from the underside. *Geology,* 31**,** 849-852.

DUPONT-NIVET, G., GUO, Z., BUTLER, R. F. & JIA, C. 2002. Discordant paleomagnetic direction in Miocene rocks from the central Tarim Basin: evidence for local deformation and inclination shallowing. *Earth and Planetary Science Letters,* 199**,** 473-482.

DUPONT-NIVET, G., HOORN, C. & KONERT, M. 2008. Tibetan uplift prior to the Eocene-Oligocene climate transition: Evidence from pollen analysis of the Xining Basin. *Geology,* 36**,** 987-990.

DUPONT-NIVET, G., KRIJGSMAN, W., LANGEREIS, C. G., ABELS, H. A., DAI, S. & FANG, X. 2007. Tibetan plateau aridification linked to global cooling at the Eocene-Oligocene transition. *Nature,* 445**,** 635-638.

DUPONT-NIVET, G., LIPPERT, P. C., VAN HINSBERGEN, D. J., MEIJERS, M. J. & KAPP, P. 2010. Palaeolatitude and age of the Indo–Asia collision: palaeomagnetic constraints. *Geophysical Journal International,* 182**,** 1189-1198.

DUVALL, A. R., CLARK, M. K., VAN DER PLUIJM, B. A. & LI, C. 2011. Direct dating of Eocene reverse faulting in northeastern Tibet using Ar-dating of fault clays and low-temperature thermochronometry. *Earth and Planetary Science Letters,* 304**,** 520-526.

EHLERINGER, J. R. 1989. Carbon isotope ratios and physiological processes in aridland plants. *Stable isotopes in ecological research.* Springer.

EHLERINGER, J. R. 2005. The influence of atmospheric CO2, temperature, and water on the abundance of C3/C4 taxa. *A history of atmospheric CO2 and its effects on plants, animals, and ecosystems*. Springer.

EHLERINGER, J. R., CERLING, T. & DEARING, M. D. 2006. *A history of atmospheric CO2 and its effects on plants, animals, and ecosystems*, Springer Science & Business Media.

EHLERINGER, J. R., CERLING, T. E. & HELLIKER, B. R. 1997. C4 photosynthesis, atmospheric CO2, and climate. *Oecologia,* 112**,** 285-299.

EHLERINGER, J. R. & MONSON, R. K. 1993. Evolutionary and ecological aspects of photosynthetic pathway variation. *Annual Review of Ecology and Systematics,* 24**,** 411-439.

ENGLAND, P., HOUSEMAN, G. & SONDER, L. 1985. Length scales for continental deformation in convergent, divergent, and strike-slip environments: Analytical and approximate solutions for a thin viscous sheet model. *Journal of Geophysical Research: Solid Earth (1978–2012),* 90**,** 3551-3557.

ENGLAND, P. & MOLNAR, P. 1990. Right-lateral shear and rotation as the explanation for strike-slip faulting in eastern Tibet. *Nature,* 344**,** 140-142.

ESQUEVIN, J. 1969. Influence de la composition chimique des illites sur leur cristallinité. *Bull. Centre Rech. Pau-SNPA,* 3**,** 147-153.

EXON, N. F., KENNETT, J. P. & MALONE, M. J. Leg 189 synthesis: Cretaceous–Holocene history of the Tasmanian gateway. Proceedings of the ocean drilling program, scientific results, 2004. 1-37.

FAN, G., NI, J. F. & WALLACE, T. C. 1994. Active tectonics of the Pamirs and Karakorum. *Journal of Geophysical Research: Solid Earth,* 99**,** 7131-7160.

FAN, M. J., DETTMAN, D. L., SONG, C. H., FANG, X. M. & GARZIONE, C. N. 2007. Climatic variation in the Linxia basin, NE Tibetan Plateau, from 13.1 to 4.3 Ma: The stable isotope record. *Palaeogeography Palaeoclimatology Palaeoecology,* 247**,** 313-328.

FARQUHAR, G. D., EHLERINGER, J. R. & HUBICK, K. T. 1989. Carbon isotope discrimination and photosynthesis. *Annual review of plant biology,* 40**,** 503-537.

FISHER, R. 1953. Dispersion on a sphere. *Proceedings of the Royal Society of London. Series A. Mathematical and Physical Sciences,* 217**,** 295-305.

FLOWER, B. P. & KENNETT, J. P. 1994. The middle Miocene climatic transition: East Antarctic ice sheet development, deep ocean circulation and global carbon cycling. *Palaeogeography, palaeoclimatology, palaeoecology,* 108**,** 537-555.

FOSTER, G. L., LEAR, C. H. & RAE, J. W. B. 2012. The evolution of pCO_2, ice volume and climate during the middle Miocene. *Earth and Planetary Science Letters,* 341-344**,** 243-254.

FOX, D. L. & KOCH, P. L. 2003. Tertiary history of C-4 biomass in the Great Plains, USA. *Geology,* 31**,** 809-812.

FOX, D. L. & KOCH, P. L. 2004. Carbon and oxygen isotopic variability in Neogene paleosol carbonates: constraints on the evolution of the C-4-grasslands of the Great Plains, USA. *Palaeogeography Palaeoclimatology Palaeoecology,* 207**,** 305-329.

FRASER, J. E., SEARLE, M. P., PARRISH, R. R. & NOBLE, S. R. 2001. Chronology of deformation, metamorphism, and magmatism in the southern Karakoram Mountains. *Geological Society of America Bulletin,* 113**,** 1443-1455.

FREED, R. L. & PEACOR, D. R. 1989. Variability in temperature of the smectite/illite reaction in Gulf Coast sediments. *Clay Minerals,* 24**,** 171-180.

FRIZON DE LAMOTTE, D., SOUQUE, C., GRELAUD, S. & ROBION, P. 2002. Early record of tectonic magnetic fabric during inversion of a sedimentary basin. Short review and examples from the Corbières transfer zone (France). *Bulletin de la Société Géologique de France,* 173**,** 461-469.

GABRIEL, K. R. 1971. The biplot graphic display of matrices with application to principal component analysis. *Biometrika,* 58**,** 453-467.

GALBRAITH, R. F. 2005. *Statistics for fission track analysis,* Raton, Florida, CRC Press.

GALY, V., BEYSSAC, O., FRANCE-LANORD, C. & EGLINTON, T. 2008. Recycling of graphite during Himalayan erosion: a geological stabilization of carbon in the crust. *Science,* 322**,** 943-945.

GAO, J., LONG, L., KLEMD, R., QIAN, Q., LIU, D., XIONG, X., SU, W., LIU, W., WANG, Y. & YANG, F. 2009. Tectonic evolution of the South Tianshan orogen and adjacent regions, NW China: geochemical and age constraints of granitoid rocks. *International Journal of Earth Sciences,* 98**,** 1221.

GARVER, J. I., BRANDON, M. T., RODEN-TICE, M. & KAMP, P. J. 1999. Exhumation history of orogenic highlands determined by detrital fission-track thermochronology. *Geological Society, London, Special Publications,* 154**,** 283-304.

GARVER, J. I. & KAMP, P. J. 2002. Integration of zircon color and zircon fission-track zonation patterns in orogenic belts: application to the Southern Alps, New Zealand. *Tectonophysics,* 349**,** 203-219.

GARZANTI, E., AL-JUBOURY, A. I., ZOLEIKHAEI, Y., VERMEESCH, P., JOTHERI, J., AKKOCA, D. B., OBAID, A. K., ALLEN, M. B., ANDÓ, S. & LIMONTA, M. 2016. The Euphrates-Tigris-Karun river system: Provenance,

recycling and dispersal of quartz-poor foreland-basin sediments in arid climate. *Earth-Science Reviews,* 162**,** 107-128.

GARZANTI, E. & ANDÒ, S. 2007. Heavy mineral concentration in modern sands: implications for provenance interpretation. *Developments in Sedimentology,* 58**,** 517-545.

GARZANTI, E., ANDÒ, S. & VEZZOLI, G. 2009. Grain-size dependence of sediment composition and environmental bias in provenance studies. *Earth and Planetary Science Letters,* 277**,** 422-432.

GARZANTI, E. & RESENTINI, A. 2016. Provenance control on chemical indices of weathering (Taiwan river sands). *Sedimentary Geology,* 336**,** 81-95.

GARZANTI, E. & VEZZOLI, G. 2003. A classification of metamorphic grains in sands based on their composition and grade: Research Methods Papers. *Journal of Sedimentary Research,* 73**,** 830-837.

GILDER, S., CHEN, Y. & SEN, S. 2001. Oligo-Miocene magnetostratigraphy and rock magnetism of the Xishuigou section, Subei (Gansu Province, western China) and implications for shallow inclinations in central Asia. *Journal of Geophysical Research: Solid Earth,* 106**,** 30505-30521.

GOVERS, R. & WORTEL, M. 2005. Lithosphere tearing at STEP faults: Response to edges of subduction zones. *Earth and Planetary Science Letters,* 236**,** 505-523.

GRADSTEIN, F. M., OGG, J. G., SCHMITZ, M. & OGG, G. 2012. *The geologic time scale 2012 2-volume set,* elsevier.

GUGGENHEIM, S., BAIN, D. C., BERGAYA, F., BRIGATTI, M. F., DRITS, V. A., EBERL, D. D., FORMOSO, M. L., GALÁN, E., MERRIMAN, R. J. & PEACOR, D. R. 2002. Report of the Association Internationale pour l'Etude des Argiles (AIPEA) Nomenclature Committee for 2001: Order, disorder and crystallinity in phyllosilicates and the use of the 'Crystallinity Index'. *Clay Minerals,* 37**,** 389-393.

HACKER, B., LUFFI, P., LUTKOV, V., MINAEV, V., RATSCHBACHER, L., PLANK, T., DUCEA, M., PATIÑO-DOUCE, A., MCWILLIAMS, M. & METCALF, J. 2005. Near-ultrahigh pressure processing of continental crust: Miocene crustal xenoliths from the Pamir. *Journal of Petrology,* 46**,** 1661-1687.

HAMBURGER, M. W., SAREWITZ, D. R., PAVLIS, T. L. & POPANDOPULO, G. A. 1992. Structural and seismic evidence for intracontinental subduction in the Peter the First Range, central Asia. *Geological Society of America Bulletin,* 104**,** 397-408.

HAO, Y. & ZENG, X. 1984. On the evolution of the west Tarim gulf from Mesozoic to Cenozoic in terms of characteristics of foraminiferal fauna. *Acta Micropalaeontologica Sinica,* 1**,** 1-13.

HAQ, B. U., HARDENBOL, J. & VAIL, P. R. 1987. Mesozoic and Cenozoic chronostratigraphy and cycles of sea-level change. *Special Publications of SEPM,* 42**,** 71-108.

HARNOIS, L. 1988. The CIW index: A new chemical index of weathering. *Sedimentary Geology,* 55**,** 319-322.

HARRIS, N. 2006. The elevation history of the Tibetan Plateau and its implications for the Asian monsoon. *Palaeogeography, Palaeoclimatology, Palaeoecology,* 241**,** 4-15.

HARRISON, T. M., COPELAND, P., KIDD, W. & YIN, A. 1992. Raising tibet. *science,* 255**,** 1663-1670.

HARZHAUSER, M., DAXNER-HÖCK, G., LÓPEZ-GUERRERO, P., MARIDET, O., OLIVER, A., PILLER, W. E., RICHOZ, S., ERBAJEVA, M. A., NEUBAUER, T. A. & GÖHLICH, U. B. 2016. Stepwise onset of the Icehouse world and its impact on Oligo-Miocene Central Asian mammals. *Scientific Reports,* 6.

HASEGAWA, H., TADA, R., ICHINNOROV, N. & MINJIN, C. 2009. Lithostratigraphy and depositional environments of the Upper Cretaceous Djadokhta Formation, Ulan Nuur basin, southern Mongolia, and its paleoclimatic implication. *Journal of Asian Earth Sciences,* 35**,** 13-26.

HATCH, M., SLACK, C. & JOHNSON, H. S. 1967. Further studies on a new pathway of photosynthetic carbon dioxide fixation in sugar-cane and its occurrence in other plant species. *Biochemical Journal,* 102**,** 417.

HATCH, M. D. 1987. C4 photosynthesis: a unique elend of modified biochemistry, anatomy and ultrastructure. *Biochimica et Biophysica Acta (BBA)-Reviews on Bioenergetics,* 895**,** 81-106.

HEERMANCE, R. V., CHEN, J., BURBANK, D. W. & WANG, C. 2007. Chronology and tectonic controls of Late Tertiary deposition in the southwestern Tian Shan foreland, NW China. *Basin Research,* 19**,** 599-632.

HELLER, P. L., TABOR, R. W., O'NEIL, J. R., PEVEAR, D. R., SHAFIQULLAH, M. & WINSLOW, N. S. 1992. Isotopic provenance of Paleogene sandstones from the accretionary core of the Olympic Mountains, Washington. *Geological Society of America Bulletin,* 104**,** 140-153.

HENDRIX, M. S., GRAHAM, S. A., CARROLL, A. R., SOBEL, E. R., MCKNIGHT, C. L., SCHULEIN, B. J. & WANG, Z. 1992. Sedimentary record and climatic implications of recurrent deformation in the Tian Shan: Evidence from Mesozoic strata of the north Tarim, south Junggar, and Turpan basins, northwest China. *Geological Society of America Bulletin,* 104**,** 53-79.

HONG, H., LI, Z., XUE, H., ZHU, Y., ZHANG, K. & XIANG, S. 2007. Oligocene clay mineralogy of the Linxia Basin: evidence of paleoclimatic evolution subsequent to the initial-stage uplift of the Tibetan Plateau. *Clays and Clay Minerals,* 55**,** 491-503.

HOU, Z. F., LI, J. J., SONG, C. H., MENG, J. J. & ZHANG, J. 2015. Late-Miocene palaeoecological evolution of the Tianshui Basin, NE Tibetan Plateau: Evidence from stable organic carbon isotope record. *Journal of Asian Earth Sciences,* 98**,** 296-303.

HSU, J. 1976. On the palaeobotanical evidence for continental drift and Himalayan uplift. *Palaeobotanist,* 25.

HU, X., GARZANTI, E., MOORE, T. & RAFFI, I. 2015. Direct stratigraphic dating of India-Asia collision onset at the Selandian (middle Paleocene, 59±1 Ma). *Geology,* 43**,** 859-862.

HU, X., GARZANTI, E., WANG, J., HUANG, W., AN, W. & WEBB, A. 2016. The timing of India-Asia collision onset – Facts, theories, controversies. *Earth-Science Reviews,* 160**,** 264-299.

HUANG, W., HINSBERGEN, D. J., LIPPERT, P. C., GUO, Z. & DUPONT-NIVET, G. 2015. Paleomagnetic tests of tectonic reconstructions of the India-Asia collision zone. *Geophysical Research Letters,* 42**,** 2642-2649.

HUBER, M. & GOLDNER, A. 2012. Eocene monsoons. *Journal of Asian Earth Sciences,* 44**,** 3-23.

HUBERT, J. F. 1962. A zircon-tourmaline-rutile maturity index and the interdependence of the composition of heavy mineral assemblages with the gross composition and texture of sandstones. *Journal of Sedimentary Research,* 32**,** 440-450.

HUI, Z., LI, J., XU, Q., SONG, C., ZHANG, J., WU, F. & ZHAO, Z. 2011. Miocene vegetation and climatic changes reconstructed from a sporopollen record of the Tianshui Basin, NE Tibetan Plateau. *Palaeogeography, Palaeoclimatology, Palaeoecology,* 308**,** 373-382.

HURFORD, A. J. 1990. Standardization of fission track dating calibration: Recommendation by the Fission Track Working Group of the IUGS Subcommission on Geochronology. *Chemical Geology: Isotope Geoscience Section,* 80**,** 171-178.

HUYGHE, P., GUILBAUD, R., BERNET, M., GALY, A. & GAJUREL, A. P. 2011. Significance of the clay mineral distribution in fluvial sediments of the Neogene to Recent Himalayan Foreland Basin (west-central Nepal). *Basin Research,* 23**,** 332-345.

IAFFALDANO, G., BODIN, T. & SAMBRIDGE, M. 2013. Slow-downs and speed-ups of India–Eurasia convergence since: Data-noise, uncertainties and dynamic implications. *Earth and Planetary Science Letters,* 367**,** 146-156.

INGERSOLL, R. V., BULLARD, T. F., FORD, R. L., GRIMM, J. P., PICKLE, J. D. & SARES, S. W. 1984. The effect of grain size on detrital modes: a test of the Gazzi-Dickinson point-counting method. *Journal of Sedimentary Research,* 54**,** 103-116.

ISCHUK, A., BENDICK, R., RYBIN, A., MOLNAR, P., KHAN, S. F., KUZIKOV, S., MOHADJER, S., SAYDULLAEV, U., ILYASOVA, Z. & SCHELOCHKOV, G. 2013. Kinematics of the Pamir and Hindu Kush regions from GPS geodesy. *Journal of geophysical research: solid earth,* 118**,** 2408-2416.

JAEGER, J.-J., COURTILLOT, V. & TAPPONNIER, P. 1989. Paleontological view of the ages of the Deccan Traps, the Cretaceous/Tertiary boundary, and the India-Asia collision. *Geology,* 17**,** 316-319.

JAY, C. N., FLESCH, L. M. & BENDICK, R. O. 2017. Kinematics and dynamics of the Pamir, Central Asia: Quantifying surface deformation and force balance in an intracontinental subduction zone. *Journal of Geophysical Research: Solid Earth,* 122**,** 1-22.

JELINEK, V. 1981. Characterization of the magnetic fabric of rocks. *Tectonophysics,* 79**,** T63-T67.

JIA, C. 1997. *Tectonic characteristics and petroleum, Tarim basin, China,* Beijing, Petroleum Industry Press.

JIA, C. Z., S. WU, S. 2004. Stratigraphy of the Tarim Basin and Adjacent Areas. *Beijing: Ke Xue Chu Ban She,* 1/2**,** 1063.

JIA, G., PENG, P. A., ZHAO, Q. & JIAN, Z. 2003a. Changes in terrestrial ecosystem since 30 Ma in East Asia: Stable isotope evidence from black carbon in the South China Sea. *Geology,* 31**,** 1093-1096.

JIA, G. D., PENG, P. A., ZHAO, Q. H. & JIAN, Z. M. 2003b. Changes in terrestrial ecosystem since 30 Ma in East Asia: Stable isotope evidence from black carbon in the South China Sea. *Geology,* 31**,** 1093-1096.

JIA, Y., FU, B., JOLIVET, M. & ZHENG, S. 2015. Cenozoic tectono-geomorphological growth of the SW Chinese Tian Shan: Insight from AFT and detrital zircon U–Pb data. *journal of asian earth Sciences,* 111**,** 395-413.

JIANG, X.-D. & LI, Z.-X. 2014. Seismic reflection data support episodic and simultaneous growth of the Tibetan Plateau since 25 Myr. *Nat Commun,* 5**,** 5453.

JIANG, X., LI, Z.-X. & LI, H. 2013. Uplift of the West Kunlun Range, northern Tibetan Plateau, dominated by brittle thickening of the upper crust. *Geology,* 41**,** 439-442.

JIANG, X., PAN, Z., XU, J., LI, X., XIE, G. & XIAO, Z. 2008. Late Cretaceous aeolian dunes and reconstruction of palaeo-wind belts of the Xinjiang Basin, Jiangxi Province, China. *Palaeogeography, Palaeoclimatology, Palaeoecology,* 257**,** 58-66.

JIANG, Y.-H., LIU, Z., JIA, R.-Y., LIAO, S.-Y., ZHOU, Q. & ZHAO, P. 2012. Miocene potassic granite–syenite association in western Tibetan Plateau: Implications for shoshonitic and high Ba–Sr granite genesis. *Lithos,* 134**,** 146-162.

JIN, X., WANG, J., CHEN, B. & REN, L. 2003. Cenozoic depositional sequences in the piedmont of the west Kunlun and their paleogeographic and tectonic implications. *Journal of Asian Earth Sciences,* 21**,** 755-765.

JOLIVET, M., BRUNEL, M., SEWARD, D., XU, Z., YANG, J., ROGER, F., TAPPONNIER, P., MALAVIEILLE, J., ARNAUD, N. & WU, C. 2001. Mesozoic and Cenozoic tectonics of the northern edge of the Tibetan plateau: fission-track constraints. *Tectonophysics,* 343**,** 111-134.

JOLIVET, M., DOMINGUEZ, S., CHARREAU, J., CHEN, Y., LI, Y. & WANG, Q. 2010. Mesozoic and Cenozoic tectonic history of the central Chinese Tian Shan: reactivated tectonic structures and active deformation. *Tectonics,* 29.

JOLIVET, M., ROGER, F., XU, Z., PAQUETTE, J.-L. & CAO, H. 2015. Mesozoic–Cenozoic evolution of the Danba dome (Songpan Garzê, East Tibet) as inferred from LA-ICPMS U–Pb and fission-track data. *Journal of Asian Earth Sciences,* 102**,** 180-204.

KADEREIT, G., BORSCH, T., WEISING, K. & FREITAG, H. 2003. Phylogeny of Amaranthaceae and Chenopodiaceae and the evolution of C-4 photosynthesis. *International Journal of Plant Sciences,* 164**,** 959-986.

KAPP, P., DECELLES, P. G., GEHRELS, G. E., HEIZLER, M. & DING, L. 2007. Geological records of the Lhasa-Qiangtang and Indo-Asian collisions in the Nima area of central Tibet. *Geological Society of America Bulletin,* 119**,** 917-933.

KÄßNER, A., RATSCHBACHER, L., JONCKHEERE, R., ENKELMANN, E., KHAN, J., SONNTAG, B. L., GLOAGUEN, R., GADOEV, M. & OIMAHMADOV, I. 2016. Cenozoic intracontinental deformation and exhumation at the northwestern tip of the India-Asia collision—southwestern Tian Shan, Tajikistan, and Kyrgyzstan. *Tectonics,* 35**,** 2171-2194.

KELLY, S. B. & OLSEN, H. 1993. Terminal fans—a review with reference to Devonian examples. *Sedimentary Geology,* 85**,** 339-374.

KEMP, S. J., ELLIS, M. A. & KENDER, S. 2016. Palaeoclimatic implications of high-resolution clay mineral assemblages preceding and across the onset of the Palaeocene–Eocene Thermal Maximum, North Sea Basin. *Clay Minerals,* 51**,** 793-813.

KENNETT, J. P. 1977. Cenozoic evolution of Antarctic glaciation, the circum-Antarctic Ocean, and their impact on global paleoceanography. *Journal of geophysical research,* 82**,** 3843-3860.

KENT-CORSON, M. L., RITTS, B. D., ZHUANG, G., BOVET, P. M., GRAHAM, S. A. & PAGE CHAMBERLAIN, C. 2009. Stable isotopic constraints on the tectonic, topographic, and climatic evolution of the northern margin of the Tibetan Plateau. *Earth and Planetary Science Letters,* 282**,** 158-166.

KINGSTON, J. D., MARINO, B. D. & HILL, A. 1994. ISOTOPIC EVIDENCE FOR NEOGENE HOMINID PALEOENVIRONMENTS IN THE KENYA RIFT-VALLEY. *Science,* 264**,** 955-959.

KISSEL, C., BARRIER, E., LAJ, C. & LEE, T. Q. 1986. Magnetic fabric in "undeformed" marine clays from compressional zones. *Tectonics,* 5**,** 769-781.

KLOOTWIJK, C., CONAGHAN, P. & POWELL, C. M. 1985. The Himalayan Arc: large-scale continental subduction, oroclinal bending and back-arc spreading. *Earth and Planetary Science Letters,* 75**,** 167-183.

KOHN, M. J. 2010. Carbon isotope compositions of terrestrial C3 plants as indicators of (paleo) ecology and (paleo) climate. *Proceedings of the National Academy of Sciences,* 107**,** 19691-19695.

KOOIJMAN, E., SMIT, M. A., RATSCHBACHER, L. & KYLANDER-CLARK, A. R. 2017. A view into crustal evolution at mantle depths. *Earth and Planetary Science Letters,* 465**,** 59-69.

KÜFNER, S.-K., SCHURR, B., SIPPL, C., YUAN, X., RATSCHBACHER, L., ISCHUK, A., MURODKULOV, S., SCHNEIDER, F., MECHIE, J. & TILMANN, F. 2016. Deep India meets deep Asia: Lithospheric indentation, delamination and break-off under Pamir and Hindu Kush (Central Asia). *Earth and Planetary Science Letters,* 435**,** 171-184.

KUKLA, G., HELLER, F., MING, L. X., CHUN, X. T., SHENG, L. T. & SHENG, A. Z. 1988. Pleistocene climates in China dated by magnetic susceptibility. *Geology,* 16**,** 811-814.

LACASSIN, R., VALLI, F., ARNAUD, N., LELOUP, P. H., PAQUETTE, J. L., HAIBING, L., TAPPONNIER, P., CHEVALIER, M.-L., GUILLOT, S. & MAHEO, G. 2004. Large-scale geometry, offset and kinematic evolution of the Karakorum fault, Tibet. *Earth and Planetary Science Letters,* 219**,** 255-269.

LAGABRIELLE, Y., GODDÉRIS, Y., DONNADIEU, Y., MALAVIEILLE, J. & SUAREZ, M. 2009. The tectonic history of Drake Passage and its possible impacts on global climate. *Earth and Planetary Science Letters,* 279**,** 197-211.

LAMB, M. A. & BADARCH, G. 1997. Paleozoic sedimentary basins and volcanic-arc systems of southern Mongolia: New stratigraphic and sedimentologic constraints. *International Geology Review,* 39**,** 542-576.

LAN, X. & WEI, J. 1995. Late Cretaceous–early Tertiary marine bivalve fauna from the western Tarim Basin. *Chinese Science Pubilishing House, Beijing***,** 212.

LANGEREIS, C. G., KRIJGSMAN, W., MUTTONI, G. & MENNING, M. 2010. Magnetostratigraphy–concepts, definitions, and applications. *Newsletters on Stratigraphy,* 43**,** 207-233.

LEASE, R. O., BURBANK, D. W., ZHANG, H., LIU, J. & YUAN, D. 2012. Cenozoic shortening budget for the northeastern edge of the Tibetan Plateau: Is lower crustal flow necessary? *Tectonics,* 31.

LI, C., DUPONT-NIVET, G. & GUO, Z. 2011. Magnetostratigraphy of the Northern Tian Shan foreland, Taxi He section, China. *Basin Research,* 23**,** 101-117.

LI, D. & YIN, A. 2008. Orogen-parallel, active left-slip faults in the Eastern Himalaya: Implications for the growth mechanism of the Himalayan Arc. *Earth and Planetary Science Letters,* 274**,** 258-267.

LICHT, A., VAN CAPPELLE, M., ABELS, H. A., LADANT, J. B., TRABUCHO-ALEXANDRE, J., FRANCE-LANORD, C., DONNADIEU, Y., VANDENBERGHE, J., RIGAUDIER, T., LECUYER, C., TERRY JR, D., ADRIAENS, R., BOURA, A., GUO, Z., SOE, A. N., QUADE, J., DUPONT-NIVET, G. & JAEGER, J. J. 2014. Asian monsoons in a late Eocene greenhouse world. *Nature,* 513**,** 501-506.

LIU, D., LI, H., SUN, Z., CAO, Y., WANG, L., PAN, J., HAN, L. & YE, X. 2017. Cenozoic episodic uplift and kinematic evolution between the Pamir and Southwestern Tien Shan. *Tectonophysics*.

LIU, H., WANG, G.-C., CAO, K., MENG, Y.-N., WANG, A. & ZHANG, K. 2010. The detrital zircon fission-track ages constraint to tectonic process in west Kunlun and adjacent regions. *Earth Science Frontiers,* 17**,** 64-78.

LIU, J., ZHANG, P., LEASE, R. O., ZHENG, D., WAN, J., WANG, W. & ZHANG, H. 2013. Eocene onset and late Miocene acceleration of Cenozoic intracontinental extension in the North Qinling range–Weihe graben: insights from apatite fission track thermochronology. *Tectonophysics,* 584**,** 281-296.

LIU, Q., ROBERTS, A. P., LARRASOANA, J. C., BANERJEE, S. K., GUYODO, Y., TAUXE, L. & OLDFIELD, F. 2012a. Environmental magnetism: principles and applications. *Reviews of Geophysics,* 50**,** 1-50.

LIU, W., LIU, Z., AN, Z., SUN, J., CHANG, H., WANG, N., DONG, J. & WANG, H. 2014. Late Miocene episodic lakes in the arid Tarim Basin, western China. *Proceedings of the National Academy of Sciences*, 111**,** 16292-16296.

LIU, Y., WU, G., HONG, J., DONG, B., DUAN, A., BAO, Q. & ZHOU, L. 2012b. Revisiting Asian monsoon formation and change associated with Tibetan Plateau forcing: II. Change. *Climate dynamics*, 39**,** 1183-1195.

LIU, Z., JIANG, Y.-H., JIA, R.-Y., ZHAO, P. & ZHOU, Q. 2015. Origin of Late Triassic high-K calc-alkaline granitoids and their potassic microgranular enclaves from the western Tibet Plateau, northwest China: Implications for Paleo-Tethys evolution. *Gondwana Research*, 27**,** 326-341.

LIVERMORE, R., NANKIVELL, A., EAGLES, G. & MORRIS, P. 2005. Paleogene opening of Drake passage. *Earth and Planetary Science Letters*, 236**,** 459-470.

LONG, X., WILDE, S. A., WANG, Q., YUAN, C., WANG, X.-C., LI, J., JIANG, Z. & DAN, W. 2015. Partial melting of thickened continental crust in central Tibet: Evidence from geochemistry and geochronology of Eocene adakitic rhyolites in the northern Qiangtang Terrane. *Earth and Planetary Science Letters*, 414**,** 30-44.

LU, H. & XIONG, S. 2009. Magnetostratigraphy of the Dahonggou section, northern Qaidam Basin and its bearing on Cenozoic tectonic evolution of the Qilian Shan and Altyn Tagh Fault. *Earth and Planetary Science Letters*, 288**,** 539-550.

LUKENS, C. E., CARRAPA, B., SINGER, B. S. & GEHRELS, G. 2012. Miocene exhumation of the Pamir revealed by detrital geothermochronology of Tajik rivers. *Tectonics*, 31**,** TC2014.

LUPKER, M., FRANCE-LANORD, C., GALY, V., LAVÉ, J., GAILLARDET, J., GAJUREL, A. P., GUILMETTE, C., RAHMAN, M., SINGH, S. K. & SINHA, R. 2012. Predominant floodplain over mountain weathering of Himalayan sediments (Ganga basin). *Geochimica et Cosmochimica Acta*, 84**,** 410-432.

LUPKER, M., FRANCE-LANORD, C., GALY, V., LAVÉ, J. & KUDRASS, H. 2013. Increasing chemical weathering in the Himalayan system since the Last Glacial Maximum. *Earth and Planetary Science Letters*, 365**,** 243-252.

MAHÉO, G., BLICHERT-TOFT, J., PIN, C., GUILLOT, S. & PÊCHER, A. 2009. Partial melting of mantle and crustal sources beneath South Karakorum, Pakistan: implications for the Miocene geodynamic evolution of the India–Asia convergence zone. *Journal of Petrology*, 50**,** 427-449.

MAHÉO, G., GUILLOT, S., BLICHERT-TOFT, J., ROLLAND, Y. & PÊCHER, A. 2002. A slab breakoff model for the Neogene thermal evolution of South Karakorum and South Tibet. *Earth and Planetary Science Letters*, 195**,** 45-58.

MAHER, B. A. & THOMPSON, R. 1995. Paleorainfall reconstructions from pedogenic magnetic susceptibility variations in the Chinese loess and paleosols. *Quaternary Research*, 44**,** 383-391.

MAKISHIMA, A. & NAKAMURA, E. 1997. Suppression of Matrix Effects in ICP-MS by High Power Operation of ICP: Application to Precise Determination of

Rb, Sr, Y, Cs, Ba, REE, Pb, Th and U at ng g-1 Levels in Milligram Silicate Samples. *Geostandards and Geoanalytical Research,* 21**,** 307-319.

MAO, S. & NORRIS, G. 1988. *Late Cretaceous-early Tertiary dinoflagellates and acritarchs from the Kashi area, Tarim Basin, Xinjiang Province, China,* Beijing, Chinese Science House.

MATTE, P., TAPPONNIER, P., ARNAUD, N., BOURJOT, L., AVOUAC, J. P., VIDAL, P., QING, L., YUSHENG, P. & YI, W. 1996. Tectonics of Western Tibet, between the Tarim and the Indus. *Earth and Planetary Science Letters,* 142**,** 311-330.

MCCAFFREY, R. & NABELEK, J. 1998. Role of oblique convergence in the active deformation of the Himalayas and southern Tibet plateau. *Geology,* 26**,** 691-694.

MCCALLISTER, A. T., TAYLOR, M. H., MURPHY, M., STYRON, R. H. & STOCKLI, D. F. 2014. Thermochronologic constraints on the late Cenozoic exhumation history of the Gurla Mandhata metamorphic core complex, Southwestern Tibet. *Tectonics,* 33**,** 27-52.

MELILLO, J. M., ABER, J. D., LINKINS, A. E., RICCA, A., FRY, B. & NADELHOFFER, K. J. 1989. Carbon and nitrogen dynamics along the decay continuum: plant litter to soil organic matter. *Plant and soil,* 115**,** 189-198.

MENG, Q.-R. & ZHANG, G.-W. 1999. Timing of collision of the North and South China blocks: controversy and reconciliation. *Geology,* 27**,** 123-126.

MERRIMAN, R. J. & KEMP, S. J. 1996. Clay minerals and sedimentary basin maturity. *Mineralogical Society Bulletin,* 111**,** 7-8.

METCALFE, I. 2013. Gondwana dispersion and Asian accretion: tectonic and palaeogeographic evolution of eastern Tethys. *Journal of Asian Earth Sciences,* 66**,** 1-33.

MEYER, B., TAPPONNIER, P., GAUDEMER, Y., PELTZER, G., SHUNMIN, G. & ZHITAI, C. 1996. Rate of left-lateral movement along the easternmost segment of the Altyn Tagh fault, east of 96° E (China). *Geophysical Journal International,* 124**,** 29-44.

MIALL, A. D. 1977. A review of the braided-river depositional environment. *Earth-Science Reviews,* 13**,** 1-62.

MIALL, A. D. 1985. Architectural-element analysis: a new method of facies analysis applied to fluvial deposits. *Earth Science Reviews,* 22**,** 261-308.

MILLER, K. G., FAIRBANKS, R. G. & MOUNTAIN, G. S. 1987. Tertiary oxygen isotope synthesis, sea level history, and continental margin erosion. *Paleoceanography,* 2**,** 1-19.

MILLER, K. G. & MOUNTAIN, G. S. 1996. Drilling and dating New Jersey Oligocene-Miocene sequences: ice volume, global sea level, and Exxon records. *Science,* 271**,** 1092.

MOHADJER, S., BENDICK, R., ISCHUK, A., KUZIKOV, S., KOSTUK, A., SAYDULLAEV, U., LODI, S., KAKAR, D., WASY, A. & KHAN, M. 2010. Partitioning of India-Eurasia convergence in the Pamir-Hindu Kush from GPS measurements. *Geophysical Research Letters,* 37.

MOLNAR, P., BOOS, W. R. & BATTISTI, D. S. 2010. Orographic controls on climate and paleoclimate of Asia: thermal and mechanical roles for the Tibetan Plateau. *Annual Review of Earth and Planetary Sciences,* 38**,** 77-102.

MOLNAR, P. & ENGLAND, P. 1990. Late Cenozoic uplift of mountain ranges and global climate change: chicken or egg? *Nature,* 346**,** 29-34.

MOLNAR, P., ENGLAND, P. & MARTINOD, J. 1993. Mantle dynamics, uplift of the Tibetan Plateau, and the Indian monsoon. *Reviews of Geophysics,* 31**,** 357-396.

MOLNAR, P. & LYON-CAEN, H. 1988. Some simple physical aspects of the support, structure, and evolution of mountain belts. *Geological Society of America Special Papers,* 218**,** 179-208.

MOLNAR, P. & STOCK, J. M. 2009. Slowing of India's convergence with Eurasia since 20 Ma and its implications for Tibetan mantle dynamics. *Tectonics,* 28.

MOLNAR, P. & TAPPONNIER, P. 1975. Cenozoic tectonics of Asia: effects of a continental collision. *Science,* 189**,** 419-426.

MOORE, D. & REYNOLDS, R. 1997. *X-Ray-Diffraction and the Identification and Analysis of Clay Minerals* Oxford, Oxford Univ. Press.

MORTON, A. C. 1991. Geochemical studies of detrital heavy minerals and their application to provenance research. *Geological Society, London, Special Publications,* 57**,** 31-45.

MURPHY, M., YIN, A., HARRISON, T., DÜRR, S., CHEN, Z., RYERSON, F., KIDD, W., WANG, X. & ZHOU, X. 1997. Did the Indo-Asian collision alone create the Tibetan plateau? *Geology,* 25**,** 719-722.

MURPHY, M., YIN, A., KAPP, P., HARRISON, T., LIN, D. & JINGHUI, G. 2000. Southward propagation of the Karakoram fault system, southwest Tibet: Timing and magnitude of slip. *Geology,* 28**,** 451-454.

MURPHY, M., YIN, A., KAPP, P., HARRISON, T., MANNING, C., RYERSON, F., LIN, D. & JINGHUI, G. 2002. Structural evolution of the Gurla Mandhata detachment system, southwest Tibet: Implications for the eastward extent of the Karakoram fault system. *Geological Society of America Bulletin,* 114**,** 428-447.

MURPHY, M. A. & COPELAND, P. 2005. Transtensional deformation in the central Himalaya and its role in accommodating growth of the Himalayan orogen. *Tectonics,* 24.

NAESER, N. D., NAESER, C. W. & MCCULLOH, T. H. 1989. The application of fission-track dating to the depositional and thermal history of rocks in sedimentary basins. *Thermal history of sedimentary basins*. Springer.

NAJMAN, Y., APPEL, E., BOUDAGHER-FADEL, M., BOWN, P., CARTER, A., GARZANTI, E., GODIN, L., HAN, J., LIEBKE, U. & OLIVER, G. 2010. Timing of India-Asia collision: Geological, biostratigraphic, and palaeomagnetic constraints. *Journal of Geophysical Research: Solid Earth (1978–2012),* 115.

NEGREDO, A. M., REPLUMAZ, A., VILLASEÑOR, A. & GUILLOT, S. 2007. Modeling the evolution of continental subduction processes in the Pamir–Hindu Kush region. *Earth and Planetary Science Letters,* 259**,** 212-225.

NESBITT, H. & YOUNG, G. 1982. Early Proterozoic climates and plate motions inferred from major element chemistry of lutites. *Nature,* 299**,** 715-717.

O'LEARY, M. H. 1981. Carbon isotope fractionation in plants. *Phytochemistry,* 20**,** 553-567.

O'LEARY, M. H. 1988. Carbon isotopes in photosynthesis. *Bioscience,* 38**,** 328-336.

O'LEARY, M. H. 1995. Environmental effects on carbon isotope fractionation in terrestrial plants. *Stable isotopes in the biosphere***,** 78-91.

OZACAR, A. 2000. *Tibet* [Online]. Geo Arizona: Geo Arizona. Available: http://www.geo.arizona.edu/~ozacar/paleot~1.htm [Accessed 29/09/2017 2017].

PAGANI, M., ZACHOS, J. C., FREEMAN, K. H., TIPPLE, B. & BOHATY, S. 2005. Marked decline in atmospheric carbon dioxide concentrations during the Paleogene. *Science,* 309**,** 600-603.

PAN, Y. 1990. The tectonic characteristics and evolution of West Kunlun region. *Scientia Geologica Sinica,* 3**,** 224-232.

PARÉS, J. M., VAN DER PLUIJM, B. A. & DINARÈS-TURELL, J. 1999. Evolution of magnetic fabrics during incipient deformation of mudrocks (Pyrenees, northern Spain). *Tectonophysics,* 307**,** 1-14.

PEARCE, N. J., PERKINS, W. T., WESTGATE, J. A., GORTON, M. P., JACKSON, S. E., NEAL, C. R. & CHENERY, S. P. 1997. A compilation of new and published major and trace element data for NIST SRM 610 and NIST SRM 612 glass reference materials. *Geostandards and Geoanalytical Research,* 21**,** 115-144.

PEARSON, P. N. & PALMER, M. R. 2000. Atmospheric carbon dioxide concentrations over the past 60 million years. *Nature,* 406**,** 695-699.

PELTZER, G. & TAPPONNIER, P. 1988. Formation and evolution of strike-slip faults, rifts, and basins during the India-Asia collision: An experimental approach. *Journal of Geophysical Research: Solid Earth,* 93**,** 15085-15117.

PHILLIPS, R. J., PARRISH, R. R. & SEARLE, M. P. 2004. Age constraints on ductile deformation and long-term slip rates along the Karakoram fault zone, Ladakh. *Earth and Planetary Science Letters,* 226**,** 305-319.

PHILLIPS, R. J. & SEARLE, M. P. 2007. Macrostructural and microstructural architecture of the Karakoram Fault: Relationship between magmatism and strike-slip faulting. *Tectonics,* 26.

POBLETE, F., ROPERCH, P., HERVÉ, F., DIRAISON, M., ESPINOZA, M. & ARRIAGADA, C. 2014. The curved Magallanes fold and thrust belt: Tectonic insights from a paleomagnetic and anisotropy of magnetic susceptibility study. *Tectonics,* 33**,** 2526-2551.

POWELL, C. M. 1986. Continental underplating model for the rise of the Tibetan Plateau. *Earth and Planetary Science Letters,* 81**,** 79-94.

PULLEN, A., KAPP, P., GEHRELS, G. E., VERVOORT, J. D. & DING, L. 2008. Triassic continental subduction in central Tibet and Mediterranean-style closure of the Paleo-Tethys Ocean. *Geology,* 36**,** 351-354.

QUADE, J., CATER, J. M. L., OJHA, T. P., ADAM, J. & HARRISON, T. M. 1995. LATE MIOCENE ENVIRONMENTAL-CHANGE IN NEPAL AND THE NORTHERN INDIAN SUBCONTINENT - STABLE ISOTOPIC EVIDENCE FROM PALEOSOLS. *Geological Society of America Bulletin,* 107**,** 1381-1397.

QUADE, J. & CERLING, T. E. 1995. EXPANSION OF C-4 GRASSES IN THE LATE MIOCENE OF NORTHERN PAKISTAN - EVIDENCE FROM STABLE ISOTOPES IN PALEOSOLS. *Palaeogeography Palaeoclimatology Palaeoecology,* 115**,** 91-116.

QUADE, J., CERLING, T. E. & BOWMAN, J. R. 1989. DEVELOPMENT OF ASIAN MONSOON REVEALED BY MARKED ECOLOGICAL SHIFT DURING THE LATEST MIOCENE IN NORTHERN PAKISTAN. *Nature,* 342**,** 163-166.

RAMSTEIN, G., FLUTEAU, F., BESSE, J. & JOUSSAUME, S. 1997. Effect of orogeny, plate motion and land-sea distribution on Eurasian climate change over the past 30 million years. *Nature,* 386**,** 788-795.

RATSCHBACHER, L., FRISCH, W., LIU, G. & CHEN, C. 1994. Distributed deformation in southern and western Tibet during and after the India-Asia collision. *Journal of Geophysical Research: Solid Earth,* 99**,** 19917-19945.

RAYMO, M. E., RUDDIMAN, W. F. & FROELICH, P. N. 1988. Influence of late Cenozoic mountain building on ocean geochemical cycles. *Geology,* 16**,** 649-653.

REES, A. 1965. The use of anisotropy of magnetic susceptibility in the estimation of sedimentary fabric. *Sedimentology,* 4**,** 257-271.

REPLUMAZ, A., NEGREDO, A. M., VILLASENOR, A. & GUILLOT, S. 2010. Indian continental subduction and slab break-off during Tertiary collision. *Terra Nova,* 22**,** 290-296.

REYNOLDS, R. C. & REYNOLDS, R. C. 1996. *Description of Newmod-for-Windows™. The Calculation of one-Dimensional X-ray Diffraction Patterns of Mixed Layered Clay Minerals.* , 8 Brook Road, Hanover, New Hampshire, USA, R.C. Reynolds Jr

RICHOZ, S., BALDERMANN, A., FRAUWALLNER, A., HARZHAUSER, M., DAXNER-HÖCK, G., KLAMMER, D. & PILLER, W. E. 2017. Geochemistry and mineralogy of the Oligo-Miocene sediments of the Valley of Lakes, Mongolia. *Palaeobiodiversity and Palaeoenvironments,* 97**,** 233-258.

RITTNER, M., VERMEESCH, P., CARTER, A., BIRD, A., STEVENS, T., GARZANTI, E., ANDÒ, S., VEZZOLI, G., DUTT, R., XU, Z. & LU, H. 2016. The provenance of Taklamakan desert sand. *Earth and Planetary Science Letters,* 437**,** 127-137.

RITTS, B. D. & BIFFI, U. 2000. Magnitude of post–Middle Jurassic (Bajocian) displacement on the central Altyn Tagh fault system, northwest China. *Geological Society of America Bulletin,* 112**,** 61-74.

ROBERT, C. & KENNETT, J. P. 1994. Antarctic subtropical humid episode at the Paleocene-Eocene boundary: Clay-mineral evidence. *Geology,* 22**,** 211-214.

ROBINSON, A. C. 2009. Geologic offsets across the northern Karakorum fault: Implications for its role and terrane correlations in the western Himalayan-Tibetan orogen. *Earth and Planetary Science Letters,* 279**,** 123-130.

ROBINSON, A. C. 2015. Mesozoic tectonics of the Gondwanan terranes of the Pamir plateau. *Journal of Asian Earth Sciences,* 102**,** 170-179.

ROBINSON, A. C., DUCEA, M. & LAPEN, T. J. 2012. Detrital zircon and isotopic constraints on the crustal architecture and tectonic evolution of the northeastern Pamir. *Tectonics,* 31**,** TC2016.

ROBINSON, A. C., YIN, A., MANNING, C. E., HARRISON, T. M., ZHANG, S.-H. & WANG, X.-F. 2007. Cenozoic evolution of the eastern Pamir: Implications for strain-accommodation mechanisms at the western end of the Himalayan-Tibetan orogen. *Geological Society of America Bulletin,* 119**,** 882-896.

ROBINSON, A. C., YIN, A., MANNING, C. E., HARRISON, T. M., ZHANG, S. H. & WANG, X. F. 2004. Tectonic evolution of the northeastern Pamir: Constraints from the northern portion of the Cenozoic Kongur Shan extensional system, western China. *Geological Society of America Bulletin,* 116**,** 953-973.

ROBINSON, D. M., DUPONT-NIVET, G., GEHRELS, G. E. & ZHANG, Y. 2003. The Tula uplift, northwestern China: Evidence for regional tectonism of the northern Tibetan Plateau during late Mesozoic–early Cenozoic time. *Geological Society of America Bulletin,* 115**,** 35-47.

ROBION, P., DE LAMOTTE, D. F., KISSEL, C. & AUBOURG, C. 1995. Tectonic versus mineralogical contribution to the magnetic fabrics of epimetamorphic slaty rocks: an example from the Ardennes Massif (France-Belgium). *Journal of Structural Geology,* 17**,** 1111-1124.

ROECKER, S., SOBOLEVA, O., NERSESOV, I., LUKK, A., HATZFELD, D., CHATELAIN, J.-L. & MOLNAR, P. 1980. Seismicity and fault plane solutions of intermediate depth earthquakes in the Pamir-Hindu Kush Region. *Journal of Geophysical Research: Solid Earth* 85**,** 1358-1364.

ROGER, F., JOLIVET, M., CATTIN, R. & MALAVIEILLE, J. 2011. Mesozoic-Cenozoic tectonothermal evolution of the eastern part of the Tibetan Plateau (Songpan-Garzê, Longmen Shan area): insights from thermochronological data and simple thermal modelling. *Geological Society, London, Special Publications,* 353**,** 9-25.

ROGER, F., JOLIVET, M. & MALAVIEILLE, J. 2010. The tectonic evolution of the Songpan-Garzê (North Tibet) and adjacent areas from Proterozoic to Present: A synthesis. *Journal of Asian Earth Sciences,* 39**,** 254-269.

ROPERCH, P., CARLOTTO, V. & CHAUVIN, A. 2010. Using anisotropy of magnetic susceptibility to better constrain the tilt correction in paleomagnetism: A case study from southern Peru. *Tectonics,* 29.

ROPERCH, P., CARLOTTO, V., RUFFET, G. & FORNARI, M. 2011. Tectonic rotations and transcurrent deformation south of the Abancay deflection in the Andes of southern Peru. *Tectonics,* 30.

ROWLEY, D. B. 1996. Age of initiation of collision between India and Asia: A review of stratigraphic data. *Earth and Planetary Science Letters,* 145**,** 1-13.

ROYDEN, L. H., BURCHFIEL, B. C. & VAN DER HILST, R. D. 2008. The geological evolution of the Tibetan Plateau. *science,* 321**,** 1054-1058.

RUDDIMAN, W. & KUTZBACH, J. 1989. Forcing of late Cenozoic northern hemisphere climate by plateau uplift in southern Asia and the American West. *Journal of Geophysical Research: Atmospheres,* 94**,** 18409-18427.

RUTTE, D., RATSCHBACHER, L., KHAN, J., STÜBNER, K., HACKER, B. R., STEARNS, M. A., ENKELMANN, E., JONCKHEERE, R., PFÄNDER, J. A. & SPERNER, B. 2017a. Building the Pamir-Tibet Plateau—Crustal stacking, Extensional Collapse, and Lateral Extrusion in the Central Pamir: 2. Timing and Rates. *Tectonics,* 36**,** 385-419.

RUTTE, D., RATSCHBACHER, L., SCHNEIDER, S., STÜBNER, K., STEARNS, M. A., GULZAR, M. A. & HACKER, B. R. 2017b. Building the Pamir-Tibetan Plateau—Crustal stacking, extensional collapse, and lateral extrusion in the Central Pamir: 1. Geometry and kinematics. *Tectonics,* 36**,** 342-384.

SAGE, R. F. 2003. The evolution of C_4 photosynthesis. *New Phytologist,* 161**,** 341-370.

SAGE, R. F., WEDIN, D. A. & LI, M. 1999. The biogeography of C4 photosynthesis: patterns and controlling factors. *C4 plant biology***,** 313-373.

SAGNOTTI, L. & WINKLER, A. 1999. Rock magnetism and palaeomagnetism of greigite-bearing mudstones in the Italian peninsula. *Earth and Planetary Science Letters,* 165**,** 67-80.

SAVIN, S. M., DOUGLAS, R. G. & STEHLI, F. G. 1975. Tertiary marine paleotemperatures. *Geological Society of America Bulletin,* 86**,** 1499-1510.

SCHER, H. D. & MARTIN, E. E. 2006. Timing and climatic consequences of the opening of Drake Passage. *Science,* 312**,** 428-430.

SCHMIDT, J., HACKER, B. R., RATSCHBACHER, L., STÜBNER, K., STEARNS, M., KYLANDER-CLARK, A., COTTLE, J. M., ALEXANDER, A., WEBB, G., GEHRELS, G. & MINAEV, V. 2011. Cenozoic deep crust in the Pamir. *Earth and Planetary Science Letters,* 312**,** 411-421.

SCHOENE, B. 2014. U-Th-Pb Geochronology. *Treatise on Geochemistry* 4**,** 341-378.

SCHUBERT, B. A. & JAHREN, A. H. 2012. The effect of atmospheric CO 2 concentration on carbon isotope fractionation in C 3 land plants. *Geochimica et Cosmochimica Acta,* 96**,** 29-43.

SCHULTZ, L. G. 1964. Quantitative interpretation of mineralogical composition from X-ray and chemical data for the Pierre Shale. *Professional Paper*. USGS Nubered Series.

SCHURR, B., HABERLAND, C., SIPPL, C., YUAN, X., MECHIE, J., SCHNEIDER, F. & TEAM, T. Imaging continental collision and subduction in the Pamir mountain range, Central Asia, by seismic attenuation tomography. EGU General Assembly Conference Abstracts, 2014a. 13637.

SCHURR, B., RATSCHBACHER, L., SIPPL, C., GLOAGUEN, R., YUAN, X. & MECHIE, J. 2014b. Seismotectonics of the Pamir. *Tectonics,* 33**,** 1501-1518.

SCHWAB, M., RATSCHBACHER, L., SIEBEL, W., MCWILLIAMS, M., MINAEV, V., LUTKOV, V., CHEN, F., STANEK, K., NELSON, B., FRISCH, W. & WOODEN, J. L. 2004. Assembly of the Pamirs: Age and origin of magmatic belts from the southern Tien Shan to the southern Pamirs and their relation to Tibet. *Tectonics,* 23**,** TC4002.

SEARLE, M., WEINBERG, R. & DUNLAP, W. 1998. Transpressional tectonics along the Karakoram fault zone, northern Ladakh: constraints on Tibetan extrusion. *Geological Society, London, Special Publications,* 135**,** 307-326.

SEARLE, M., WINDLEY, B., COWARD, M., COOPER, D., REX, A., REX, D., TINGDONG, L., XUCHANG, X., JAN, M. & THAKUR, V. 1987. The closing of Tethys and the tectonics of the Himalaya. *Geological Society of America Bulletin,* 98**,** 678-701.

SEARLE, M. P. 1986. Structural evolution and sequence of thrusting in the High Himalayan, Tibetan—Tethys and Indus suture zones of Zanskar and Ladakh, Western Himalaya. *Journal of Structural Geology,* 8**,** 923-936.

SEARLE, M. P. 1996. Geological evidence against large-scale pre-Holocene offsets along the Karakoram Fault: Implications for the limited extrusion of the Tibetan plateau. *Tectonics,* 15**,** 171-186.

SEEBER, L. & ARMBRUSTER, J. 1984. Some elements of continental subduction along the Himalayan front. *Tectonophysics,* 105**,** 263-278.

SEEBER, L. & PÊCHER, A. 1998. Strain partitioning along the Himalayan arc and the Nanga Parbat antiform. *Geology,* 26**,** 791-794.

SEN, K., MUKHERJEE, B. K. & COLLINS, A. S. 2014. Interplay of deformation and magmatism in the Pangong Transpression Zone, eastern Ladakh, India: Implications for remobilization of the trans-Himalayan magmatic arc and initiation of the Karakoram Fault. *Journal of Structural Geology,* 62**,** 13-24.

SENGÖR, A. C. & NATAL'IN, B. A. 1996. Turkic-type orogeny and its role in the making of the continental crust. *Annual Review of Earth and Planetary Sciences,* 24**,** 263-337.

SHACKLETON, N. J. & KENNETT, J. P. 1975. Paleotemperature history of the Cenozoic and the initiation of Antarctic glaciation: oxygen and carbon isotope analyses in DSDP Sites 277, 279, and 281. *Initial reports of the deep sea drilling project,* 29**,** 743-755.

SHEN, Z. K., WANG, M., LI, Y., JACKSON, D. D., YIN, A., DONG, D. & FANG, P. 2001. Crustal deformation along the Altyn Tagh fault system, western China, from GPS. *Journal of Geophysical Research: Solid Earth,* 106**,** 30607-30621.

SIPPL, C., SCHURR, B., YUAN, X., MECHIE, J., SCHNEIDER, F., GADOEV, M., ORUNBAEV, S., OIMAHMADOV, I., HABERLAND, C. & ABDYBACHAEV, U. 2013. Geometry of the Pamir-Hindu Kush intermediate-depth earthquake zone from local seismic data. *Journal of Geophysical Research: Solid Earth,* 118**,** 1438-1457.

SLÁMA, J., KOŠLER, J., CONDON, D. J., CROWLEY, J. L., GERDES, A., HANCHAR, J. M., HORSTWOOD, M. S., MORRIS, G. A., NASDALA, L. & NORBERG, N. 2008. Plešovice zircon—a new natural reference material for U–Pb and Hf isotopic microanalysis. *Chemical Geology,* 249**,** 1-35.

SLATER, C., PRESTON, T. & WEAVER, L. T. 2001. Stable isotopes and the international system of units. *Rapid Communications in Mass Spectrometry,* 15**,** 1270-1273.

SOBEL, E. 1995. *Basin analysis and apatite fission-track thermochronology of the Jurassic-Paleogene southwest Tarim basin, NW China.* PhD, Stanford University.

SOBEL, E. R. 1999. Basin analysis of the Jurassic–Lower Cretaceous southwest Tarim basin, northwest China. *Geological Society of America Bulletin,* 111**,** 709-724.

SOBEL, E. R. & ARNAUD, N. 1999. A possible middle Paleozoic suture in the Altyn Tagh, NW China. *Tectonics,* 18**,** 64-74.

SOBEL, E. R., ARNAUD, N., JOLIVET, M., RITTS, B. D. & BRUNEI, M. 2001. Jurassic to Cenozoic exhumation history oftheAltyn Tagh range, northwest China, constrained by 40Ar/39Ar and apatite fission track thermochronology. *Paleozoic and Mesozoic tectonic evolution of central and eastern Asia,* 194**,** 247.

SOBEL, E. R., CHEN, J. & HEERMANCE, R. V. 2006. Late Oligocene–Early Miocene initiation of shortening in the Southwestern Chinese Tian Shan: Implications for Neogene shortening rate variations. *Earth and Planetary Science Letters,* 247**,** 70-81.

SOBEL, E. R., CHEN, J., SCHOENBOHM, L. M., THIEDE, R., STOCKLI, D. F., SUDO, M. & STRECKER, M. R. 2013. Oceanic-style subduction controls late Cenozoic deformation of the Northern Pamir orogen. *Earth and Planetary Science Letters,* 363**,** 204-218.

SOBEL, E. R. & DUMITRU, T. A. 1997. Thrusting and exhumation around the margins of the western Tarim basin during the India-Asia collision. *Journal of Geophysical Research: Solid Earth,* 102**,** 5043-5063.

SOBEL, E. R., SCHOENBOHM, L. M., CHEN, J., THIEDE, R., STOCKLI, D. F., SUDO, M. & STRECKER, M. R. 2011. Late Miocene–Pliocene deceleration of dextral slip between Pamir and Tarim: Implications for Pamir orogenesis. *Earth and Planetary Science Letters,* 304**,** 369-378.

SOTO, R., LARRASOAÑA, J. C., ARLEGUI, L. E., BEAMUD, E., OLIVA-URCIA, B. & SIMÓN, J. L. 2009. Reliability of magnetic fabric of weakly deformed mudrocks as a palaeostress indicator in compressive settings. *Journal of Structural Geology,* 31**,** 512-522.

STAISCH, L. M., NIEMI, N. A., CLARK, M. K. & CHANG, H. 2016. Eocene to late Oligocene history of crustal shortening within the Hoh Xil Basin and implications for the uplift history of the northern Tibetan Plateau. *Tectonics,* 35**,** 862-895.

STEARNS, M., HACKER, B., RATSCHBACHER, L., RUTTE, D. & KYLANDER-CLARK, A. 2015. Titanite petrochronology of the Pamir gneiss domes:

Implications for middle to deep crust exhumation and titanite closure to Pb and Zr diffusion. *Tectonics,* 34**,** 784-802.

STEARNS, M. A., HACKER, B. R., RATSCHBACHER, L., LEE, J., COTTLE, J. M. & KYLANDER-CLARK, A. 2013. Synchronous Oligocene–Miocene metamorphism of the Pamir and the north Himalaya driven by plate-scale dynamics. *Geology,* 41**,** 1071-1074.

STECKLER, M. & WATTS, A. 1978. Subsidence of the Atlantic-type continental margin off New York. *Earth and Planetary Science Letters,* 41**,** 1-13.

STRECKER, M. R., FRISCH, W., HAMBURGER, M. W., RATSCHBACHER, L., SEMILETKIN, S., ZAMORUYEV, A. & STURCHIO, N. 1995. Quaternary deformation in the Eastern Pamirs, Tadzhikistan and Kyrgyzstan. *Tectonics,* 14**,** 1061-1079.

STÜBNER, K., RATSCHBACHER, L., RUTTE, D., STANEK, K., MINAEV, V., WIESINGER, M. & GLOAGUEN, R. 2013a. The giant Shakhdara migmatitic gneiss dome, Pamir, India-Asia collision zone: 1. Geometry and kinematics. *Tectonics,* 32**,** 948-979.

STÜBNER, K., RATSCHBACHER, L., WEISE, C., CHOW, J., HOFMANN, J., KHAN, J., RUTTE, D., SPERNER, B., PFÄNDER, J. A., HACKER, B. R., DUNKL, I., TICHOMIROWA, M., STEARNS, M. A., BAHRAM, I., GADOEV, M., GLOAGUEN, R., JONCKHEERE, R., KANAEV, E., MINAEV, V., OIMAHMADOC, I., RAJABOV, N. & STANEK, K. P. 2013b. The giant Shakhdara migmatitic gneiss dome, Pamir, India–Asia collision zone, II: Timing of dome formation. *Tectonics,* 32**,** 1404-1431.

SUN, D., BLOEMENDAL, J., YI, Z., ZHU, Y., WANG, X., ZHANG, Y., LI, Z., WANG, F., HAN, F. & ZHANG, Y. 2011. Palaeomagnetic and palaeoenvironmental study of two parallel sections of late Cenozoic strata in the central Taklimakan Desert: Implications for the desertification of the Tarim Basin. *Palaeogeography, Palaeoclimatology, Palaeoecology,* 300**,** 1-10.

SUN, J., ALLOWAY, B., FANG, X. & WINDLEY, B. F. 2015. Refuting the evidence for an earlier birth of the Taklimakan Desert. *Proceedings of the National Academy of Sciences,* 112**,** E5556-E5557.

SUN, J. & JIANG, M. 2013. Eocene seawater retreat from the southwest Tarim Basin and implications for early Cenozoic tectonic evolution in the Pamir Plateau. *Tectonophysics,* 588**,** 27-38.

SUN, J. & LIU, T. 2006. The age of the Taklimakan Desert. *Science,* 312**,** 1621-1621.

SUN, J., LÜ, T., GONG, Y., LIU, W., WANG, X. & GONG, Z. 2013. Effect of aridification on carbon isotopic variation and ecologic evolution at 5.3 Ma in the Asian interior. *Earth and Planetary Science Letters,* 380**,** 1-11.

SUN, J., WINDLEY, B. F., ZHANG, Z., FU, B. & LI, S. 2016a. Diachronous seawater retreat from the southwestern margin of the Tarim Basin in the late Eocene. *Journal of Asian Earth Sciences,* 116**,** 222-231.

SUN, J., XIAO, W., WINDLEY, B. F., JI, W., FU, B., WANG, J. & JIN, C. 2016b. Provenance change of sediment input in the northeastern foreland of Pamir related to collision of the Indian Plate with the Kohistan-Ladakh arc at around 47 Ma. *Tectonics,* 35**,** 315-338.

SUN, J., XU, Q. & HUANG, B. 2007. Late Cenozoic magnetochronology and paleoenvironmental changes in the northern foreland basin of the Tian Shan Mountains. *Journal of Geophysical Research: Solid Earth,* 112**,** 1-14.

SUN, J., YE, J., WU, W., NI, X., BI, S., ZHANG, Z., LIU, W. & MENG, J. 2010. Late Oligocene–Miocene mid-latitude aridification and wind patterns in the Asian interior. *Geology,* 38**,** 515-518.

SUN, J. & ZHANG, Z. 2008. Palynological evidence for the mid-Miocene climatic optimum recorded in Cenozoic sediments of the Tian Shan Range, northwestern China. *Global and Planetary Change,* 64**,** 53-68.

SUN, J., ZHANG, Z. & ZHANG, L. 2009. New evidence on the age of the Taklimakan Desert. *Geology,* 37**,** 159-162.

SUN, J., ZHU, R. & AN, Z. 2005. Tectonic uplift in the northern Tibetan Plateau since 13.7 Ma ago inferred from molasse deposits along the Altyn Tagh Fault. *Earth and Planetary Science Letters,* 235**,** 641-653.

SUN, J., ZHU, R. & BOWLER, J. 2004. Timing of the Tianshan Mountains uplift constrained by magnetostratigraphic analysis of molasse deposits. *Earth and Planetary Science Letters,* 219**,** 239-253.

SUN, X. & WANG, P. 2005. How old is the Asian monsoon system?—Palaeobotanical records from China. *Palaeogeography, Palaeoclimatology, Palaeoecology,* 222**,** 181-222.

TAGAMI, T., CARTER, A. & HURFORD, A. J. 1996. Natural long-term annealing of the zircon fission-track system in Vienna Basin deep borehole samples: constraints upon the partial annealing zone and closure temperature. *Chemical Geology,* 130**,** 147-157.

TAGAMI, T., GALBRAITH, R. F., YAMADA, G. M. & LASLETT, G. M. (eds.) 1998. *Revised annealing kinetics of fission-tracks in zircon and geological implications.,* Amsterdam: Kluwer Academic Press.

TAHIRKHELI, R. K. & JAN, M. 1979. Geology of Kohistan: Karakoram Himalaya, Northern Pakistan. *Geol. Bull. Univ. Peshawar, Spec. Issue,* 13**,** 1-187.

TANG, T., YANG, H., LAN, X., YU, C., XUE, Y., ZHANG, Y., HU, L., ZHONG, S., AND WEI, J. 1989. Marine late Cretaceous and Early Tertiary Stratigraphy and Petroleum Geology in Western Tarim Basin, China. *Science Press, Beijing***,** 133-140.

TANG, Z., DONG, X., WANG, X. & DING, Z. 2015. Oligocene-Miocene magnetostratigraphy and magnetic anisotropy of the Baxbulak section from the Pamir-Tian Shan convergence zone. *Geochemistry, Geophysics, Geosystems,* 16**,** 3575-3592.

TAPPONNIER, P., MATTAUER, M., PROUST, F. & CASSAIGNEAU, C. 1981. Mesozoic ophiolites, sutures, and arge-scale tectonic movements in Afghanistan. *Earth and Planetary Science Letters,* 52**,** 355-371.

TAPPONNIER, P. & MOLNAR, P. 1976. Slip-line field theory and large-scale continental tectonics. *Nature,* 264**,** 319-324.

TAPPONNIER, P. & MOLNAR, P. 1977. Active faulting and tectonics in China. *Journal of Geophysical Research,* 82**,** 2905-2930.

TAPPONNIER, P., PELTZER, G. & ARMIJO, R. 1986. On the mechanics of the collision between India and Asia. *Geological Society, London, Special Publications,* 19**,** 113-157.

TAPPONNIER, P., ZHIQIN, X., ROGER, F., MEYER, B., ARNAUD, N., WITTLINGER, G. & JINGSUI, Y. 2001. Oblique stepwise rise and growth of the Tibet Plateau. *science,* 294**,** 1671-1677.

TARLING, D. & HROUDA, F. 1993. *Magnetic anisotropy of rocks,* Suffolk, Chapman and Hall.

TAUXE, L. 1998. Paleomagnetic principles and practice. Modern approaches in geophysics *Dordrecht ; Boston: Kluwer Academic Publishers* 299pp.

TCHERKEZ, G. G., FARQUHAR, G. D. & ANDREWS, T. J. 2006. Despite slow catalysis and confused substrate specificity, all ribulose bisphosphate carboxylases may be nearly perfectly optimized. *Proceedings of the National Academy of Sciences,* 103**,** 7246-7251.

TENG, Z., YUE, L., PU, R., DENG, X. & BIAN, X. 1996. The magnetostratigraphic age of the Xiyu Formation. *Geol. Rev,* 42**,** 481-489.

THIEDE, R. C., SOBEL, E. R., CHEN, J., SCHOENBOHM, L. M., STOCKLI, D. F., SUDO, M. & STRECKER, M. R. 2013. Late Cenozoic extension and crustal doming in the India-Eurasia collision zone: New thermochronologic constraints from the NE Chinese Pamir. *Tectonics,* 32**,** 763-779.

THIRY, M. 2000. Palaeoclimatic interpretation of clay minerals in marine deposits: an outlook from the continental origin. *Earth-Science Reviews,* 49**,** 201-221.

THOMAS, J., GAPAIS, D., COBBOLD, P., MEYER, V. & BURTMAN, V. 1996. Tertiary kinematics of the Tadjik Depression (Central Asia): inferences from fault and fold patterns. *Geodynamic Evolution of Sedimentary Basins. Editions Technip, Paris***,** 171-180.

TIAN, Z., CHAI, G. & KANG, Y. 1989. Tectonic evolution of the Tarim basin. In: Zhu, X. (Ed.),Chinese Sedimentary Basins *Sedimentary Basins of the World***,** 33-42.

TIESZEN, L. L. 1991. Natural variations in the carbon isotope values of plants: implications for archaeology, ecology, and paleoecology. *Journal of Archaeological Science,* 18**,** 227-248.

TIPPLE, B. J. & PAGANI, M. 2007. The early origins of terrestrial C4 photosynthesis. *Annu. Rev. Earth Planet. Sci.,* 35**,** 435-461.

TORSVIK, T. H., MULLER, R. D., VAN DER VOO, R., STEINBERGER, B. A. & GAINA, C. 2008. Global Plate Miotion Frames: Toward a Unified Model. *Reviews of Geophysics,* 46.

TRIFONOV, V. G. 1978. Late Quaternary tectonic movements of western and central Asia. *Geological society of America bulletin,* 89**,** 1059-1072.

UNO, I., EGUCHI, K., YUMIMOTO, K., TAKEMURA, T., SHIMIZU, A., UEMATSU, M., LIU, Z., WANG, Z., HARA, Y. & SUGIMOTO, N. 2009. Asian dust transported one full circuit around the globe. *Nature Geoscience,* 2**,** 557-560.

VALLI, F., LELOUP, P. H., PAQUETTE, J. L., ARNAUD, N., LI, H., TAPPONNIER, P., LACASSIN, R., GUILLOT, S., LIU, D. & DELOULE, E. 2008. New U-Th/Pb constraints on timing of shearing and long-term slip-rate on the Karakorum fault. *Tectonics,* 27.

VAN HINSBERGEN, D. J., KAPP, P., DUPONT-NIVET, G., LIPPERT, P. C., DECELLES, P. G. & TORSVIK, T. H. 2011. Restoration of Cenozoic deformation in Asia and the size of Greater India. *Tectonics,* 30.

VAN HINSBERGEN, D. J., LIPPERT, P. C., DUPONT-NIVET, G., MCQUARRIE, N., DOUBROVINE, P. V., SPAKMAN, W. & TORSVIK, T. H. 2012. Greater India Basin hypothesis and a two-stage Cenozoic collision between India and Asia. *Proceedings of the National Academy of Sciences,* 109**,** 7659-7664.

VAN HINTE, J. 1978. Geohistory analysis--application of micropaleontology in exploration geology. *AAPG Bulletin,* 62**,** 201-222.

VANDAMME, D. 1994. A new method to determine paleosecular variation. *Physics of the Earth and Planetary Interiors,* 85**,** 131-142.

VERMEESCH, P. 2013. Multi-sample comparison of detrital age distributions. *Chemical Geology,* 341**,** 140-146.

VICENTE, M., ELSASS, F., MOLINA, E. & ROBERT, M. 1997. Palaeoweathering in slates from the Iberian Hercynian Massif (Spain); investigation by TEM of clay mineral signatures. *Clay Minerals,* 32**,** 435-451.

VÖGELI, N., HUYGHE, P., VAN DER BEEK, P., NAJMAN, Y., GARZANTI, E. & CHAUVEL, C. 2017. Weathering regime in the Eastern Himalaya since the mid-Miocene: Indications from detrital geochemistry and clay mineralogy of the Kameng River Section, Arunachal Pradesh, India. *Basin Research,* 1-16.

VOLKMER, J. E., KAPP, P., GUYNN, J. H. & LAI, Q. 2007. Cretaceous-Tertiary structural evolution of the north central Lhasa terrane, Tibet. *Tectonics,* 26.

WANG, C., HONG, H., ABELS, H. A., LI, Z., CAO, K., YIN, K., SONG, B., XU, Y., JI, J. & ZHANG, K. 2016. Early middle Miocene tectonic uplift of the northwestern part of the Qinghai–Tibetan Plateau evidenced by geochemical and mineralogical records in the western Tarim Basin. *International Journal of Earth Sciences,* 105**,** 1021-1037.

WANG, C., HONG, H., LI, Z., YIN, K., XIE, J., LIANG, G., SONG, B., SONG, E. P. & ZHANG, K. 2013. The Eocene–Oligocene climate transition in the Tarim Basin, Northwest China: Evidence from clay mineralogy. *Applied Clay Science,* 74**,** 10-19.

WANG, E. 1997. Displacement and timing along the northern strand of the Altyn Tagh fault zone, northern Tibet. *Earth and Planetary Science Letters,* 150**,** 55-64.

WANG, E., WAN, J. & LIU, J. 2003. Late Cenozoic geological evolution of the foreland basin bordering the West Kunlun range in Pulu area: Constraints on timing of uplift of northern margin of the Tibetan Plateau. *Journal of Geophysical Research: Solid Earth,* 108**,** 2401.

WANG, P. 1990. Neogene stratigraphy and paleoenvironments of China. *Palaeogeography, Palaeoclimatology, Palaeoecology,* 77**,** 315-334.

WANG, Q., NISHIDAI, T. & COWARD, M. 1992. The Tarim Basin, NW China: formation and aspects of petroleum geology. *Journal of Petroleum Geology,* 15**,** 5-34.

WANG, S. & PENG, S. 2013. Regional Geological Survey reports People's Republic of China, 1: 250.000 Yecheng pieces J43C003004, Chinese Edition. *Chinese Geology University Press***,** 183 pp.

WANG, X., SUN, D., CHEN, F., WANG, F., LI, B., POPOV, S. V., WU, S., ZHANG, Y. & LI, Z. 2014. Cenozoic paleo-environmental evolution of the Pamir–Tien Shan convergence zone. *Journal of Asian Earth Sciences,* 80**,** 84-100.

WANG, Z. & WANG, X. 2016. Late Cenozoic Deformation Sequence of a Thrust System along the Eastern Margin of Pamir, Northwest China. *Acta Geologica Sinica (English Edition),* 90**,** 1664-1678.

WARR, L. & RICE, A. 1994. Interlaboratory standardization and calibration of day mineral crystallinity and crystallite size data. *Journal of metamorphic Geology,* 12**,** 141-152.

WEI, H.-H., MENG, Q.-R., DING, L. & LI, Z.-Y. 2013. Tertiary evolution of the western Tarim basin, northwest China: a tectono-sedimentary response to northward indentation of the Pamir salient. *Tectonics,* 32**,** 558-575.

WHITE, A. F. & BRANTLEY, S. L. 1995. Chemical weathering rates of silicate minerals: an overview. *Chemical Weathering Rates of Silicate Minerals,* 31**,** 1-22.

WIEDENBECK, M., HANCHAR, J. M., PECK, W. H., SYLVESTER, P., VALLEY, J., WHITEHOUSE, M., KRONZ, A., MORISHITA, Y., NASDALA, L. & FIEBIG, J. 2004. Further characterisation of the 91500 zircon crystal. *Geostandards and Geoanalytical Research,* 28**,** 9-39.

WILKE, F. D., SOBEL, E. R., O'BRIEN, P. J. & STOCKLI, D. F. 2012. Apatite fission track and (U–Th)/He ages from the higher Himalayan crystallines, Kaghan Valley, Pakistan: implications for an eocene plateau and oligocene to pliocene exhumation. *Journal of Asian Earth Sciences,* 59**,** 14-23.

WINDLEY, B. 1988. Tectonic framework of the Himalaya, Karakoram and Tibet, and problems of their evolution. *Philosophical Transactions of the Royal Society of London. Series A, Mathematical and Physical Sciences***,** 3-16.

WINDLEY, B. F., ALEXEIEV, D., XIAO, W., KRÖNER, A. & BADARCH, G. 2007. Tectonic models for accretion of the Central Asian Orogenic Belt. *Journal of the Geological Society,* 164**,** 31-47.

WITTLINGER, G., TAPPONNIER, P., POUPINET, G., MEI, J., DANIAN, S., HERQUEL, G. & MASSON, F. 1998. Tomographic evidence for localized lithospheric shear along the Altyn Tagh fault. *Science,* 282**,** 74-76.

WRIGHT, J. D. & MILLER, K. G. 1993. Southern Ocean Influences on Late Eocene to Miocene Deepwater Circulation. *The Antarctic paleoenvironment: a perspective on global change,* 60**,** 1-25.

WU, F.-Y., JI, W.-Q., WANG, J.-G., LIU, C.-Z., CHUNG, S.-L. & CLIFT, P. D. 2014. Zircon U–Pb and Hf isotopic constraints on the onset time of India-Asia collision. *American Journal of Science,* 314**,** 548-579.

WU, G., LIU, Y., DONG, B., LIANG, X., DUAN, A., BAO, Q. & YU, J. 2012. Revisiting Asian monsoon formation and change associated with Tibetan Plateau forcing: I. Formation. *Climate dynamics,* 39**,** 1169-1181.

XIAO, G., GUO, Z., DUPONT-NIVET, G., LU, H., WU, N., GE, J., HAO, Q., PENG, S., LI, F. & ABELS, H. A. 2012a. Evidence for northeastern Tibetan Plateau uplift between 25 and 20Ma in the sedimentary archive of the Xining Basin, Northwestern China. *Earth and Planetary Science Letters,* 317**,** 185-195.

XIAO, S., MCFADDEN, K. A., PEEK, S., KAUFMAN, A. J., ZHOU, C., JIANG, G. & HU, J. 2012b. Integrated chemostratigraphy of the Doushantuo Formation at the northern Xiaofenghe section (Yangtze Gorges, South China) and its implication for Ediacaran stratigraphic correlation and ocean redox models. *Precambrian Research,* 192–195**,** 125-141.

XIAO, W., HAN, F., WINDLEY, B. F., YUAN, C., ZHOU, H. & LI, J. 2003. Multiple Accretionary Orogenesis and Episodic Growth of Continents: Insights from the Western Kunlun Range, Central Asia. *International Geology Review,* 45**,** 303-328.

XIAO, W. J., WINDLEY, B. F., CHEN, H. L., ZHANG, G. C. & LI, J. L. 2002. Carboniferous-Triassic subduction and accretion in the western Kunlun, China: Implications for the collisional and accretionary tectonics of the northern Tibetan Plateau. *Geology,* 30**,** 295-298.

YANG, W., DUPONT-NIVET, G., JOLIVET, M., GUO, Z., BOUGEOIS, L., BOSBOOM, R., ZHANG, Z., ZHU, B. & HEILBRONN, G. 2015. Magnetostratigraphic record of the early evolution of the southwestern Tian Shan foreland basin (Ulugqat area), interactions with Pamir indentation and India–Asia collision. *Tectonophysics,* 644**,** 122-137.

YANG, W., JOLIVET, M., DUPONT-NIVET, G. & GUO, Z. 2014. Mesozoic–Cenozoic tectonic evolution of southwestern Tian Shan: Evidence from detrital zircon U/Pb and apatite fission track ages of the Ulugqat area, Northwest China. *Gondwana Research,* 26**,** 986-1008.

YANG, W., JOLIVET, M., DUPONT-NIVET, G., GUO, Z., ZHANG, Z. & WU, C. 2013. Source to sink relations between the Tian Shan and Junggar Basin (northwest China) from Late Palaeozoic to Quaternary: evidence from detrital U-Pb zircon geochronology. *Basin Research,* 25**,** 219-240.

YANG, Y. & LIU, M. 2002. Cenozoic deformation of the Tarim plate and the implications for mountain building in the Tibetan Plateau and the Tian Shan. *Tectonics,* 21**,** 1059.

YIN, A. & HARRISON, T. M. 2000. Geologic evolution of the Himalayan-Tibetan orogen. *Annual Review of Earth and Planetary Sciences,* 28**,** 211-280.

YIN, A., ROBINSON, A. & MANNING, C. Oroclinal bending and slab-break-off causing coeval east-west extension and east-west contraction in the Pamir-

Nanga Parbat syntaxis in the past 10 my. AGU Fall Meeting Abstracts, 2001. 03.

YIN, A., RUMELHART. P, BUTLER. R, E., E;, C., HARRISON.T.M, A;, F. D., R.V;, I., ZHANG;, Q., XIAN-QIANG, Z., XIAO-FENG, W., HANSON, A. & RAZA, A. 2002. Tectonic history of the Altyn Tagh fault system in the northern Tibet inferred from Cenozoic sedimentation. *Geological Society of America Bulletin,* 114**,** 1257-1295.

YOUNGUN, Y. & HSÜ, K. 1994. Origin of the Kunlun Mountains by arc-arc and arc-continent collisions. *Island Arc,* 3**,** 75-89.

YUAN, D. Y., GE, W. P., CHEN, Z. W., LI, C. Y., WANG, Z. C., ZHANG, H. P., ZHANG, P. Z., ZHENG, D. W., ZHENG, W. J. & CRADDOCK, W. H. 2013. The growth of northeastern Tibet and its relevance to large-scale continental geodynamics: A review of recent studies. *Tectonics,* 32**,** 1358-1370.

YUAN, W., DONG, J., SHICHENG, W. & CARTER, A. 2006. Apatite fission track evidence for Neogene uplift in the eastern Kunlun Mountains, northern Qinghai–Tibet Plateau, China. *Journal of Asian Earth Sciences,* 27**,** 847-856.

YUE, Y., GRAHAM, S. A., RITTS, B. D. & WOODEN, J. L. 2005. Detrital zircon provenance evidence for large-scale extrusion along the Altyn Tagh fault. *Tectonophysics,* 406**,** 165-178.

ZACHOS, J., PAGANI, M., SLOAN, L., THOMAS, E. & BILLUPS, K. 2001. Trends, Rhythms, and Aberrations in Global Climate 65 Ma to Present. *Science,* 292**,** 686-693.

ZACHOS, J. C., STOTT, L. D. & LOHMANN, K. C. 1994. Evolution of early Cenozoic marine temperatures. *Paleoceanography,* 9**,** 353-387.

ZAHRT, J. D. 1983. X-ray polarization: Bragg diffraction and X-ray fluorescence. *Advances in X-Ray Analysis*. New York: Springer.

ZAN, J., FANG, X., YAN, M., ZHANG, W. & LU, Y. 2015. Lithologic and rock magnetic evidence for the Mid-Miocene Climatic Optimum recorded in the sedimentary archive of the Xining Basin, NE Tibetan Plateau. *Palaeogeography, Palaeoclimatology, Palaeoecology,* 431**,** 6-14.

ZHANG, K.-J., ZHANG, Y.-X., LI, B. & ZHONG, L.-F. 2007a. Nd isotopes of siliciclastic rocks from Tibet, western China: constraints on provenance and pre-Cenozoic tectonic evolution. *Earth and Planetary Science Letters,* 256**,** 604-616.

ZHANG, P., MOLNAR, P. & DOWNS, W. R. 2001. Increased sedimentation rates and grain sizes 2-4 Myr ago due to the influence of climate change on erosion rates. *Nature,* 410**,** 891.

ZHANG, Y., NIU, Y., HU, Y., LIU, J., YE, L., KONG, J. & DUAN, M. 2015. The syncollisional granitoid magmatism and continental crust growth in the West Kunlun Orogen, China–Evidence from geochronology and geochemistry of the Arkarz pluton. *Lithos,* 245**,** 191-204.

ZHANG, Y. G., PAGANI, M., LIU, Z., BOHATY, S. M. & DECONTO, R. 2013. A 40 million year history of atmospheric CO_2. *Philosophical Transactions of the*

Royal Society a-Mathematical Physical and Engineering Sciences, 371**,** 201330096.

ZHANG, Z., FLATØY, F., WANG, H., BETHKE, I., BENTSEN, M. & GUO, Z. 2012. Early Eocene Asian climate dominated by desert and steppe with limited monsoons. *Journal of Asian Earth Sciences,* 44**,** 24-35.

ZHANG, Z., HUIJUN, W., ZHENGTANG, G. & DABANG, J. 2007b. Impacts of tectonic changes on the reorganization of the Cenozoic paleoclimatic patterns in China. *Earth and Planetary Science Letters,* 257**,** 622-634.

ZHANG, Z., WANG, H., GUO, Z. & JIANG, D. 2007c. What triggers the transition of palaeoenvironmental patterns in China, the Tibetan Plateau uplift or the Paratethys Sea retreat? *Palaeogeography, Palaeoclimatology, Palaeoecology,* 245**,** 317-331.

ZHAO, H., WEI, Y., SHEN, Y., XIAO, A., MAO, L., WANG, L., GUAN, J. & WU, L. 2016. Cenozoic tilting history of the south slope of the Altyn Tagh as revealed by seismic profiling: Implications for the kinematics of the Altyn Tagh fault bounding the northern margin of the Tibetan Plateau. *Geosphere,* 12**,** 884-899.

ZHAO, W. L. & MORGAN, W. J. 1987. Injection of Indian crust into Tibetan lower crust: A two-dimensional finite element model study. *Tectonics,* 6**,** 489-504.

ZHENG, H., HUANG, X. & BUTCHER, K. 2006. Lithostratigraphy, petrography and facies analysis of the Late Cenozoic sediments in the foreland basin of the West Kunlun. *Palaeogeography, Palaeoclimatology, Palaeoecology,* 241**,** 61-78.

ZHENG, H., POWELL, C. M., AN, Z., ZHOU, J. & DONG, G. 2000. Pliocene uplift of the northern Tibetan Plateau. *Geology,* 28**,** 715-718.

ZHENG, H., TADA, R., JIA, J., LAWRENCE, C. & WANG, K. 2010. Cenozoic sediments in the southern Tarim Basin: implications for the uplift of northern Tibet and evolution of the Taklimakan Desert. *Geological Society, London, Special Publications,* 342**,** 67-78.

ZHENG, H., WEI, X., TADA, R., CLIFT, P. D., WANG, B., JOURDAN, F., WANG, P. & HE, M. 2015a. Late Oligocene–early Miocene birth of the Taklimakan Desert. *Proceedings of the National Academy of Sciences,* 112**,** 7662-7667.

ZHENG, H., WEI, X., TADA, R., CLIFT, P. D., WANG, B., JOURDAN, F., WANG, P. & HE, M. 2015b. Reply to Sun et al.: Confirming the evidence for Late Oligocene− Early Miocene birth of the Taklimakan Desert. *Proceedings of the National Academy of Sciences,* 112**,** E5558-E5559.

ZHOU, Z. Y. 2000. *Stratigraphy of the Tarim Basin,* Beijing, Beijing Science Press.

ZUBOVICH, A., SCHÖNE, T., METZGER, S., MOSIENKO, O., MUKHAMEDIEV, S., SHARSHEBAEV, A. & ZECH, C. 2016. Tectonic interaction between the Pamir and Tien Shan observed by GPS. *Tectonics,* 35**,** 283-292.

ZUZA, A. V., CHENG, X. & YIN, A. 2016. Testing models of Tibetan Plateau formation with Cenozoic shortening estimates across the Qilian Shan–Nan Shan thrust belt. *Geosphere,* 12**,** 501-532.

9. Table of Figures

10. Supplementary Material

Appendix 1 – Full sample list with ages

Appendix 2 - full sample and field log location diagram

Appendix 3 - Full Paleomagnetic dataset

Appendix 4 – Backstripping dataset

Appendix 5 - Rotational dataset

Appendix 6 – εNd dataset

Appendix 7 – Chapter 4 SI file

Appendix 8 – Petrography and heavy mineral analysis dataset

Appendix 9 – Zircon U-Pb dataset

Appendix 10 – Zircon fission track dataset

Appendix 11 – Zircon U-Pb and zircon fission track double dating dataset

Appendix 12 – X-Ray florescence dataset

Appendix 13 – X-Ray diffraction dataset

Appendix 14 – Clay mineralogy dataset

Appendix 15 – Organic carbon dataset

Appendix 16 – Anisotropy of magnetic susceptibility dataset

Appendix 17 – Chapter 5 methods

Appendix 18 – Conglomerate clast counts for the Aertashi section

Supplementary item 1 - Magnetic susceptibility figure

Supplementary item 2 – Unit D thickening figure

Supplementary item 3 Accumulation rate diagram

Supplementary item 4 Comparison figure for Kent – Corson et al (2009) dataset